Order Number 9507291

An investigation of the dynamics of the mesopause: Fabry-Perot observations of winds and temperatures from nightglow emissions

Conner, James F., Ph.D.

University of Alaska Fairbanks, 1994

U·M·I
300 N. Zeeb Rd.
Ann Arbor, MI 48106

AN INVESTIGATION OF THE DYNAMICS OF THE MESOPAUSE: FABRY-PEROT OBSERVATIONS OF WINDS AND TEMPERATURES FROM NIGHTGLOW EMISSIONS

A

THESIS

Presented to the Faculty of the University of Alaska

in Partial Fulfillment of the Requirements

for the Degree of

DOCTOR OF PHILOSOPHY

By

James F. Conner, B.S.

Fairbanks, Alaska

May 1994

AN INVESTIGATION OF THE DYNAMICS OF THE MESOPAUSE:
FABRY-PEROT OBSERVATIONS OF WINDS AND TEMPERATURES
FROM NIGHTGLOW EMISSIONS

by

James F. Conner

RECOMMENDED:

R. W. Smith, Chairman, Advisory Committee

Physics Department Head

APPROVED:

Dean of the College of Natural Sciences

Dean of the Graduate School

April 7, 1994

Date

Abstract

This work is a study of the behavior of tidal and planetary waves in the upper-middle atomosphere near the geographic south pole. This is accomplished with a characterization of the dynamic state of these motions. I used ground-based Fabry-Perot Spectrometer (FPS) measurements of the multiple-line, $P_1(2)_{c,d}$, nightglow emissions from the $X^2\Pi$ band of the neutral OH^* molecule. I developed analytical techniques to determine a space and time distribution of spectral amplitudes and phases for the dynamic parameters of kinetic temperature and neutral wind in the OH^* layer.

Spectral analysis of the variations in this layer indicates the existence of two groups: a planetary wave group (periods of ~1-10 days), with eastward phase progression, and a near semi-diurnal group (periods of ~8-13 hours), with westward phase progression. Specific periods vary slightly for different years; this is most likely due to remote propagation conditions. Further separation of each group shows the wind oscillations exhibit wave-number one behavior with associated wave-number zero temperature oscillations, (with a few exceptions). The periodicities in the planetary group neutral wind motions are consistent with the model results of Salby, 1984, for propagation to high latitudes through realistic mean flows.

The characterization of the dynamics of this layer has led to the discovery of a basic azimuthal asymmetry in the distribution of spectral amplitude for a given oscillation, that is, preferred azimuths. These preferred azimuths appear to be associated with changes in the direction, not the amplitude, of a cross-polar mean wind. This finding, in conjunction with the evanescence of some features, uncovered two cases of planetary wave dissipation. These occur when oscillations attempt to maintain their preferred alignment with a changing mean wind direction resulting in a decay of wind amplitude and a burst of thermal oscillation. Both cases occur at the same time. Coincident with these decays are enhancements in the wind and thermal energy of other, longer period, oscillations which share the same azimuthal preferences. Also coincident is an acceleration of the mean wind.

Table of Contents

List of Figures

Acknowledgements

I would like to thank my family: Thank you Becky for your patience and steadfast support throughout my undergraduate and graduate education. I do not understand why there does not exist a spousal Ph.D. for surviving mates, but you deserve one. Thank you Jake for helping me to keep a close watch on my priorities and to see in different ways. Thank you Zoey for keeping me on my toes all the time.

I also wish to acknowledge my advisor and friend Dr. Roger W. Smith who allowed me the time and freedom to find my own direction and then to follow it to its fruitful completion.

The data used in this thesis was the result of a collaboration between the University of Washingtion in Seattle and the University of Alaska in Fairbanks led by Dr. Gonzalo Hernandez. I thank Gonzalo Hernandez for his accessibility which led to many helpful conversations and I wish him the best of luck in his quest for the deepest and richest cup of coffee.

To some of the many friends I have made during my student life some of whom have risked their lives with me to obtain data in Svalbard, thank you for the never ending opportunity to talk Physics regardless of physical laws: Tony and Clodagh Alcock, Gerard Fasel, John Luick, Joe Minow, Gina Price, Fred Sigernes, Rodney Viereck, Gerald Walker, and Dorothy Woolum. Thank you Ilya Kornilov, you taught me Russian electronics in two days. Thank you Geir Jacobson for teaching me Norwegian.

Finally, thanks to the Northern Lights which taught me to look up in wonder as it connects *inner* to *outer* space through our terrestrial atmosphere.

This work was conducted under grants ATM86-02956, DPP-8615099, DPP-8814563, DPP-8917320, and DPP-9017484 from the National Science Foundation and AFOSR89-0316 from the Air Force Office of Scientific Research.

Foreword

The fundamental problem addressed here is a basic lack of information about the upper-middle atmosphere (UMA) near the planetary rotation poles. This lack of knowledge hinders the interpretation of observations and limits the theoretical development of global circulation models needed to account for the complexity of this region. Typical modelling efforts begin with simplifying assumptions, some of which are related to the regions near the planetary rotation poles, such as the neglect of the horizontal component of the Coriolis force in the derivation of Laplace's tidal equations from the *primative equations*. Also boundary conditions, set at the rotation poles, cannot avoid limiting the sensitivity to detailed processes.

In the absence of adequate satellite coverage the study of this problem is confined to ground-based studies. During the last few decades observational and theoretical studies related to non-polar latitudes have revealed a wide range of dynamical, radiative, and chemical processes that act (and interact) to control the circulation, thermal structure, and composition of the middle atmosphere, (Fritts, 1984, 1989; Walterscheid, 1987a,b; Viereck, 1991). Solar radiation is primarily responsible for the mean thermal forcing and structure of this region via diurnal UV absorption by O_3 in the stratosphere and mesosphere and H_2O insolation absorption in the troposphere and lower stratosphere, (Andrews et al, 1987). The importance of the dynamic structure of the atmosphere became apparent when Murgatroyd and Goody (1958) showed that the middle atmosphere, particularly in the high latitude regions, was always colder in the summer and warmer in the winter than indicated if solar UV were the only heat source. This additional forcing is now generally thought to be due to gravity wave activity, (Fritts et al, 1987, 1989; Walterschied et al., 1987a,b) however, this may not be the whole story. Gravity wave drag contributes to a minimum of the zonal mean wind near the tropopause, while increasing drag at greater heights results in reversal of the vertical shear of the zonal mean wind, closure of the mesospheric jets in the summer and winter hemispheres, and a strong vertical and meridional circulation near the high-latitude mesopause, (Fritts, 1983). This wave-driven circulation directly couples the summer and winter polar mesospheres and drives the thermal field far from radiative equilibrium with differences of -45°K and +100°K respectively, at 80 km, (from comparison of Fels (1985) and the 1986 COSPAR International Reference Atmosphere (CIRA86)). The induced diabatic circulation (the lower thermosphere polar vortex) likewise warms the winter mesopause and

reverses the mean meridional temperature gradient relative to the radiatively balanced structure at lower levels (stratospheric polar vortex).

The dissipation of planetary waves has, as yet, unknown effects. Miyahara et al. (1991) has stated that there are significant regions, (high latitude UMA), of mean heating and acceleration which are not accounted for by the effects of gravity waves and tides. He has proposed planetary waves as the source of the momentum and heat flux which would require a ducting channel between the northern and southern hemisphere's UMA region and Forbes (1992) has suggested the possibility of mid to high latitude ducting of 16-day planetary waves.

Observational studies of the dynamical properties of the southern hemisphere high-latitude middle atmosphere have been mainly based on wind data inferred from radar measurements, from optical FPS Doppler measurements in the OH layer, and from lidars. It is only in the last decade that studies of this layer over Antarctica have been made and only one contribution prior to 1987 from optical techniques, (Stubbs, et al., 1983). In general, the wind data derived from radars exhibit planetary wave, tidal, gravity wave and other fluctuations (Fraser, 1984, 1989; Fraser et al., 1992; Manson et al., 1987; Avery et al., 1989). The optical measurements have shown planetary scale, quasi-tidal, and gravity wave structure, (Sivjee et al.,1987; Williams, 1987; Price, 1987; Hernandez et al., 1992b, 1993; Collins et al., 1992). Oscillations, with periods in the range 2, 3-5, and 15-20 days, have been reported as regular features seen from the meteor radar at Molodezhnaya Station in Antarctica, (from Miyahara, et al., 1991). Recent data from the South Pole, (Conner, et al., 1992), show the wave spectra to contain a high degree of spatial and temporal variability. Hernandez et al. (1992b); Conner, et al. (1992); Fraser (1984, 1989); and Fraser et al. (1992) show the existence of relatively strong daily mean winds.

From classical tidal theory (Chapman and Lindzen, 1970; Forbes, 1982a,b) tides asymptotically reach zero amplitude at the poles. Walterscheid, (Walterscheid, 1981; Walterscheid, et al., 1986; and Walterscheid and Schubert, 1987b) suggested gravity wave interactions with tidal oscillations could produce large amplitude 'pseudo-tides' and would be an efficient mechanism at polar latitudes. Planetary waves are also theorized to asymptotically decay near the poles, since their restoring force is the planetary vorticity and as such they may not cross the rotation poles.

Ducting offers an alternative solution to the transfer of mid-latitude tidal oscillation to high latitudes. Chimonas and Hines (1986) have discussed a ducting process which

depends only upon the Doppler shifting of the wave frequency to below the Brunt-Vaisala (BV) frequency due to propagation in the vicinity of an extremum in the vertical wind profile. They suggest that such ducting may be effective for waves observed at auroral altitudes, i.e., the lower thermosphere. Other ducting processes, involving critical levels and thereby including temperature extrema, have been discussed by Francis (1973), Fritts and Yuan (1989).

In equatorial regions, wave forcing results in a semiannual oscillation of the zonal mean wind with maxima near the stratopause and the mesopause that are anticorrelated in time, creating a shear region. At greater heights, dissipation of the diurnal tide appears to contribute a westward zonal mean motion. The vertical wind shear and temperature structure of the mid and low latitude mesopause creates a natural wave guide for ducting tidal waves to high latitudes where they are dissipated thus coupling different latitude regions. The interaction of gravity and planetary waves with these ducts may modulate or sustain the structure in a variable manner. If leaky or intermittent ducting processes exist, allowing the poleward propagation of lower latitude tidal and planetary oscillations then periods of unexpected large quasi-tidal and planetary oscillations may be observable.

Other modeling efforts (Roble et al., 1977; Forbes, 1982a) indicates that the mean mesospheric wind at South Pole should be weak, as well as to show very small effects from planetary waves and the existence of a polar vortex, since the station should be under the center of this vortex and should, as well, have negligible tidal amplitudes.

Planetary waves, tides and long-period gravity waves can affect the mean flow of the atmosphere through saturation processes (Vial and Forbes, 1989) or appear as mean-flow modifications to the shorter-period gravity waves (Fritts and Vincent, 1987). By the same token the mean flow can dissipate incident waves and to this extent travelling waves are differentially filtered as they pass through latitudinal varying mean zonal flows.

The previous discussion clearly demonstrates the complexity of the polar UMA. With planetary and tidal oscillations, modified and filtered by mid-latitude zonal wind shears, dissipating near the poles where a variable cross-polar mean wind and a polar vortex may exist the wavefields would be complicated. Added to these are the possibility of ducts from mid-latitudes, which may have longitudinal variations from mid-latitude gravity wave saturation processes. Finally the dissipation of a local gravity wave spectrum, wave-mean flow interactions, wave-wave interactions, and variability in the wave forcing may combine to further complicate matters.

Clearly we do not fully understand the major energy inputs, their source distributions and temporal character, and the detailed responses to periodic and secular forcings. The wave energy input to the region must be either dissipated or channeled elswhere, perhaps to other modes of oscillation. Dissipation implies either turbulent processes leading to heating or modification of the mean flow. Coupling requires modification of other, perhaps, pre-existing modes. What is needed is a characterization of the dynamic state of these motions. Ideally this characterization should contain the mean state of the pressure, temperature, and density in the UMA with spatial and temporal spectral information. Some limitations apply to the current data set, for instance no vertical information is availiable.

As stated in the abstract the purpose of this work is to advance this characterization and improve our understanding of the behavior of tidal and planetary waves in this region. I have used Fabry-Perot Spectrometer (FPS) measurements of the emission lineshape from the neutral OH molecule (confined in a thin layer near the mesopause) to begin this task. The location of the FPS at South Pole station allows zonal sampling of the dynamic atmosphere for the first time. This provides the opportunity to produce *space-time* pictures of the line-of-sight neutral motion, kinetic temperature, and relative intensity, wavefields as well as the wave-number of specific oscillations. In addition to the dynamic variables mentioned above this work can offer time dependent spectral amplitudes and phases. In addition the relative phase between associated thermal and wind oscillations should indicate whether the propagation conditions are stable.

The experimental portion of this work has two fronts: the optimization of the instrumental setup, and the acquistion and analysis of the data. The original setup of the instrumental parameters for observation of the OH feature was performed as a compromise between the requirements of the singlet observations of OI λ5577, OI λ6300, and the OHλ8399, this was achieved experimentally. I performed optimization analysis after the fact and this is the subject of chapter 2. This optimization of the FPS for observation of *doubled* spectral features had not been done previously.

On the second front, the subject of chapter 3 and Conner et al. (1993) the analysis of the raw data involved development of the old but abandoned technique of non-linear least-squares fitting which had been supplanted by the Fourier transform technique. Motivation for this revival effort was the continuing failure of the Fourier method to analyze multiple-line data profiles. Further spectral analysis techniques of the derived parameters were invented to determine the time dependence of spectral features.

Chapter 1 Atmospheric Structure

1.0 Introduction

The intent for this chapter is to outline the nature of the upper-middle atmosphere in particular as it pertains to the polar OH layer. In section 1.1 an overview of atmospheric regions and classifications is given. The basic thermal and density structure of an atmosphere in hydrostatic equilibrium is derived. Section 1.2 is a discussion of the hydroxyl layer. Included here is a discussion of the altitude distribution of the OH species and the characteristic width of the layer, the sources of the neutral OH molecule, the collision frequency of the molecule and the relevance to the derivation of kinetic and rotational temperatures, the spectroscopic nature of the emitting OH^* including a calculation of the $\Lambda-$type doubling of the emission line and an order of magnitude calculation of the expected intensity and brightness of the emission feature, and finally an estimate of the Doppler shifts and widths expected.

Sections 1.3-1.5 are intended to provide the language for interpreting the results of the data reduction. Specifically, a theoretical basis for comparision of periodicities and wave-numbers of the observed oscillations with theoretically approved atmospheric oscillations and the the expected phase relations between thermal and pressure oscillations. These phase relations are not limited to normal propagation but are to include dissipation and coupling effects. In section 1.3 a discussion of atmospheric oscillations is given. A general overview and classification of wave types begins the section and a discussion of selected results from the literature on classical tidal theory and the solutions of Laplace's equation. (The derivation of Laplace's tidal equation is included as appendix 4.) In particular the discussion addresses the large scale Rossby (planetary) waves and tidal oscillations in polar regions. Implicit in this overview is the discussion of the assumptions and relevance to the polar environment.

In section 1.4 the propagation of Rossby and tidal oscillations is discussed. In particular the behavior at critical layers resulting in dissapation or reflection and energy

and momentum transfer. This involves a discussion of the interaction of the waves with the mean background and other waves. Also hidden in this terse description is the concept of wave ducting as a wave-wave and wave-mean flow phenomena.

Finally in section 1.5 the effects of the interactions discussed in section 1.4.

1.1 The static atmosphere

The atmosphere is conventionally divided into layers based on the vertical structure in the temperature field, the molecular compostion, particle density, electrical properties, etc.. These layers, the troposphere, statosphere, mesophere, and thermosphere are separated by the tropopause, the stratopause, and the mesopause. The term 'middle atmosphere ' here is used as defined by Andrews et al (1987) as that region of the atmosphere between 10 and 100 km Within which the atmospheric species are kept well mixed and ionization plays only a minor role. Above this region the 'upper atmosphere' is defined as the region where molecular diffusion begins to dominate over eddy mixing so that constituents become separated vertically according to their molecular masses, and increased ionization makes electromagnetic forces significant in the dynamics. The region of interest in this study is the upper portion of this middle atmosphere or the upper middle-atmosphere (UMA).

The thermodynamic state of the atmosphere at any point is determined by the values of pressure p, absolute temperature T, and density ρ. These field variables are related to each other by the equation of state for an ideal gas

$$p = nkT \tag{1.1.1}$$

where n is the concentration or particle number density and k is the Boltzmann constant. In the absence of atmospheric motions a force balance will obtain between the pressure gradient and gravitation as

$$-\frac{dp}{dh} = nmg = \rho g \tag{1.1.2}$$

with the molecular mass denoted by M (in atomic units) and m (in conventional units) such that $\rho = nm$ and $M/m =$ Avogadro's number N_0 such that the universal gas constant $R = N_0 k$. Combining the above eqns gives

$$-\frac{1}{p}\frac{dp}{dh} = \frac{Mg}{RT} = \frac{mg}{kT} \equiv \frac{1}{H} \tag{1.1.3}$$

thereby defining the pressure scale height H. Equation (1.1.3) is derived for each individual gas and is consistant at any level where diffusive separation exists and where

the distribution is determined solely by the balance of the the partial pressure gradient against gravity. It is also valid for a gas in a completely mixed atmosphere, in which processes such as turbulence are strong enough to cause each gas to conform to the scale of the mixture as a whole. The masses M and m then refer to the "composite" gas- air.

From equation (1.1.3)

$$p(z) = p(0)exp(-\frac{z}{H})$$

and for an isothermal atmosphere $\rho(z) \propto p(z)$ so that

$$\rho(z) = \rho(0)exp(-\frac{g}{RT}z). \tag{1.1.4}$$

Equation (1.1.4) is the *Hydrostatic Equation* .

Knowing the emission height of a species or a layer we can determine a *Characteristic temperature* as the value satisfying

$$T = mgH/k = \frac{17\times1.67\times10^{-27}kg(9.8\,m/s^2)H}{1.38\times10^{-23}J/K}$$

Which for $T = 200°\,K$ gives $H_{OH} = 10$km or $H \simeq .85\frac{T}{M}$ km. Here $R = 287\,J/kg-°K$ and k is the Boltzmann constant.

1.2 The Hydroxyl layer and the Mesopause

The OH nightglow layer is considered to be a thin layer and thus a good potential tracer for dynamic processes with large characteristic lengths compared to the layer thickness. Even though four decades have passed since Meinel (1950) identified the emission source some uncertainty remains about this layer. Specifically the altitude, its intensity response to chemical and dynamic forcing, and its thermodynamic state.

The mesopause is located in a region of the middle atmosphere between the thermosphere and the mesosphere, termed the *'upper-middle atmosphere'* (UMA). Just below the homopause, the mesopause is near the transition between the heterogeneous nature of the collisionless thermosphere above to that of the homogeneous collisionally dominated mesophere below. More recently the mesopause has been included in the "middle atmosphere" defined and gaining acceptance as the region between 20 and 100 km (CIRA 86 part II) and therefore includes the mesosphere and lower thermosphere.

Localization of OH* molecules near the Mesopause

Of the many OH* production and loss mechanisms I list here only the major channels, as identified by Walterscheid and Schubert (1987b) for reference in the following text.

$$O_3 + H \rightarrow OH^* + O_2^* \tag{1.2.1}$$

$$OH^* + O \rightarrow H + O_2^* \tag{1.2.2}$$

$$O + HO_2 \rightarrow OH^* + O_2^* \tag{1.2.3}$$

$$O + O_2 + M \rightarrow O_3^* + M^* \tag{1.2.4}$$

$$O_2 + H + M \rightarrow M + HO_2. \tag{1.2.5}$$

Bates and Nicolet (1950) proposed an ozone mechanism for the production of the atmospheric OH molecule. Assuming this ozone production channel Eq. (1.2.1) with an atomic Oxygen recombination mechanism Eq. (1.2.2) Krassovsky (1955) argued that there would be a strong localization around the layer maximum for O_3. (This was believed to be around 70 km at the time.)

Roach et. al. (1950) attempted to locate the height of the airglow layer with a photometer and the use of the Van Rhijn effect. The group used the equipment of C.T. Elvey which included a gas filled photoelectric cell, and collected light on the long wavelength side of 6400 Å to the infrared limit of the detector. They collected photocurrent readings from the horizon to the zenith and corrected these for most of the known non-airglow variations and deduced a mean height of the emitting layer as 70±20 km. Krassovsky (1955) criticized this work for underestimating the effects of atmospheric water vapor and placed the layer at 100 km.

The rocket measurements of Witt et al. (1979) taken from Esrange, Sweden (68°N) placed the OH (8-3) emission layer at at a height of 88 km with a half thickness of emission of 11 km.

Sivjee et al. (1987) argued on the basis of the rocket-borne measurements of Rogers et al. (1973) and Baker (1978) that the $\nu' > 6$ emissions are $1.3 \pm 0.5km$ higher than the $\nu' < 6$ thereby reducing the expected layer height of the (6-2) band.

Ulwick et al. (1987) concluded that the altitude of the OH* layer is at 86 km from rocket and ground based measurements. Neuber (1988) made Doppler width measurements from Andenes, Norway of the laser-excited Na D_2 resonance line with a lidar and

placed the winter mesopause at 70 km and the OH layer at 100 km. He also found an average temperature of 193± 5°K and claimed good agreement with the model of Groves (1967).

I adopt the results of Witt et al. (1979) with the adjustment of Sivjee et al. (1987) for a (6-2) band layer height of 87km and a half width of 11km.

Collision frequencies near the Mesopause

Prior to the results from this work OH derived mesopause temperatures were confined to the rotational temperature determination. Much use has been made of rotational temperatures derived from low resolution spectrometric measurements of both the (6-2) and the (8-3) bands of this molecule, some of which are Sivjee et al. (1987), Viereck et al. (1989), Suzuki et al. (1976), McPherson (1960), Shepard (1968), Kvifte (1967), and Yashimoto (1990). The assumption is made that the rotational temperature is in thermodynamic equilibrium with its surrounding atmosphere and therefore equivalent to the kinetic temperature. Walterscheid et al. (1987a) has stated that about 10 collisions are sufficient to thermalize the OH^* molecule.

I will estimate how many collisions we should expect in this layer. Chapman and Cowling (1952) derive that the number of collisions per second, N_{ij}, between particle species i & j is

$$N_{ij} = n_i n_j \sigma_{ij}^2 \left[\frac{8\pi k T M_0}{m_i m_j}\right]^{1/2} \tag{1.2.6}$$

where

$$M_0 = m_i + m_j = \text{ atomic masses}$$

$$\sigma_{ij} = \frac{\sigma_i + \sigma_j}{2} = \text{ collision cross sections}$$

$$n_i = \text{ number density of species i}$$

$$T = \text{ temperature } °K$$

$$k = \text{ Boltzmann's constant}$$

so

$$\frac{N_{ij}}{lifetime\ of\ the\ state} = \text{collisions/lifetime.} \tag{1.2.7}$$

Letting $n_{OH} = 1/cm^3$ then for OH^*, N_2, and O_2 and with T = 200°K get:

$$N_{OH-O_2} \approx 1.7 \times 10^4\ collisions/sec$$

for $n_{O_2} \approx 7 \times 10^{13}/cm^3$.

$$N_{OH-N_2} \approx 2.6 \times 10^3 \, collisions/sec \; .$$

for $n_{N_2} \approx 1 \times 10^{13}/cm^3$.

$$N_{OH-O_2-N_2} \approx 2.3 \times 10^4 \, collisions/sec$$

or more generally

$$N_{OH} \approx 2.07 \times 10^{-11} n_{O_2+N_2} T^{\frac{1}{2}} \, collisions/sec$$

For a 1 $msec$ lifetime and $T \approx 200°K$ I get

$$2.9 \times 10^{-13} n_{O_2+N_2} collisions/lifetime. \tag{1.2.8}$$

From Eq. (1.2.8) it can readily be seen that if the number density of background collision centers is $3 \times 10^{13}/cm^3$or greater then this argument may hold although with the highly fluctuating nature of this region the number density and temperature may make rotational temperatures unreliable as a kinetic parameter. From Hedin (1983) $n_{O_2+N_2} \simeq 8 \times 10^{13}/cm^3$ whereas CIRA (1972) gives $\simeq 1.2 \times 10^{14}/cm^3$. This implies 24-36 collisions/lifetime which is probably sufficient to thermalize the rotational distribution. Furthermore the lifetime of 1 msec may be an underestimation as Heaps and Herzberg (1952) report a 10 msec lifetime. If an atmospheric disturbance were to decrease the number density by an order of magnitude resulting in 2.4-3.6 collisions/lifetime then the rotational temperature would be unrepresentatively higher than the Doppler temperature which in turn would indicate a larger temperature oscillation than might otherwise have been expected.

Estimation of the amount of the difference between these temperatures depends on the estimation of the amount of rotational energy transport per collision. Then one could estimate the number of collisions needed to insure collisional deactivation as well as estimation of the non-Boltzmann nature of insufficient collisions.

From Battaner (1984) an estimate of the error in the temperature of a gas with two distinct thermal populations can be made using

$$\frac{\delta T}{T} \simeq \frac{\epsilon \delta E}{\frac{3}{2} kT} \simeq 11372.7 \frac{\epsilon \delta E}{T} \tag{1.2.9}$$

where ϵ = fraction of the population not thermalized and δE = the excess energy of the non-thermalized population.

If emission takes place when $\frac{1}{2}\%$ of the population is non-thermalized then $\epsilon = .005$. The excess energy from the Bates and Nicolet (1950) exothermic ozone process, (expression 1.2.1), is $+76\,kcals/mole$ which corresponds to $\simeq 3.298\,eV$. The vibrational energy associated with the $\nu = 9$ is 3.248 eV where that for $\nu = 10$ is 3.502 eV, (Krassovsky, 1962). Thus for (6-2) transitions from a thermalized population the excess energy would be

$$\delta E = 3.298\,eV - \frac{hc}{8.399 \times 10^{-5}\,cm} \simeq 1.828\,eV. \qquad (1.2.10)$$

Whence for temperatures around 200°K $\frac{\delta T}{T} \simeq .53$.

If I assume that the OH molecule undergoes purely translational elastic collisions with the dominant species- namely O_2 and N_2, then the redistribution of momentum and energy would take place so that the OH molecule would lose $\approx 2/3$ of its excess energy per collision due to the mass ratio between these colliding species. The ratio $\frac{\delta T}{T}$ would then go as

$$\frac{\delta T}{T} \simeq .53, .17, .05, .01, ...$$

for 0, 1, 2, 3, ... collisions which would lead to temperatures of

$$T \simeq 306, 234, 210, 202, ...$$

when the actual temperature is 200°K.

In addition to the previous difference between kinetic and rotational temperatures another source of uncertainty in the assumed initial rotational distribution is possible. The perhydroxyl mechanism (expression 1.2.2) introduces OH^* molecules with less excess energy than the ozone mechanism where

$$HO_2 + O = OH(\nu \leq 6) + O_2 + 60\,kcals.$$

From Krassovsky (1962) I find 60 kcals ($\simeq 2.6\,eV$) is only capable of exciting $\nu \leq 6$. Suzuki (1976) found that the rotational temperature derived from spectrometric data dropped from $\nu = 9 \rightarrow 8 \rightarrow 7$ and then abruptly rose at $\nu = 6$ only to fall off again for $\nu < 6$. Assuming the perhydroxyl mechanism as the source of 100% of the OH^* then for a 1% non-thermalized population the excess energy, $\delta E \simeq .25\,eV$, would only give a kinetic temperature error of 28°K.

The spreads in the results reported of rotational temperature measurements may be indications of these two possible sources of variations, and the larger spreads perhaps due

to the presence of large amplitude wave activity or a latitude dependent altitude for the OH layer. McPherson and Jones (1960) reported a rotational airglow temperature range from Saskatoon (52.1°N) of 200-300°K. Further the means from Saskatoon, Churchill (58.8°N), and Resolute Bay (74.7°N) from 1957-1958 were 227-296°K. Shepherd (1968) shows a bifurcated temperature distribution as a function of latitude and no satisfactory explanation has been offered. As

$$60°N\,T = 230 - 270°K$$

$$67°N\,T = 240 - 300°K$$

$$75°N\,T = 220 - 315°K$$

The data Shepherd (1968) presented was repeated from Kvifte (1967) where some of Kvifte's data is presented with many other workers data. The catalogue of data clearly indicates a difference between the temperatures derived from the $\nu = 6$ band and the $\nu > 6$ bands of $\approx 30°K$. Even with the recent work of Yoshimoto (1990) on the altitude distribution of the different OH^* bands and an adiabatic lapse rate of $-9.5\,°K/km$ (Neuber et. al., 1988) this would indicate a $3\,km$ difference between the $\nu = 6$ band and the $\nu > 6$ bands. From Witt (1979) the altitude difference between the $\nu = 9$ band and the $\nu = 1$ band was determined to be only $2\,km$.

Noxon (1964) flew a spectrometer from 55°N to 85°N and measured the P branch of the (5-3) band of OH. He found a drop in temperature as latitude increased, as opposed to the previously suggested dependence. As a final note the use of the (8-3) band for rotational temperature derivation would eliminate the ambiguity produced by the perhydroxyl production mechanism.

Λ−type doubling of the $P_1(2)$ feature of the $X^2\Pi_{3/2}$state OH (6-2) *band*

The stationary state of a diatomic molecule is described by a wave function $|\psi>$ and the total energy E which can be determined by solving Schrodinger's with the total molecular Hamiltonian (H),

$$H|\psi> = E|\psi>\,. \tag{1.2.11}$$

Separating the nuclear and electronic parts of the Hamiltonian, $H = H_n + H_e$ and using the Born-Oppenheimer approximation for the total wave function allows me to write

$$H_n|\psi_n> = E_n|\psi_n> \tag{1.2.12}$$

and

$$H_e|\psi_e> = E_e|\psi_e> \tag{1.2.13}$$

for

$$|\psi(\overline{r},\overline{R})> = |\psi(\overline{r},\overline{R})_e> |\psi(\overline{R})_n> . \tag{1.2.14}$$

Where $\overline{R}$ is the nuclear coordinate and $\overline{r}$ the electronic coordinate.

At mesopause temperatures ($\approx$ 200°K) the OH molecule is in its ground electronic state and the observed emissions are from vibrational/rotational transitions. The ground electronic state is written as $X^2\Pi_{3/2}$.

Some explanation of the spectroscopic notation is in order. For the molecular term $\xi^{2S+1}\Lambda_\Omega$ the variables are ξ =X (ground state), A (first excited), B (second excited), etc. S is the magnitude of the projection of the spin angular momentum vector onto the internuclear axis. $\Lambda = \Sigma, \Pi, \Delta$, etc. for the magnitude of the projection of $|L| = 0, 1, 2$, etc. the electronic angular momentum vector onto the internuclear axis.

$\Omega = \Lambda + \Sigma$ thus for the $X^2\Pi_{3/2}$ state we have the ground state, $S = 1/2$ indicating a doublet, with $K = L = 1$. Figure (1.2.1) shows the relevant geometry.

As mentioned earlier the major source of OH* populates the vibrational levels $\nu = 0 \rightarrow 9$ and the rotational energy levels are generally assumed to be populated according to the Maxwell-Boltzmann distribution for thermal equilibrium with the surrounding mesopause gases, although as pointed out earlier (section 1.2.3) this is not necessarily the case.

The observed emissions are combinations of vibrational/rotational transitions and thus the nuclear Hamiltonian eqn. (1.2.12) is solved as an anharmonic non-rigid vibrating rotator. The energy $E_n(\nu, J)$ for a state occupying vibrational quantum number ν and rotational quantum number J is given by (Herzberg, 1950) as

$$E_n(\nu, J) = E_{vib}(\nu) + E_{rot}(J) = hc[G(\nu) + F(J)] \tag{1.2.15}$$

for $E_{vib}(\nu)$ and $E_{rot}(J)$ the vibrational and rotational energies and $G(\nu)$ and $F(J)$ the vibrational and rotational term values.

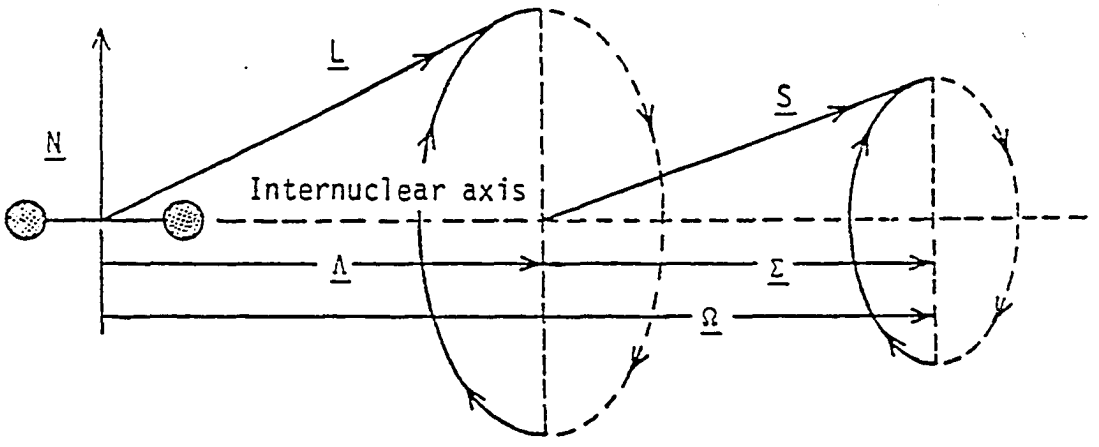

$\underline{L}$ = electronic orbital angular momentum vector

$\underline{S}$ = electronic spin angular momentum vector

$\underline{N}$ = nuclear rotation angular momentum vector

$\underline{\Lambda}$ = projection of $\underline{L}$ on internuclear axis

$\underline{\Sigma}$ = projection of $\underline{S}$ on internuclear axis

$\underline{\Omega} = \underline{\Lambda} + \underline{\Sigma}$

not shown:

$\underline{K} = \underline{\Lambda} + \underline{N}$ = total angular momentum without spin

$\underline{J} = \underline{K} + \underline{S}$ = total angular momentum

Figure 1.2.1 Angular momentum vector coupling geometry associated with the OH molecule (reprinted from Hamwey, 1985).

For the $X^2\Pi_{3/2}$ state the allowed values for ν and J are

$$\nu = 0, 1, 2, ...$$

and

$$J = K + 1/2 = 3/2, 5/2, 7/2, ...$$

since $K = 1, 2, 3, ...$.

The vibrational energy $G(\nu)$ is determined from the formula (Krassovsky, et al., 1962, p.895)

$$G(\nu) = \omega_e(\nu + \frac{1}{2}) - \omega_e x_e(\nu + \frac{1}{2})^2 + \omega_e y_e(\nu + \frac{1}{2})^3 - \omega_e z_e(\nu + \frac{1}{2})^4 + ... \quad (1.2.16)$$

and with the vibrational constants as calculated by Chamberlain and Roesler (1955) eqn. (1.2.16) becomes

$$G(\nu) = 3737.90(\nu + \frac{1}{2}) - 84.965(\nu + \frac{1}{2})^2 + 0.5398(\nu + \frac{1}{2})^3 +$$
$$- 0.01674(\nu + \frac{1}{2})^4 - 0.001637(\nu + \frac{1}{2})^5. \quad (1.2.17)$$

The calculated vibrational energies have been tabulated by Krassovsky, et al. (1962).

The rotational structure of the vibrational levels are determined by the formulae of Hill and van Vleck (1928) for example, for the $X^2\Pi_{3/2}$ state

$$^2\Pi_{3/2} : F_1(J) = B_\nu[(J + \frac{1}{2})^2 - 1 - \frac{1}{2}\sqrt{4(J + \frac{1}{2})^2 + Y_\nu(Y_\nu - 4)}] - D_\nu J^4. \quad (1.2.18)$$

The constants D_ν and Y_ν are tabulated in Krassovsky, et al. (1962, p. 896). According to Herman and Hornbeck (1953)

$$B_\nu = B_e - \alpha_e(\nu + \frac{1}{2}) + \gamma_e(\nu + \frac{1}{2})^2 \quad (1.2.19)$$

$$B_e = 18.867\, cm^{-1}$$

$$\alpha_e = 0.708\, cm^{-1}$$

$$\gamma_e = 0.0207\, cm^{-1}.$$

Note that $kT \approx 200° \times 8.6171 \times 10^{-5} eV/deg = .017\, eV$ so

$$\Delta E_e \approx 4\, eV > 3.34\, eV >> kT$$

$$\Delta E_{vib} \approx .4\, eV >> kT$$

$$\Delta E_{rot} \approx .01\, eV < kT.$$

The interaction of $\overline{L}$ and $\overline{N}$ further split the $X^2\Pi_{3/2}$ levels and thus the term values are further differentiated which is indicated in the subscripting. According to Krassovsky

(1962) $\Lambda-$doubling for $X^2\Pi_{3/2}$ level is $F_d(K)-F_c(K) = q_\nu K(K+1)$. Using this obtain

$$q_6 K(K+1) = 0.0269(2) \approx .0538\, cm^{-1}$$

and

$$q_2 K(K+1) = 0.0377(6) \approx .2262\, cm^{-1}$$

so that the expected observed line separation Δ should be

$$\Delta = (q_2 K(K+1) - q_6 K(K+1))) \approx .172\, cm^{-1} \text{ or } 121.4\, m\mathring{A}\,.$$

Better laboratory results have made it possible for workers (Coxon, 1979, Coxon et al., 1980, 1982) to deduce the term values to a higher degree of accuracy. The term values are $f_{ik}(J)$ where i = '1' or '2' for the lower ($X^2\Pi_{3/2}$) or higher ($X^2\Pi_{1/2}$) lying state. The subscript k = 'e' or 'f' for the lower or higher doubled level, respectively. When determining the separation observed in the mesopause emissions

$$X^2\Pi_{3/2}\,(J=3/2) \rightarrow X^2\Pi_{3/2}\,(J=5/2)$$

the spin $\overline{S}$ does not change so that the transition is from an 'e' state to an 'e' state or similarly an 'f' to an 'f'. This gives rise to two lines only separated by the difference in the $\Lambda-$doubling values between the $\nu = 6, J = 3/2$ and the $\nu = 2, J = 5/2$ levels. For $\nu = 2$ and $J = 5/2$ get

$$f_{1e}(5/2) - f_{1f}(5/2) = .172\, cm^{-1} \text{ or } 121.4\, m\mathring{A}$$

for $\nu = 6$ and $J = 3/2$ get

$$f_{1e}(3/2) - f_{1f}(3/2) = .030\, cm^{-1} \text{ or } 21.1\, m\mathring{A}$$

Therefore the difference observed will be $\approx 100.3\, m\mathring{A}$.

Intensity and apparent brightness of the feature

From Chamberlain (1961) the integrated column intensity, I is given by:

$$I(photons/sec) = (A\Omega/4\pi)\int_0^\infty F(r)dr$$

where F(r), (photons/sec), is the column emission rate and the integration is along the line-of-sight. From this I calculate a brightness of 50-80 R for the 8400Å line as follows.

Intensity in cts/sec: 120 counts above background at line center × 10 bins fwhh ≈ 1200 counts for each line of the doubled feature. These counts were accumulated in 800 seconds, (100 scans × 8 seconds/scan), which are divided into 256 data bins. This is the value after subtraction of the background of about 40 counts. Thus

$$I \approx 1200\,counts/(10 \times (\frac{800\,secs}{256}) = 19.2\,counts/sec.$$

The background is about 8 counts/sec making a total countrate of 27.2 cps.

The 'AΩ' factor for the south pole instrument is as follows for $A = \frac{\pi}{4}(13\,cm)^2$ for the etalon area. For the aperture at the focal length of L2' $\Omega = \frac{\pi}{4}(.225\,cm)^2/(65\,cm)^2$ in steradians so that

$$A\Omega = (\frac{\pi}{4})^2(13\,cm)^2(.225\,cm)^2/(65\,cm)^2 \approx 1.25 \times 10^{-3}\,cm^2 - ster$$

Where the relationship for the solid angle $\frac{dA}{L^2} = d\Omega$ has been used.

Then the uncorrected brightness in rayleighs is given as

$$B \approx \frac{4\pi}{A\Omega 10^6}19.2\,cps \approx \frac{4\pi}{1.249 \times 10^{-3}\,cm^2 - ster 10^6}19.2\,cps \approx .19\,R$$

This result must be corrected according to the total transmission (Tx) of the optical system with an ideal etalon. The transmission of each component is detailed in section 2.2 where it is found that

$$Tx \approx .014$$

Thus yielding for the single line of the doublet feature $B \approx 13.5\,R$ and for the doubled line $B \approx 27\,R$. The assumption of an ideal etalon gives an etalon transmission of 1 and is not expected to be less than .5, giving a brightness range of 27-54 Rayleighs for the doubled feature.

The Doppler shifts and widths expected

As a representation of the literature I have produced Figure (1.2.2) for an altitude range of 82-92 km.

The data included span the non-polar portion of the globe for summer and winter seasons. These panels indicate a meridional mean of ~ 5 m/s southward (from the equator and a semi-diurnal amplitude of ~ 5-10 m/s. These results are due to Salah et.al. (1991), Forbes and Hagan (1988), Forbes and Vial (1989, 1990), Johnson (1991), Johnson and Virdi (1991), Tetenbaum et. al. (1990), Manson et. al. (1990, 1991), Manson et al. (1990), and Johnson et al. (1987). None of these results reach the polar

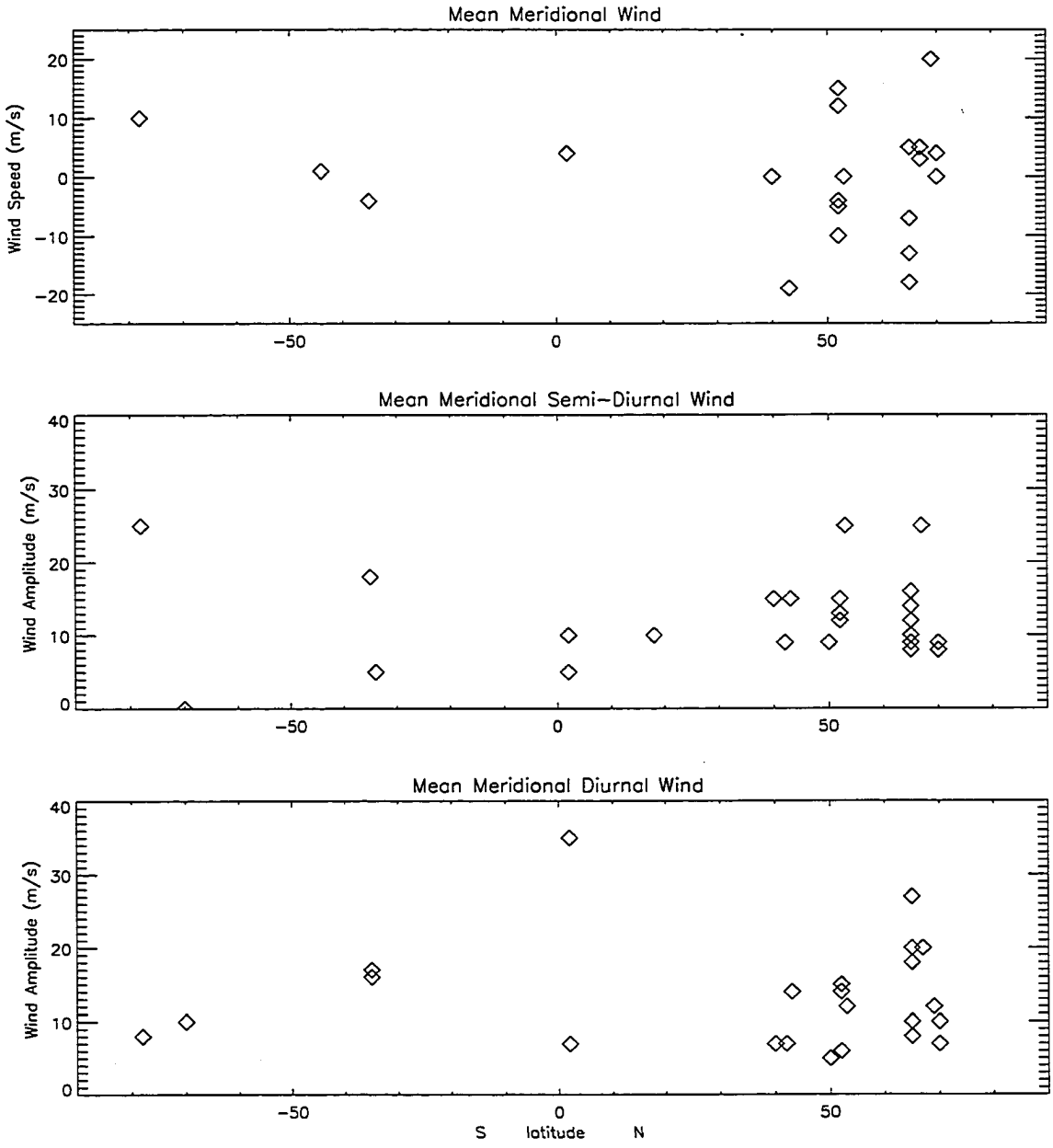

Figure 1.2.2 Tidal decomposition of wind measurements and model results from various latitudes from the literature. Altitudes range from 82-92 km. (See the text for references.)

regions, even the CIRA 1986 model gives no meridional means. Other model results from Salby (1980) give theoretical amplitudes of ~0-1 m/s for all planetary wave periods in the winter southern polar region. For the temperatures CIRA 1986 gives $\sim$ 213°K at 80°S latitude and 80 km altitude. From these results it seems reasonable to assume the expected temperature range to be $\sim 100 - 300$°K. And a conservative estimate of the wind range is $\pm$50m/s.

1.3 Atmospheric Oscillations- the dynamic atmosphere

An important dynamical property of the atmosphere is its ability to support wave motions. The wave motions of interest in this work are oscillations of neutral species assumed free from electrodynamic effects. The restoring forces considered here are provided by the stable density or entropy stratification of the atmosphere, represented by positive values of N^2 the static stability and by the rotation of the Earth as represented by the Coriolis parameter $2\Omega\sin\phi$. I also only consider linear waves, that is- a small amplitude quasi-periodic transfer of information without the corresponding transport of fluid parcels.

In atmospheric dynamics waves are classified in a variety of ways. They can be classified according to their restoring force, their source mechanism, their propagation characteristics, and the way they dissipate.

Classification by the restoring force separates gravity, inertio-gravity, and planetary waves. Buoyancy, or gravity, waves owe their existance to atmospheric stratification and are confined to frequencies below the Brunt-Vaisälä (B-V) frequency. Inertio-gravity waves result from a combination of stratification and Coriolis effects. Planetary and Rossby-Haurwitz waves result from the northward potential vorticity gradient.

Classification by source mechanisms leads to the distinction between *forced* and *free* waves. Forced waves are continually maintained by an excitation mechanism of a given phase speed and wavenumber such as thermal tides induced by solar diurnal heating fluctuations. Free waves include global normal modes.

Classification by propagation characteristics can distinguish between trapped (or evanescent) waves. For example under some circumstances horizontally propagating planetary waves are trapped in the vertical, while equatorial waves can propagate vertically and zonally but are trapped between certain latitudes.

Classification by dissipation is used to examine the way in which waves dump their energy and one way involves interaction with the mean or backround flow. Mean-flow acceleration is generally caused by non-linear waves or linear waves which have become unstable.

Although not an exhaustive treatment the relevant classifications needed for this work are mentioned above. Of interest in this work are are planetary scale, global normal modes (stationary and travelling) and tidal oscillations. Global normal modes are also called Rossby waves, Rossby-Haurwitz waves, and Lamb modes. Some treatment of gravity wave propagation is given as some aspects of gravity wave dissipation are similar to planetary wave dissipation.

Horizontal Modal Structure: Wave disturbances to a resting spherical atmosphere

Laplace first studied the solutions for a stratified spherical atmosphere at rest with respect to the rotating planet. Small disturbances to this layer result in excitation of what are termed tidal and global normal modes. The derivation of Laplace's tidal equations is in many standard texts such as Andrews (1987), Volland (1988) and Holton (1979) and is given in appendix D.

As shown in appendix D for the conservative or unforced case a sinusoidal solution is posed as

$$(\tilde{u},\tilde{v},\tilde{\phi}) = Re\left[(\hat{u}(\phi),\hat{v}(\phi),\hat{\Phi}(\phi))exp(i[s\lambda - 2\Omega\sigma t])\right]$$

for the zonal wavenumber s and the period $1/2\sigma$ in days. Standard practice is to solve eqns. (D.16a,b) and eliminate $\hat{u}$ and $\hat{v}$ to obtain *Laplace's tidal equation*,

$$\mathcal{L}\hat{\Phi} + \gamma\hat{\Phi} = 0 \tag{1.3.1}$$

$\gamma \equiv 4\Omega^2 a^2/gh$ is Lamb's parameter and $\mathcal{L}$ is a second-order ordinary differential operator

$$\mathcal{L} \equiv \frac{d}{d\mu}\left[\frac{(1-\mu^2)}{(\sigma^2-\mu^2)}\frac{d}{d\mu}\right] - \frac{1}{\sigma^2-\mu^2}\left[\frac{-s(\sigma^2+\mu^2)}{\sigma(\sigma^2-\mu^2)} + \frac{s^2}{(1-\mu^2)}\right] \tag{1.3.2}$$

for $\mu \equiv sin\phi$ and thus $(-1 \leq \mu \leq 1)$. Requiring bounded solutions at the poles and specification of s and σ gives the eigenvalue problem

$$\mathcal{L}\Theta_n^{(\sigma,s)} + \gamma_n^{(\sigma,s)}\Theta_n^{(\sigma,s)} = 0 \tag{1.3.3}$$

whose solutions are the well known Hough functions $\Theta_n^{(\sigma,s)}$. At this point one usually chooses s the zonal wavenumber and the phase speed σ and then proceeds to examine the

various regions for the solutions. For example in Figure (1.3.1) with $\gamma > 0$ the following unforced solutions obtain.

Laplace's tidal equations cast into divergence and rotational components

An alternative derivation gives the divergence (curl free) and rotational (source free) components of the horizontal wind field from which the eigenvalues of Laplace's equations can be discussed. Perhaps a more natural and physical presentation, is found in this expression, which is more intuitive. I merely adapt the previous results following Volland (1976) and Longuet-Higgins (1968).

The horizontal wind vector is represented as

$$\mathbf{U} = -\nabla\xi + \nabla \times \psi\mathbf{r} \tag{1.3.4}$$

with $\mathbf{r}$ the unit vector in the radial direction. The component ξ is the velocity potential. The curl-free wind is directed orthogonal to the lines of constant ξ, flowing in the direction of decreasing ξ. The component ψ is a streamfunction. The lines of constant ψ are streamlines of the source-free wind. The wind direction is to the right of the direction of increasing ψ. Here ∇, (the horizontal gradient), and $\nabla\times$, (the curl operator) are defined as

$$\nabla A \equiv \frac{1}{a}\left[-\frac{\partial A}{\partial\phi}; \frac{1}{cos\phi}\frac{\partial A}{\partial\lambda}\right] \qquad \text{and} \qquad \nabla \times A\mathbf{r} \equiv \frac{1}{a}\left[\frac{1}{cos\phi}\frac{\partial A}{\partial\lambda}; \frac{\partial A}{\partial\phi}\right]. \tag{1.3.5}$$

The horizontal Laplace operator is

$$\nabla^2 A \equiv \frac{1}{a^2 cos^2\phi}\left[cos\phi\frac{\partial}{\partial\phi}\left(cos\phi\frac{\partial A}{\partial\phi}\right) + \frac{\partial^2 A}{\partial\lambda^2}\right] \tag{1.3.6}$$

and the modified Laplace operator is given by

$$\hat{\nabla}^2 A \equiv \left[sin\phi\nabla^2 A + \frac{cos\phi}{a^2}\frac{\partial A}{\partial\phi}\right]. \tag{1.3.7}$$

ξ and ψ are functions of ϕ and λ only. The wind components are related to ξ and ψ as

$$u = -\frac{\partial\xi}{\partial x} + \frac{\partial\psi}{\partial y} \text{ and } v = -\frac{\partial\xi}{\partial y} - \frac{\partial\psi}{\partial x} \tag{1.3.8}$$

with

$$\frac{\partial}{\partial x} = \frac{1}{acos\phi}\frac{\partial}{\partial\lambda} \text{ and } \frac{\partial}{\partial y} = \frac{1}{a}\frac{\partial}{\partial\phi}. \tag{1.3.9}$$

Furthermore, introduce the horizontal components of the momentum force in the form

$$\mathbf{F} = -\nabla M + \nabla \times L\mathbf{r}, \tag{1.3.10}$$

where M and L are also functions of ϕ and λ. As with the approach in appendix D this system allows separation of vertical and latitude dependence where introducing the

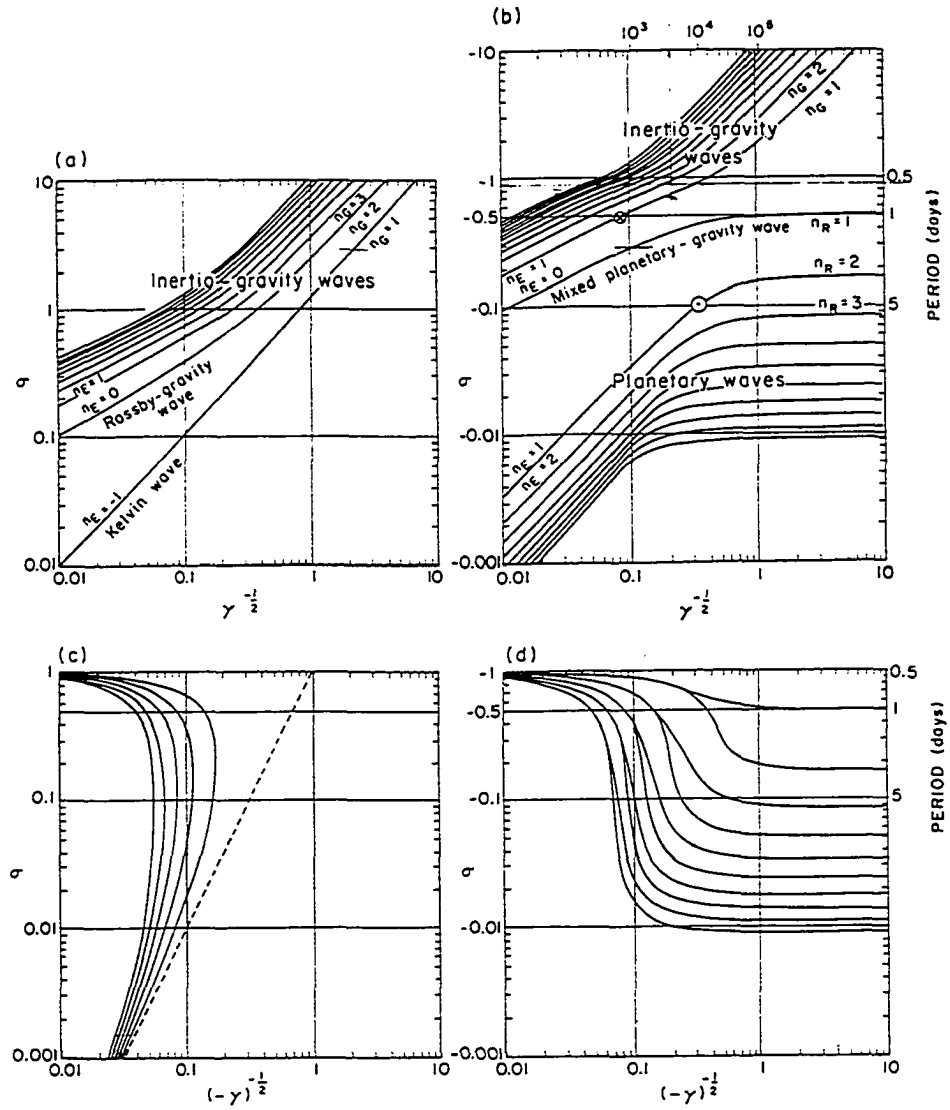

Figure 1.3.1 Plots of $\gamma^{-1/2} \equiv (g|h|)^{1/2}/2\Omega a$ verses frequency σ for zonal wave number $s = 1$, equivalent depths (γ), eastward phase speed ($\sigma > 0$), and westward phase speed ($\sigma < 0$). Reproduced from Andrews (1987), p. 156.

auxiliary equation (Volland, 1976),

$$\nabla \cdot \mathbf{U} = -\nabla^2 \xi = \frac{i\omega\varepsilon(\Phi + M)}{4\Omega a^2} \tag{1.3.11}$$

relates the horizontal divergence of the wind to the geopotential. ε is the separation constant known as the Lamb parameter and is equivalent to γ in the preceeding derivation. This parameter is the eigenvalue of the modal structure. It is related to the equivalent depth h by

$$\varepsilon = \frac{4h_s}{h} \tag{1.3.12}$$

with the normalizing factor $h_s = \Omega^2 a^2/g = 22$ km. The terminology 'equivalent depth' is derived from tidal theory of oceanic currents. In this application this eigenvalue can have positive, negative, and even complex values.

In order to separate the vertical and latitudinal dependences in the eigensolutions put

$$\xi = i\omega a \xi_n^m(\phi,\omega) U_n^m(z,\omega) exp[i(m\lambda - \omega t)] \tag{1.3.13a}$$

$$\psi = a\psi_n^m(\phi,\omega) U_n^m(z,\omega) exp[i(m\lambda - \omega t)] \tag{1.3.13b}$$

$$L = i\Omega\omega a \mathrm{L}_n^m(\phi,\omega) U_n^m(z,\omega) exp[i(m\lambda - \omega t)] \tag{1.3.13c}$$

and for the height dependent eigenfunctions

$$\Phi = \Phi_n^m(z,\omega)\theta_n^m(\phi,\omega) exp[i(m\lambda - \omega t)] \tag{1.3.14a}$$

$$w = W_n^m(z,\omega)\theta_n^m(\phi,\omega) exp[i(m\lambda - \omega t)] \tag{1.3.14b}$$

$$Q = Q_n^m(z,\omega)\theta_n^m(\phi,\omega) exp[i(m\lambda - \omega t)] \tag{1.3.14c}$$

$$M = M_n^m(z,\omega)\theta_n^m(\phi,\omega) exp[i(m\lambda - \omega t)] \tag{1.3.14d}$$

with

$$T = \frac{H}{R}\frac{\partial \Phi}{\partial z} \tag{1.3.15}$$

and

$$U_n^m(z,\omega) = \frac{[\Phi_n^m(z,\omega) + M_n^m(z,\omega)]}{2a\Omega}. \tag{1.3.16}$$

Ω is the zonal frequency. $\Upsilon = \sqrt{|\varepsilon_n^m|}$ a normalization factor which is determined such that the total kinetic and potential energy , $K + P = 1$ after Longuet Higgens, (1968).

With this representation Laplace's equations become:

$$\left[\frac{\omega^2\nabla^2}{2} - \frac{m\omega}{a^2}\right]\xi_n^m - \hat{\nabla}^2\psi_n^m - \frac{\nabla^2\theta_n^m}{\Upsilon} = 0 \qquad (1.3.22a)$$

$$\left[\frac{\nabla^2}{2} - \frac{m}{\omega a^2}\right]\psi_n^m - \hat{\nabla}^2\xi_n^m + \frac{\nabla^2 L_n^m}{2} = 0 \qquad (1.3.22b)$$

$$\nabla^2\xi + \frac{\varepsilon_n^m}{2a^2\Upsilon}\theta_n^m = 0$$

and for completeness I add

$$\frac{dW_n^m}{dz} - \frac{W_n^m}{H} + \frac{i\varepsilon_n^m\omega}{4\Omega a^2}(\Phi_n^m + M_n^m) = 0 \qquad (1.3.23a)$$

$$i\omega\Omega\frac{d\Phi_n^m}{dz} - N^2 W_n^m + \frac{RQ_n^m}{c_p H} = 0 \qquad (1.3.23b)$$

for

$$N^2 = \frac{g}{\theta_0}\frac{d\theta_0}{dz} = \frac{R\Gamma}{H} \qquad (1.3.24)$$

and

$$\theta_0 = T_0\left[\frac{p_s}{p_0}\right]^{R/c_p} \qquad (1.3.25).$$

System (1.3.22) describes the latitude structure of the modes, and system (1.3.23) describes their vertical structure. The Lamb parameter ε connects both structures. The source-free part of the momentum force 'L' drives system (1.3.22), while the curl-free part 'M' and the heat input 'Q' are the external forces to drive system (1.3.23). System (1.3.22) is called Laplace's equations.

As stated the eigenvalues are equivalent to those in Figure (1.3.1). These panels were derived, (Andrews, 1987), by solving the homogeneous form of eqns (1.3.22) with the momentum force $L = 0$.

Imaginary eigenvalues ε_n^m, or negative equivalent depths, are necessary for the complete expansion of any arbitrary function in terms of the eigenfunctions of the Laplace equations, they can apply to *forced oscillations* or *free* oscillations with negative equivalent depths such as a thin layer on the inside of a rotating spherical shell with gravity directed toward the center, (Longuet-Higgins, 1968). These waves would have positive kinetic energy and negative potential energy.

I will now outline the method for determination of the eigenvalues or Lamb parameters, for the horizontal structure and note that a complete solution exists in Longuet-Higgins (1968) and Volland (1976). Also a tabulation of the Lamb parameters is contained in Longuet-Higgins (1968). For the characteristic horizontal modes set the momentum force L = 0. Then cast the horizontal solutions as series of spherical functions,

$$\xi_n^m = \sum_s A_{s,n}^m(\omega) P_s^m(\phi),$$
$$\psi_n^m = \sum_s B_{s,n}^m(\omega) P_s^m(\phi),$$
$$\theta_n^m = \sum_s C_{s,n}^m(\omega) P_s^m(\phi).$$

Next use the properties of the associated Legendre functions to eliminate $B_{s,n}^m$ and $C_{s,n}^m$ and then plug into the Laplace equations (1.3.22) and equate the coefficients of P_s^m to zero to obtain an infinite number of homogeneous equations for the $A_{s,n}^m$ which can be separated into two independent infinite systems, which as it turns out, correspond to the symmetric and anti-symmetric motions about the equator. Solve for the eigenvalues of the normal modes by setting the determinant of the matrix of these systems to zero. To find the eigenfunctions use eq. (2.4.6) to find the horizontal eigenfunctions for u and v as

$$u_n^m(\phi,\omega) = \frac{m\omega}{cos\phi}\sum_s A_{s,n}^m(\omega)P_s^m(\phi) + \sum_s B_{s,n}^m(\omega)\frac{dP_s^m(\phi)}{d\phi} = \sum_s [D_{s,n}^m P_{s-1}^{m-1} + E_{s,n}^m P_{s-1}^{m+1}]$$

and

$$v_n^m(\phi,\omega) = -\omega\sum_s A_{s,n}^m(\omega)\frac{dP_s^m(\phi)}{d\phi} - \frac{m}{cos\phi}\sum_s B_{s,n}^m(\omega)P_s^m(\phi) = \sum_s [F_{s,n}^m P_s^{m-1} + G_{s,n}^m P_s^{m+1}]$$

where

$$D_{s,n}^m = .5\omega(s+m-1)[(s+m)A_{s,n}^m - (s-m)B_{s-1,n}^m],$$
$$E_{s,n}^m = .5[\omega A_{s,n}^m + B_{s-1,n}^m],$$
$$F_{s,n}^m = .5\omega(s+m)[(s-m+1)A_{s,n}^m - (s+m+1)B_{s+1,n}^m],$$
$$G_{s,n}^m = -.5[\omega A_{s,n}^m + B_{s+1,n}^m], \quad (m > 0).$$

and

$$E_{s,n} = B_{s-1,n}, \quad G_{s,n} = -.5\omega A_{s,n}, \quad D_{s,n} = F_{s,n} = 0, \quad \text{for } m = 0.$$

As with ξ and ψ the relation in (1.3.13) for casting u and v into the surface functions

places an 'i' between them and places a phase difference between them.

Inertio-Gravity waves

These waves are not, strictly speaking, buoyancy waves. The distinction is that inertio-Gravity waves derive their restoring force from both the bouyancy and the rotation of the Earth. For high frequencies though the Coriolis force becomes small. In this case for periods of several hours the divergence part is more important than the curl part

$$|\xi_n^m| \gg |\psi_n^m|$$

of the horizontal velocity. Then eq. (1.3.22) reduces to, after eliminating θ,

$$\left[\frac{4a^2}{\varepsilon_n^m}\nabla^4 + \omega^2\nabla^2\right]\xi_n^m = 0.$$

These have positive eigenvalues and real frequencies. The horizontal components become

$$u_n^m(\phi,\omega) = \frac{m}{cos\phi}A_n^m(\omega)P_n^m(\phi)$$

$$v_n^m(\phi,\omega) = -A_n^m(\omega)\frac{dP_n^m(\phi)}{d\phi}$$

and take the wave-number one, m=1, n=1 component of the series at a period of .4 days (9.6 hours) and assume a westward phase speed I find

$$u_1^1(\phi,2.5) = \frac{1}{sin\phi}A_1^1(2.5)cos\phi$$

$$v_1^1(\phi,2.5) = -A_1^1(2.5)sin\phi$$

with $P_1^1 = sin(colatitude) = cos(\phi)$. This mode can be found in panel (b) of Figure (1.3.1) labeled $n_g = 1$ at a period of .4 days and is symmetric about the equator. Near the pole where $\phi \rightarrow \frac{\pi}{2}$ the zonal wind is seen to vanish and the meridional is $v_1^1(\frac{\pi}{2},2.5) = -A_1^1(2.5) \approx -.075$. For the first anti-symmetric component of the meridional wind

$$v_2^1(\phi,2.5) = -A_2^1(2.5)3(cos^2\phi - sin^2\phi) = 0.$$

Free planetary or Rossby-Haurwitz waves

The waves are source, or divergence free, unforced waves with long periods so that they derive thier restoring force from the planetary rotation. Setting $L = 0$ and $\xi = 0$ gives $\varepsilon = 0$ and

$$\left[\frac{\nabla^2}{2} - \frac{m}{\omega a^2}\right] \psi_n^m = 0.$$

$$\hat{\nabla}^2 \psi_n^m - \frac{\nabla^2 \theta_n^m}{\Upsilon} = 0.$$

Strictly speaking the Lamba parameter is not exactly zero but approaches zero from positive or negative values (positive or negative equivalent depths). The solutions to this second equation have only real discrete frequencies,

$$\omega = -\frac{2m}{s(s+1)}, \quad (m > 0)$$

The horizontal components become

$$u_{s,-n}^m(\phi,\omega) = -B_{s,-n}^m \frac{dP_s^m(\phi)}{d\phi}$$

$$v_{s,-n}^m(\phi,\omega) = \frac{mB_{s,-n}^m}{cos\phi} P_s^m(\phi)$$

$$\theta_{s,-n}^m = \frac{B_{s,-n}^m}{2s+1}\left[\frac{s(s-m+1)}{s+1} P_{s+1}^m(\phi) + \frac{(s+1)(s+m)}{s} P_{s-1}^m(\phi)\right].$$

For example the wave-number one, first component horizontal winds would be

$$u_{1,-1}^1(\phi,\omega) = -B_{1,-1}^1 sin\phi$$

$$v_1^1(\phi,\omega) = 0$$

as for the gravity wave modes, and I find that there is no appreciable meridional wave-number one should exist, at any frequency The Hough functions for the geopotential are graphed in Figure (1.3.2) to show their latitude dependence.

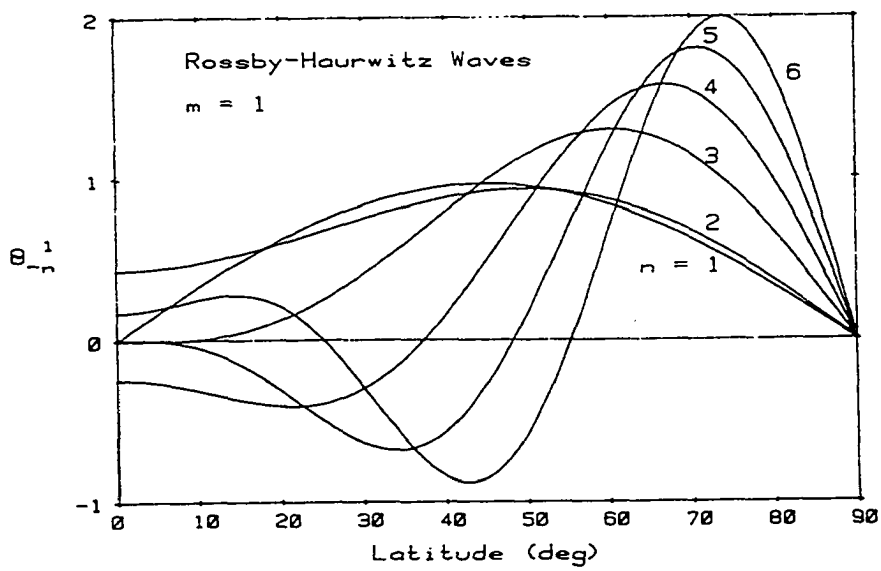

Figure 1.3.2 Meridional Hough functions for the geopotential zonal wavenumber m = 1 solutions of Laplace's tidal equations for unforced global normal modes, (reprinted from Volland (1988).

Chapter 2 Instrumentation: Theory, Design, and Usage

2.0 The Suitability of the Fabry-Perot Spectrometer for this work

In order to study the dynamics of the high latitude OH airglow layer at the neutral mesopause we choose to measure the bulk motion and kinetic temperature of the gas in this layer. To this end we set out to determine the Doppler width and shift of the light emanating from this region. The emissions from the OH^* molecule in this layer are on the order of 100 Rayleighs so that measurement requires a high luminosity† instrument. Also the determination of Doppler lineshapes require a high resolution instrument. The $P_1(2)$ feature of the OH (6-2) Meinel band in the near infrared at 8399 Å was selected due to its relative brightness ($\approx$ 60 R) within the OH spectra and its freedom from auroral contamination. A Fabry-Perot spectrometer (FPS) with a cooled photomultiplier tube can be setup to fulfill these requirements. The particular setup of this instrument is detailed in this chapter.

In section 2.1 the general mathematical theory of the FPS, as derived in appendix B, is discussed. In this discussion the effects of a real etalon with plate defects on the derived profiles is addressed. In section 2.2 the south pole instrument is described and the optical path detailed allowing the determination of the instrumental throughput. In section 2.3 I include a discussion of the instrumental parameters and how they affect the operation and performance the FPS and their relation to optimal parameters. The actual parameters used and the instrumental setup for each of the three instruments are given and compared with the optimal theoretical minimum uncertainties for the dynamic parameters of wind and temperature.

† Luminosity is defined as the flux passed per unit monochromatic source irradiance in units of (photon s^{-1})/(photon cm^{-2} sr^{-1} s^{-1})

2.1 Mathematical discussion of the derivations for the FPS theory

In this section I introduce the FPS in general terms using the results of appendix B. I derive the doubled-line reduction and discuss the various effects which broaden the measured profiles.

The Fabry-Perot spectrometer consists of two parallel, flat, semi-transparent mirrors separated by a fixed distance. This arrangement is called an etalon (Fabry and Perot, 1897). We use optically flat fused silica plates with semi-transparent dielectric coatings. The spacing between the two plates is termed the gap whose width will be given as 't' here and was 'd' in appendix B. Anti-reflection coatings are applied to the outer surfaces of the plates whereas the inner surface coatings are applied to increase the reflectivity '$\mathcal{R}$' within the gap. With a reflectivity near unity, light passing through the first plate of the etalon into the gap will be reflected many times in the gap before all the wave's energy passes out of the gap region. Each time a light wave impinges on one of these surfaces some of the light transmits through the interface and some is reflected back across the gap. Most of the energy of the reflected wave will return to this surface with a shift in phase due to the reflections as well as the the extra distance it travelled across the gap and back. The energy which now transmits will be in phase with the energy deposited on the previous encounter only if the optical path across the gap is just the right length to match these phases. In this manner the size of the gap determines the geometry necessary for constructive or destructive interference of the light exiting the etalon. If a lens is used to focus the light exiting this arrangement onto a screen a circular pattern of alternating bright and dark rings is formed. The radii of these rings is a result of the angles for constructive and destructive interference at this gap. If we place a small hole of size 'f' (see appendix E) in the screen at the center of the light pattern and vary the size of the gap (decrease it for example) the radii of the rings will decrease until they vanish into the central hole. If we also place a photon counting device on the other side of the hole and monitor its output we can record a time series of the light intensity. If we vary the gap linearly and at least enough to change the optical path between reflections by one wavelength of the incident light we will get a periodic time series, the period being termed the *free spectral range* (or fsr). In appendix B the total flux $\mathcal{P}(x)$ received by a detector from a source with intensity I as a function of the scan variable x (equation

(B.18)) is

$$\mathcal{P}(x) = IA\epsilon\tau_L 4\pi f^* n_0{}^{-1}\left[1-\frac{\mathcal{A}_e}{(1-\mathcal{R})}\right]^2\frac{(1-\mathcal{R})}{(1+\mathcal{R})}\left[1+2\sum_{k=1}^{k=\infty}a_k cos(2\pi k[\frac{x-x_0}{T}])\right] \tag{2.1.1}$$

for a general quasi-monochromatic source $\mathcal{S}$. $\mathcal{A}_e$ is the etalon absorption/scattering coefficient, $\mathcal{R}$ the etalon reflectivity coefficient, A is the useful area of the etalon, ϵ is the quantum efficiency of the detector, τ_L is the etalon loss not included in $\tau_{e,\Omega}$ (see appendix B), and n_0 is the central order of interference from the relationship

$$2\mu t\cos(\theta) = n\lambda$$

with $\theta = 0$, and optical thickness μt at wavelength λ.

The gaussian distribution in intensity of a small wavenumber range of a Doppler broadened spectral emission from a particular molecular species the source distribution $\mathcal{S}$ can be represented as

$$\mathcal{S} = \left[\frac{ln(2)}{\pi}\right]^{1/2}\frac{1}{dg}exp[-(\frac{\sigma-\sigma_0}{dg})^2 ln(2)] \tag{2.1.2}$$

with the source transform coefficients (as in appendix B)

$$s_k = exp[-(\frac{\pi^2 k^2 dg^{*2}}{ln(2)})]. \tag{2.1.3}$$

The use of wavenumbers 'σ' in units of cm^{-1} (or milli-Kaysers) is mathematically convenient and the relationship to wavelength is simply $\sigma = 1/\lambda$. The Doppler width *dg normalized* to the free spectral range $\Delta\sigma$ is given by

$$dg^* = dg/\Delta\sigma = \sigma(c\,\Delta\sigma)^{-1}(2\tau kAM^{-1}ln2)^{1/2} \tag{2.1.4}$$

If the line is lambda-doubled and the doublet separation is σ_{cd} then the source can be represented as the sum of two single lines

$$\mathcal{S} = \left[\frac{ln(2)}{\pi}\right]^{1/2}\frac{1}{dg}\left(exp[-(\frac{\sigma-\sigma_0-\frac{\sigma_{cd}}{2}}{dg})^2 ln(2)] + exp[-(\frac{\sigma-\sigma_0+\frac{\sigma_{cd}}{2}}{dg})^2 ln(2)]\right) \tag{2.1.5}$$

with source coefficients

$$s_k = \frac{1}{\sqrt{2}}exp[-\frac{\pi^2 dg^{*2}k^2}{ln2}(1+[\frac{\sigma_{cd}}{2\sigma_0}]^2)]\times[cosh(4\pi^2 dg^{*2}k^2[\frac{\sigma_{cd}}{2\sigma_0}]) + cos(2\pi k\sigma_{cd})]^{1/2} \tag{2.1.6}$$

The coefficients a_k contain the instrumental effects as well as the source coefficients. The theoretical development, including the involvement of the etalon reflectivity and the

finite scanning aperture is given in appendix B but there are other as yet unmentioned effects. I consider only the etalon plate defects and discount as negligible all other forms of line-shape broadening which may distort the pure Doppler broadening of the assumed Gaussian line, specifically Lorentz or collisional broadening. Collisions distort the internuclear distance creating a pseudo molecule which will emit at a slightly different wavelength than the original molecule. This broadening is of the order of $\approx 4\times10^{-5}\ cm^{-1}$ for each collision during the lifetime of the state. This effect will appear as the convolution of a Lorentzian of this width with the Gaussian line shape to produce a so-called "Voigt" profile, (Rees, 1988). At the altitude of the mesopause and for this species the values calculated in chapter 1 give 24-360 collisions/lifetime and thus only a $10^{-3} - 10^{-1}\ cm^{-1}$ range which is less than 2% of the Doppler width.

The ratio of the fsr to the profile width is called the *Finesse* ($\mathcal{N}$). The instrumental finesse consists of at least three contributions: the *aperture finesse* ($\mathcal{N}_{ap}$) as characterized by a gate function, the *reflective finesse* ($\mathcal{N}_R$) as characterized by the Airy function, and the *defects finesse* ($\mathcal{N}_D$) assumed gaussian is a function of the flatness and roughness of the optical flats themselves.

The normalized full width of the aperture function f, in orders, has a finesse $\mathcal{N}_{ap}$ of $1/f$. The affect of the various broadening effects on the transmitted light can be seen in the way the different finesses add to give a total finesse ($\mathcal{N}_{tot}$)

$$1/\mathcal{N}_{tot} = \sum\nolimits_i 1/\mathcal{N}_i \;=\; 1/\mathcal{N}_R + 1/\mathcal{N}_{ap} + 1/\mathcal{N}_D. \tag{2.1.7}$$

Where $\mathcal{N}_R$ is the Reflective finesse and $\mathcal{N}_{ap}$ is the aperture finesse. With

$$1/\mathcal{N}_D \;=\; 1/\mathcal{N}_{rough} + 1/\mathcal{N}_{As}$$

where $\mathcal{N}_{rough}$ is the finesse due to plate roughness and $\mathcal{N}_{As}$ is the finesse due to asphericity.

The following estimation of the effects of known types of plate imperfections is limited to the asphericity and roughness of the etalon surfaces. Asphericity can be due to "doming" or "wedging" where doming is the radial variation of the plate thickness and wedging is the linear variation in plate thickness across a diameter. The self-aligning servo corrects for parallelism of the plates and therefore we need not worry about wedging. The sources of doming can be limitations of the polishing technique and sagging of the thick heavy plates. I consider doming and sagging as having the same defect- spherical

deformation. If we imagine a domed plate as an assembly of concentric annuli decreasing in length towards the center then the effect of this defect, as determined by Chabbal (1953) for small errors relative to the size of the plates and the spacing, can be related to a finesse $\mathcal{N}_{As} = q/2$. Where the parameter q is the fraction of a wavelength change in the gap from the center of the aperture to it's edge. Our plates are polished flat to within $\lambda_0/100$[†] and thus $\mathcal{N}_{As} \approx 50$ at $\lambda_0 = 546.1\,nm$. At other wavelengths the fraction q varies which yields a wavelength dependent finesse

$$\mathcal{N}_{As} \approx 50(\lambda/\lambda_0) \tag{2.1.8}$$

This finesse is large compared to the contributions from the reflective and aperture finesse in equation (2.1.7) and becomes larger at longer wavelengths. Hernandez (1986) determines the coefficients (in a discrete Fourier transform (DFT) representation of the function) to be related to a sinc function ($sinc(x) = \frac{sin(x)}{x}$) as

$$dfc_k = sinc(2kdf_C^*) \tag{2.1.9}$$

where $df_C^* = q/2$ is the normalized half-width at the half-height (hwhh) of the broadening, in orders. Roughness can be thought of as an assembly of microscopic etalons of various gaps. The surface imperfections in this assembly are assumed to be randomly distributed across the plates. From the interference condition:

$$2\mu t \cos(\theta) = p\lambda \tag{2.1.10}$$

where μ is the index of refraction of the material in the gap (set equal to unity for the dry air gap, t is the gap spacing, θ is the angle of incidence for the incoming light, p is the order of the interference, and λ is the wavelength of the incoming radiation. From equation (2.1.10) (Chabbal, 1953) get

$$\frac{\Delta\lambda}{\lambda} = \frac{\Delta t}{t} \tag{2.1.11}$$

where Δt is the variation in the gap and $\Delta\lambda$ is the variation in the position of a gaussian lineshape at λ. Now if the variation in the gap is within the coating expert's stated tolerances then $\Delta t = \Delta t_{Hg} = \lambda_{Hg}/100$ and for the nominal values

[†] RWS: $\lambda_0 = 546.1\,nm$

$$\Delta\lambda = \frac{\Delta t_{Hg}}{t}\lambda = \left(\frac{5.461\times10^{-5}\,cm}{100\,(2\,cm)}\right)\lambda \approx 2.73\times10^{-7}\lambda \qquad (2.1.12)$$

Thus the finesse is

$$\mathcal{N}_{rough} = \frac{fsr_{Hg}}{\Delta\lambda_{Hg}} \approx \frac{86\,m\mathring{A}}{1.49\,m\mathring{A}} = 57.7 \qquad (2.1.13)$$

and the effects of the roughness is seen to be small with respect to the total finesse however a broadening of $\approx 2\,m\mathring{A}$ will affect the derived temperature if completely ignored.

The analytical treatment of a random assembly of microscopic etalons as for example Hernandez (1986) can be represented as a Gaussian distribution of phase deviations about the value of the gap. The coefficients r_k resulting from this treatment follow from the same basis as that for a Doppler broadened source profile

$$r_k = exp[-(\pi^2 k^2 df_G^{*2}/ln(2))] \qquad (2.1.14)$$

for df_G^* the normalized hwhh of the phase distribution in orders. Relating this result to those of Chabbal (1953) who defined a surface finesse $\mathcal{N}_{rough}$

$$\mathcal{N}_{rough} = q/4.71 = 1/2df_G^* \qquad (2.1.15)$$

which, for $q = 100$ gives a finesse $\mathcal{N}_{rough} = 100/4.71 \approx 21$ and a Gaussian hwhh $df_G^* \approx 23.5$ milli-orders. In terms of wavelength for the nominal values used in the above expression (an 86 mÅ fsr and a 2 cm gap) I find that $df_G = 2.35(86/100) = 2.02$mÅ for the roughness and $df_C = (86/100) = .86$mÅ for the asphericity. And for the asphericity

$$\mathcal{N}_{As} = \frac{fsr}{\Delta\lambda} \qquad (2.1.16)$$

so that at $5461\mathring{A}$

$$\Delta\lambda = \frac{fsr}{\mathcal{N}_{As}} \approx \frac{86\,m\mathring{A}}{57.7} \approx 1.49\,m\mathring{A}$$

Formulas (2.1.8) and (2.1.12) also show how to translate a defects function derived at one wavelength λ_0 say into a defects function at another wavelength λ as:

$$\Delta\lambda = \Delta\lambda_{\lambda_0}(\lambda/\lambda_0) \qquad (2.1.17)$$

The asphericity and roughness defects are then given by

$$1/\mathcal{N}_D = 1/\mathcal{N}_{rough} + 1/\mathcal{N}_{As} = \frac{\Delta\lambda_{\lambda_0}}{fsr}(\lambda/\lambda_0) + \frac{2}{q} \tag{2.1.18}$$

or with $q = \lambda_0/100$

$$1/\mathcal{N}_D = \frac{\Delta\lambda_{\lambda_0}}{fsr}(\lambda/\lambda_0) + \frac{\lambda_0}{50\lambda}. \tag{2.1.19}$$

Finally substituting in $\lambda^2/2t$ for fsr get

$$1/\mathcal{N}_D = (\frac{1}{\lambda})\left[\frac{2t\Delta\lambda_{\lambda_0}}{\lambda_0} + \frac{\lambda_0}{50}\right] \approx 38.3 \tag{2.1.20}$$

And it can be seen that the effective finesse limited by defects is small and improves with increasing wavelength as one would expect from physical arguments.

2.2 The Instrument

In Figure (2.2.1) the optical path and instrumental block diagram is shown. Light from the sky is reflected off the gold coated front surfaced mirror (M) which is tilted 60° from the vertical. This light is collected in the first lens (L1) which focuses the light through aperture (a) at the focal plane of lens (L2). The collimated light from L2 is then passed through a double paned window (ps) into the wedge-shaped etalon (e). After the etalon the collimated light is focused by lens L2′ through the second aperture (a′) and onto a dichroic element (diC) which splits the slightly diverging rays into its red and blue components. Each of these spectrally separated components are received in their own detection channel. For example in channel #1, after the dichroic, the light is collimated by lens l1 and passed through an interference filter (fl). The filter further spectrally isolates the light which is then refocused by lens l2 through a double paned window (dq) onto the sensitive area of a cooled photomultiplier tube (PMT). The photomultiplier tube is cooled to ≈ -30°C in order to reduce thermionic emissions.

The instrument is designed to conserve the quantity AΩ which is the product of the area of an optical element and the solid angle of acceptance.

The etalon plates are made of fused silica (a non-crystalline quartz). These plates are ground and polished on the outer surfaces so that the entire etalon when assembled forms a wedge. All surfaces are ground flat to within ± 55Å and then coated with a multilayer dielectric coatings by Optical Surfaces, Ltd.. There are four surfaces to consider in the design of this etalon. With two optical plates and a gap each plate and the gap may act

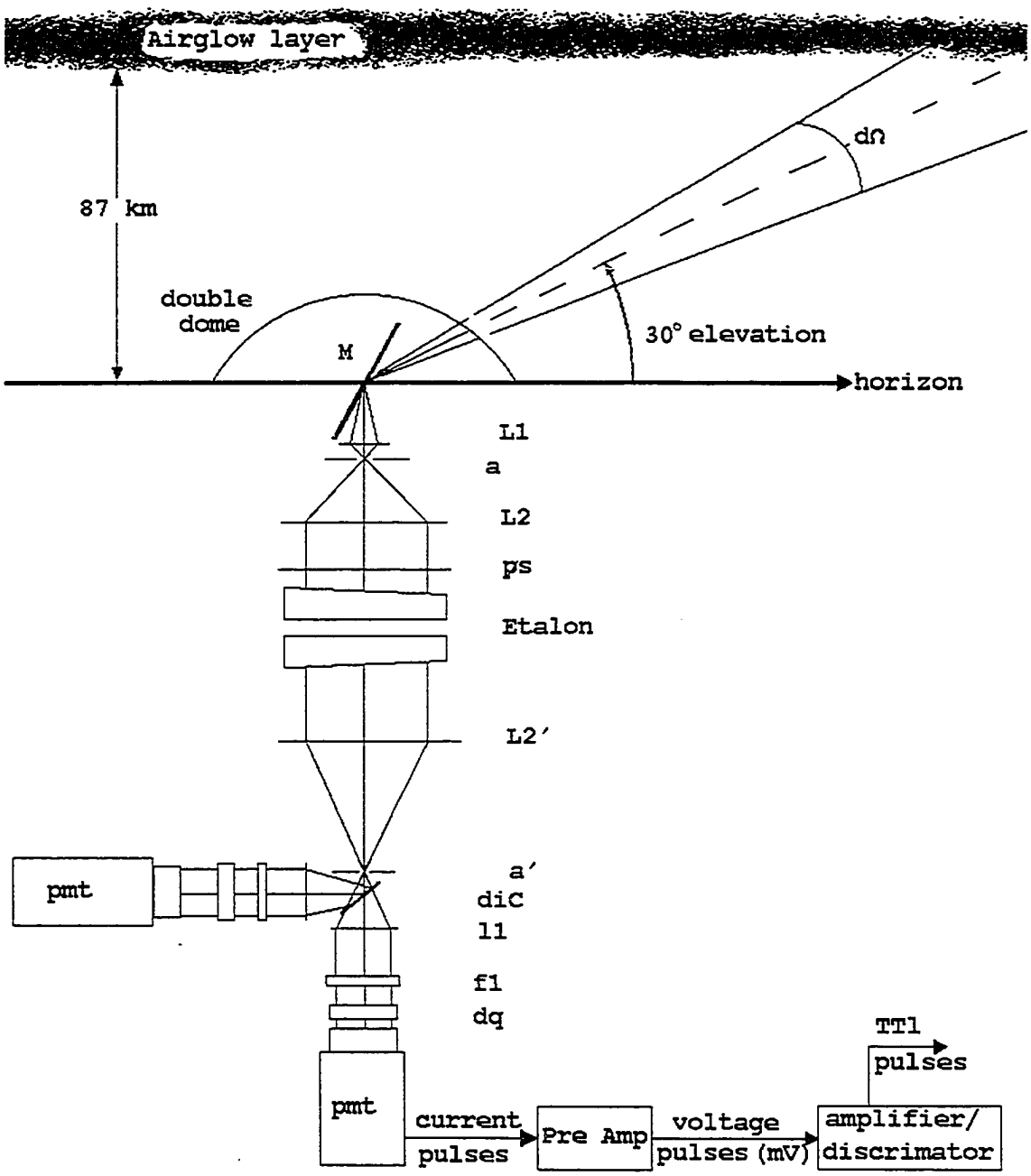

Figure 2.2.1 Sketch of the optical path of the South Pole instrument showing relavent geometry and data collection components.

as independent etalons. The wedge shape removes the parallelism of the outer surfaces of each substrate limiting the substrates ability to independently act as etalons. The first and last (outer) surfaces are coated to be antireflective and the second and third (inner) surfaces are coated to have a reflectivity near 80%. The wedge shape of the outer surfaces refracts the light reflected inside the substrate from the substrate side of the inner surfaces away from the optical axis. The light exiting the etalon is focused onto the scanning aperture (a'). The circular symmetry of the instrument produces fringes of equal inclination and the radii of these fringes is dependent on the etalon spacing. By varying this spacing we can collapse the intensity pattern into the aperture where these variations can be detected.

In each channel, after the dichroic, the light is collimated and passed through a, narrow band (~3Å), interference filter after which is it focused onto the PMT. The Hammamatsu R943-02 Head-on GaAs(Cs) PMT has a quantum efficiency of 10% in the near IR and is operated in the pulse counting mode with -1650 volts on the cathode and a grounded anode. Light incident onto the photoemissive Gallium-Arsenide cathode releases photoelectrons which are accelerated and focused through a ten dynode electron multiplier toward the positive anode. At each dynode collisions of the accelerating electrons with the metal surface produces secondary electrons. For each incident photon we collect approximately 10^5 electrons. A pulse preamplifier converts the charge pulses from the anode to voltage pulses in the mV range for transmission to the amplifier/discriminator which outputs well-shaped TTL pulses for the counting electronics.

The variation of the etalon spacing or gap is achieved by applying a variable high voltage to the piezoelectric gap spacers. The linear anisotropic response of the ceramic spacer, as a result of the application of high voltage (HV) causes them to expand or contract with a known response. A cyclic linear variation of this HV creates a cyclic linear variation in the gap. Each of these cycles produces a profile of counts recorded verses time and these are summed until a minimum total number of counts are obtained. An example of these raw data profiles is shown here in Figure (2.2.2). The etalon and interference filters are thermally controlled to $\pm 1\,^{\circ}C$.

Optical details for the South pole instrument

The solid angle of acceptance $d\Omega$ is calculated for the limiting scanning aperture as The focal length of L2' $= 65\,cm$ the gap $t \approx 2\,cm$ $\lambda = 8399$Å and $ap = 17.92$mK thus

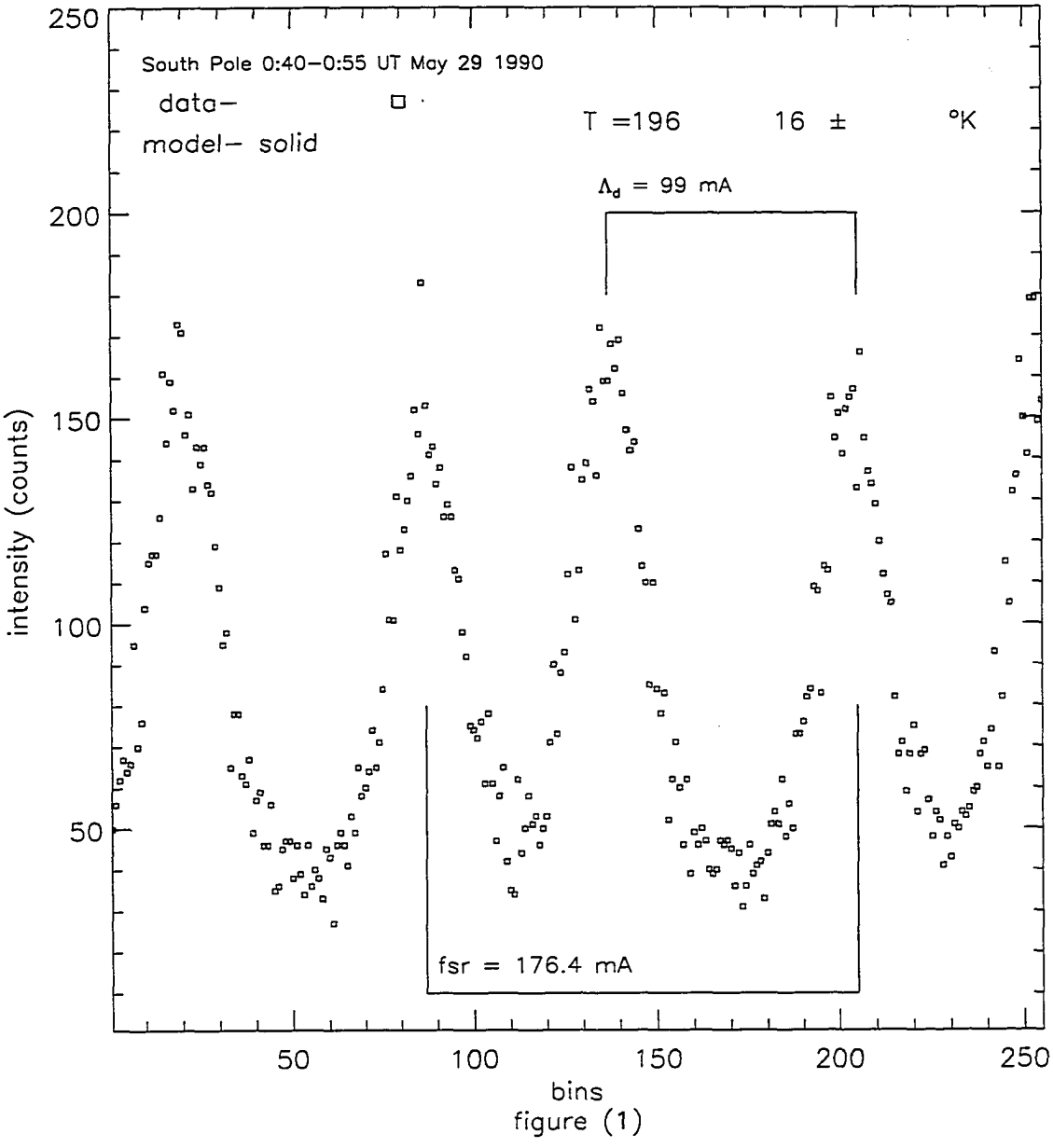

Figure 2.2.2 Typical raw data profile from South Pole OH emissions showing the relative countrate and resolution.

from appendix E for $ap = 2L\sqrt{2\lambda d\sigma} \approx .225\,cm$. Then since $\frac{dA}{L^2} = d\Omega = \frac{\pi}{4}(\frac{.225\,cm}{65\,cm})^2 \approx \frac{\pi}{4}1.198 \times 10^{-5}\,sr$ giving the value of

$$A\Omega = dAd\Omega = (\frac{\pi}{4}ap^2)^2\frac{1}{L^2} \approx 1.25 \times 10^{-3}\,sr - cm^2.$$

Thus the the diameter of the circular area d_{obs} in the sky at height $h = 87$km from which the instrument receives light to be $d_{obs} = 2(h/sin30)\sqrt{d\Omega/\pi}$ or about 600 meters.

The etalon plate reflectivities are: $R \simeq .811$ at 5577Å; $R \simeq .793$ at 6328Å; and $R \simeq .805$ at 8400Å. The scanning aperature is .027 Kaysers (or 27 mK = 27 cm^{-1}) at 5577 Å. For the elements in Figure (2.2.1) I use the following values:

double dome $.96^4$ (4 surfaces with a transmission coefficient of .96 each)

M .96 reflective coefficient

L1 $.96^2$ fl=10 cm (2 surfaces with a transmission coefficient of .96 each)

a .45 cm diameter opening

L2 $.96^2$ fl=65 cm diameter=6in (as for L1)

ps $.96^2$ double pane glass shield

e etalon four coated surfaces with a 13 cm useful diameter

L2′ $.96^4$ fl=65 cm diameter=6in doublet (4 coated surfaces)

a′ .225 cm diameter opening

DiC 90% transmission(red)/reflection(blue)

inclined at 45° from the optical axis (1.5x1.5 cm^2 elliptical area)

"hot" type reflects red, transmits blue

"cold" type reflects blue, transmits red

each of two channels

l1 $.96^2$ diameter= 1.5in (two surfaces as for L1)

f1 .4 3 Å diameter=1.5in

l1′ $.96^2$ diameter=1.5in (two surfaces as for L1)

double-pane window $.96^4$ (four surfaces at .96 each)

quantum efficiency .1 Hammamatsu 943-02 5577-8400 Å

Assuming an ideal etalon with unity transmission I calculate the overall instrumental transmission as $.96^{23} \times .4 \times .1 \approx .0156$. The etalon transmission is expected to be between 1 and .5 giving a system total transmission of $\sim 1\%$

2.3 Optimization of the Fabry-Perot Parameters

The problem I wish to address in this section is what are the best parameters for the setup of the Jacquinot and Dufour single aperture type planer Fabry-Perot spectrometer we have for simultaneously measuring the relative position and shape of two different spectral lines. An optimization scheme using the minimum uncertainty criteria for single-line profiles is extended from the current literature to include lambda-doubled lines. Theoretical results are derived for estimating the uncertainty in the measurement of line positions and widths of lambda-doubled line profiles from a FPS.

I outlined the optimization procedure of Hernandez (1982b and 1986) for a singlet structure in appendix C. This procedure parameterizes the instrument and derives the desired measurements in terms of these parameters. Propagating the measurement errors (from counting statistics), expressions for the uncertainties in the derived measurements, in terms of the instrument parameters, were given in equations (C.24) and (C.30). By varying these parameters a minimum in the measurement error is obtained. These results are applicable to singlet structures only and do not account for the problems of partially overlapping Gaussians aperiodically spaced. I extend the optimization results for use with doubled structures, in particular the OH doublet.

Inclusion of an additional line in the profile source coefficients S_k is merely the sum of two Gaussians, and with a little manipulation these are expressed as

$$s_k = \frac{1}{\sqrt{2}} exp[-\frac{\pi^2 dg^{*2} k^2}{ln2}(1+[\frac{\sigma_{cd}}{2\sigma_0}]^2)] \times [cosh(4\pi^2 dg^{*2} k^2 [\frac{\sigma_{cd}}{2\sigma_0}]) + cos(4\pi k \sigma^*_{cd})]^{1/2}. \quad (2.3.6)$$

Here σ^*_{cd} is half the doublet spacing σ_{cd} as derived in appendix B divided by the fsr $\Delta\sigma$. For small values of $\frac{\sigma_{cd}}{2\sigma_0}$ (i.e., for this $P_1(2)$ line where $[\frac{\sigma_{cd}}{2\sigma_0}] \approx 5.89 \times 10^{-6}$) the cosh term is set equal to '1' and $[\frac{\sigma_{cd}}{2\sigma_0}]^2$ is neglected in the exponential so that with the inclusion of the instrumental effects the new coefficients for the total flux b_k are

$$b_k = Q\mathcal{R}^k d_k sinc(2kf^*) exp[-\gamma k^2 \tau] \sqrt{\frac{1 + cos(4\pi k \sigma^*_{cd})}{2}}. \quad (2.3.1)$$

The use of the b_k does not affect the derivation for the uncertainty in the line position and equation (C.24) can be used with the modified b_k substituted for the a_k.

From appendix C I rewrite equation (C.24) for the variance in the wind determination as

$$\sigma_v{}^2 IAT\epsilon\tau_L dg^{*2} n_0 = \left(32\frac{\pi^3}{c^2}\left[1-\frac{\mathcal{A}_e}{(1-\mathcal{R})}\right]^2\frac{(1-\mathcal{R})}{(1+\mathcal{R})}\right)^{-1}$$

$$\times\left(f^*(dg^*)^2\left[\sum_{k=1}^{N}(b_k k)^2\left[1+J-b_{2k}cos^2(4\pi k\frac{x_0}{T})\right]^{-1}\right]\right)^{-1} \qquad (2.3.2)$$

Where I is the irradiance of the source (photons/unit time-unit area-steradian), A is the useful area of the etalon, ϵ is the quantum effeciency, τ_L is the combined etalon and system transmission loss, $f^* = f/2$ where f is the aperture size (in orders), n_0 is the central order of interference, T the profile periodicity in x units, and $\mathcal{A}_e$ is the combined etalon absorption and scattering coefficient.

The analysis for the temperature uncertainty is more complicated. In the singlet analysis it was possible to define a new set of coefficients U_k as

$$U_k = ln(b_k/d_k) = ln(Q) - \gamma k^2\tau \qquad (2.3.3)$$

which eliminated the unknown defect coefficients d_k and reduced the determination of the temperature to that of a linear least-squares fit to a straight line with τ vs. k^2. With the inclusion of the additional modulation term I would obtain

$$U_k = ln(b_k/d_k) = ln(Q) - \gamma k^2\tau + ln(\sqrt{\frac{1+cos(4\pi k\sigma^*_{cd})}{2}}). \qquad (2.3.4)$$

Neither the b_k nor the U_k can be reasonably linearized and a non-linear fit must be used to determine the parameters and estimate the uncertainties. From the non-linear least squares method of Levenberg-Marquardt the best value of the temperature is found through an iterative process. The uncertainty in the derived parameters are obtained from the inversion of the curvature matrix.

Here I use a two parameter fit for b_k. There are three explicit parameters in equation (2.3.1); f^*, τ, and σ^*_{cd}. f^* is normalized by the fsr $\Delta\sigma$ which is related to τ through dg^*. I allow $f/2$, the aperture size, to vary independently so as to maintain f^* constant leaving only τ and σ^*_{cd} for the fit.

For a least-squares fit to an arbitrary function the uncertainties in the parameters are related to the elements of the curvature matrix α which are given by

$$\alpha_{jl} = \sum_{i=0}^{T} \frac{1}{\sigma_i^2} \left(\frac{\partial y(x_i, \mathbf{a})}{\partial a_j} \right) \left(\frac{\partial y(x_i, \mathbf{a})}{\partial a_l} \right) = \sum_{k=0}^{N} \frac{1}{\sigma_{b_k}^2} \left(\frac{\partial b_k(\mathbf{a})}{\partial a_j} \right) \left(\frac{\partial b_k(\mathbf{a})}{\partial a_l} \right), \qquad (2.3.5)$$

as derived from a first order expansion of χ^2. $\mathbf{a} = [\tau, \sigma_{cd}^*]$ is the parameter vector. For the two parameter fit α is a 2×2 matrix and the elements of the error matrix ϵ are given by

$$\epsilon_{jk} = [\alpha^{-1}]_{jk} = \frac{[\alpha^{\dagger}]_{jk}}{|\alpha|} \qquad (2.3.6)$$

and the uncertainty is given by

$$\sigma_{a_j} = \sqrt{\epsilon_{jj}}. \qquad (2.3.7)$$

With b_k as in equation (2.3.1) the partial derivatives are

$$\frac{\partial b_k}{\partial \tau} = -\gamma k^2 b_k \qquad (2.3.8)$$

$$\frac{\partial b_k}{\partial \sigma_{cd}^*} = -4\pi k \frac{sin(4\pi k \sigma_{cd}^*)}{1 + cos(4\pi k \sigma_{cd}^*)} b_k \qquad (2.3.9)$$

so that

$$(\sigma_\tau)^2 = \frac{\sum_{k=1}^{N} \frac{1}{\sigma_{b_k}^2} \left(\frac{\partial b_k}{\partial \sigma_{cd}^*} \right)^2}{\sum_{k=1}^{N} \frac{1}{\sigma_{b_k}^2} \left(\frac{\partial b_k}{\partial \tau} \right)^2 \sum_{k=1}^{N} \frac{1}{\sigma_{b_k}^2} \left(\frac{\partial b_k}{\partial \sigma_{cd}^*} \right)^2 - \left[\sum_{k=1}^{N} \frac{1}{\sigma_{b_k}^2} \left(\frac{\partial b_k}{\partial \tau} \right) \left(\frac{\partial b_k}{\partial \sigma_{cd}^*} \right) \right]^2} \qquad (2.3.10)$$

where as before I have ignored the instrument contribution as independent of τ and very precisely known.

Now with equation (C.13) from appendix C

$$\sigma_{b_k}^2 = \frac{Q}{2T} [1 + J + a_{2k} cos(\frac{4\pi k x_0}{T})] \qquad (2.3.11)$$

I can write

$$(\frac{\sigma_\tau}{\tau})^2 \frac{IAT\epsilon\tau_L}{n_0} = \left(\frac{8\pi^5}{(ln2)^2} \left[1 - \frac{\mathcal{A}_e}{(1-\mathcal{R})} \right]^2 \frac{(1-\mathcal{R})}{(1+\mathcal{R})} f^* (dg^*)^4 \right)^{-1}$$

$$\times \left[\sum_{k=1}^{N} w_k k^4 - \left[\sum_{k=1}^{N} w_k k^3 \left(\frac{sin(4\pi k \sigma_{cd}^*)}{1 + cos(4\pi k \sigma_{cd}^*)} \right) \right]^2 \left(\sum_{k=1}^{N} w_k k^2 \left[\frac{sin(4\pi k \sigma_{cd}^*)}{1 + cos(4\pi k \sigma_{cd}^*)} \right)^2 \right]^{-1} \right]^{-1} \qquad (2.3.12)$$

for the relative variance in τ.

From the numerical solution of expressions (2.3.2) and (2.3.12) for the generalized minimum uncertainties can be obtained for each set of input parameters. In Figures (2.3.1) and (2.3.2) I give these results with the values of f^* at which I have found the minimum uncertainty. In appendix C the temperature determination for a single-line shows the most stringent requirements (minima are in steeper wells) and I defered to these for the limiting factors, for instance, the minimum number of "useful" coefficients 'N' and samples/fsr 'T' ($T \geq 2N$ for the Nyquist limit) needed will be different for width and position determinations. The values determined from equation (C.18) are 7 and 4 for the width or temperature and the line position determinations, respectively (Hernandez, 1986). Thus the value of 7 was used in both calculations for Figures (C.1) and (C.2) as well as in Figures (2.3.1) and (2.3.2). For the case of the low snr OH analyses the use of more than 6 coefficients is usually impossible. The use of less than this critical number of coefficients is discussed in Hernandez (1982b) where he shows that in fact the use of only 3 coefficients is adequate to limit the uncertainty to within a few percent of the minimum relative uncertainty for the temperature determination and 2 coefficients for the line position.

The oscillatory nature of the analytic solution is demonstrated in Figure (2.3.1) and (2.3.2). The normalized gaussian width dg* can be related to $\sigma^*_{c,d}$ with

$$dg = \frac{\sigma}{c}\sqrt{\frac{2\tau k A ln(2)}{M}} \approx 14.6mK \tag{2.3.13}$$

thus

$$\Delta\sigma = \frac{dg^*}{dg} \tag{2.3.14}$$

where $\sigma = 11906.17\,cm^{-1}$ (the wavenumber related to 8399Å), $\tau = 200°$K, $k = 1.3802 \times 10^{-16}$erg/°K (Boltzmann's constant), A is Avogadros number, $c = 3 \times 10^8$m/s, and M is 17 AMU. From section 1.2 $\sigma_{cd} \approx 141\,mK$ so that

$$\frac{\sigma_{cd}}{\Delta\sigma} \approx dg^*(141/14.6) \tag{2.3.15}$$

Then for the line position error and is a minimum when $dg^* \sim .11, .21$ or $\Delta\sigma \approx \sigma_{cd}, 2\sigma_{cd}$ that is when the fsr is the same as the doublet spacing or twice that. Similarly for the width errors the minima occur for $dg^* \sim .7, .157, .25$ or $\Delta\sigma \approx \frac{2}{3}\sigma_{cd}, \frac{3}{2}\sigma_{cd}, \frac{5}{2}\sigma_{cd}$. This indicates that all the peaks are separated (no overlap) with regular spacing and the deepest minimum occurs for complete separation in both the winds and temperatures.

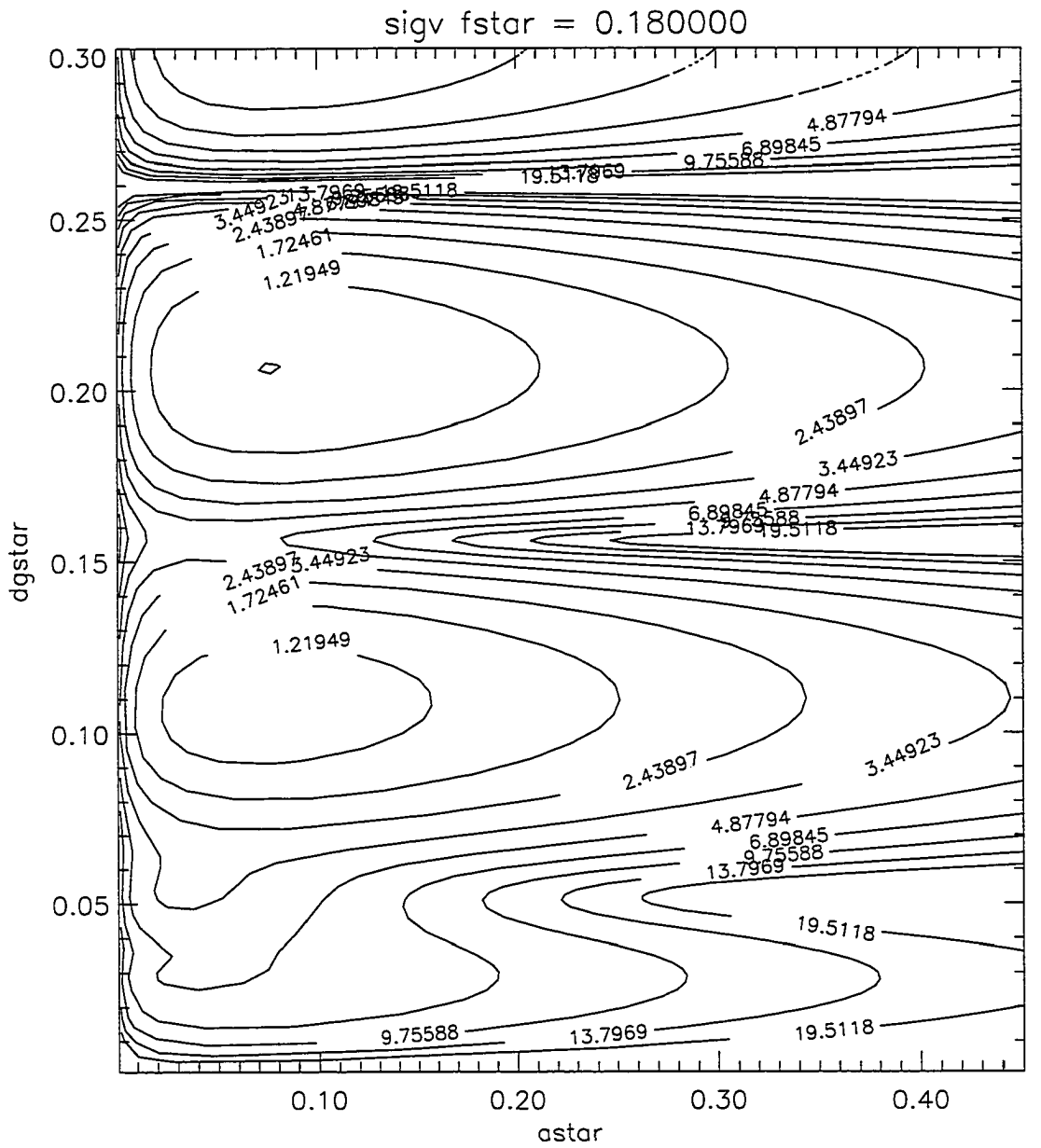

Figure 2.3.1 Uncertainty topology for the determination of the line center of a doubled-line Doppler profile ($f^* = .180$) as measured with an FPI. Where 'dgstar' = dg^* and 'astar' = a^*. The panel is generated with the value of $f^* = .180$ for the neutral winds. Note the absolute minimum at .208 .

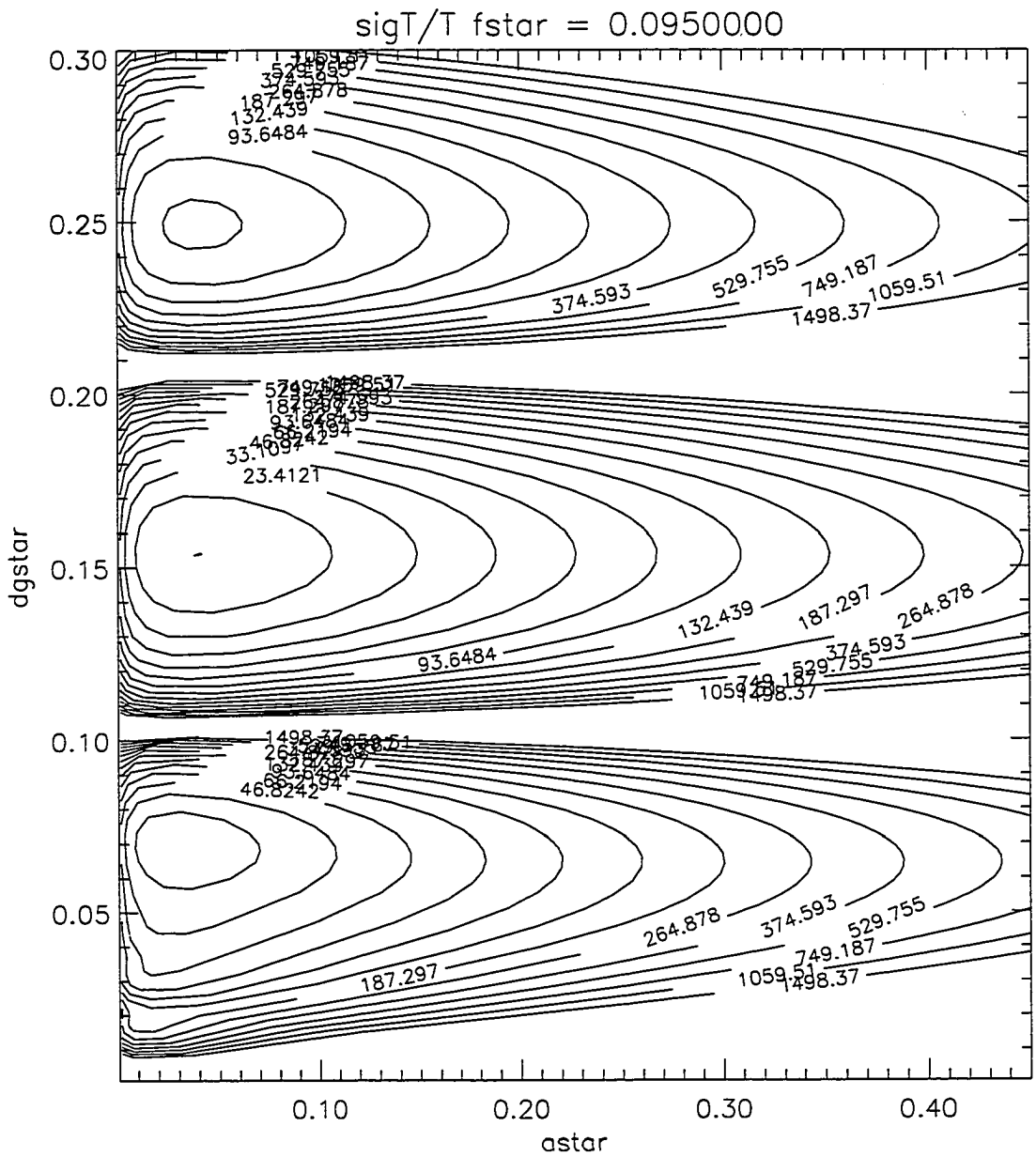

Figure 2.3.2 Uncertainty topology for the determination of the line width of a doubled-line Doppler profile ($f^* = .095$) from an FPI. The panel is generated with the value of $f^* = .095$ for the temperature.

In order to observe two different emission lines simultaneously it is clear that a compromise between the different optimal parameter sets is called for. The connection between the normalized aperture parameter f^* for the different wavelengths is as follows. For example choosing the 5577Å line $\sigma = 17930.78$K as the standard the minimum uncertainty is found in the panel where $f^* = .064$ (Figure C.1) gives an aperture width of $f = 2\Delta\sigma f^* = 2(.250)(.064) \approx 32mK$. This comes from the fractional order change 'Δn' across 1/2 the aperture. Where Δn is related to the physical dimensions of the aperture. This must be specified at some wavelength $1/\sigma_0$. The formula derived is

$$\mu_0(1 - \frac{\Delta n}{\mu_0}) = f/2 \tag{2.3.16}$$

then the translation to σ_i is achieved as

$$(f/2)_{\sigma_i} = (f/2)_{\sigma_0}\frac{\sigma_i}{\sigma_0} \tag{2.3.17}$$

Which in terms of the normalized half-width f^* becomes

$$(f/2)_{\sigma_i} = 2\Delta\sigma f^*\frac{\sigma_i}{\sigma_0}. \tag{2.3.18}$$

Then for OH the aperture seen will have the width

$$(f/2)_{11906.17} = 32mK\frac{11906.17}{17930.78} \approx 21.23mK.$$

If I had four different instruments, one each for the measurement of wind and temperature for each line then what parameters should be used to obtain the minimum uncertainties? To answer this question I conducted a parameter search for the global minima and found these at $f^* = .08$ and$f^* = .175$ for the single-line temperature and wind determinations, respectively. These lead to the following instrumental setup

$$\frac{\sigma_\tau}{\tau}\sqrt{\frac{IAT\epsilon\tau_L}{n_0}} \approx 13.97 \qquad \sigma_v\sqrt{IAT\epsilon\tau_L(dg^*)^{-2}n_0} \approx .84\times10^9$$

$$dg^* \approx .12 \qquad dg^* \approx .18$$

$$a^* \approx .034 \qquad a^* \approx .075$$

$$\Delta\sigma \approx .189\,cm^{-1} \qquad \Delta\sigma \approx .126\,cm^{-1}$$

$$d \approx 2.63cm \qquad d \approx 3.95cm.$$

And for the doubled-line the results were $f^* = .095$ for the temperature and $f^* =$

.180 for the winds which imply the following

$$\frac{\sigma_\tau}{\tau}\sqrt{\frac{IAT\epsilon\tau_L}{n_0}} \approx 11.696 \qquad \sigma_v\sqrt{IAT\epsilon\tau_L(dg^*)^{-2}n_0} \approx .86\times10^9$$

$$dg^* \approx .154 \qquad dg^* \approx .208$$

$$a^* \approx .039 \qquad a^* \approx .075$$

$$\Delta\sigma \approx .0948\,cm^{-1} \qquad \Delta\sigma \approx .070\,cm^{-1}$$

$$d \approx 5.27cm \qquad d \approx 7.12cm$$

where only the values for the deepest minimum are shown.

I continue this general examination now adopting a typical brightness value of 100 Rayleighs for the 5577Å line, (Chamberlain, 1961), and 28 Rayleighs for each component of the doubled line, (section 1.2). Furthermore I choose the nominal values of I, A, T, ϵ, and τ_L (.01) from the South Pole instrument, without discussion yet, in order to compare the results at the optimal parameters. Here I must discuss the ratio T/n_0. For the equal-time/equal-distance operation of the FPS we scan the etalon gap the same distance regardless of the initial gap value so that as the central order changes the number of samples for the entire scan remains constant. The change in the number of samples which now fit into one fsr is in the inverse proportion as the change in the order number. I fix this ratio at a known value for our instruments. With these I find that

$$(T/n_0)_{\sigma_2} = (T/n_0)_{\sigma_1}(\frac{\sigma_1}{\sigma_2})^2 \tag{2.3.19}$$

so that for the 5577Å line $T/n_0 \approx .0010$ and for the 8399Å line $T/n_0 \approx .0024$. Similarly in the factor for the wind uncertainty I have

$$(Tn_0/(dg^*)^2) \propto Tn_0/{n_0}^2 = T/n_0 \tag{2.3.20}$$

and will scale in wavelength as in expression (2.3.19). I then obtain the 5577Å results

$$\sqrt{\frac{IAT\epsilon\tau_L}{n_0}} \approx 543.37 \qquad \sqrt{IAT\epsilon\tau_L(dg^*)^{-2}n_0} \approx .426\times10^9$$

$$n_0 = 17930.78/.189 \approx 94871 \qquad n_0 = 17930.78/.126 \approx 142307$$

giving the uncertainties

$$\sigma_\tau = 200(13.97/543.37) \approx 5.1°K \qquad \sigma_v = (.84/.426) \approx 1.9\, m/s.$$

For the 8399Å line

$$\sqrt{\frac{IAT\epsilon\tau_L}{n_0}} \approx 433.89 \qquad \sqrt{IAT\epsilon\tau_L(dg^*)^{-2}n_0} \approx .341\times10^9$$

$$n_0 = 11906.17/.0948 \approx 125592 \qquad n_0 = 11906,17/.070 \approx 170088$$

giving the uncertainties

$$\sigma_\tau = 200(11.696/433.89) \approx 7.5°K \qquad \sigma_v = (.86/.341) \approx 3.4\, m/s.$$

Where the major contribution to the difference in the uncertainties between the doubled-line and single-line results has been reduced to the difference in the irradiance I and the central order of interference n_0. So it could be if I had four independent instruments to make these four measurements. It turns out that the rate of increase in the uncertainties is not very large as we move away from the optimal parameters.

The actual parameters used at south pole are as shown in section 2.2 with a .225 cm aperture and a 2 cm gap. The following expected minimum uncertainties are then theoretically possible

$5577Å$	$8399Å$
$\mathcal{R} = .811$	$\mathcal{R} = .805$
$f^* = .054$	$f^* = .0355$
$a^* = .0334$	$a^* = .0345$
$dg^* = .0910$	$dg^* = .0584$
$n_0 = 71723$	$n_0 = 47624$
$\sqrt{\frac{IAT\epsilon\tau_L}{n_0}} \approx 543.37$	$\sqrt{\frac{IAT\epsilon\tau_L}{n_0}} \approx 433.89$
$\sqrt{IAT\epsilon\tau_L(dg^*)^{-2}n_0} \approx .426\times10^9$	$\sqrt{IAT\epsilon\tau_L(dg^*)^2n_0} \approx .341\times10^9$

These results are applied to derive the uncertainty panels of Figures (2.3.3)-(2.3.5). From these figures the uncertainties are found to be at 5577Å

$$\sigma_\tau = 200(14.76/543.37) \approx 5.4°K \qquad \sigma_v = (1.15/.426) \approx 2.7\, m/s.$$

For the 8399Å line

$$\sigma_\tau = 200(19.56/433.89) \approx 9.0°K \qquad \sigma_v = (2/.341) \approx 5.8\, m/s.$$

These values are not far from the calculated theoretical global minima.

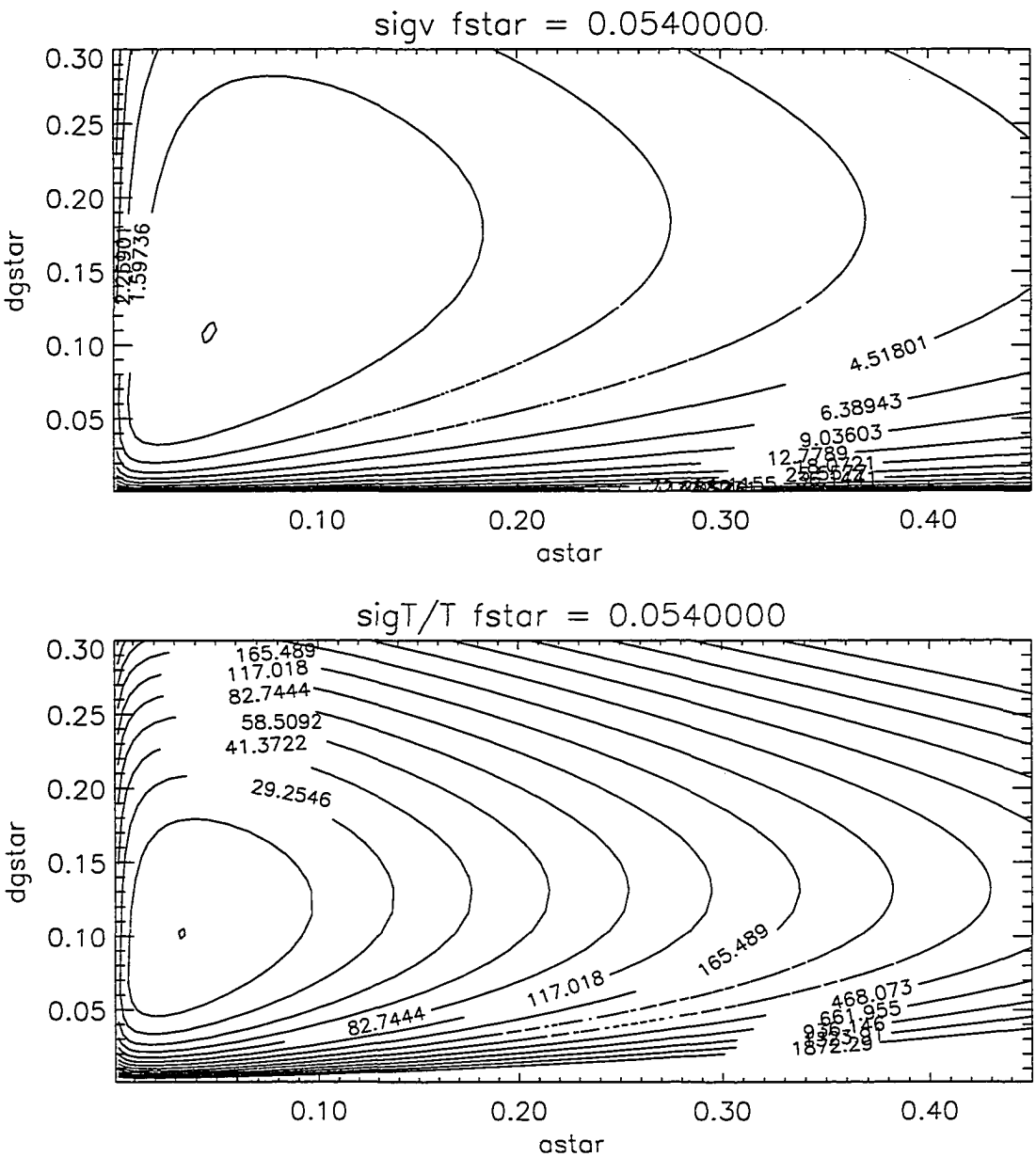

Figure 2.3.3 Uncertainty topology for the determination of the line center and line width of a single-line Doppler profile (f^*= .054) from an FPI. The upper panel shows the topology for the line center determination and the lower panel is for the line width. Both determinations are generated with the value of $f^* = .054$. For the upper panel the minimum is found at 1.12 and in the lower panel at 14.62.

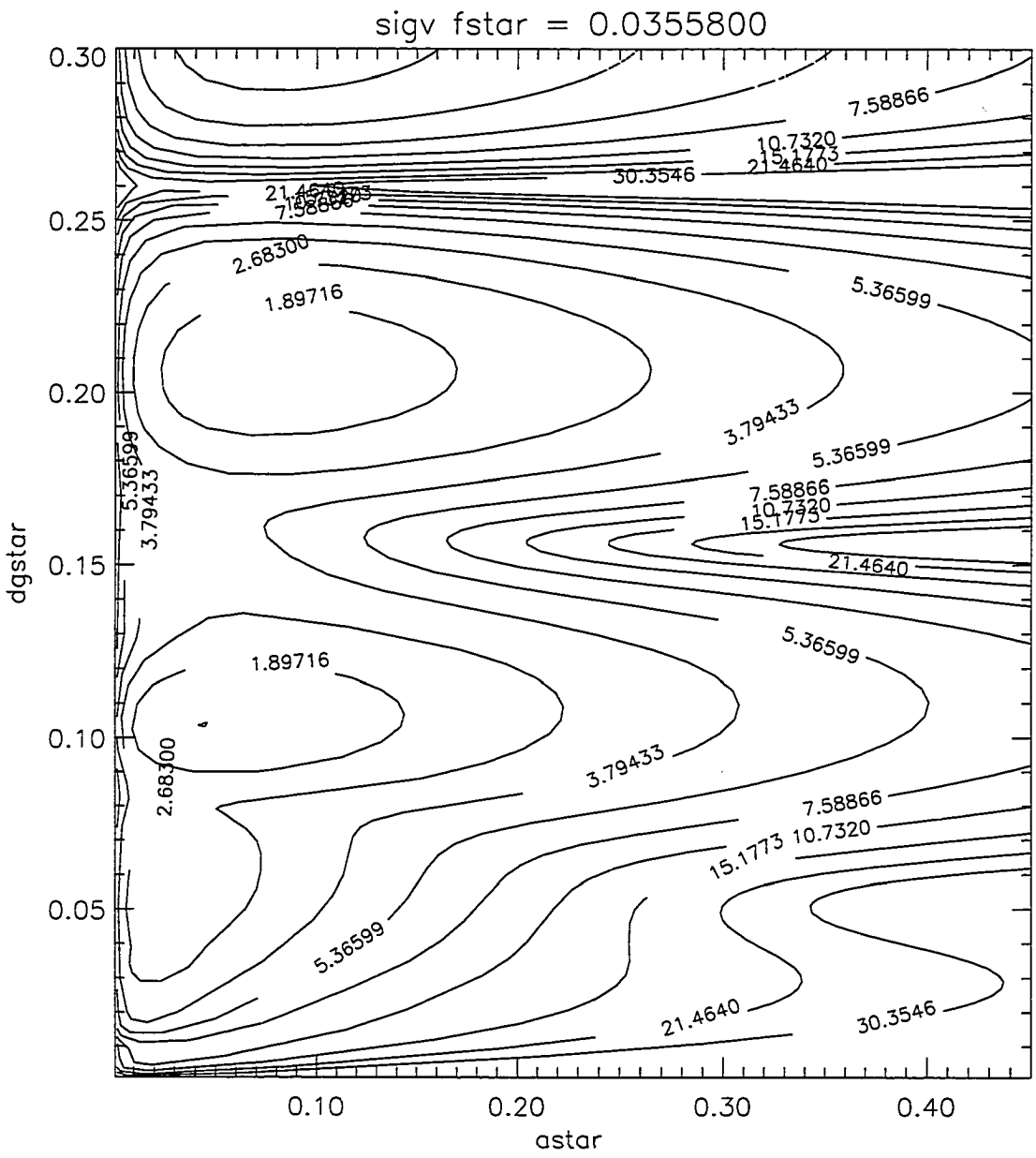

Figure 2.3.4 Uncertainty topology for the determination of the line center of a doubled-line Doppler profile ($f^* = .03558$) from an FPI. The panel is generated with the value of $f^* = .03558$ for the neutral winds. The minimum is found at 1.34.

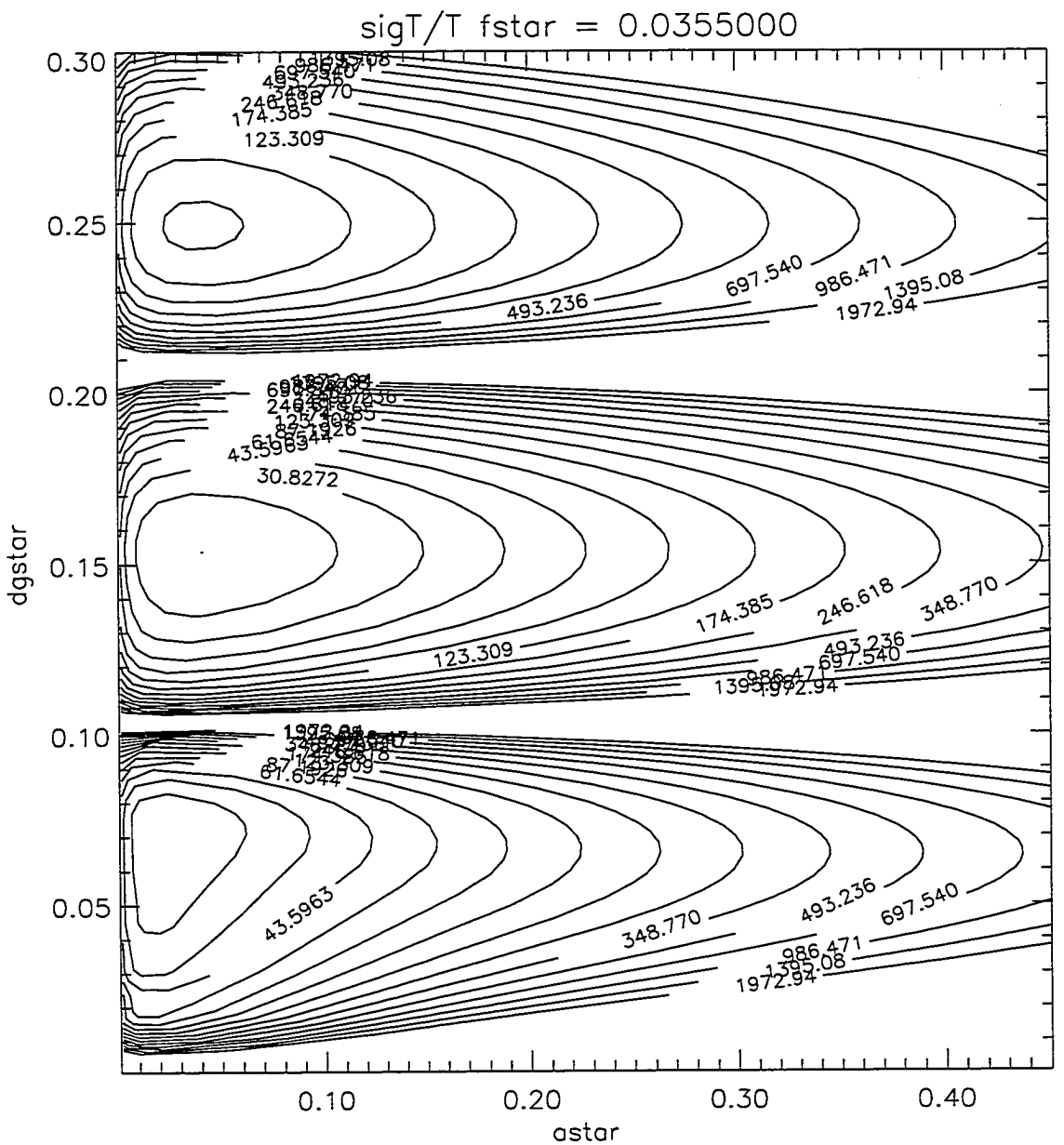

Figure 2.3.5 Uncertainty topology for the determination of the line width of a doubled-line Doppler profile ($f^* = .0355$) from an FPI. The panel is generated with the value of $f^* = .0355$ for the temperature. The minimum is found at 21.79.

Chapter 3 Analysis Techniques

3.0 Introduction

This chapter describes the analysis procedures used to reduce the data. As described in chapter 2, the FPS raw data profiles analyzed in this work are segments of a periodic intensity pattern and as such they are commonly treated with discrete Fourier transform (DFT) methods. One result of this study is a comparison between a DFT treatment and a non-linear least-squares (NL^2S) direct fit reduction of the raw data profiles. The motivation and results of this comparison are discussed in section 3.1.1. In section 3.1.2 the NL^2S direct fit method is developed and in section 3.1.3 the error analysis for the uncertainties in the derived parameters is given.

The preceding analyses produce time series of peak positions (line-of-sight Doppler wind), kinetic temperatures, and photon countrates (from the relative intensity measurement) from the data. These time series are treated with standard spectral analysis techniques (DFT) in order to characterize the wave fields for these parameters. In section 3.2.1 the DFT method used is shown and in section 3.2.2 the error analysis of the uncertainties is given.

The polar mesopause wavefields show spatial and temporal variations in spectral content which are not adequately characterized by the analysis of long data periods as a whole. Although useful in determining the persistence of long period spectral features and perhaps the interaction of these waves with the global mean background, the dynamics of these waves for short time periods (~2-3 cycles of a wavetrain) may give us the clues needed for the elucidation of the wave interactions with other waves and the local mean background. For this reason the time dependence of the spectral amplitudes was sought. This is accomplished with the use of a 'sliding window' on the data.

The DFT derived spectral coefficients, although orthogonal, are limited to harmonics of the data window. In a sense this requires a-priori knowledge of the spectral content in selecting the window length if the best resolution is desired. In addition to this limitation

the unequal time spacing of the data requires interpolation techniques which may skew the spectral content recovered. By using an harmonic analysis the interpolation is obviated and spectral resolution is improved, although the orthogonality of the coefficients is not preserved. In section 3.3.1 the harmonic analysis method is shown and in section 3.3.2 the error analysis and uncertainties are discussed. For the same reasons as given above a sliding time window analysis is used for the harmonic fit and the windowing is discussed in section 3.3.3.

3.1.1 Treatment of raw data- the DFT and Non-Linear Least-Squares method

The first attempt to measure an upper atmosphere temperature using the Doppler broadening was apparently made by Babcock (1923) and his method, in its essentials, has been employed in most, if not all, subsequent attempts. He photographed the night sky through a Fabry-Perot interferometer of high resolution and estimated the width of the 5577Å spectral line from the intensity profile of the fringes produced. He used five different orders of interference and inferred a width of .035Å . Although the actual width of $\approx$.015Åwas beyond the resolving power of his instrument this work did allow an upper limit to be set. Since then improved technology has led to increased resolution and routine collection and computer storage of interference profiles with $\approx$ .0004Åresolution every 5 minutes as in the case for the brighter emissions.

The determination of the temperature of a gas from its Doppler broadened spectral lineshape requires two elements; an emission intensity profile, and a model of the lineshape dependent on temperature. The spectral lines obtained with the FPS for this work, as described in chapter 2, are segments of a periodic intensity pattern of Doppler line profiles. The modelling of this pattern involves the determination of the peak centers and widths. One method for this determination is the use of discrete Fourier transform methods (DFT). Hays and Roble (1971) demonstrated a technique for the recovery of the Doppler information in these patterns for low SNR from single-line emissions. This technique involved non-linear least-squares (NL^2S) fitting of the low order discrete Fourier transform (DFT) coefficients of an observed profile to a Fourier decomposition of a model profile using an ideal instrument function. By taking the natural logarithm of the low order DFT coefficients one can use a linear least-squares fit to obtain the temperature as outlined in Hernandez (1978).

Although the DFT technique has been quite successful in the analysis of low signal-to-noise ratio (SNR) single-line emission features, and is well described by Hernandez (1978 and 1986) in the case of low SNR (nightglow) multiple-line structures it has failed to resolve the multiple-line information necessary for determination of the lineshape.

One of the primary tasks set for my graduate work was the successful recovery of the temperature information from these lineshapes. This led to the development of a non-linear least-squares (NL^2S) direct fit reduction of the raw data profiles. One result of this study is a comparision between a DFT and the NL^2S treatments, (Conner, et al., 1993). Briefly, the DFT method performs a linear least-squares fit of the low order DFT coefficients from one period of the data, after deconvolution of the instrument function, The slope of the fitted line is proportional to the temperature, assuming the etalon plate defects and the emission lineshape are gaussian. The NL^2S direct fit method also assumes gaussian shapes for the plate defects function and the source profile and fits a convolution of a model profile and instrument function to the raw data, the temperature of the model source profile being the derived temperature. The conclusions given were that in the case of low SNR (nightglow) multiple-line structures the NL^2S direct fit to the raw data provides more consistent results with smaller uncertainties in the derived temperatures. The difference in the uncertainties being a factor of $\sqrt{2}$. In actual practice this improvement is partially reduced by the additional uncertainty from the doublet spacing but is recovered with the use of more than one fsr in the NL^2S method. Both methods also provide the relative peak position which is related to wavelength and thus the line-of-sight Doppler shift due to bulk motion of the emitting layer.

3.1.2 NL^2S method derivation of the time series

The *direct fit* for determination of the Doppler shift and width begins with trial profile parameters for first guess values of peak positions, temperature, maximum intensity, and background intensity, from which a model singlet or doublet is generated. A final model profile is produced from the convolution of this singlet or doublet profile with a model instrument function. After a rough peak position alignment is found for the trial profile, the Levenberg-Marquardt method (Press et al., 1986) is then used to locate the best set of values for the above mentioned parameters which minimizes the least-square-error, in the χ^2 sense, between the model and the data. This method is a combination of the inverse Hessian and the steepest descent methods. The steepest descent method is used

to get close to the minimum and then the inverse Hessian method takes over as it is approached. Figure (3.1.1) shows an example of a direct fit to measurements of upper atmosphere OH emissions.

The model instrument function, Hernandez (1986) was constructed from the convolution of an Airy function and a model 'top hat', describing a perfect scanning etalon of given reflectivity and scanning aperture. The incorporation of the effects of plate defects is made by analyzing an observation of a He-Ne laser source which is assumed to be a very narrow spectral line. After removal of the Airy and aperture functions, from the laser observation, by deconvolution the residual is assumed to be a Gaussian-shaped function, the width of which gives an effective 'defects temperature'. In order to translate this defects function from the laser emission wavelength to that of other species, the effective defects temperature is scaled by the ratio of the mass of the new species to the mass of the Ne species from the laser. The 'scaled effective temperature' is then subtracted from the deduced sky temperature.

The Singlet Analysis

The singlet source profile was assumed to be Gaussian since in the cases of interest it is dominated by Doppler broadening. The analytic representation of a singlet Gaussian source profile, $g(\lambda)$ follows from the line-of-sight Maxwell-Boltzmann distribution of molecular speeds (Gill, 1965):

$$g(\lambda) = N + \frac{g_0}{\pi^{1/2}}\left[\frac{dg}{\sqrt{4\ln(2)}}\right]^{-1} exp\left[-(\lambda-\lambda_0)^2\left(\frac{dg}{\sqrt{4\ln(2)}}\right)^{-2}\right] \qquad (3.1.1)$$

where $dg = \left[\frac{AkT\lambda^2 8ln2}{mc^2}\right]^{\frac{1}{2}} = 7.15\times10^{-7}\lambda\sqrt{\frac{T}{m}}$ = the Gaussian linewidth, T = temperature in degrees Kelvin, c = the speed of light, k = Boltzmann's constant, λ_0 the non-Doppler shifted emission wavelength, λ the Doppler shifted emission wavelength, m is the mass in units of AMU, g_0 and N are signal and background intensity counts, and A is Avogadro's number.

The Doublet Analysis

For a doublet of equal intensities, set .

$$g(\lambda) = N + \frac{g_0}{\pi^{1/2}}\left[\frac{dg_1}{\sqrt{4\ln(2)}}\right]^{-1} exp\left[-(\lambda-\lambda_1)^2\left(\frac{dg_1}{\sqrt{4\ln(2)}}\right)^{-2}\right]$$
$$+\frac{g_0}{\pi^{1/2}}\left[\frac{dg_2}{\sqrt{4\ln(2)}}\right]^{-1} exp\left[-(\lambda-\lambda_2)^2\left(\frac{dg_2}{\sqrt{4\ln(2)}}\right)^{-2}\right] \qquad (3.1.2a)$$

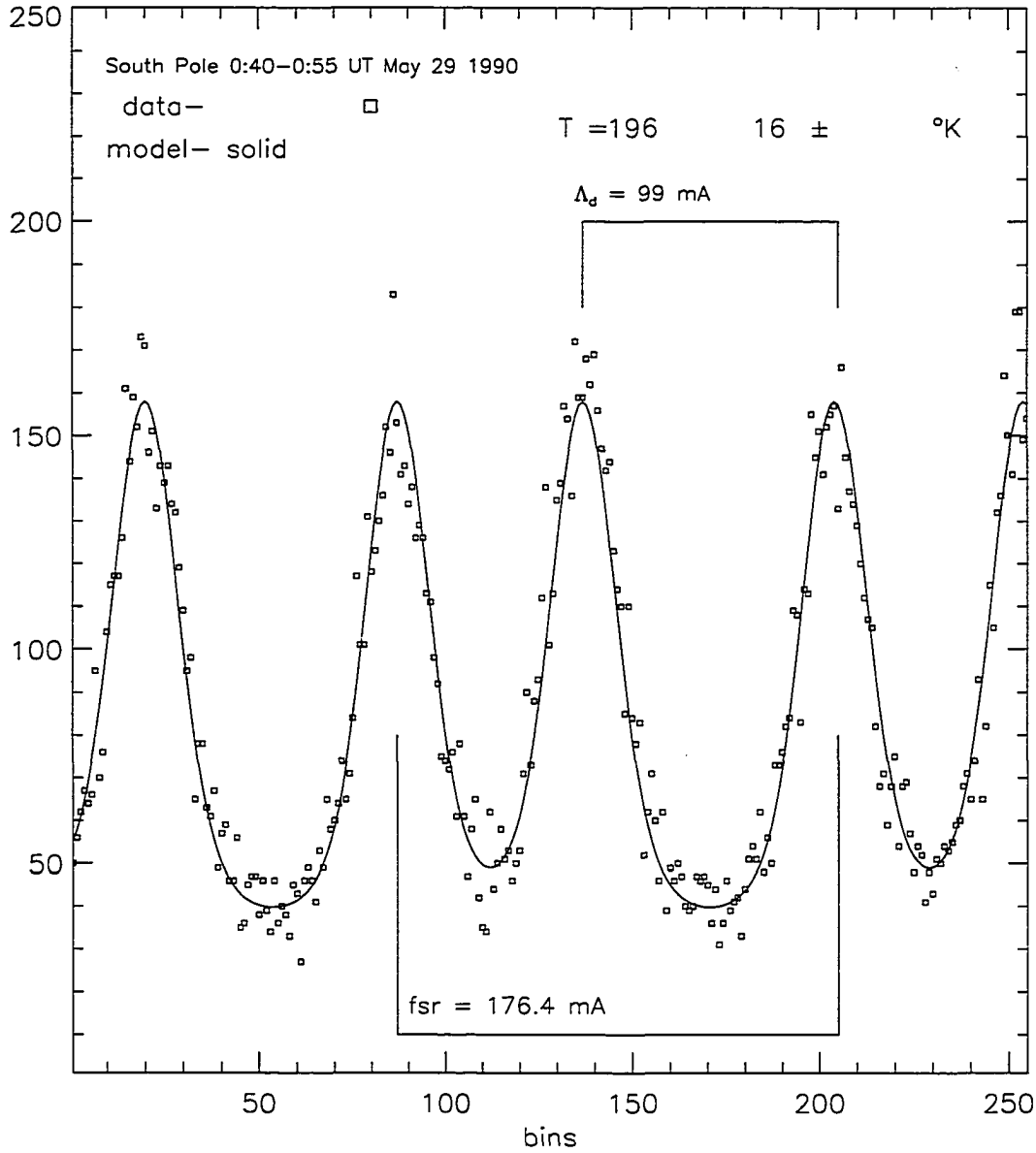

Figure 3.1.1 Typical raw data with fitted model results for two orders of the South Pole OH emissions at 8399Å . One profile from 0:40-0:55 UT of May 29, 1990 was analyzed with the NL^2S method to find the temperature indicated in the panel. The fsr and Λ-type doubled spacing are also shown. The horizontal axis is in data bins where each bin is equivalent to 1.2 mÅ .

where now

$$\lambda_1 = \lambda_0 - \Delta$$

$$\lambda_2 = \lambda_0 + \Delta$$

for Δ = one-half the value of the distance between the doublet. When the spectrum is sampled equation (3.1.2a), expressed in terms of samples 'x_j', becomes

$$g(x_j) = N + \frac{g_0}{\pi^{1/2}}\left[\frac{dg_1}{\sqrt{4\ln(2)}}\right]^{-1} exp\left[-(x_j - x_{0_1})^2(xcal)^2\left(\frac{dg_1}{\sqrt{4\ln(2)}}\right)^{-2}\right]$$

$$+\frac{g_0}{\pi^{1/2}}\left[\frac{dg_2}{\sqrt{4\ln(2)}}\right]^{-1} exp\left[-(x_j - x_{0_2})^2(xcal)^2\left(\frac{dg_2}{\sqrt{4\ln(2)}}\right)^{-2}\right] \qquad (3.1.2b)$$

with

$$xcal = \frac{(\text{mÅ})}{(\text{sample units})}.$$

The Model Instrument Function

The aperture function $\mathcal{F}$ is described by a "top hat" function of unit area and arbitrary width '$d\mathcal{F}$' so that

$$\mathcal{F}(x_j) = 1/d\mathcal{F} \text{ for } (x_j - x_0)\,\epsilon\,[-1/d\mathcal{F}, +1/d\mathcal{F}] * xcal \qquad (3.1.3)$$

The Airy function $\mathcal{A}$ is a periodic function of the etalon reflectivity $\mathcal{R}$, as described in chapter 2. From equation (2.2.8) get:

$$\mathcal{A}(\delta) = \frac{1}{1 + F\sin^2(\delta/2)} \qquad (3.1.4)$$

In order to discretize $\mathcal{A}$ put $\delta = x_j(2\pi/fsr)$ for the discrete variable x_j. In order to normalize $\mathcal{A}(x_j)$ over one period or fsr set

$$\int_0^{fsr} \mathcal{A}(x_j)dx_j = \int_0^{fsr} \frac{1}{1 + F\sin^2\left(x_j\frac{\pi}{fsr}\right)}dx_j = 1$$

ignoring the fact that x_j is a discrete variable. A change of variables gives:

$$x_j' = (\frac{\pi}{fsr})x_j \text{ and } dx_j' = (\frac{\pi}{fsr})dx_j$$

$$\int_0^{\pi} \frac{\left(\frac{fsr}{\pi}\right)}{1 + F\sin^2(x_j')} dx_j' = 1$$

and from *Dwight 436.5* I find, for the anti-symmetric $\mathcal{A}$:

$$2\int_0^{\pi/2} \frac{\left(\frac{fsr}{\pi}\right)}{1 + F\sin^2(x_j')} dx_j' =$$

$$\frac{fsr}{\pi\sqrt{1+F}}\left[\tan^{-1}\left[\sqrt{1+F}\tan(\pi)\right] - \tan^{-1}\left[\sqrt{1+F}\tan(0)\right]\right] = \frac{fsr}{\sqrt{1+F}}$$

Thus $\mathcal{A}(x_j)$ becomes

$$\mathcal{A}(x_j) = \frac{1}{1 + F\sin^2\left(x_j\frac{\pi}{fsr}\right)}\frac{\sqrt{1+F}}{fsr} \tag{3.1.5}$$

The Final Model

Finally these functions are convolved together to produce an instrument function $\mathcal{I}$ and a model profile $\mathcal{M}$, see Figure (3.1.2),

$$\mathcal{M}(T, g_0, N, x_0) = \mathcal{A}(\mathcal{R})\otimes\mathcal{F}\otimes g(T, g_0, N, x_0, \Delta) = \mathcal{I}(\mathcal{R})\otimes g(T, g_0, N, x_0, \Delta) \tag{3.1.4}$$

where g_0 = intensity in counts, N = background level in counts, and x_{0_i} = peak position in bins. In Figure (3.1.2) the instrument function $\mathcal{I}$ and its constituent functions A and F are graphed against x_j.

The analysis procedure finds values of T, g_0, N, x_0, and Δ by minimizing χ^2 for the model function to the observed data and in Figure (3.1.1) one such determination is shown where the final model, $\mathcal{M}$, fitted is overplotted with the data profile. In this case the source temperature was found to be 196 $\pm$ 16 °K.

3.1.3 Errors in the line center and width determination

The uncertainties are determined from the inversion of the error (or curvature) matrix from the non-linear analysis, (Press et. al., 1986). Each data bin is weighted according to its uncertainty which is assumed to be due to Poisson counting statistics. Thus the uncertainty is $1/\sqrt{N_j}$ for N_j = counts in data bin 'x_j'.

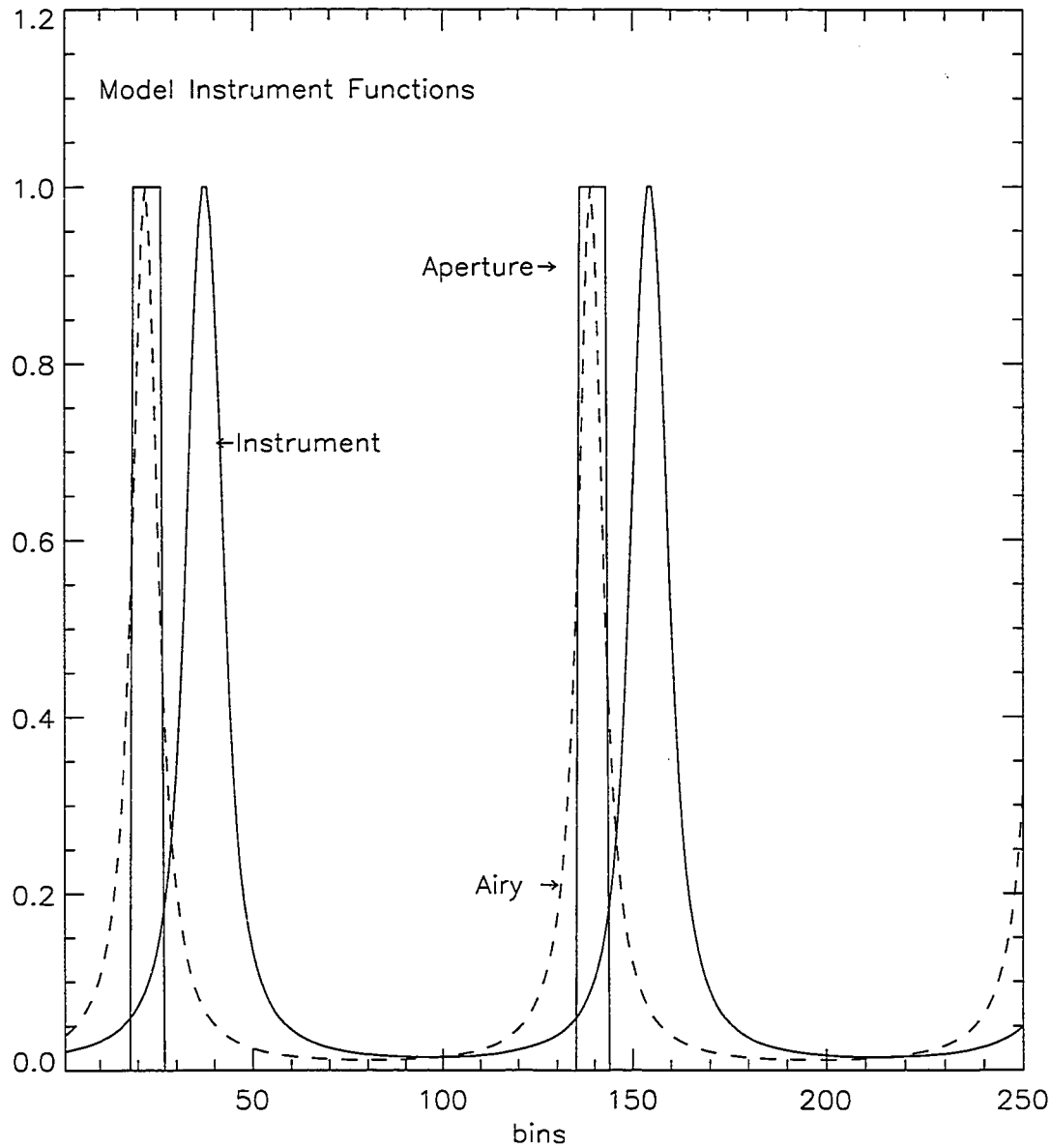

Figure 3.1.2 Model instrument functions for the NL^2S method showing the relative contribution to the width of the final gaussian model instrument function. For demonstration the function heights are set to unity, in fitting the areas are set to unity so that no additional power is added in the convolutions.

The model profile was constructed without the incorporation of defects broadening. I assume these defects to have a gaussian shape. A He-Ne laser is used to examine this residual unmodelled instrument profile. We pass laser light at 6328Å through the instrument and analyze the laser profiles with the same assumptions as for the sky profiles. The actual width of the laser is very narrow so that its kinetic temperature may be assumed to be near 0°K and the derived temperature is then taken to be a measure of the instrumental gaussian width. In order to account for this additional broadening the derived laser temperature is subtracted from the derived sky temperature since according to Minkowski and Bruck (1935) the Doppler line width and the instrumental widths add together as a simple sum. However the removal of an effective width in terms of temperature involves the adjustment by the ratio of the masses of the emitting species. For the frequency stabilized single-mode He-Ne lasers we typically find an instrumental width corresponding to ~40°K. Thus the removal of $40°K$ from a He-Ne emission source of mass 20.179 amus from the line width of an OH* molecular emission with a mass of 17 amus requires the removal of

$$40\left(\frac{m_{laser}}{m_{OH}}\right)\,°K \approx 47.48\,°K \tag{3.1.6}$$

with the additional affect that the temperature analysis takes place at a higher temperature and creates larger uncertainties.

Instrumental drift and 'zero wind' estimation

Until now I have not mentioned an important step in the determination of winds. The instrument gives me a set of fringe profiles from which the *relative* shift between profiles can be obtained and related to a Doppler shift due to bulk motion of the emitting gas. In order to calibrate this *relative* wind time series a 'zero-shifted' Doppler profile must be obtained. There are several methods used to obtain this 'zero-shifted' Doppler profile. I assume the net horizontal outflow from the region is zero when averaged over one day and use the averaged profile positions as my 'zero-shifted' profile. Another method is to assume that the zenith winds average to zero over some time period and use the zeniths to determine the zero position. A laser profile can be used if one assumes any change in wavelength from the laser emissions to the sky wavelength is negligible (ie., OI(6300Å) emissions). I view the zenith measurements as a diagnostic in that the Doppler shifting they exhibit is usually small and any large variations indicate instrumental changes or improper Doppler-zero determination.

3.2.1 Spectral Analysis of the Time Series Using the DFT

In order to examine the spectral contents of the various times series a DFT is used. Initial analysis is performed using a DFT of the entire time series to generate a power spectrum from the d.c. component to the Nyquist frequency. The raw data and derived time series are somewhat irregularly sampled since the profiles are summed until a minimum number of counts is obtained. In order to use the DFT the data is splined, (a cubic spline), to regular time steps. The spline interval is the mean time step. The data is tapered with a cosine bell as 1-cos$[\frac{2\pi}{10}j]$ for the first and last 5 data points so as to reduce end effects.

Calling the time series '$f(t_j)$' at time '$t_j \epsilon [0, N\Delta t]$' with the time step Δt and series length $\tau = N\Delta t$ the DFT is taken as

$$F(k) = \frac{1}{N}\Sigma_{j=0}^{N} f(t_j) exp[-i\frac{2\pi k}{\tau}t_j] \tag{3.2.1}$$

Simulated time series for temperature and wind were made according to

$$T(t_j) = 200 + 20sin[\frac{2\pi}{2160}t_j + \phi(az)] \tag{3.2.2}$$

$$w(t_j) = .5\, sin[\frac{2\pi}{4320}t_j + \phi(az)] + 2sin(\phi(az) + \frac{\pi}{4}), \tag{3.2.3}$$

respectively, for $t_j = 0 \rightarrow 7*4938$ minutes , $N = 617$ with 56 minute intervals between same azimuth data points. The uncertainties assigned are $\pm 10°K$ and $\pm$ 5m/s. These are plotted in Figures (3.2.1) and (3.2.2) where $\phi(az)$ is the azimuth dependent spatial phase shift that a wavenumber one oscillation would have, (8 steps of 45°). In the figure eight azimuths are shown indicating the spatial phase shift as one proceeds down the panel (azimuthally westward). Each plot has its own ordinate indicating the amplitude range of the oscillation, about a derived mean, in each direction. The value of each derived mean wind and temperatures are shown on the right hand side. Note the determination of the 2 m/s mean wind which I have added in the NE (345°E) direction. The power spectra is calculated as $\frac{1}{2}F(k)^*F(k)$ where the '$*$' indicates the complex conjugate. The power spectrum for the neutral wind simulation results (or simzults) are shown in Figure (3.3.1) of section 3.3.1 along with the harmonic analysis. The expected 72 hour periodicity of the wind series is evident. The phase angle is the standard

$$phase(k) = tan^{-1}[Im(F(k))/Re(F(k))]. \tag{3.2.4}$$

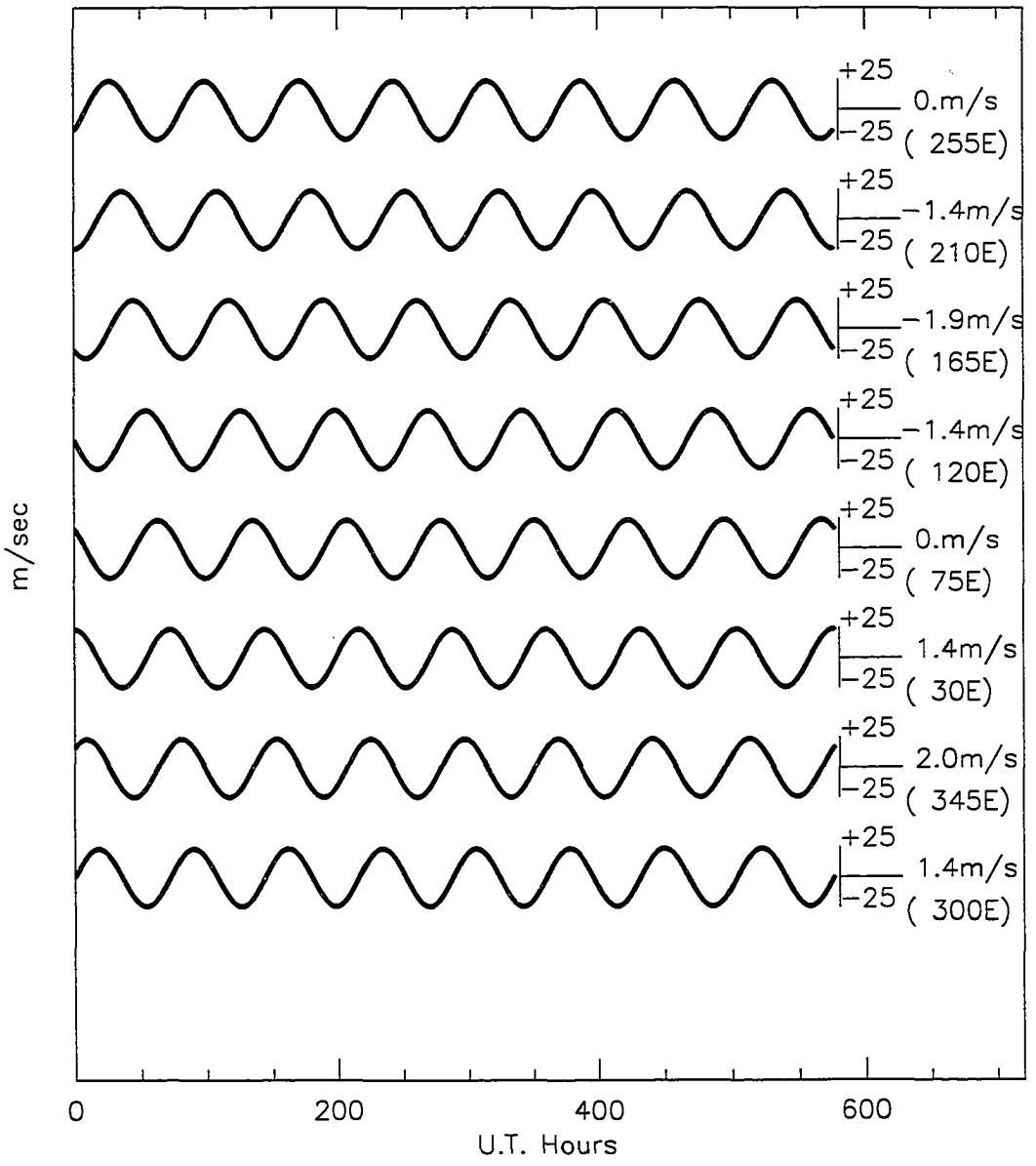

Figure 3.2.1 72 hour sinusoidal simulated wind data (simzults) are shown as the input to analysis used in this work. The form $w(t_j) = 23.7\,sin[\frac{2\pi}{4320}t_j + \phi(az)] + 2sin(\phi(az) + \frac{\pi}{4})$, in m/s as per equation (3.2.3). The derived mean values are shown to the right of each azimuthal series.

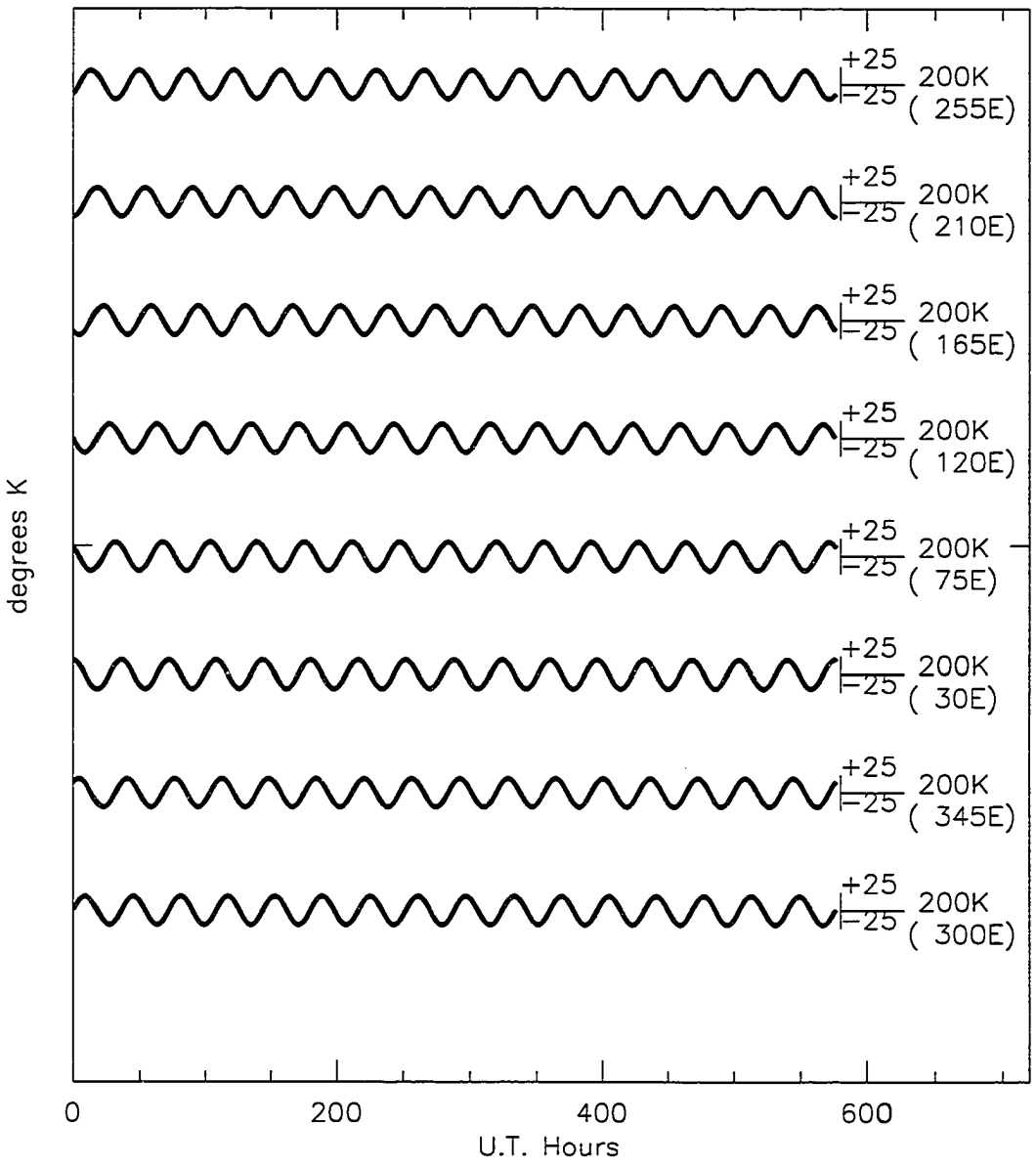

Figure 3.2.2 36 hour simulated temperature data (simzults) are shown as the input to analysis used in this work. The form $T(t_j) = 200 + 20sin[\frac{2\pi}{2160}t_j + \phi(az)]$, in °K as per equation 3.2.2. The derived mean values are shown to the right of each azimuthal series.

3.2.2 Uncertainties in the DFT derived coefficients and phase

Uncertainty in the spectral amplitude

For the times series $T(x_j)$ represented by a Fourier Series

$$T(x_j) = \frac{a_0}{2} + \Sigma_{k=1}^{\infty} a_k cos(\frac{2\pi k}{\tau} x_j) + b_k sin(\frac{2\pi k}{\tau} x_j) \tag{3.2.5}$$

where

$$a_n = \frac{2}{\tau} \int_{-\frac{\tau}{2}}^{\frac{\tau}{2}} T(x_j) cos(\frac{2\pi n}{\tau} x_j) dx_j \tag{3.2.6}$$

and

$$b_n = \frac{2}{\tau} \int_{-\frac{\tau}{2}}^{\frac{\tau}{2}} T(x_j) sin(\frac{2\pi n}{\tau} x_j) dx_j. \tag{3.2.7}$$

Then a_n and b_n are the Fourier transform coefficients of $T(x_j)$.

The spectral amplitude from the DFT at frequency $\frac{2\pi n}{\tau}$ is then

$$|G_n| = \sqrt{{a_n}^2 + {b_n}^2}. \tag{3.2.8}$$

Then the uncertainty in the estimation of $|G_n|$ is given, (Hernandez, 1978) by

$$\sigma_{|G_n|} \simeq \left[{\sigma_{a_n}}^2 \left[\frac{\partial |G_n|}{\partial a_n} \right]^2 + {\sigma_{b_n}}^2 \left[\frac{\partial |G_n|}{\partial b_n} \right]^2 \right]^{\frac{1}{2}} \tag{3.2.9}$$

For the series representation of $T(x_j)$ the uncertainties σ_{a_n} and σ_{b_n} are given by the formulae

$$\sigma_{a_n} = \left[\Sigma_{j=1}^{\tau} {\sigma_j}^2 \left[\frac{\partial a_n}{\partial T(x_j)} \right]^2 \right]^{\frac{1}{2}} \text{ and } \sigma_{b_n} = \left[\Sigma_{j=1}^{\tau} {\sigma_j}^2 \left[\frac{\partial b_n}{\partial T(x_j)} \right]^2 \right]^{\frac{1}{2}}. \tag{3.2.10}$$

These formulae assume the errors σ_j are normally distributed errors in the determination of $T(x_j)$. Thus

$$\frac{\partial |G_n|}{\partial a_n} = \frac{a_n}{|G_n|},$$

$$\frac{\partial |G_n|}{\partial b_n} = \frac{b_n}{|G_n|},$$

$$\frac{\partial a_n}{\partial T(x_j)} = \frac{2}{\tau} cos(\frac{2\pi ni}{\tau}),$$

$$\frac{\partial b_n}{\partial T(x_j)} = \frac{2}{\tau} sin(\frac{2\pi ni}{\tau}),$$

with the periodicity τ set to the time window size gives

$$\sigma_{|G_n|} = \frac{2}{\tau |G_n|} \left[\Sigma_{j=1}^{\tau} \sigma_j^2 [a_n^2 cos^2(\frac{2\pi nj}{\tau}) + b_n^2 sin^2(\frac{2\pi nj}{\tau})] \right]^{\frac{1}{2}}. \tag{3.2.12}$$

Where I note that for the application of the DFT to raw data ${\sigma_j}^2 = P(x_j)$, for the

intensity $P(x_j)$ in counts. For the case in question here the uncertainty in the derived time series values is used as ${\sigma_j}^2 = {\sigma_{T_j}}^2$ or $= {\sigma_{w_j}}^2$.

For completeness I note that in the use of the DFT for deriving temperatures the expression

$$ln(|G_n|^2) = \ln({a_n}^2 + {b_n}^2)$$

is used. This leads to

$$\sigma_{|G_n|^2} = 2|G_n|\sigma_{|G_n|}$$

and

$$\sigma_{ln(|G_n|^2)} = 2\sigma_{|G_n|}.$$

For the uncertainty in the phase

$$phase(k) = \phi = tan^{-1}[b_n/a_n] = tan^{-1}[X]$$

which by propagation of errors

$$\Delta\phi = \left(\frac{X}{1+X^2}\right)\left[\frac{\sigma_{a_n}}{a_n} + \frac{\sigma_{b_n}}{b_n}\right].$$

95% confidence levels

The above uncertainty levels can be used to establish confidence levels. That is, the 2σ value, as a function of frequency, gives a value such that if exceeded by the spectral amplitude then there is a 95% probability that this spectral peak is different from zero. Another method, (Scargle, 1982), related to the DFT and the HF method is discussed in section 3.3.2.

3.2.3 Time dependent DFT coefficients: a sliding time window

In section 4.2 I have used the DFT within a sliding window. The analysis is identical to the standard as in section 3.2.1 only the resulting coefficients are less well resolved and carry higher uncertainties. The time ascribed to the spectra in each window is the time at the center of the window.

The choice of the window size is made so that the most interesting features are harmonics of the window length and are thus resolved into one of the independent coefficients. As before the windows are tapered with a cosine bell shaped window to reduce end-effects as described in Press (1987) and Jenkins and Watts (1968).

3.3.1 Spectral analysis using an harmonic fit (HF) technique

The harmonic fit analysis is simply the three parameter fit of a sinusoid

$$y(t_j) = a_0 + a_1 sin[\frac{2\pi}{\tau} t_j + a_2].$$

One advantage of the HF method over that of the DFT is the choice of the frequency '$\frac{1}{\tau}$' and the fact that I no longer need regularly spaced data.

In general the agreement between the two methods is very good. In Figure (3.3.1) the spectral analysis for the first three azimuths of the simzults shown in Figure (3.2.1) is shown for both methods. Some of the vertical scales have been altered for ease in examining the side lobe structure. Note that the harmonic fit determinations pass through the DFT derived values. Also note the position of the DFT coefficients on the harmonic fit curve. The slight differences in the number of data points in the time series for different azimuths has causes the DFT coefficients in the 345°E direction to be displaced relative to those of the other directions.

Because of the unique location of our instrument at South Pole station the derived phase from the fitted harmonic component, as a function of azimuth, can tell us about the zonal propagation. It so happens that the physical situation favors zonal waves of wavenumber one around the pole. With eight azimuthal measurements the data is capable of discerning the phase progression of these waves. The simzults were generated as just such a wave and in the top panel of Figure (3.3.2) the derived phase from the harmonic fit is graphed against azimuth. The phase is progressing westward, (increasing as the east longitude decreases).

The reliability of statistical inference from these spectral methods can be improved by reducing the eight different azimuths to a single two component vector. In order to accomplish this each time series is interpolated to the time steps of one of the time series. The series are then reduced to two orthogonal components one along the N-S direction the other along the E-W direction. The spectral analysis of these new, what I call, 'dual-vector' components is then accomplished with the harmonic fit method. The results from this 'dual-vector' approach are shown in the bottom two panels of Figure (3.3.2).

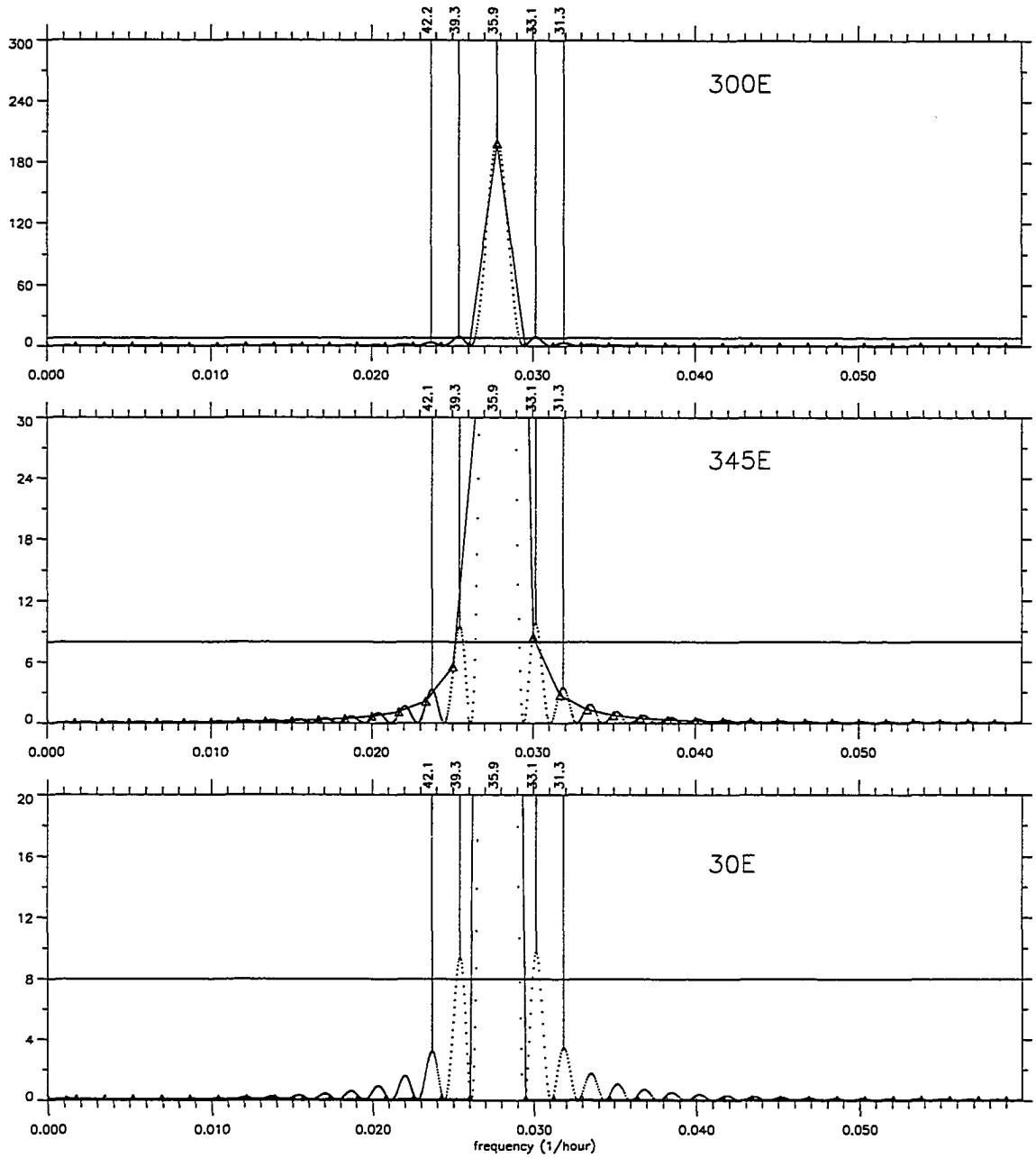

Figure 3.3.1 Spectral content of the simzults of Figure (3.2.1) derived from the harmonic fit and the DFT method. Only the first three azimuths are shown. The harmonic fit (dotted) and DFT (connected triangles) pass through the same points. The scales are chosen in order to bring out the side-lobe structure and the frequency shifting due to the mean wind. Selected periodicities (in hours) are marked. The 95% confidence levels are indicated as horizontal lines as per section 3.3.2.

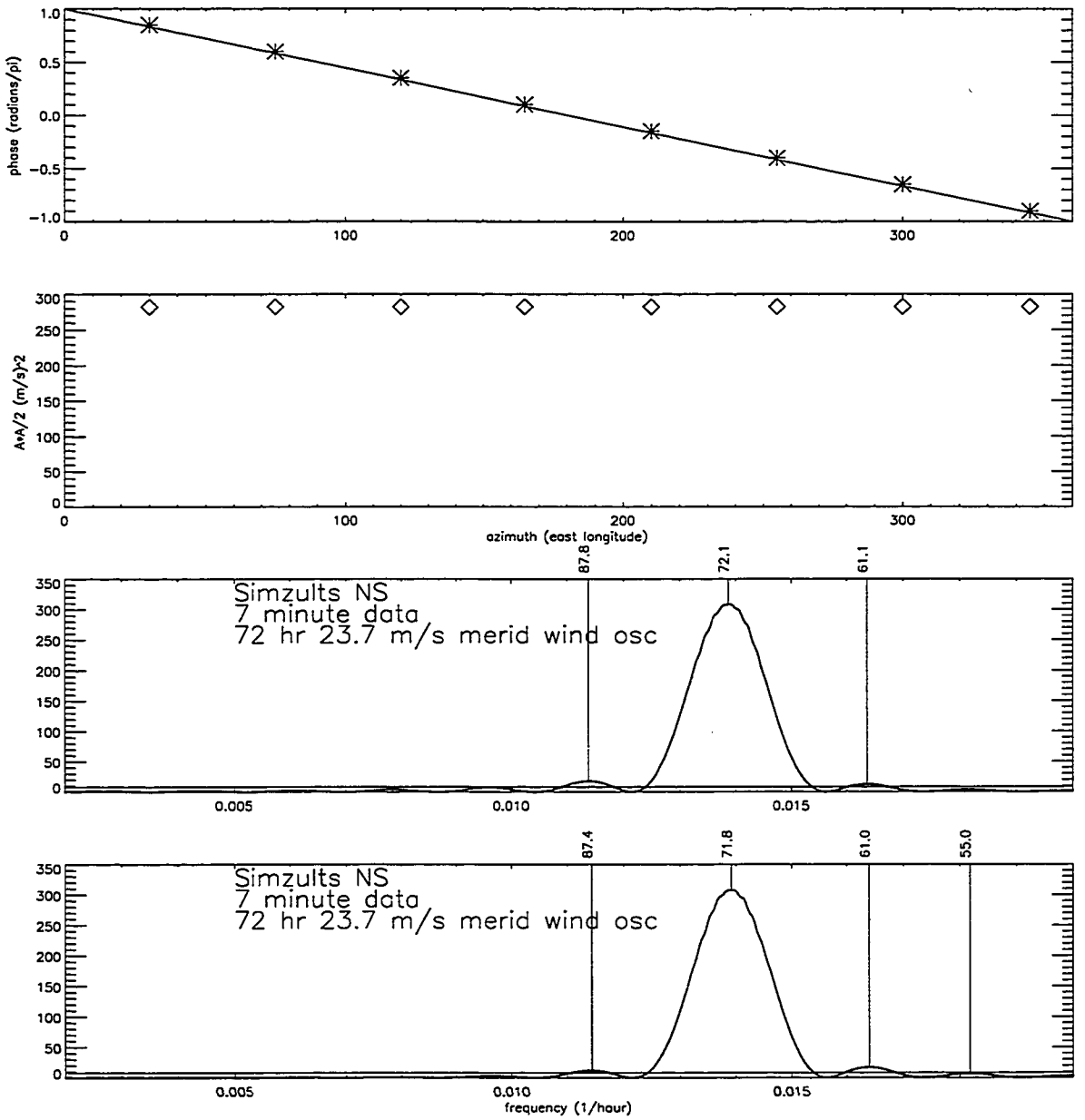

Figure 3.3.2 Wavenumber and 'dual-vector' analysis for simzults shown in Figure (3.2.1). The azimuthal phase dependence is plotted showing the progression of a wavenumber one as per the input. In the second panel from the top the derived power from the HF method are plotted against azimuth. In the lower panels the power of orthogonal horizontal components of the single-vector construction is plotted. The construction of a single vector time series from the eight azimuthal time series improves the statistical significance of marginal real features by decreasing the uncertainty by a factor of 2.

3.3.2 Uncertainties in the HF derived coefficients and phase

The uncertainties here are determined as for the DFT coefficients but for a single coefficient. Recall that the harmonic fit analysis is simply the three parameter fit of a sinusoid

$$y(t_j) = b_0 + b_1 sin[\frac{2\pi}{\tau} t_j + b_2].$$

From Eq.(3.2.10) of section 3.2.2 the variance for a coefficient is

$$\sigma_{b_n}^2 = \Sigma_{j=1}^{\tau} {\sigma_j}^2 \left[\frac{\partial b_n}{\partial T(t_j)}\right]^2 \tag{3.3.1}$$

where σ_j are the derived uncertainties in the time series parameter and

$$\frac{\partial b_n}{\partial T(t_j)} = \frac{2a_1}{\tau} sin[\frac{2\pi t_j}{\tau}]$$

so that

$$\sigma_{b_n}^2 = \Sigma_{j=1}^{\tau} {\sigma_j}^2 \left[\frac{2a_1}{\tau} sin[\frac{2\pi t_j}{\tau}]\right]$$

The 95% confidence level

This uncertainty is a function of the spectral amplitude. As discussed for the DFT results in section 3.2.2, the $2\sigma_{b_n}$ value can be compared with the 95% confidence level.

A more conventional view of a 95% confidence level with respect to statistical inference for the significance of spectral estimators is to determine the power required to exceed the 95% confidence level. That is, $\leq$5% of the time a random process may reach this level. Lomb (1976) and Scargle (1982) developed a type of periodogram (see section 3.4) for finding and testing the significance of weak periodic signals in otherwise random, *unevenly sampled* data. Lomb (1976) showed the equivalence between the *normalized periodogram* and the method of linear least-squares fitting of a sinusoid to the data. For this reason I have adopted the results of Scargle (1982) where he derived the expression

$$z_0 = -ln[1 - (1 - p_0)^{1/N}]$$

for the *normalized* power z_0 which would be exceeded by random fluctuations only $100 \times p_0$% of the time, (95% confidence level for $p_0 = .05$). *Normalized* means the power is divided by the variance ${\sigma_0}^2$ of the white noise component of the time series obtained as

$${\sigma_0}^2 = \frac{1}{N-1} \Sigma_{j=1}^{\tau} (y_j - \overline{y})^2$$

for 'N' the number of independent frequencies. In this manner the confidence level is seen to be associated with the signal-to-noise ratio. In the case of the DFT $N = \tau/2$ however

N is not quite as obvious in the case of the harmonic fit. The number of independent frequencies used to determine the spectra may be different for unequally sampled data. In practice one can numerically fit as many frequencies as one wishes but how many of these are independent? It turns out, (Press, 1988), that the probability is not very sensitive to this number in that for large differences such as 150, 300 or 600 independent frequencies the power

$$z_0 = -ln[1-(1-p_0)^{1/N}] \approx 7.98, 8.67, 9.36\sigma_0,$$

respectively. For 600 data points 150 frequencies would obtain if we sampled only to $f_{max} = \frac{1}{2} f_{Nyquist}$ and 600 for $f_{max} = 2f_{Nyquist}$. I use $f_{max} = \frac{1}{2} f_{Nyquist}$ since very little information exists above this frequency in the data used in this work. In addition because of the insensitivity I use the value ascribed by the theory for the DFT. In Figures (3.3.1) and (3.3.2) (and figures to follow in this work), where the power is plotted, the 95% confidence levels are indicated as a horizontal line. Due to the lack of noise in these simzults even the sidelobes in the spectra rise above this value but not the 99% level at $\approx 9.6\sigma^2$.

3.3.3 Time dependent HF coefficients: a sliding time window

Dynamic interactions in the derived wavefields near the mesopause may produce evanescent effects which would be difficult to observe from the analysis of a long data period. The possibility exists for ducted waves and the ducts may be modulated by gravity waves or planetary waves and again may not exist long enough to be observable in the analysis of the full data period. Variations are obvious in the daily mean winds and interactions of these steady winds with any waves may be washed out in the full period analysis. I proceed to analyze the data within time window which is slid along each time series.

This analysis is essentially the same as the full period analysis except the oscillations are less well resolved in frequency. Two presentations of the sliding window data are given; one for *all azimuths* at once, one for the analysis of a *single azimuth.* As a demonstration of these in Figure (3.3.3) the simzults, $w(j)$, of a 72 hour wind oscillation

are shown, where

$$w(j) = \overline{w}(az) + 23.8sin[\frac{2\pi j}{72(1+\beta(az))} + \phi(az)].$$

I have added a mean wind $\overline{w}(az) = 2$ m/s in the 345°E longitude direction as

$$\overline{w}(az) = 2sin[\phi(az) + \frac{\pi}{4}].$$

'$\beta(az)$' is a Doppler shift factor for the period if the mean wind were to couple with the zonally progressing wave-number one wind oscillation and is calculated as

$$\beta(az) = \frac{\overline{w}(az)}{v_\phi}$$

for the phase speed

$$v_\phi = \frac{\pi 294000.}{72 \times 3600}\, m/s.$$

In Figures (3.3.4) and (3.3.5) both the harmonic analysis and DFT results for these simzults are shown. In Figure (3.3.6) the wavenumber and dual vector analysis are shown for these simzults. Again a wave-number one has been input and the dual-vector analysis has correctly characterized the input time series. It shows the expected $72 \pm 40, \pm 28$m/s from the different azimuths. Some other features are not common to both panels.

all azimuths presentation is a single page of 6 panels. Figure (3.3.7) is an example for the results from the simzults of the 72 hour wind and temperature oscillations analyzed in section 3.3.1 but with no mean wind added. Two panels for the spectral amplitudes; one for the temperature and one for the wind. Two panels for the phases; again one for the temperature and one for the wind. One panel for the mean wind and thermal gradient magnitudes and one panel is the color key to the 4 colored panels. The spectral amplitude is exactly that- the derived amplitude $a_1(j, az)$ from the harmonic fit of the function

$$a_0(j, az) + a_1(j, az) \times sin[\frac{2\pi t_j(az)}{\tau} + \phi(j, az)]$$

where the 'j' is the time index and 'az' the azimuth index. The amplitudes are plotted in color for time vs. azimuth. In this manner the temporal and azimuthal dependences are available for inspection in the same figure. The phases $\phi(j, az)$ are plotted the same way with red$\leftrightarrow +\pi$ and blue$\leftrightarrow -\pi$. The mean wind vector, for each time window, is formed from the different azimuth means $a_0(j, az)$ by taking four pairs of wind means (in opposite

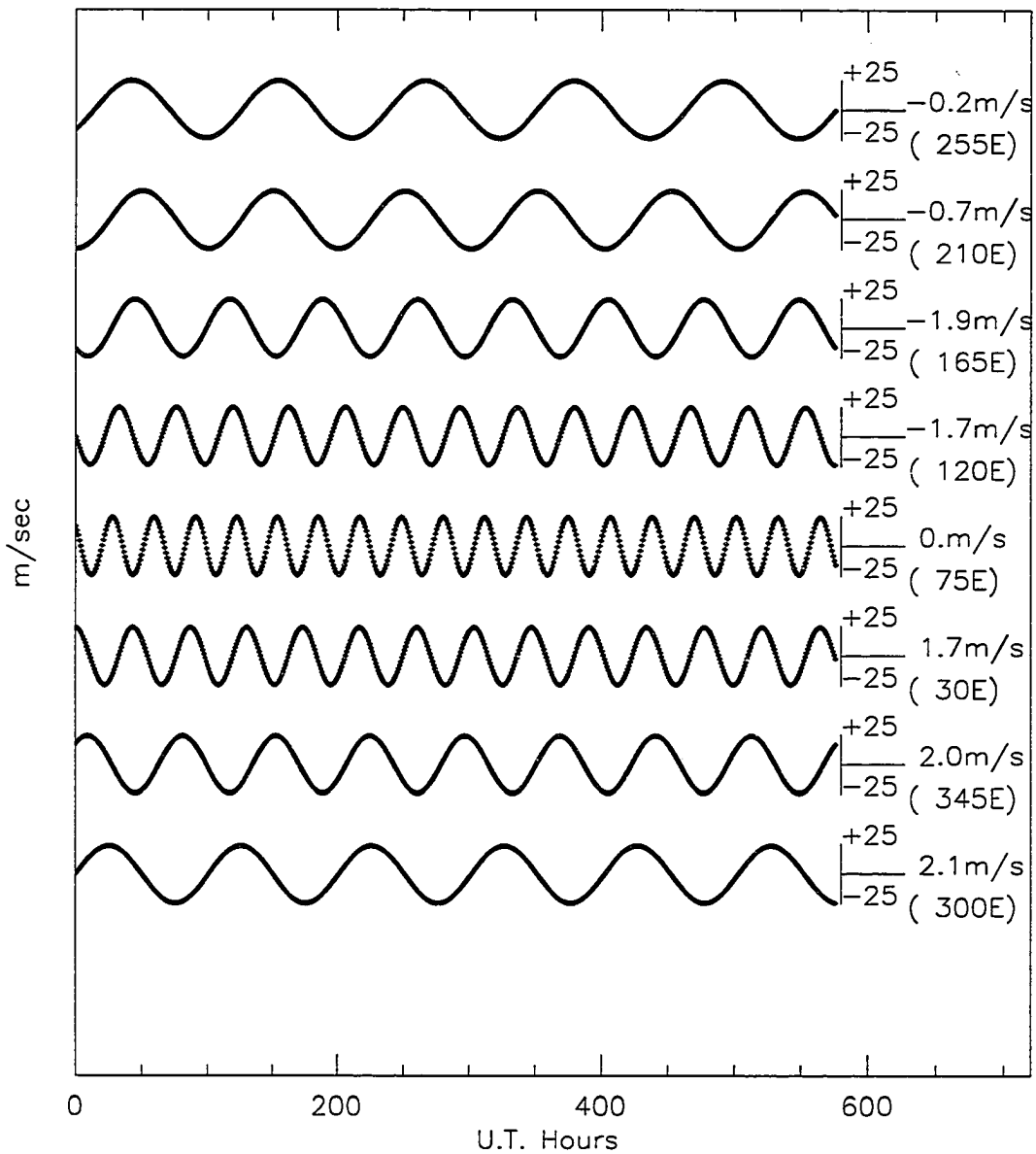

Figure 3.3.3 72 hour sinusoidal wind simzults with a Doppler effect are shown as the input to analysis used in this work. The form of the winds is as

$$w(j) = \overline{w}(az) + 23.8sin[\frac{2\pi j}{72(1+\beta(az))} + \phi(az)],$$

in m/s as per equation 3.3.2. The mean wind '$w(az)$' is towards the 345°E directions.

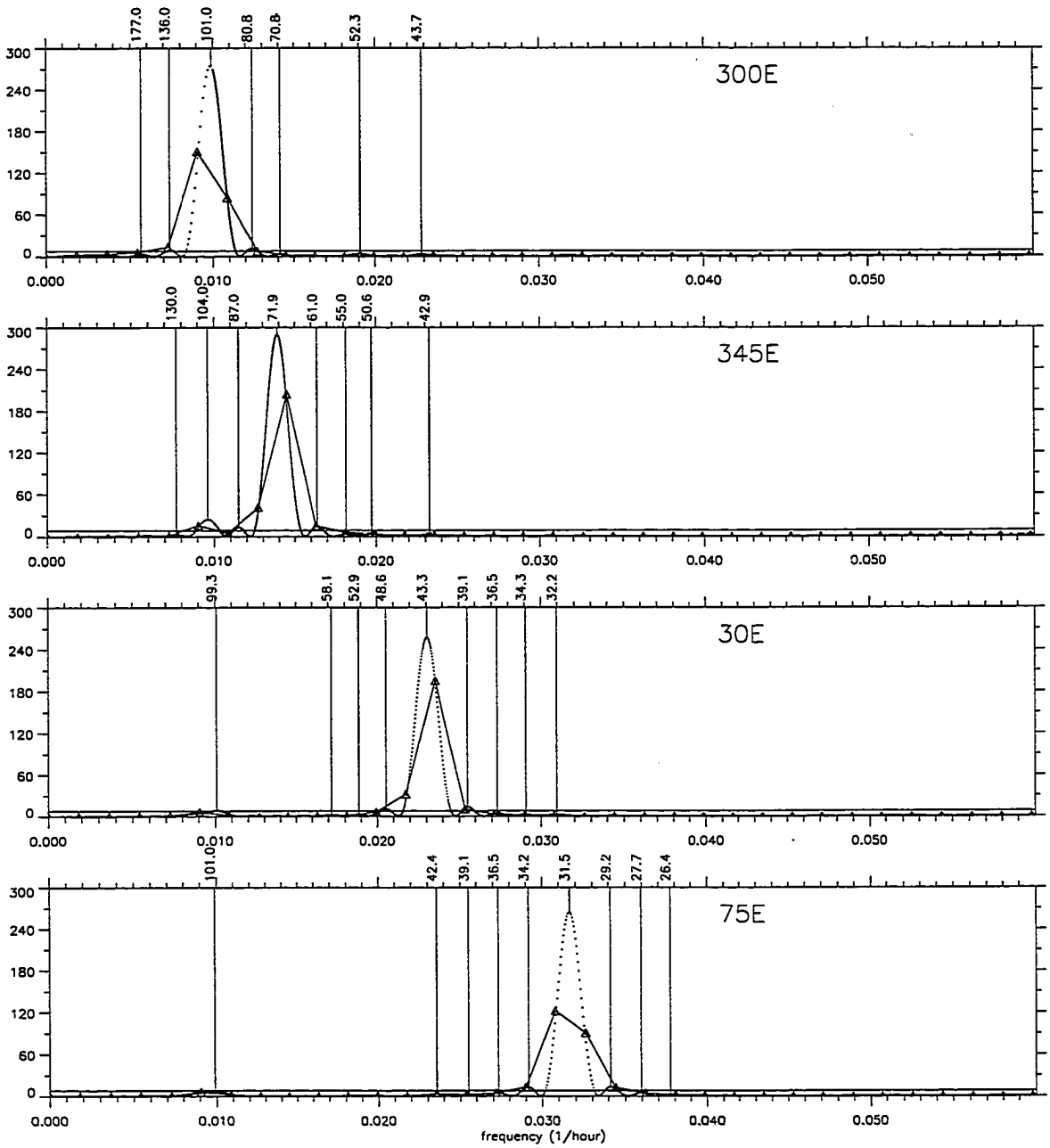

Figure 3.3.4 Spectral content of the simzults with a Doppler effect, first four azimuths. These results are derived from the harmonic fit and the DFT methods of the simzults shown in Figure (3.3.3). Selected periodicities are marked. The first four azimuths are shown. The 95% confidence levels are indicated as horizontal lines as per section 3.3.2 for 150 independent harmonics. The DFT results are also plotted (connected triangles) for comparison. Selected periodicities are marked and the periods (in hours) for each is indicated. Note the drift in frequency as a function of the azimuth.

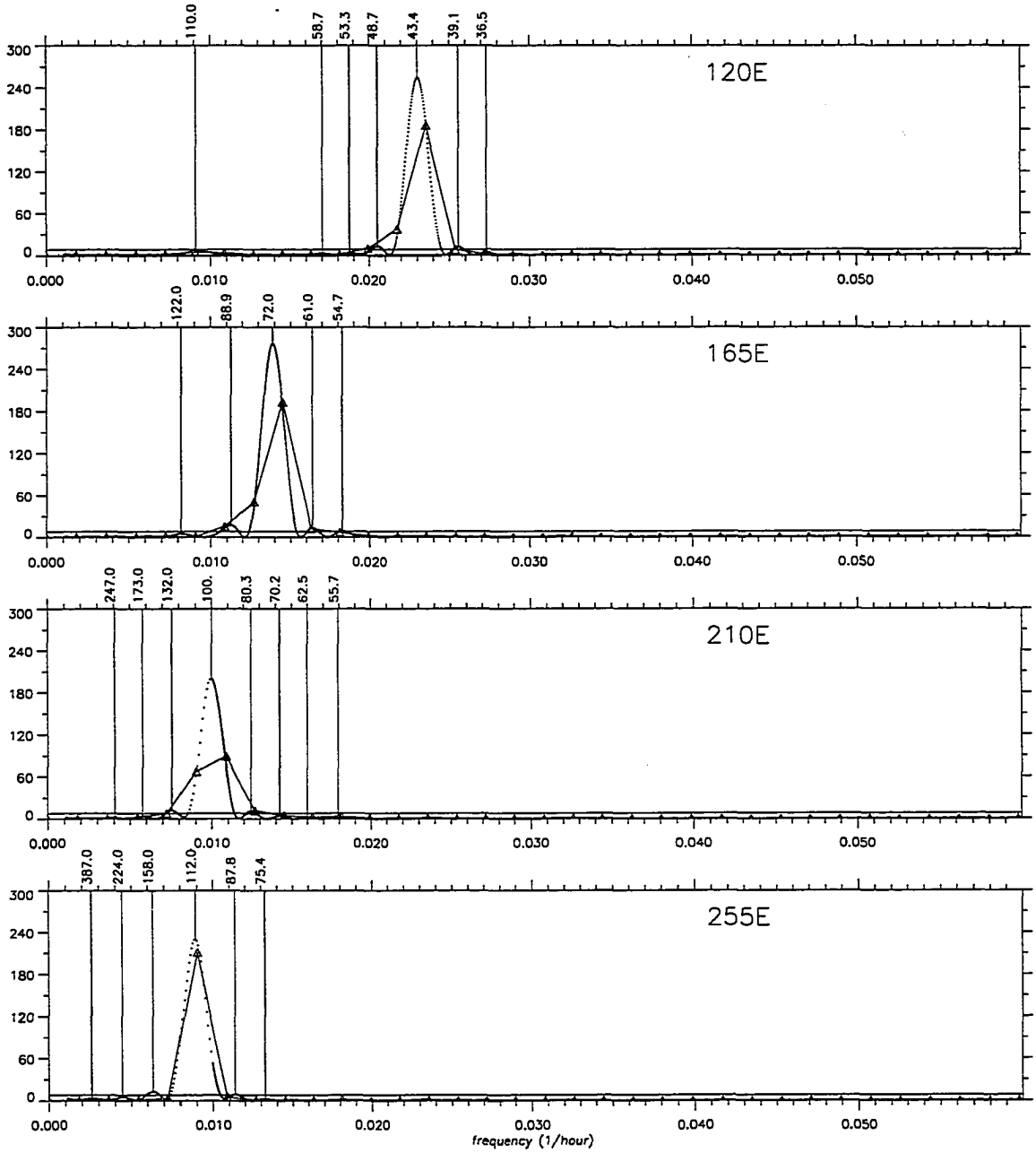

Figure 3.3.5 Spectral content of the simzults with a Doppler effect, last four azimuths. Same as in Figure (3.3.4) but for the other four azimuths.

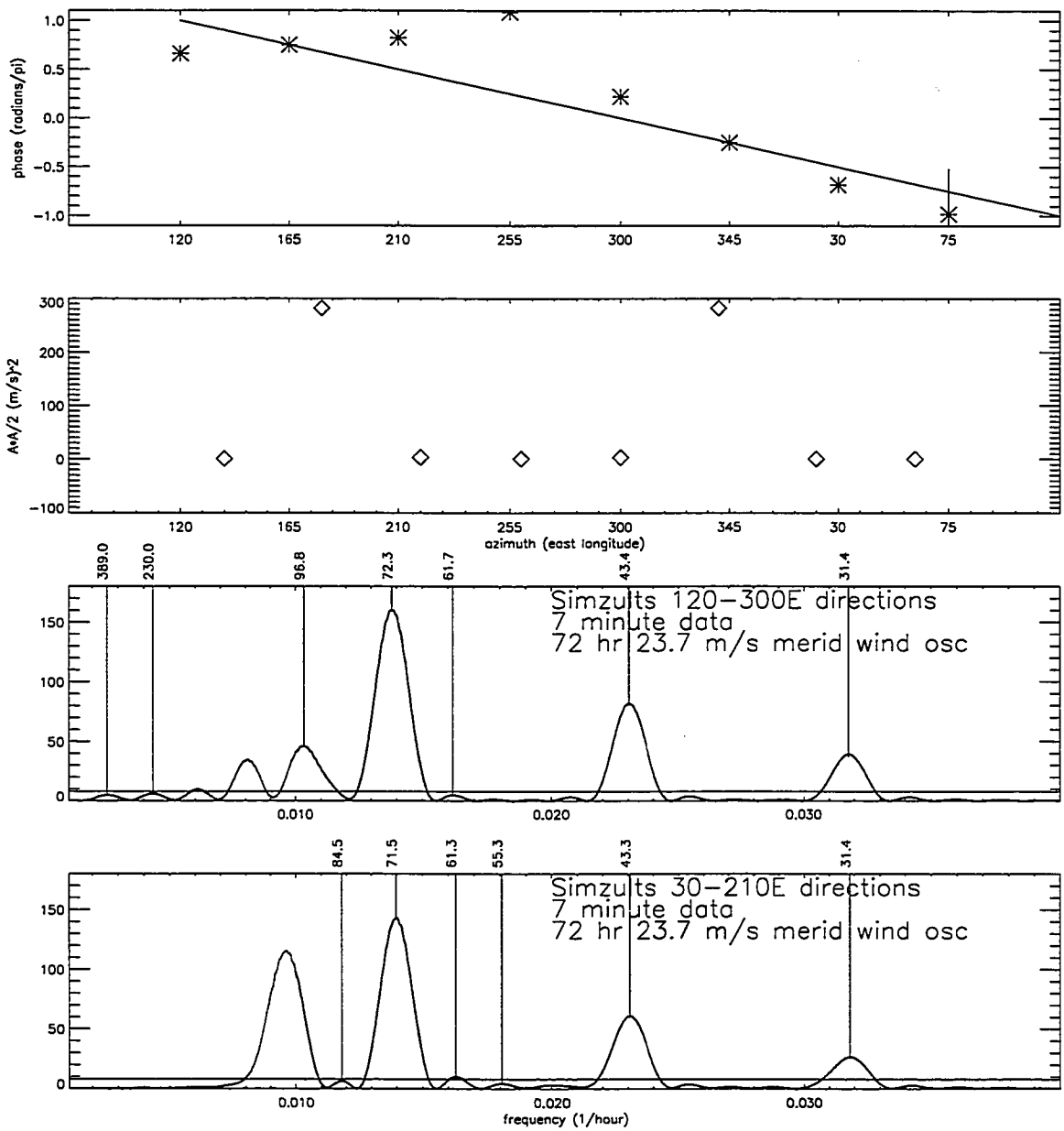

Figure 3.3.6 Wavenumber and 'dual-vector' analyses of simzults with Doppler effect. The simzults shown in Figure (3.3.3) have been resolved into the dual-vector components for this spectral analysis. The azimuthal phase dependence for the simzults of Figure (3.3.3) is plotted showing the progression of a wavenumber one. In the lower panels the power of the orthogonal components of the dual-vector construction is plotted. Selected periodicities are marked and the periods (in hours) for each is indicated.

directions) to give a single time dependent mean wind vector '$A(j)$' in the direction of '$\theta(j)$'. $A(j)$ is plotted in the upper center panel. Similarly for the temperature means, the difference between the four pairs of window means are used to derive a mean temperature gradient vector. The positive direction for this temperature gradient is taken to point in the direction of low temperature (negative temperature gradient) so as to point in the direction a thermal wind would blow. The magnitudes '$A(j)$' of these vectors are plotted in the upper center panel with the wind scale, (m/s), at the top of the panel and the temperature scale, (°K), at the bottom. The directions '$\theta(j)$' are overplotted in their respective color panels so easy visual correlation with the spectral amplitudes can be made. In Figure (3.3.7) the temperature panel is constant at 20°K with a zero thermal gradient magnitude. The phase is a steady wavenumber one. Similarly the neutral wind amplitude is constant at ~23.7 m/s with a zero mean wind speed. The phase is a steady wavenumber one. Other simzults are shown in Figure (3.3.8) where a 2 m/s mean wind and a 5°K thermal gradient have been added. The frequency is allowed to shift according to the Doppler formula. The analysis for these neutral wind simzults are shown in Figures (3.3.3)-(3.3.6). In Figure (3.3.8) the amplitude panels show azimuthal asymmetry as only the oscillations in the directions of the mean wind remain unshifted in the bandpass of the 72 hour period. The shifted period ranges from 72±40 hours in the directions perpendicular to the mean wind and 72±28.5 in those 45° from the mean wind directions. Some wave amplitude does enter the 72 hour channel for these azimuths and so the panel is not white. For the westward phase progressions, $(-\phi(az)$, for increasing 'az' the east longitude), the waves are blue shifted in azimuths 30-120°E and red shifted in azimuths 210-300°E. The beating of the fitted function with the shifted simzults is apparent in both the amplitude and phase panels. In the 75°E direction the rapid spectral amplitude and phase variations are compared to the slower ones in the 255°E direction. The window function (sinc), of the 288 hour window, has nodes at 72±36, 24, 18,...etc. hours and anti-nodes at 72±48, 28.8, 20.5,...etc. hours. Thus there are anti-nodes near the values for each azimuth which accounts for the non-zero amplitudes in all directions. Finally the varying period of the sinusoid in the different azimuths leaves varying values of the derived means as seen in its magnitude. The periodicities in the mean are also indicative of the differing spectral content which will be seen in different directions due the Doppler factor in this experiment.

The *single azimuth* presentation (see Figures (3.3.9) and (3.3.10)) is a single page of stackplots of the actual fit results as a function of the time (vertical and horizontal axes)

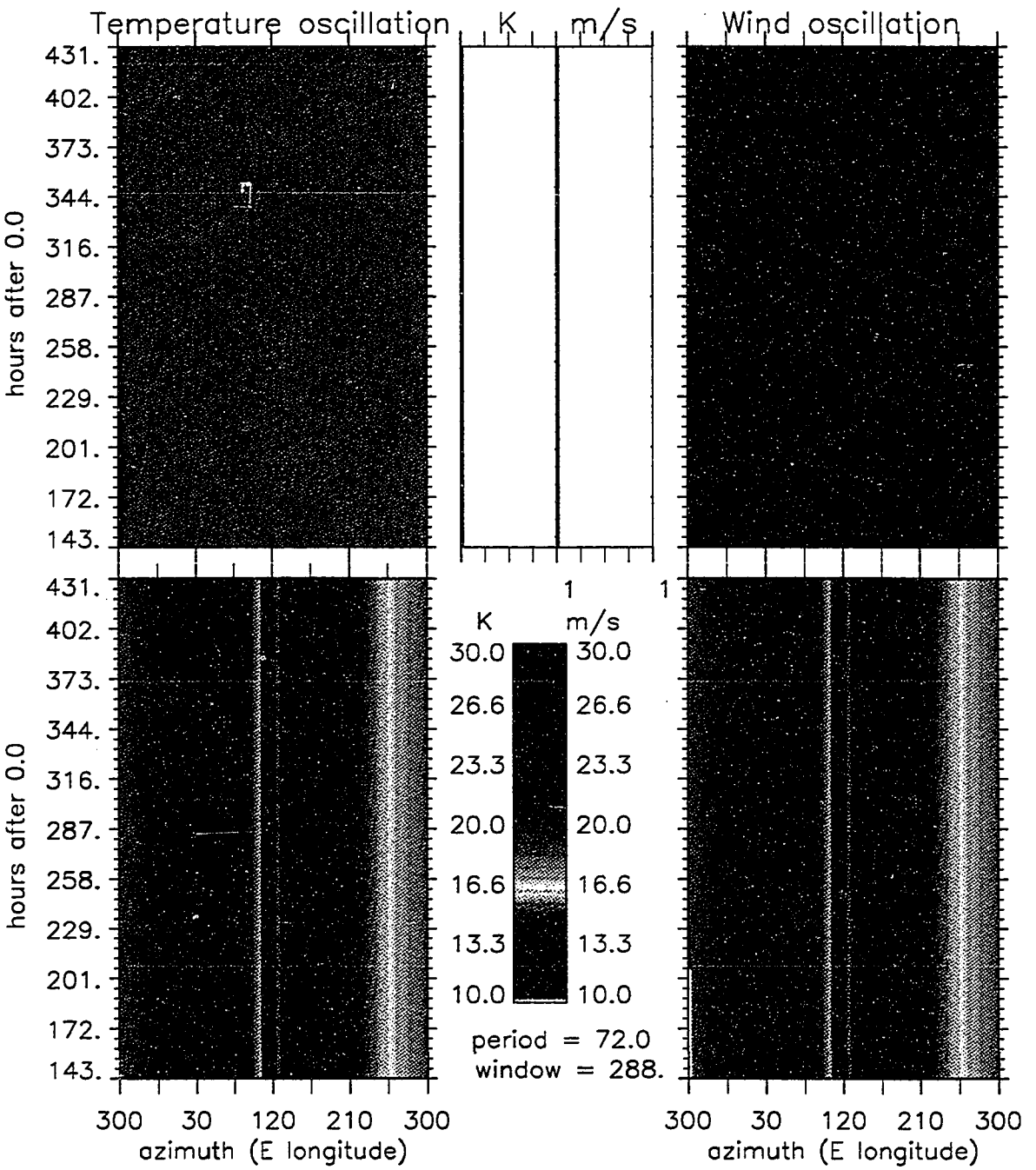

Figure 3.3.7 *All-azimuth* harmonic amplitude analysis results from the 72 hour wind and temperature simzults. A 288 hour sliding window analysis has been used. The simzults were manufactured as $w(j) = 23.8sin[\frac{2\pi j}{72} + \phi(az)]$, and $T(j) = 20sin[\frac{2\pi j}{72} + \phi(az)]$.

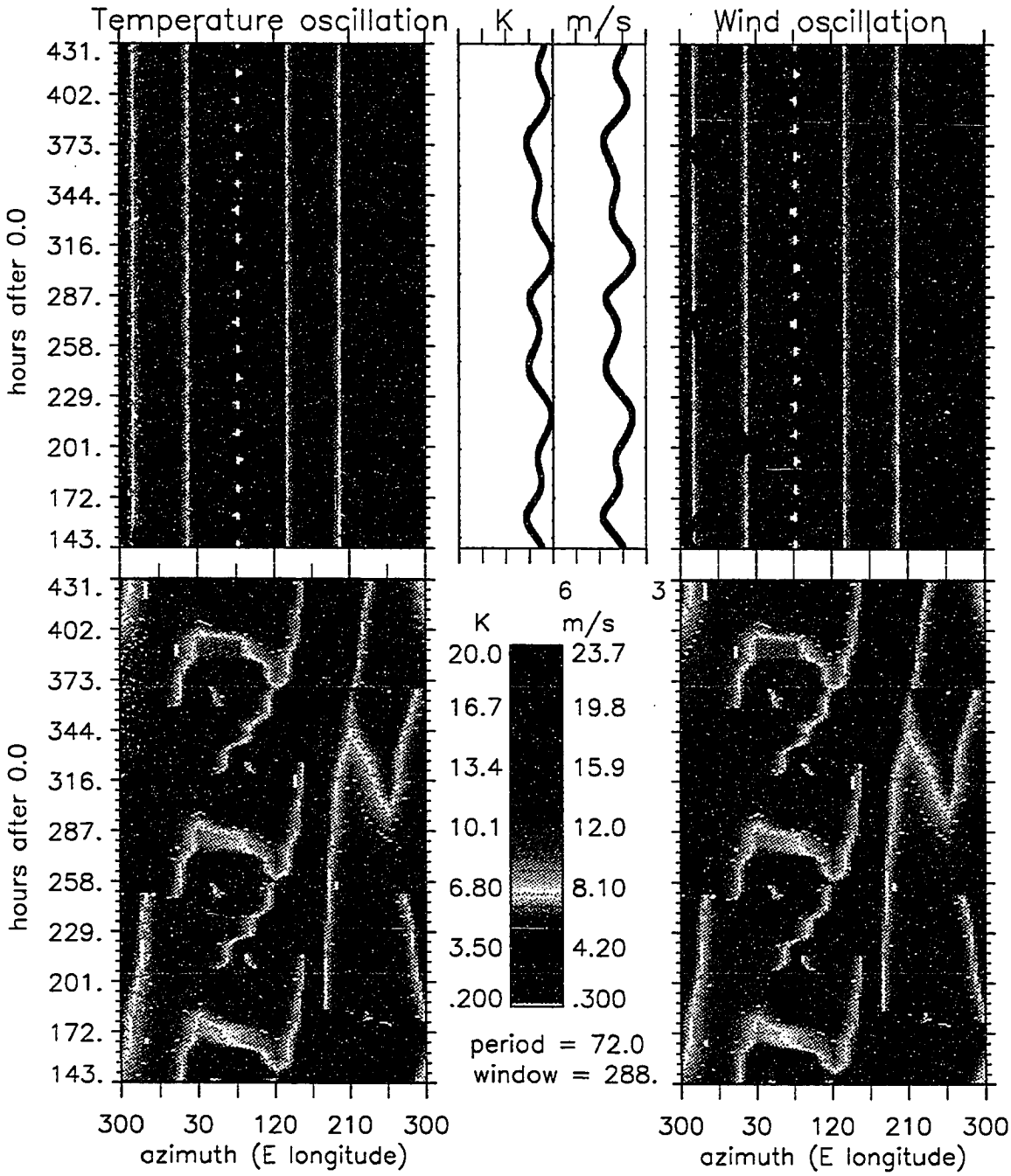

Figure 3.3.8 *All-azimuth* harmonic amplitude analysis results from the 72 hour wind and temperature simzults with the addition of mean fields and a Doppler effect. As for Figure (3.3.7) with the addition of a mean wind as $\overline{w}(az) = 2sin[\phi(az) - \frac{\pi}{4}]$, a thermal gradient as $\overline{T}(az) = 2.5sin[\phi(az) - \frac{\pi}{4}]$, and Doppler shifts as $(1 + \beta(az))$ for $\beta(az)$ the ration of the mean wind speed and the zonal phase speed. Additional analyses of these wind simzults were shown in Figures (3.3.3)-(3.3.6).

of the window center displayed directly below the portion of the time series it is derived from. These results are shown for the same neutral wind simzults as in the previous analyses but the temperature is the 72 hour oscillation with no thermal gradient and no Doppler shifting. In this manner the comparison is more meaningful. Two different directions are shown; one in the direction of the mean wind (345°E) and one 45° off this direction (300°E). Both the wind and temperature fits are shown. Between the two fit result stacks is the phase difference $\Delta\phi(j,az) = \phi_w(j,az) - \phi_T(j,az)$ between the derived wind phase '$\phi_w(j,az)$' and temperature phase '$\phi_T(j,az)$. This plot allows one to see variations in amplitude and phase of the individual fits as well as compare the wind and temperature fits for relative shifts in phase and amplitudes. In Figure (3.3.9) the amplitudes are seen to be steady and the phase difference is '0'. In Figure (3.3.10) the amplitude of the wind is reduced as the Doppler effect has red shifted the oscillation away from 72 hours and the constant frequency difference causes the fit to drift steadily as it compensates for the shift. The phase is plotted on a scale of $\pm\pi$ on the right and left respectively (solid vertical lines) and $\pm\pi/2$ for the dashed lines.

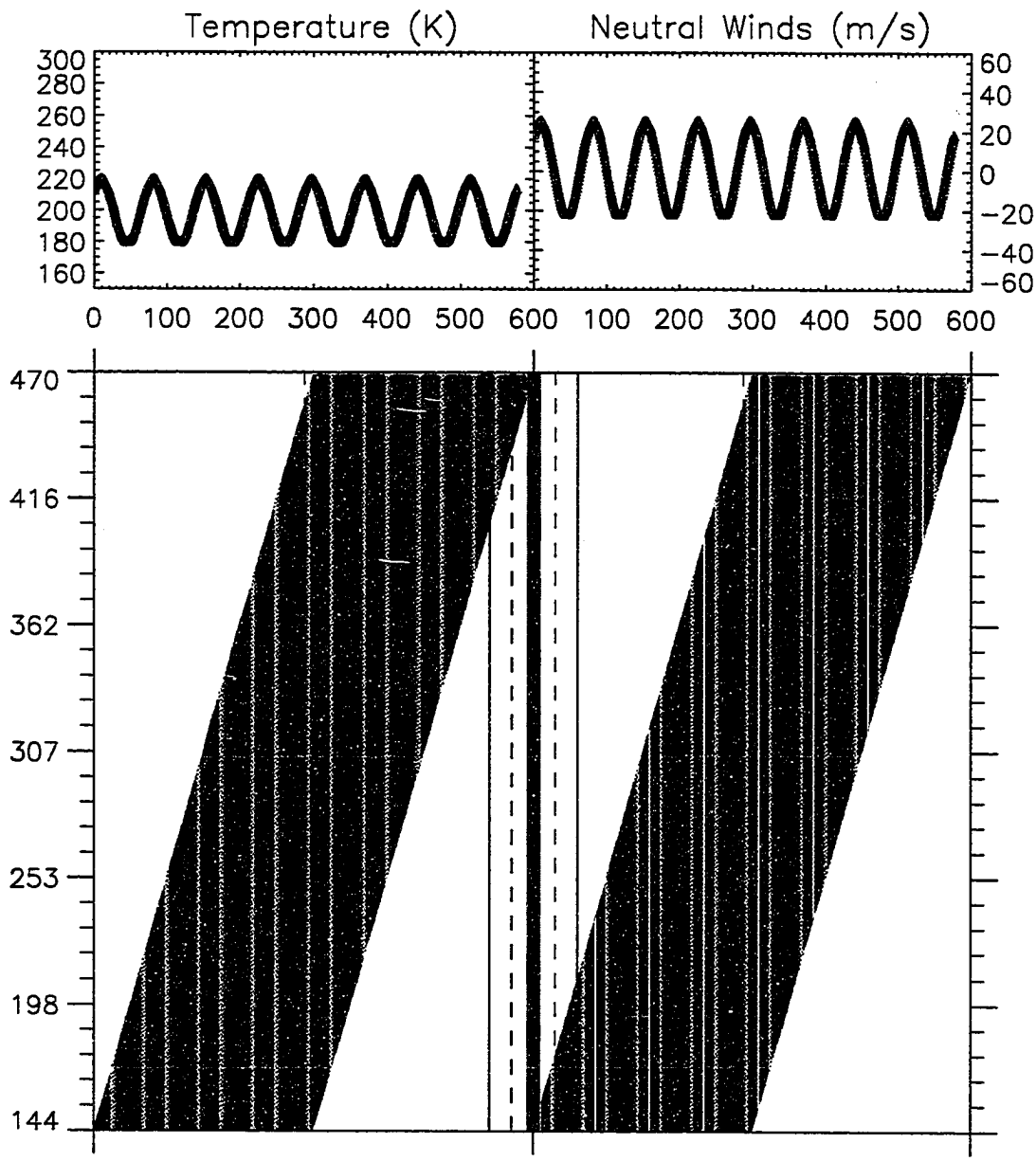

Figure 3.3.9 *Single-azimuth*(parallel to the mean wind direction) harmonic fit stacked plots from the simzult analysis. A 288 hour sliding window is used on the neutral wind simzults as in the previous analyses for the 72 hour temperature oscillation as $T(j) = 20sin[\frac{2\pi j}{72} + \phi(az)]$. Shown here is the 345°E azimuth, (parallel to the mean wind direction). The axes are window-center time vs. time. The fit amplitude is red at maximum and blue at minimum. The relative phase between the two fits are shown graphed in the center of the panel with a scale of $\pm\pi$ on the right and left respectively (solid vertical lines). Fit results are plotted directly below the actual times series fitted.

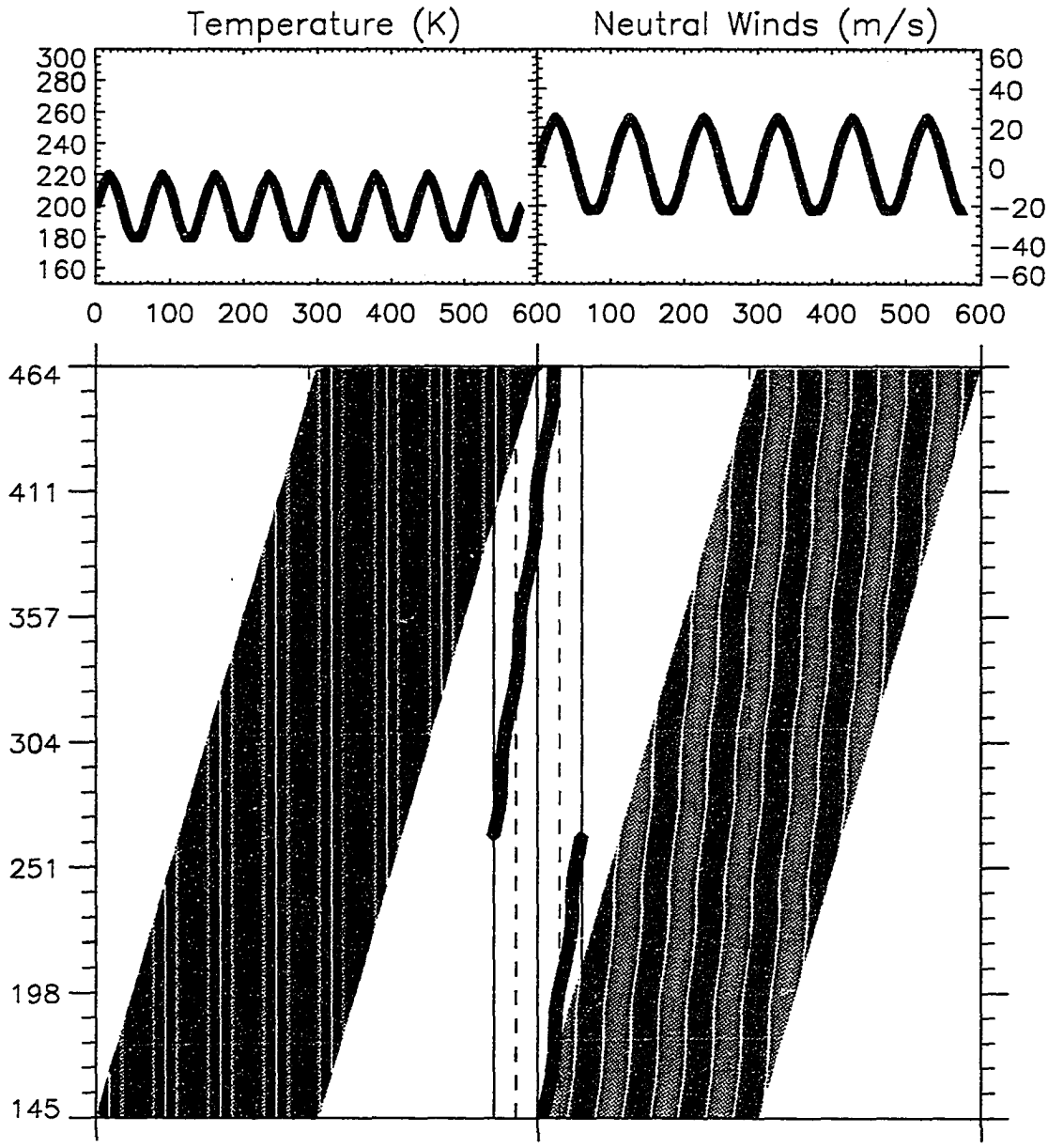

Figure 3.3.10 *Single-azimuth*(perpindicular to the mean wind direction) harmonic fit stacked plots from the simzult analysis. As per Figure (3.3.9) except for azimuth 300°E 45° ccw from the mean wind direction.

Choice of window length for a HF sliding time window

The choice of the window length is crucial to the isolation of specific spectral features. This choice is based upon three criteria:

-the available data and the period of the feature of interest

-the spectral rejection of neighboring features

-and the physical constraints of any dynamic process of interest.

available data: Normally one would wish the best resolution possible and this is used to analyze the entire data period. This still limits analysis to features whose half-period is equal to or less than the data period. For examination of the time evolution of spectral features we wish to analyze smaller time sections of the data which limits in the same way the spectra for which one can search.

neighbor rejection: Two aspects of neighbor rejection must be considered: first the peak resolution must be narrow enough to isolate the two; second the anti-nodes of the window function (sinc) should not allow leakage from nearby features.

The first consideration requires the ratio of τ^2/data (the fwhh of the sinc function) length to be at least equal to the separation of the peak centers. The second is best handled by putting nodes of the sinc function on top of the second feature. That is if $\Delta\tau$ is the peak separation and 'L' the window length then we want $\Delta\tau = L/n$ for some integer n.

physical criteria: The time scale of a particular dynamic process one is searching for, ie., wave dissipation or mode coupling time must be considered. This is the most difficult to ascribe and in this work I assume the interactions to take place on the scale of planetary wave periods. Since even for the short period waves I expect the interactions to be with the planetary waves.

It turns out that the most restrictive criterion is the neighbor rejection. The richness of the spectra required long data windows . I chose them as small as possible to just eliminate contamination and found these windows still to be quite large. In some cases the data period just wasn't long enough to justify smaller period time windows for the time-dependence studies some features, such as the 10-day oscillation.

Choice of time step

The time step was chosen to maximize temporal resolution. The window is slid the minimum of a single data point along each time series.

3.4 Lomb and Scargle periodograms for unevenly spaced data

Lomb (1976) and Scargle (1982) developed a novel type of periodogram (Fourier spectrum) analysis, for finding and testing weak periodic signals in otherwize random, unevenly sampled data.

For the data values h_j, $j = 1,...N$ at times t_j, $j = 1,...N$ the Lomb-Scargle normalized periodogram is defined by

$$P_N(\omega) \equiv \frac{1}{2\sigma^2}\left[\frac{\left[\sum_j (h_j - \overline{h}_j) cos\omega\,(t_j - \tau)\right]^2}{\sum_j cos^2\omega\,(t_j - \tau)} + \frac{\left[\sum_j (h_j - \overline{h}_j) sin\omega\,(t_j - \tau)\right]^2}{\sum_j sin^2\omega\,(t_j - \tau)}\right] \quad (3.4.1)$$

where the mean and variance are

$$\overline{h} \equiv \frac{1}{N}\sum_1^N h_j, \qquad \sigma^2 \equiv \frac{1}{N-1}\sum_1^N (h_j - \overline{h})^2 \quad (3.4.2)$$

and the time offset is given by

$$tan(2\omega\tau) = \frac{\sum_j sin2\omega t_j}{\sum_j cos2\omega t_j}, \quad (3.4.3)$$

for the angular frequency $\omega \equiv 2\pi f$.

Lomb (1976) showed that Eq. (3.4.1) is equivalent to the equation that one would obtain if one estimated the harmonic content of a data set, at a given frequency ω, by linear least-squares fitting to the model

$$h(t) = Acos\omega t + Bsin\omega t.$$

And as discussed in section 3.3.2 this is the basis for the use of the confidence estimates from the Lomb-Scargle method with the harmonic fit results. The least-squares fitting as opposed to a DFT method has the advantage of weighting the data on a 'per point' basis instead of a 'per time interval' basis which makes it particularly useful for unevenly sampled data.

One final note, in viewing the periodograms one has to keep in mind that Eq. (3.4.1) returns the *normalized* power as a signal-to-noise ratio. It is normalized to the variance σ^2 and thus all periodic signals which have had their mean values removed share the same significance testing limits, as related to the signal-to-noise ratio.

Chapter 4 Results and Observations

4.0 Introduction

This chapter contains the data analysis. The analyses used here were discussed in chapter 3. In sections 4.1.1, 4.2.1, and 4.3.1 the content of the derived time series for each period are examined and a characterization of the mean state of the atmosphere during each period is made. For the wind and temperature series of each period daily mean values are derived. A cursory examination for spectral content of the time series is made for the most obvious structure. The uncertainties are derived from propagation of the measurement errors (counting statistics) through the non-linear least-squares fit described in section 3.1.

Passive optical ground based observations are dependent on reasonable air quality. For the derivation of bulk motion of an emitting region it is essential that the photons collected to be only those which originated from the volume in our line-of-sight. Photons scattered into our acceptance cone from other regions must be excluded. Also the photons must reach the detector without interaction from intermediate regions. Clouds between the emitting layer and the detector scatter the radiation from all parts of the sky in all directions. The light scattered from clouds will have Doppler shifts in all directions. If the clouds are thin enough to allow some light through the derived Doppler shifts from it will approach a value weighted by intensity and Doppler shift of the source region. The assumed Maxwellian thermal distribution will not be significantly altered until Doppler speeds of the order of 500 m/s are reached (private communication with G.D. Price). We do not observe speeds of this order in the airglow layer at 90 km altitude hence do not expect to observe enhanced temperatures due to scattered light from clouds. At the bottom of each time series figure, for each period, are symbols indicating the quality of the data as discussed in the introduction. The raised values denote the good data collection periods, the lower ones are the bad periods (primarily for wind determination), and no symbol indicates uncertain quality.

In addition to reasonable weather conditions we need a dark background sky. With the highly sensitive GaAs(Cs) photo-multiplier tubes (PMT) a quarter Moon on the horizon can be seen in the detected signal as increased background photons. In the 1991 and 1992 periods the Moon rose above the horizon and the results in the data are noted.

In sections 4.1.2, 4.2.2, and 4.3.2 the spectral content of these time series is examined and catalogued. The analysis follows the methods of sections 3.2, 3.3, and 3.4.

Although I started my studies using the DFT method for the reduction of the raw data and spectral analysis, very little remains of this type of analysis in this work. I now use the modified periodogram of Lomb and Scargle (LS) and my own harmonic fit analysis almost exclusively. The LS periodogram (see section 3.4) returns the power $P(\omega)$ as a function of frequency 'ω ' and lends itself well to statistical inference. For this reason the full period spectral analysis is carried out with the LS periodogram. Furthermore some spectral features may be so weak that methods to reduce statistical noise are required. In these cases I have used Shannon interpolation for unevenly spaced data in order to reduce the separate azimuthal time series to one and decrease the uncertainties by a factor of 2.

The application of the harmonic analysis to the full data period yields the azimuth and frequency dependent harmonic amplitude $A(\omega, az)$ and phase $\phi(\omega, az)$. For a specific frequency 'ω' I can examine the azimuthal variation of phase and due to the position of the station this is equivalent to an examination of the azimuthal wave-number of the component. Having measurements at eight directions I can detect up to a wavenumber 4. The determination of wave-numbers for selected periodicities is shown in these sections.

The "static" viewpoint of the above discussion of spectra is useful in that it leads to discovery and possibly a general identification of spectral features but this requires long periods of data and wavetrains which are coherent for a significant portion of the period. At lower latitudes the state of the OH layer is characterized by a large degree of wave activity on top of mostly stable planetary waves. Near the South pole I expect the addition of dissipating or reflecting planetary waves to this activity. The lifetime of mid-latitude ducts may be on the order of planetary wave periods and as such the effects may not be seen in long period analyses.

One of the results of this work is the observation of azimuthal asymmetry in the spectra. This fact together with the belief that the dynamic state of the OH layer is characterized by transient oscillations has led me to examine the time dependence of the spectra. In sections 4.1.2, 4.2.2, and 4.3.2 the time dependence of the normalized power

from the LS periodogram is displayed and analyzed for steady and evanescent elements. Also selected features identified from this analysis are examined with the *all-azimuth* presentation This space-time analysis is carried out using the harmonic fit technique. The result is space and time dependent spectral amplitudes and phases for both the neutral wind and kinetic temperature.

The space-time analysis was made especially useful beginning in 1991 when the observational scheme was changed to make nine measurements per azimuthal cycle instead of five as in 1990. In addition an increased optical efficiency achieved allowed the temporal resolution to also improve. In 1992 the data period was limited to 12 days. The improved resolution and longer period make 1991 the best candidate for the space-time analyses and thus I will focus more on this period than the others.

A result of the time dependent study done in these sections is the existence of a variable cross-polar mean wind. This time dependent mean wind led me to ask whether or not the spectra I derived were the local Doppler shifting of the source spectra. To answer this question I inverted the formula for the Doppler shift and attempted to recover the source spectra. Both azimuthal and temporal variability can be produced by Doppler shifting in accordance with the derived mean wind.

The Doppler formula for the period of a transverse wave as seen by the FPS is

$$\tau = \tau_0(1 \pm \frac{w}{v_\phi \mp w})$$

for w the magnitude of the mean wind and v_ϕ the wave phase speed. The upper/lower sign is for the red/blue shift to longer/shorter periods. Inverting these, get

$$\tau_0 = (\tau s/w)(\tau \pm \frac{s}{w})^{-1}$$

where here s is the circumference of the circle of observation (862 km) and a wavenumber one is assumed so that the phase speed is s/τ_0.

Typical phase speeds are $\approx$1.2, 3.5, 10.7, 20, m/s for 9, 3, 1, .5 day wave-number one oscillations. It is easy to see that it will not take much of a mean wind to exceed the phase speed of the longer wave periods. When this happens the wave is critically Doppler shifted and dissipates, no waves can exist in regions where this phase speed is exceeded by the mean background. Typical mean winds found are 2-14 m/s and yet a 5-day wave-number one exists!

I calculated the critical frequency as a function of the mean wind, (below which nothing should exist), and compared it with the observed spectra. I found that in order

to produce the observed spectra the implied source spectra had to have structure below this frequency to be blue shifted up to the observed frequencies. I found this to be true for both westward and eastward assumed phase progressions.

These two facts lead me to conclude that the coupling to the mean wind is not efficient. This may be due to a mismatch between the wavelength and the effective width of the mean wind region.

Finally for ease in referring to the various directions I will use 'north' or N to refer to the magnetic north or 300°E longitude direction and similarly for the other directions, ie., south or S for 120°E longitude; northeast or NE for 345°E longitude; etc..

4.1.1 Results from the 1990 period: the time series

In Figure (4.1.1) winds plotted with their Doppler signs, and in Figure (4.1.2) the kinetic temperatures, for the entire period are shown for each direction. In addition the countrates are plotted in Figure (4.1.3). The mean values and azimuths for each series is indicated at the right. There is a data gap due to instrumental down time from May 19-21 after which the data collection was poor for winds until 12 UT May 26. Effectively there are two periods to consider: 0:0 UT May 18 to 24:0 UT May 20 and 12:0 UT May 22 to 18:0 UT May 31 hereafter referred to as the first and second sections.

An anti-correlation between the Doppler winds from opposing directions (those separated by 180°) is obvious in the series. These anti-correlations are aligned between NW-SE for the first section and up to about hour 170 when the alignment switches to NE-SW For the temperature series a correlation is seen in all directions except for a the period around May 24-25 (hours 144-192) in the N where the temperature reverses the trend of the other directions. This is more clearly seen in Figure (4.1.4) for the daily mean winds and temperatures. In this figure long period oscillations can be seen which are not as obvious in the time series, for example- an 8-day variation in both the temperature and the wind series.

In the daily mean temperatures the minima occur when the mean winds have their maximum amplitudes and temperatures are maximum when the winds are minimum (zero crossing). For instance at days 24, 29, and 30 the winds are maxima and the temperature is low, whereas day 26 shows a maximum temperature and minimum wind activity. A straight line fit to the temperature means indicates an increase of + .4°K/day for the period.

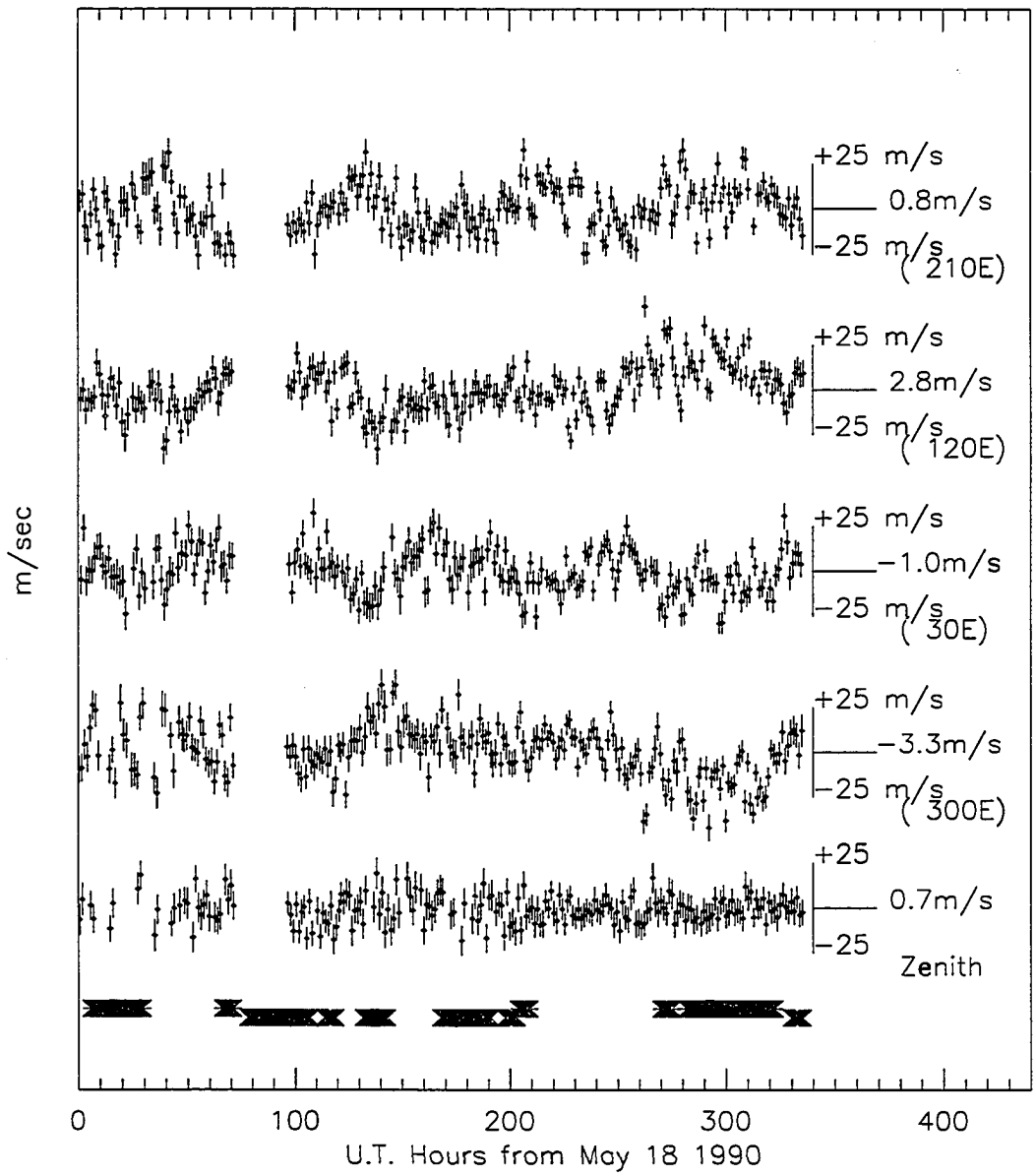

Figure 4.1.1 Doppler winds from May 18-20, 22-31 1990 derived from OH(6-2) emissions at 8399Å over South pole station. The mean wind value and the azimuth for each series is indicated. Error bars are derived from propagation of counting statistics errors through the non-linear least-squares fit.

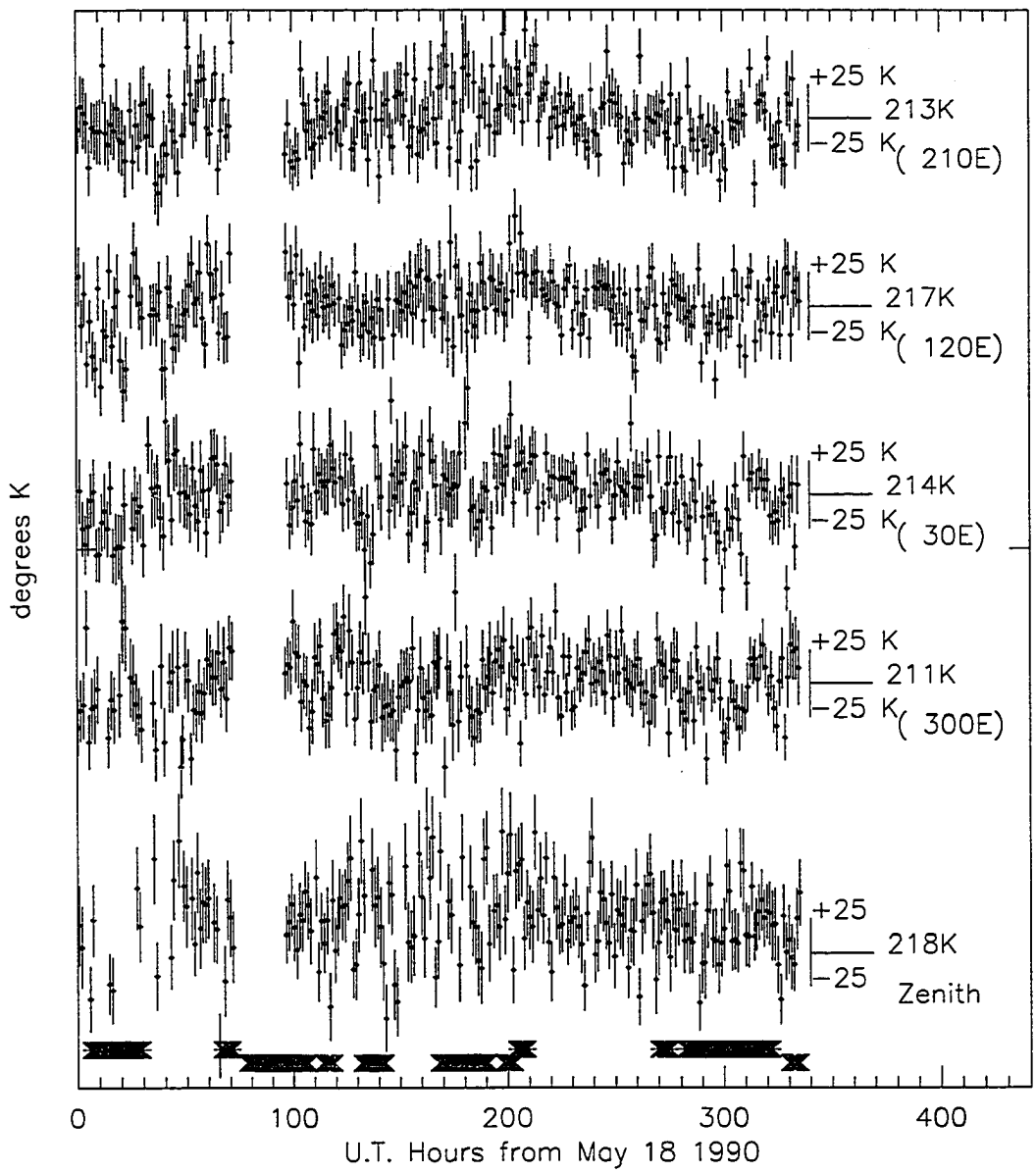

Figure 4.1.2 Kinetic temperatures from May 18-20, 22-31 1990
As for Figure (4.1.1) but for temperatures (°K).

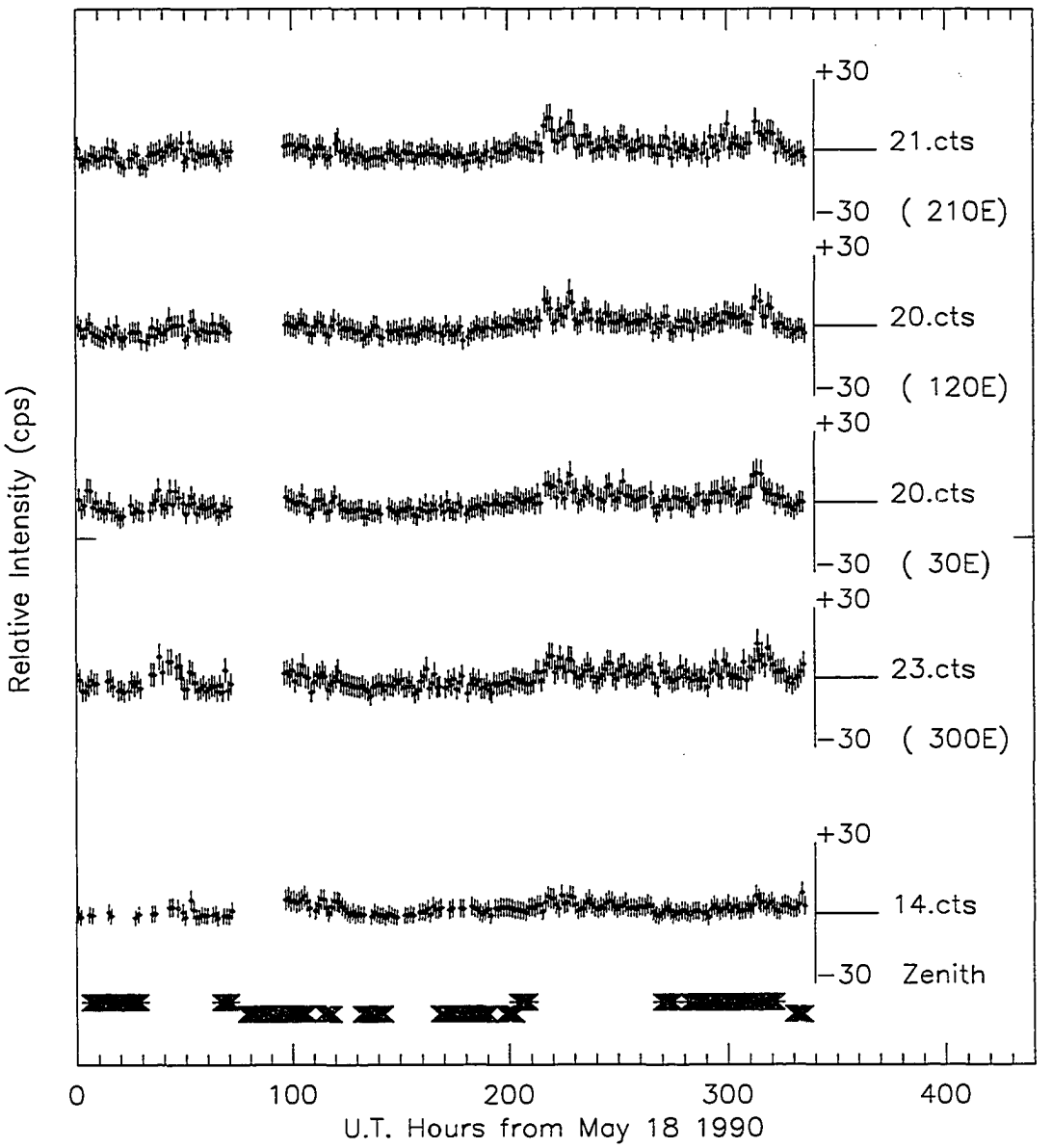

Figure 4.1.3 Countrates from May 18-20, 22-31 1990 Signal intensity and background are determined from the non-linear least-squares fit and the background has been removed. Shown as for Figure (4.1.1) but for countrate (cps).

Relative intensities in counts have been converted to counts per second (cps) above background and are shown in Figure (4.1.3) The period mean intensity is $\approx$ 21.3cps with the N (300E) direction to be on average the brightest. The zenith is the dimmest since the line-of-sight thickness of the layer is a minimum in the zenith. The intensity is depressed during the poor weather period. Shown as for Figure (4.1.1) but for countrate (cps).

4.1.2 Results from the 1990 period: Spectral content

In Figures (A.1)-(A.3) of appendix 1 the full-period normalized power spectra for wind, temperature, and intensity of the data section after the data gap are shown. In each figure five panels are shown, one for each of four azimuths and one for the zenith observations. The overall impression of the spectral panels shows two particular groups of peaks, those in the planetary regime (days) and those in the semi-diurnal regime (hours). In addition to this observation I note the existence of azimuthal asymmetry from panel to panel.

In Figures (A.1)-(A.3) the LS periodograms for the second section are shown and I note the asymmetry and the grouping of structure into two groups.

For the winds in Figure (A.1) only the long period features are statistically significant at the 95% confidence level. Varying levels of power are found in the ~8, 5, 4, 3, 2.7, 2, and 1.5 day periods. In the short period group the 12.3, 11, 10, and 8.3 hour periods are noted. In the E-W a small 23 hour peak is also seen. In the zenith are the 8 and 2.7-day and a 14.5 hour feature. Only the 8, 3, and 2-day peaks are significant above the 95% confidence level but not in all azimuths. As previously noted the 8-day oscillation could even be seen in the time series of Figure (4.1.1). The E-W and N-S wind panels are quite similar from 36-120 hours, or $\sim$ 1.5-5 days, in fact all four panels show a tendency for a ~1.5, 2, and 3-day peak triplet.

In the temperature periodograms for this second section, Figure (A.2), the grouping is not as clear as for the winds and cps spectra. Here I note the 8, 6, 3.3, 3, 2.7, 2.3, 2, and 1.1-1.6 day peaks as well as 12.4, 10.9-11.9, and 9.5 hour peaks. In addition to these groups are 7 and 19 hour peaks in all panels except W. Some of these identifications have associated wind features and some do not.

In the countrate spectra for this second section, Figure (A.3), I find all the panels to be quite similar except for a 2/3 reduction in the zenith intensity. The characteristic

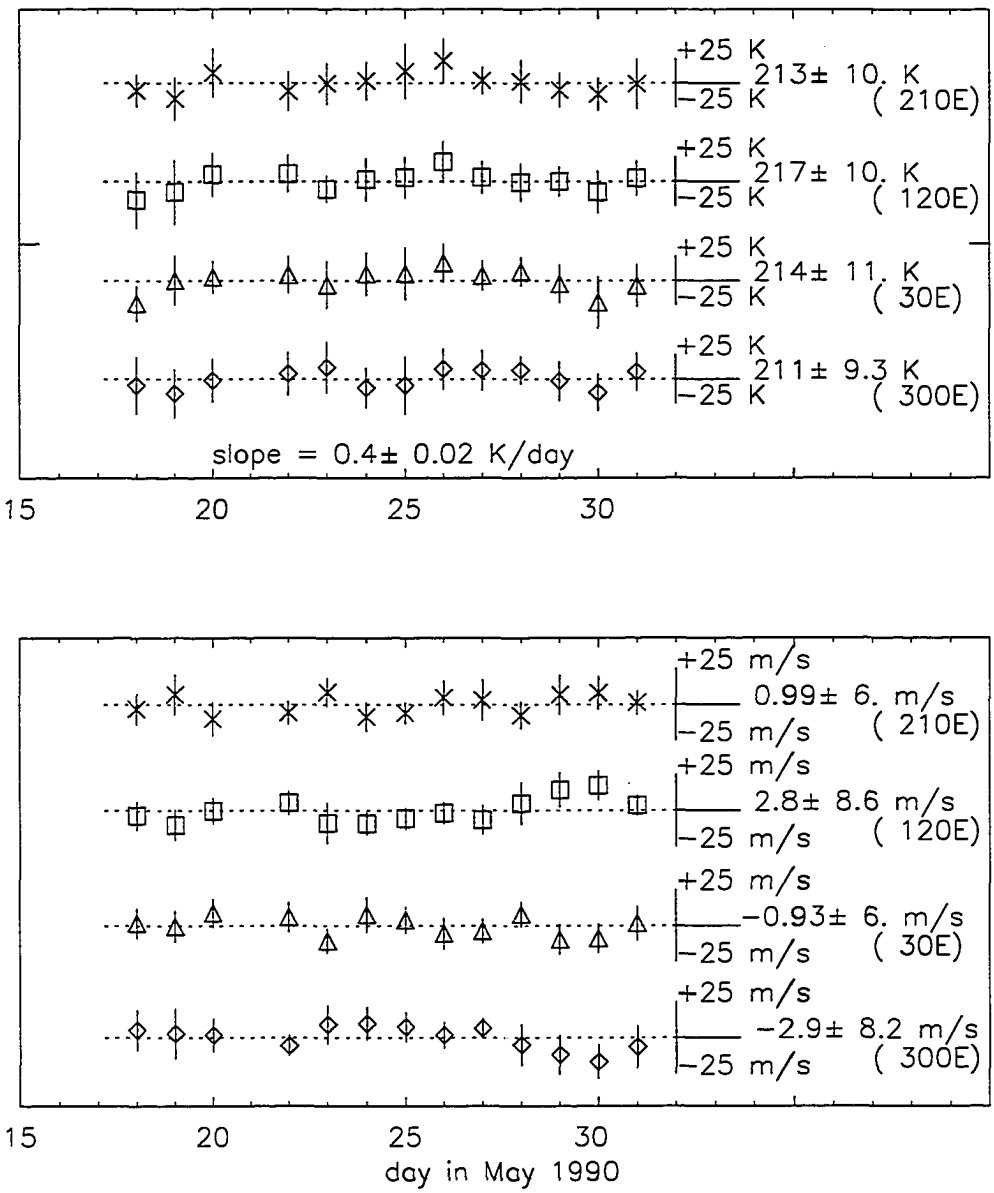

Figure 4.1.4 Daily mean Doppler winds and kinetic temperatures from May 18-20, 22-31 1990 The entire period mean wind and temperature values are indicated for each azimuth. Positive values indicate winds away from the observer, i.e., positive winds in the east azimuth indicate an eastward wind. Daily variability (standard deviation) are shown as error bars. A straight line fit to the temperature means indicates a warming trend of $+.4°K/day$ for the period.

features are ~6, 5, 3, 2, 1.4, and 1 day peaks as well as peaks at ~8.7, 8.3, and 6.9 hours. It is interesting that in all the wind, temperature, and cps non-zenith panels something shows up near 7 hours, least significant in the wind panels.

In Figure (4.1.5) the results from the dual-vector analysis is shown. For reference I mention that from analysis following the time dependent power spectra I show the cross-polar mean wind to blow ~N → S for this May 22-31 period, (see Figure (4.1.10)). The combined vector components still show asymmetry in amplitude and content. Both show the 8, 2, and 1.5 day as well as the 10 hour peak. The E-W component has an additional feature at 4-days. The N-S component has additional features at 3.3-days, 23, 12, 11.3, and 8.3 hours. In the planetary period group the distribution of power among the spectra shows the 8 and 4 day to be preferred in the N-S and the 3.3 and 2-day in the E-W. I note the descending amplitudes for the 3.3, 2, 1.5, 1, .5, .3 day harmonics in the E-W and the 8, 4, 2 day in the N-S.

With the exception of the 8-day oscillation, phase plots show each of these to have wavenumber one behavior, with the first set (days) having an eastward phase progression and the others (hours) to have westward progressing phases. The 8-day phase progression appears as a bi-level or stationary phase pattern as one might expect from a standing wave.

One outcome from this work is the discovery that the temperature oscillations in general show a wavenumber zero phase progression around the pole, (or have a very slow progression). It turns out that with the exception of the 11.3 hour temperature oscillation this observation holds for this period. (This 11.3 hour temperature feature shows a steeper slope than a wavenumber one.) This observation allows me to ignore the azimuthal dependence and analyze the temperature series as one large or 'grand' array, the results of this analysis are shown in Figure (4.1.6) for the grand arrays for each of the three parameters of wind, temperature, and cps. In this analysis I expect to find the winds, as predominantly wavenumber one, practically absent and the temperatures and cps relatively unchanged in content from the individual azimuth panels, but increased in significance. Indeed this is the case. In the temperature panel (center), the most significant feature is the broad band at 5-8 days, and the 3, 2, 1.6-day, and the ~ 13.7, 9.6, and 8 hour periods. Note also that the 11.3 hour peak is absent in this analysis as we have effectively filtered all wavenumber one information out. Comparing the results

in Figures (4.1.5) and (4.1.6) I note that the ~8, 3, 2, and 1.6-day as well as the 8 hour wind features have associated temperature oscillations.

Time dependence of the spectral amplitudes

The preceding analyses show the average spectral content ignoring any transient or evanescent behavior. I now examine the data for time dependent spectral amplitudes. The analysis of the temperature grand array is shown in Figure (4.1.7) as time verses period plots. In each figure the full spectral range from 4-150 hours is shown in the top panel. In the lower panel of Figure (4.1.7) the short period region from 4-20 hours is displayed. The times on the vertical axis is the time ascribed to the center of a sliding 150 hour window within which the Lomb-Scargle analysis has been performed. In Figures (4.1.8) and (4.1.9) the results from application of the same analysis is shown for the dual-vector components.

The time dependence of the short period group

Comparing the lower panels of Figures (4.1.7), (4.1.8), and (4.1.9) I find that there are three features which begin each panel. These are at ~8, 10, and 11 hours. In the temperatures the 11.3 hour oscillation has been removed leaving only the 8 and 9.6 hour features. These two drift toward each other as the window progresses through time. The ~8 hour peak is seen to move from ~7.8 to 8.3 hours and the ~9.6 hour peak from 9.8 to 9.4 hours. In the E-W dual-vector component these features appear at 8.3, 10.1, and 11.3 hours. The broad 8.3 hour feature splits at hour 101 and continues as the narrower and weaker, spawned, 9 hour feature continues to the end of the period. The 11.3 hour oscillation, which has the associated non-wavenumber zero thermal oscillation, also drifts to higher frequencies before returning to 11.3 hours. In the N-S dual-vector component these feature appear at 8.3, 10, and 10.7 hours. The 8.3 hour oscillation is short lived and is replaced by a weak 9 hour feature, as in the E-W panel. The 10 hour oscillation merely broadens and apparently coalesces with the 10.7 hour one.

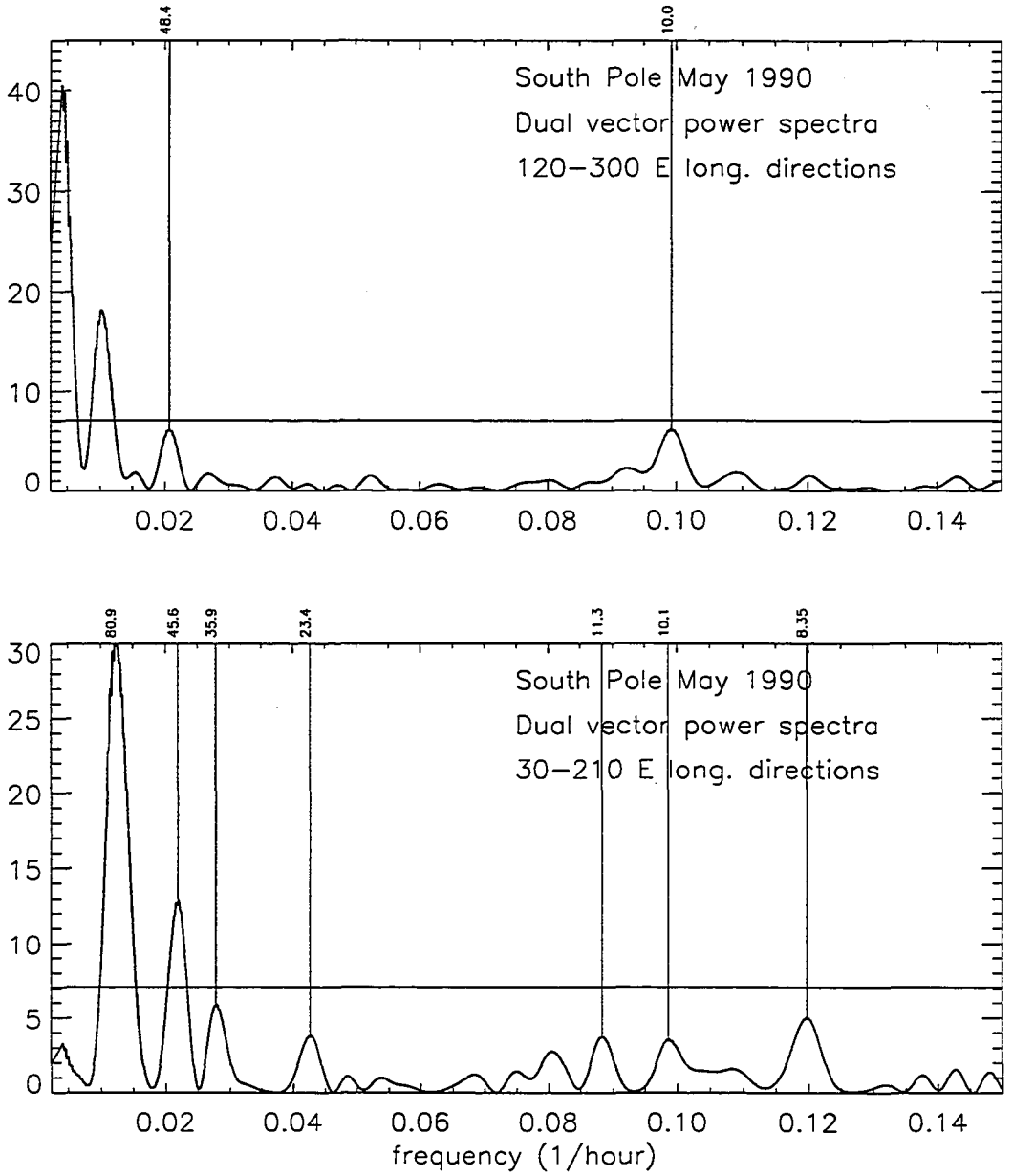

Figure 4.1.5 'Dual-vector' components of the neutral winds for May 22-31. Lomb-Scargle periodograms of the dual-vector components. Normalized power for the N-S component (upper) and the E-W component (lower) is plotted against frequency (1/hours) for 6.7-150 hour periods.

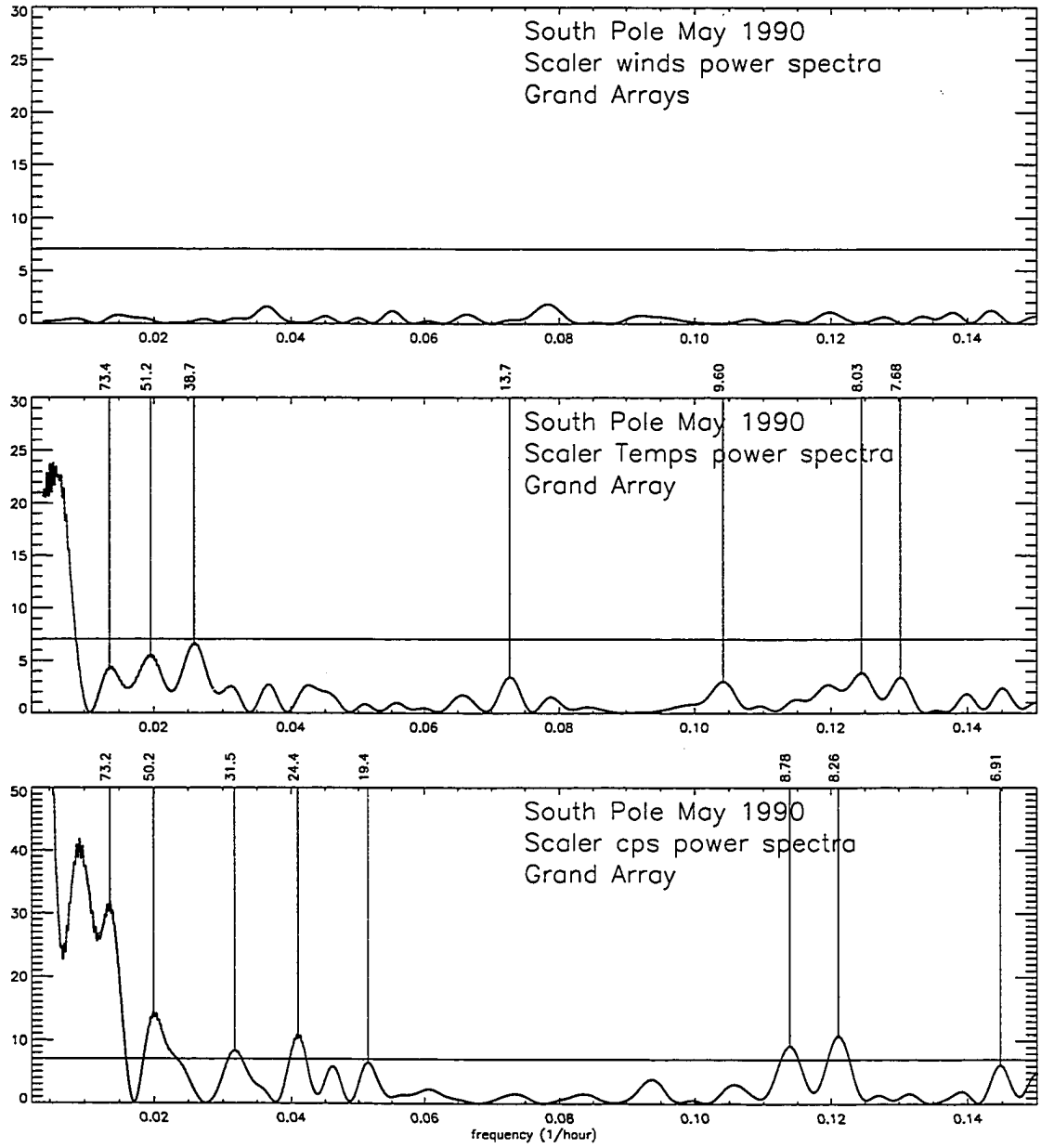

Figure 4.1.6 Grand array analyses for winds, temperatures, and countrates from May 22-31. Lomb-Scargle periodograms of the grand arrays. The normalized power is plotted against frequency (1/hours) for 6.7-150 hour periods. The 95% confidence level is shown as a horizontal line. Selected periodicities are marked (hours).

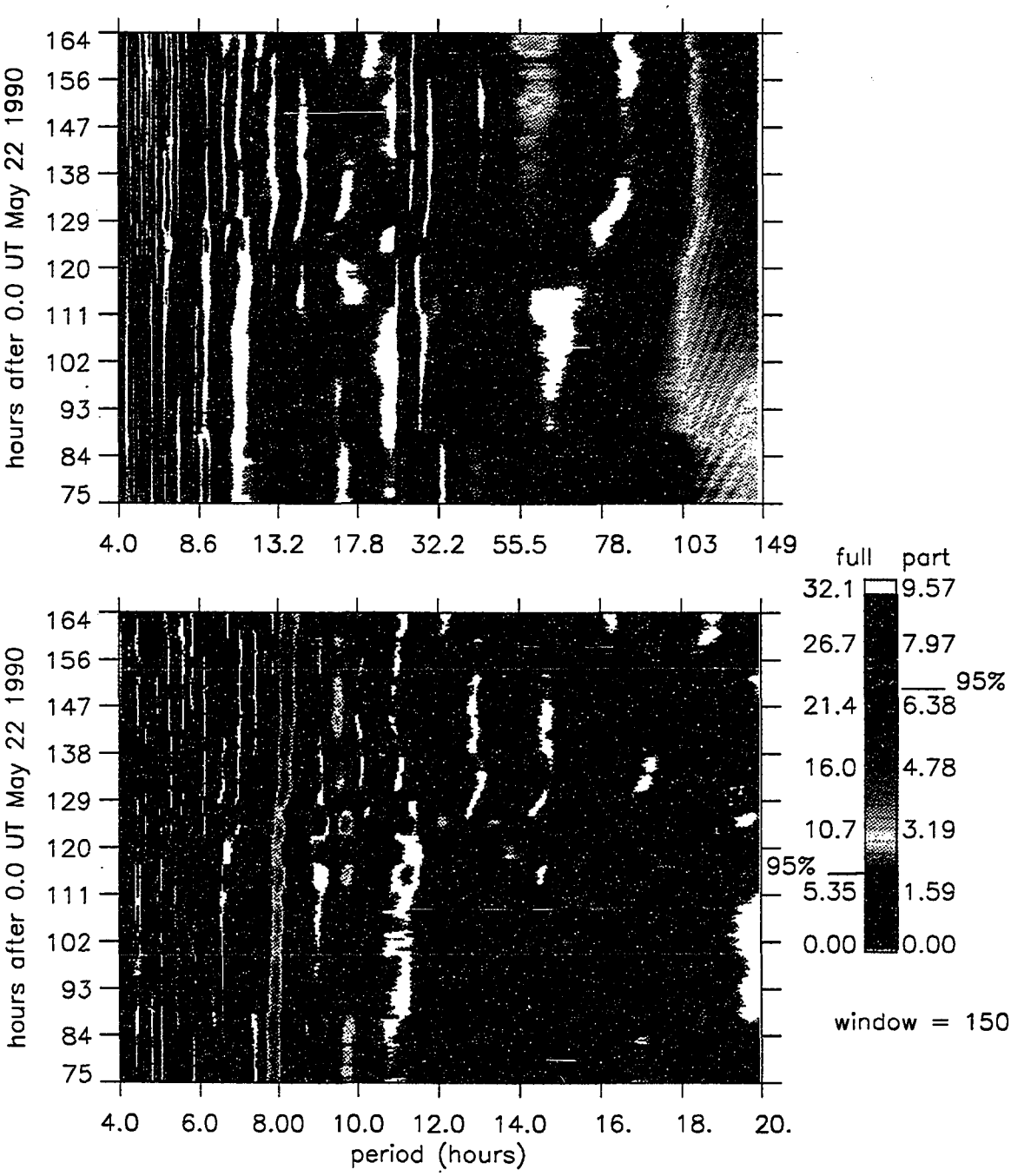

Figure 4.1.7 Time dependent grand temperature array analyses for temperature structure from May 22-31. The Lomb-Scargle periodogram is shown as a function of the window-center time (vertical axis). A sliding 150 hour data window is used. The horizontal axis is the period (hours). The color bar gives the key to the normalized power level. The 95% confidence level is indicated on the bar. The spectral ranges are 4-149 hours (upper panel) and 4-20 hours (lower panel).

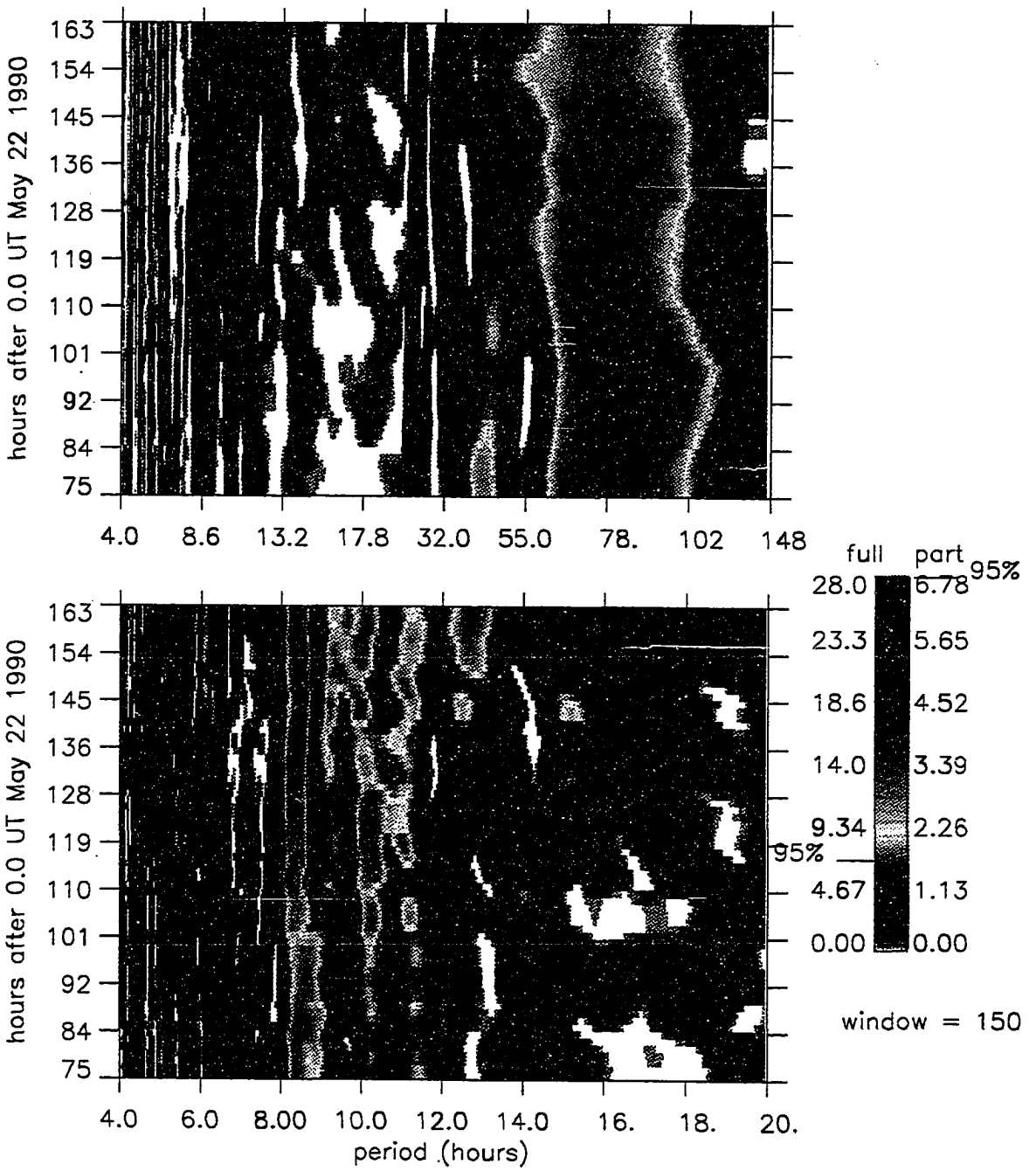

Figure 4.1.8 Time dependent 'dual-vector' wind structure from May 22-31 for the 30-210°E azimuths. As in Figure (4.1.7).

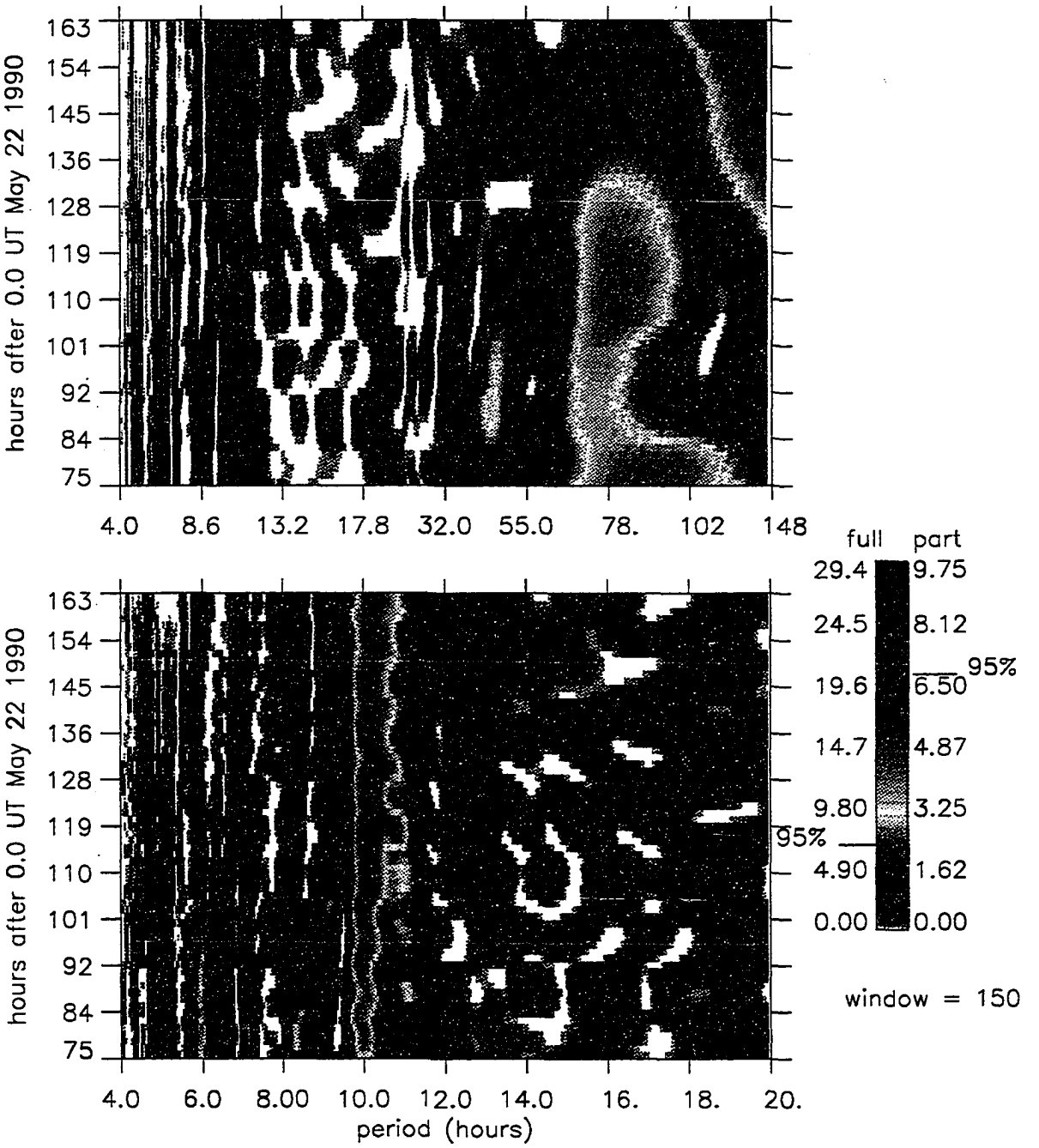

Figure 4.1.9 Time dependent 'dual-vector' wind structure from May 22-31 for the 120-300°E azimuths. As in Figure (4.1.7).

The time dependence of the long period group

The long period analyses are seen in the upper panels of Figures (4.1.7), (4.1.8), and (4.1.9). My first impression of these is that with the exception of the 1.9-day oscillation the temperature power and the E-W component of the wind power seem to exclusively occupy different spectral regions. The N-S wind component on the other hand appears to share portions of each region. In the temperature panel the broadband region occupies the 4-6 day region and goes mostly unchanged throughout the panel. In the E-W wind component the broadband 2.7-4 day power range is likewise unchanged throughout the panel except where it spreads slightly to longer periods between hours 84-110. The N-S wind component has a broadband 3-5 day power region which necks down to ~3-day during the expansion of the E-W component after which it expands to ~3-4 day periods and then vanishes around hour 136 as a 5-6 day region is enhanced.

The 1.9-day evanescent oscillation all but vanishes in all three panels and is replaced by the 1.4 and 2.7-day pair in the temperature panel. In Figure (4.1.10) the *all-azimuth* analysis of this 1.9-day feature is shown. In the wind panel the azimuthal asymmetry is clear showing the most amplitude in the E-W until hour 115 when the oscillation weakens in these directions and spreads to all directions. In this manner this oscillation is observed in Figure (4.1.5) in both N-S and E-W components and is more significant in the E-W. At about hour 130 the amplitude further diminishes. The wind phase panel shows a wavenumber one behavior. The temperature amplitude panel shows a weak response until hour 115 when the response vanishes as per Figure (4.1.7). During this period the mean wind rises steadily from 1 to 6 m/s as it changes directions from SE to S. The thermal gradient is roughly steady at 7 °K across the observing circle or 2.3°K per degree latitude (°lat). The gradient indicates the cooler sky is in the NW, ~ 90° east of the mean wind, which is consistent with geostrophic flow in the southern hemisphere. The temperature phase panel shows very little variation indicating wavenumber zero behavior.

As a final note in the various figures (4.1.7)-(4.1.9) there are 'modulations' in the power, which are here taken to be artifacts of the analysis until further investigation. The first are the slanted variations most obvious in the long period region of the upper panel of Figure (4.1.7). The other modulation is an ≈12 hour modulation seen throughout the 8-10 hour region where power exists in the lower panel of Figure (4.1.9). These

modulations may be due to variations in the derived window mean value as non-integral multiples of the fitted period are applied.

4.2.1 Results from the 1991 period: the time series

In Figures (4.2.1), (4.2.2), and (4.2.3) the Doppler winds, kinetic temperatures, and relative intensities for August 2-25 1991 are shown. The only poor weather is indicated for the last day of the period. In the latter third of the period the moon is up which increases the background light level. Here I note that the moon rose above 0° lunar depression angle at noon on August 12 (~hour 264) with 8% of the disk illuminated. By August 19 (~hour 432) it had risen to 24.7° and was 70% illuminated.

The Doppler winds derived from opposing directions (those separated by 180°) are anti-correlated. These anti-correlations are aligned between N-NE-E-SE and the S-SW-W-NW hemispheres until August 20 (or ~hour 460) when the alignment switches to between the NW-N-NE-E and the W-SW-S-SE. The temperature series are generally correlated in all directions. The temperature series NE half-circle means appear slightly colder than the SW.

The period mean countrate is $\approx$ 39cps and is highest in the NW at 42 cps. The intensity is depressed during the poor weather period. All directions appear well correlated as with the temperature series. As mentioned above the moon was rising in the last third of the season producing diurnal peaks in the intensity. This is also seen in the zenith measurements to a lesser degree. At the very end of the season during the period of bad weather the intensity drops abruptly as we would expect for poor weather.

In the temperature and intensity series I find long period (~9-day) correlations between the fluctuations in the first 200 hours of this period. In all three figures long period waves with amplitudes as high as 25 m/s, 15°K, and 30 cps can be seen. In general in the zeniths I find a reduction in the variance of the neutral winds and countrates as compared to the other directions.

In Figure (4.2.4) the daily mean winds are shown for all directions and in Figure (4.2.5) those for the daily mean kinetic temperatures is given as for the 1990 period. The daily mean winds for this period show less variability (~1/2) than for the May 1990 period. Once again a non-zero mean cross-polar wind exists. Long period oscillations stand out in both figures but are more clear in the temperature data with$\approx$ 10°K amplitudes. A clear periodicity of $\approx$ 9 and 11 days can be seen in the temperature daily

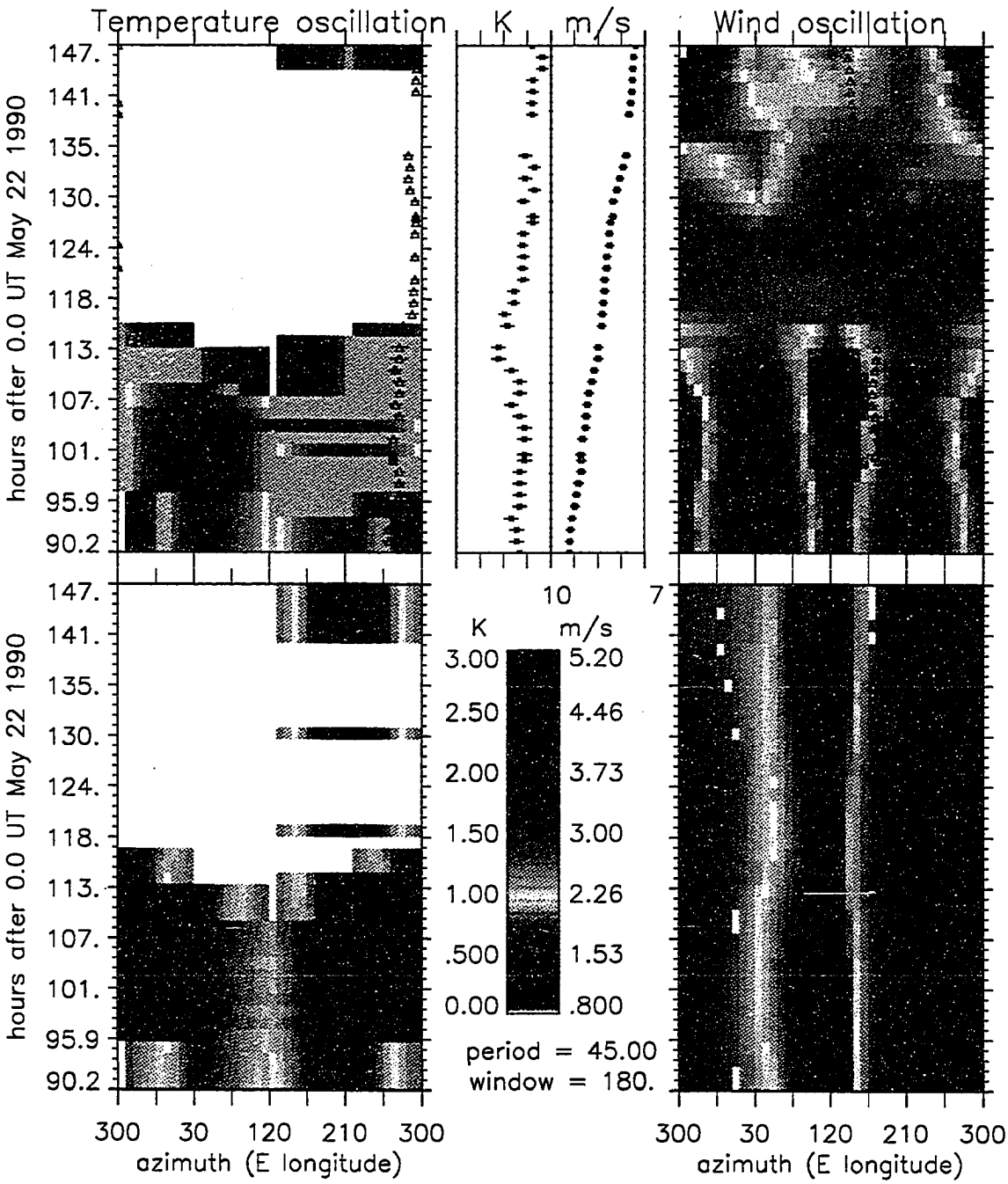

Figure 4.1.10 *All-azimuth* time dependent results for the 1.9-day oscillation amplitudes and phases derived from the harmonic fit to the time series in a 150 hour sliding window from May 22-31, 1990. Figure layout as in Figure (3.3.7).

means. In the daily mean winds there are periods where all directions have the same speed and other periods where there are 15 m/s differences. Such is the case for the first 8 day period where the mean temperature cycles through 15°K, the intensity dips and rises (Figure (4.2.3)) and the mean wind differences go from 10m/s N-NE to 0 and back to 15m/s N-NE.

4.2.2 Results from the 1991 period: Spectral content of the time series

This longer period (25 days) in August shows more neutral wind structure than for the May period of sections 4.1, in particular in the planetary scale oscillations with periods of several days. In Figures (A.4)-(A.9) the full period neutral wind, kinetic temperature, relative intensity spectra are given for all directions.

The first observation I make is that all of these figures show azimuthal asymmetry, a fact which by itself is significant. In the neutral wind spectra there are clearly two regions of enhanced activity. One in the long planetary oscillations region and the other near the semi-diurnal periods (8-16 hours).

The long period region

In the Figures (A.4)-(A.5) for the different azimuth panels the long period region has a single feature near 9-days which is significant above the 95% level in most panels. This feature ranges from 6.8 days to 9.7 days. With a bandwidth of $\pm.0008$/hr this is consistent with the presence of an 8.1 $\pm$ 1.3-day wave. This oscillation was noted in section 4.2.1 as a $\sim$ 9-10 day oscillation.

The remainder of the region has some features that are fairly well resolved. One which stands out is the 56 $\pm$ 2.5 hr or 2.3 $\pm$ .1 day which is present in almost all panels and above the 95% level in three of the 120, 210, and 255°E azimuths. Other strong features in this region are the 64 $\pm$ 3.3 hour, or 2.6 $\pm$ .13 day, which is significant at the 95% level in the 75-255°E, and 30-210°E longitude directions and the 44 $\pm$ 1.5 hour, or 1.8 $\pm$ .06 day, significant in the 120 and 75°E. Weaker features are the 72 $\pm$ 4.1 hour and the 78 $\pm$ 4.8 hour ones which although they stand out they do not reach the 95% level in any azimuth.

Assuming these features to have a global scale with zonal coherence I should be able to form a single vector, (a time series, with a single magnitude and phase), from the eight different series. In this way any weak signals should benefit from the improved statistics and possibly emerge from the noise. I used a sinc function interpolation scheme

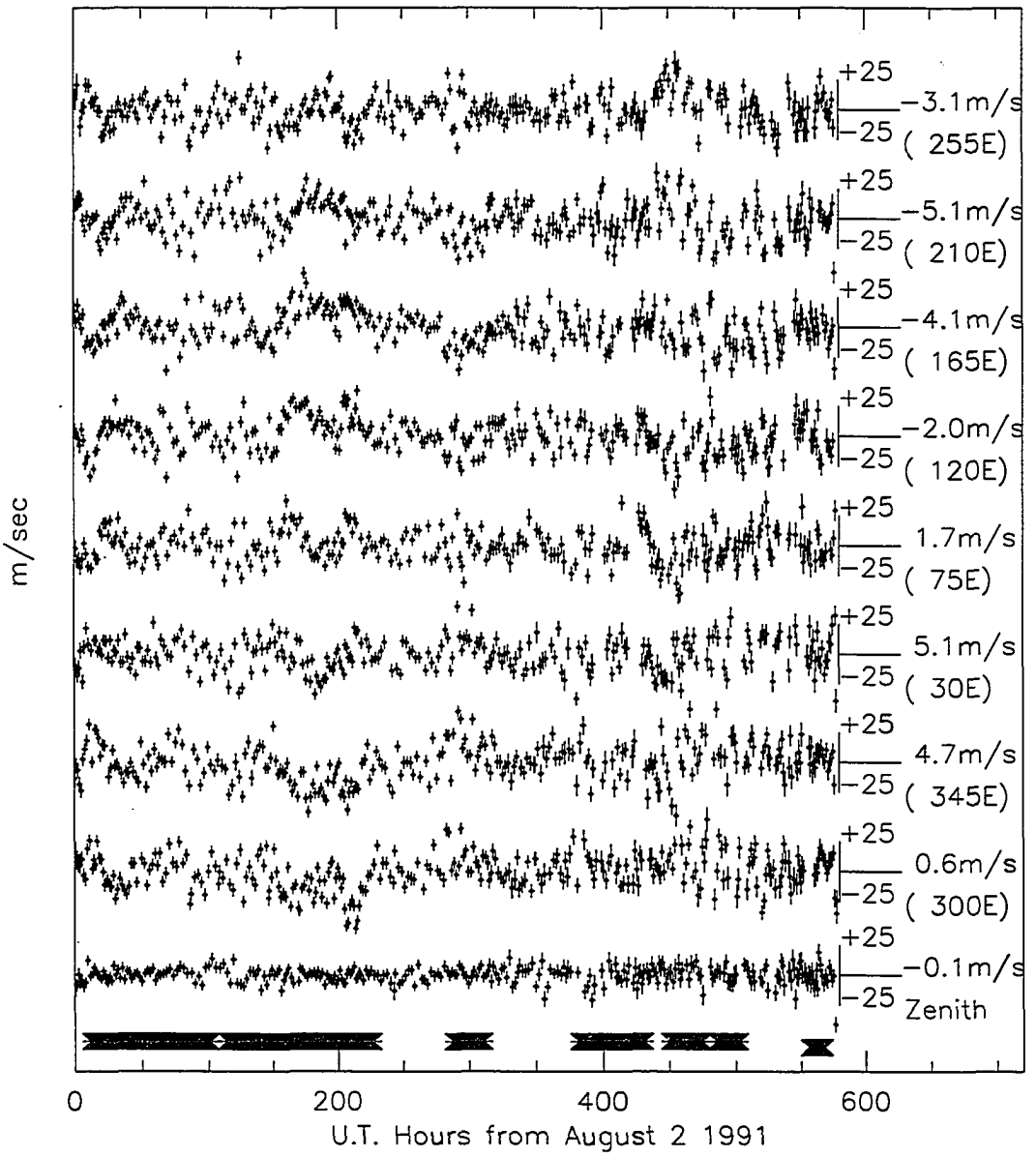

Figure 4.2.1 Doppler winds from August 2-25, 1991 derived from OH(6-2) emissions at 8399Å over South pole station for the eight different azimuths and the zenith measurements. The fluctuations about the mean wind value are shown. The mean and the azimuth for each series is indicated on the right. Each azimuth has its own vertical axis in m/s. Error bars are derived from propagation of counting statistics errors through the non-linear least-squares fit.

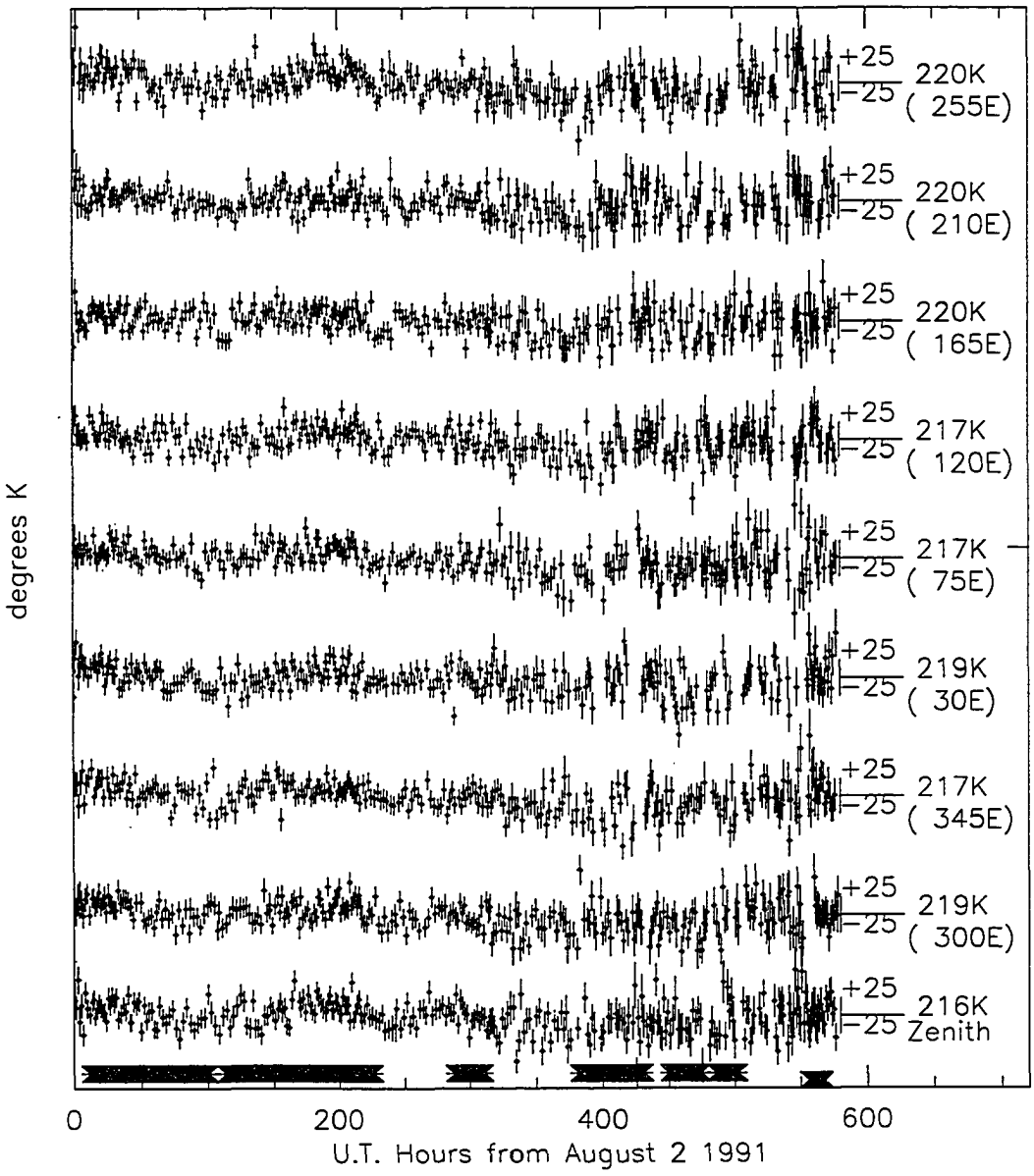

Figure 4.2.2 Kinetic temperatures from August 2-25, 1991 As in Figure (4.2.1) but for the temperature.

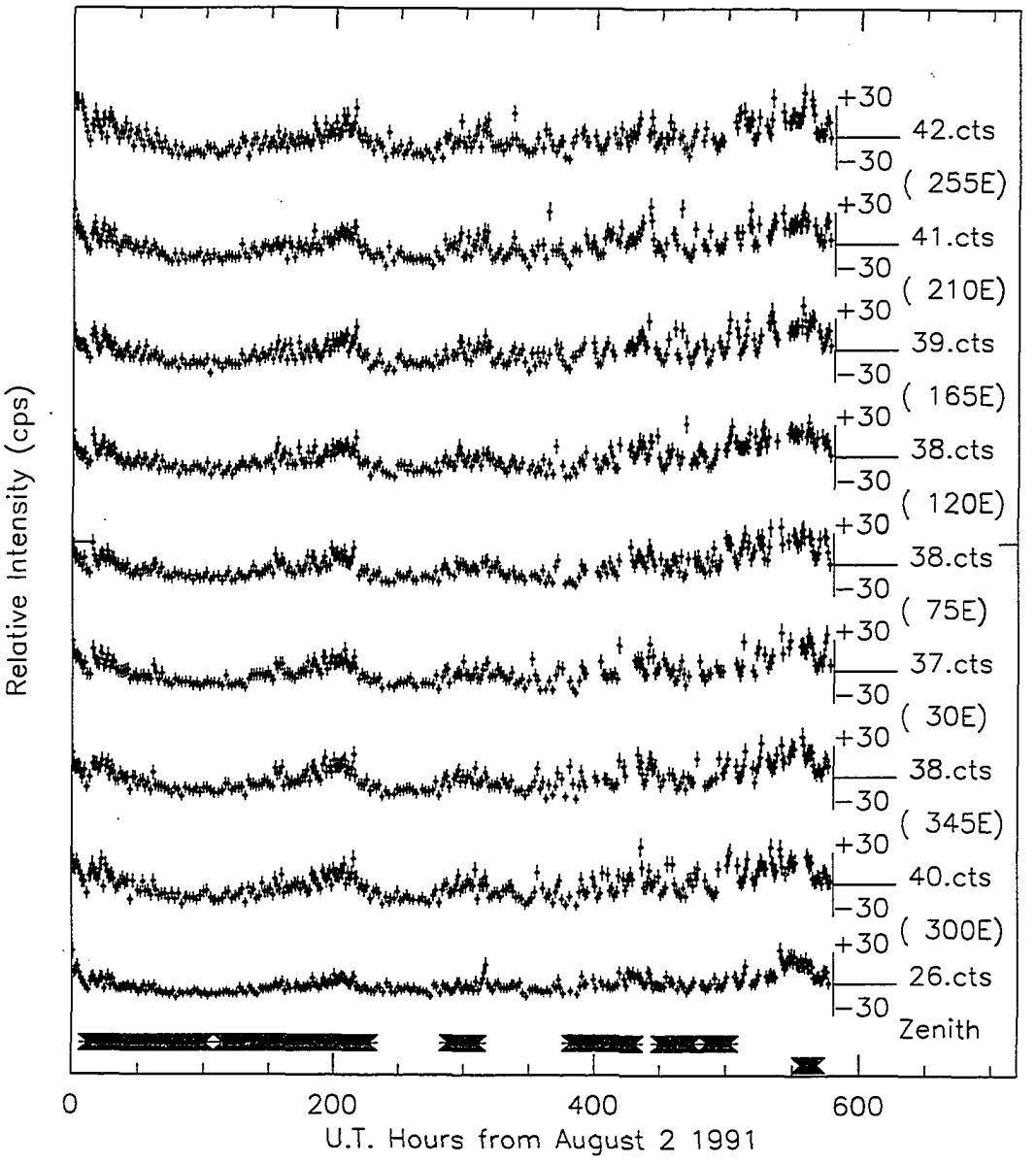

Figure 4.2.3 Countrates from August 2-25, 1991 As in Figure (4.2.1) but for the countrates.

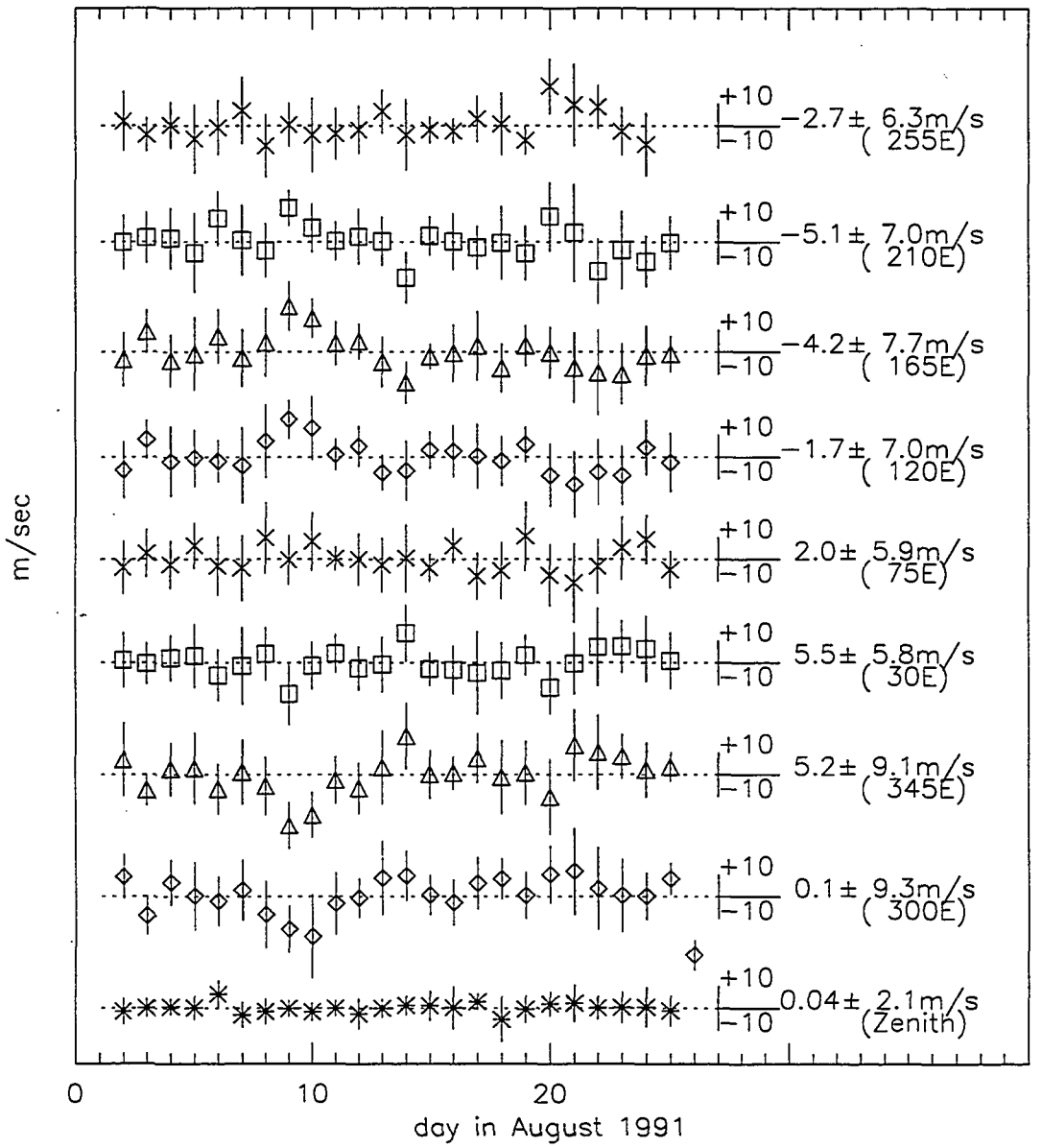

Figure 4.2.4 Daily mean Doppler winds from August 2-25, 1991
As in Figure (4.2.1) but for the daily mean values. The full period mean value is indicated on the right.

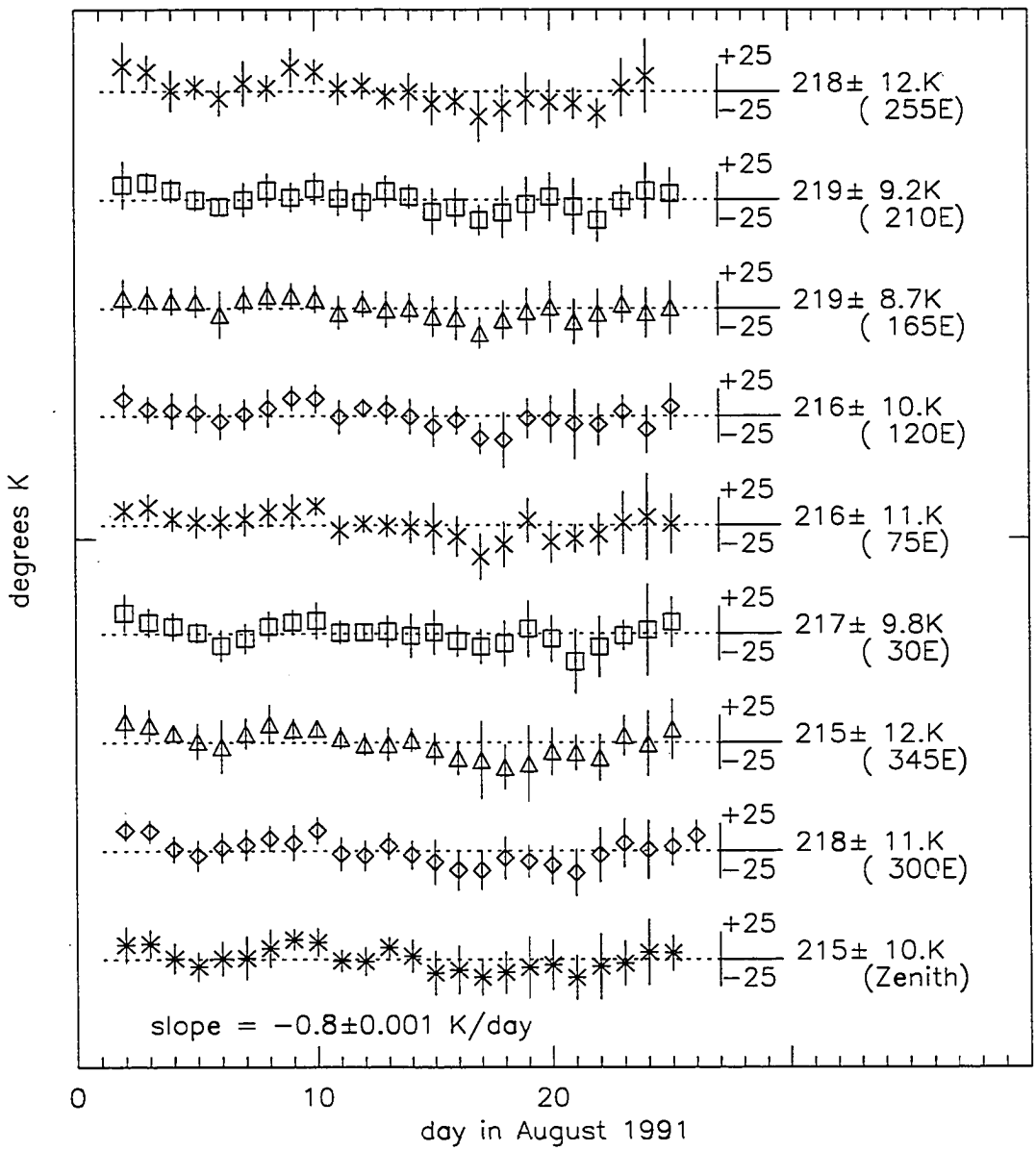

Figure 4.2.5 Daily mean Kinetic temperatures from August 2-25, 1991 As in Figure (4.2.1) but for the daily mean values. The full period mean value is indicated on the right. A straight line fit to the temperature means indicates a seasonal temperature slope of $-.8°$ K/day.

and geometrically formed the two 'dual-vector' components. I then derived the LS periodogram from each of the two orthogonal components, (30-210 and 120-300°E). These results are shown in Figure (4.2.6) for the 20-600 hour periodicities. A few differences in the spectral content can be seen. The 78 hour feature is washed out and new 2, 4 and 5 day ones appear. The most significant peaks remaining are the 9, 2.7, 2.3, and 1.8 day ones. In Figure (4.2.7) the grand arrays analyses are given for the long period region.

The short period region

The full period spectra of Figures (A.4) and (A.5) consists of five interesting peaks. The single most outstanding of these is the 10.1 $\pm$ .1 hour feature which rises above the 95% level in five panels and clearly stands out in all of them. Others are the 12.01 $\pm$ .1 hour, 11.7 $\pm$ .1 hour, 9.8 $\pm$ .08 hour, and the 8.4 $\pm$ .05 hour peaks. As in the long period region I form a single time series and derive the LS periodogram for the two orthogonal components. In Figure (4.2.8) the resulting features are the 12.5, 10.1, 9.8, 9.6, and 8.5 hour ones with the 10.1 hour significant in both panels.

From both the long and short full-period analysis it is safe to state that three zonally coherent features can be said to exist with a 95% confidence: the 10.1 hour the 9-day and the 2.3-day, with the 9 and 2.3-day ones exceeding the 99% confidence level.

The phase progression of interesting features

In Figure (4.2.10) I've plotted the progression of the derived phase and power of selected features against azimuth. In each phase panel a straight-line with the slope of a wavenumber one is graphed for comparison. It is obvious that all the periodicities in the 8.4-12.5 hour region have a negative slope implying westward phase progression around the pole. In the longer periods positive slopes dominate (eastward phase progression). In some cases (65-78 hours) no slope is indicated and a bi-level phase pattern is seen. In particular the 72 $\pm$ 4.1 hour oscillation shows a phase jump of $\approx \pi$ from the eastern hemisphere to the western hemisphere. This implies a stationary (with respect to the Earth) modulated wind pattern over the pole. It has also been suggested, (G. Fraser private communication), that this may be a standing wave, that is- a pair of zonal waves of near equal amplitudes interfering with each other. In either case this pattern has prompted further analysis. I used a student's t-test and determined that with a 99.6% probability the levels are distinctly different however, the student's t-test does not consider the uncertainties associated with the derivation of the phase values. In order to incorporate these errors I used least-squares fit to a straight line and derived a χ^2 value. From this χ^2 a "goodness-of-fit" parameter 'Q' was derived as the probability that the

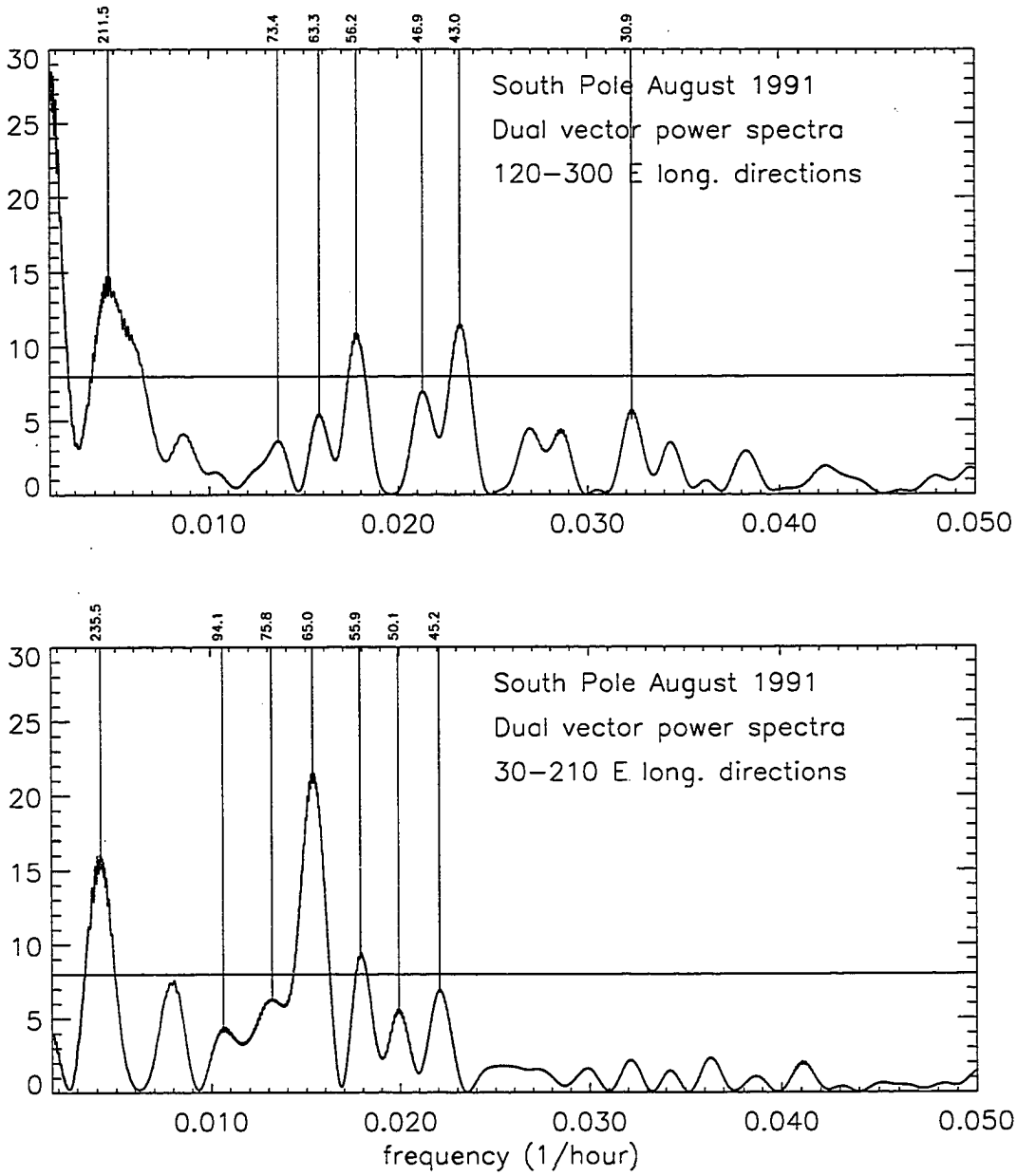

Figure 4.2.6 Planetary wave period,'Dual-vector' components of the neutral winds for August 2-25. Lomb-Scargle periodograms of the dual-vector components. Normalized power for the 120-300°E component (upper) and the 30-210°E longitude component (lower) is plotted against frequency (1/hours) for 20-600 hour periods. The 95% confidence level is shown as a horizontal line. Selected periodicities are marked (hours).

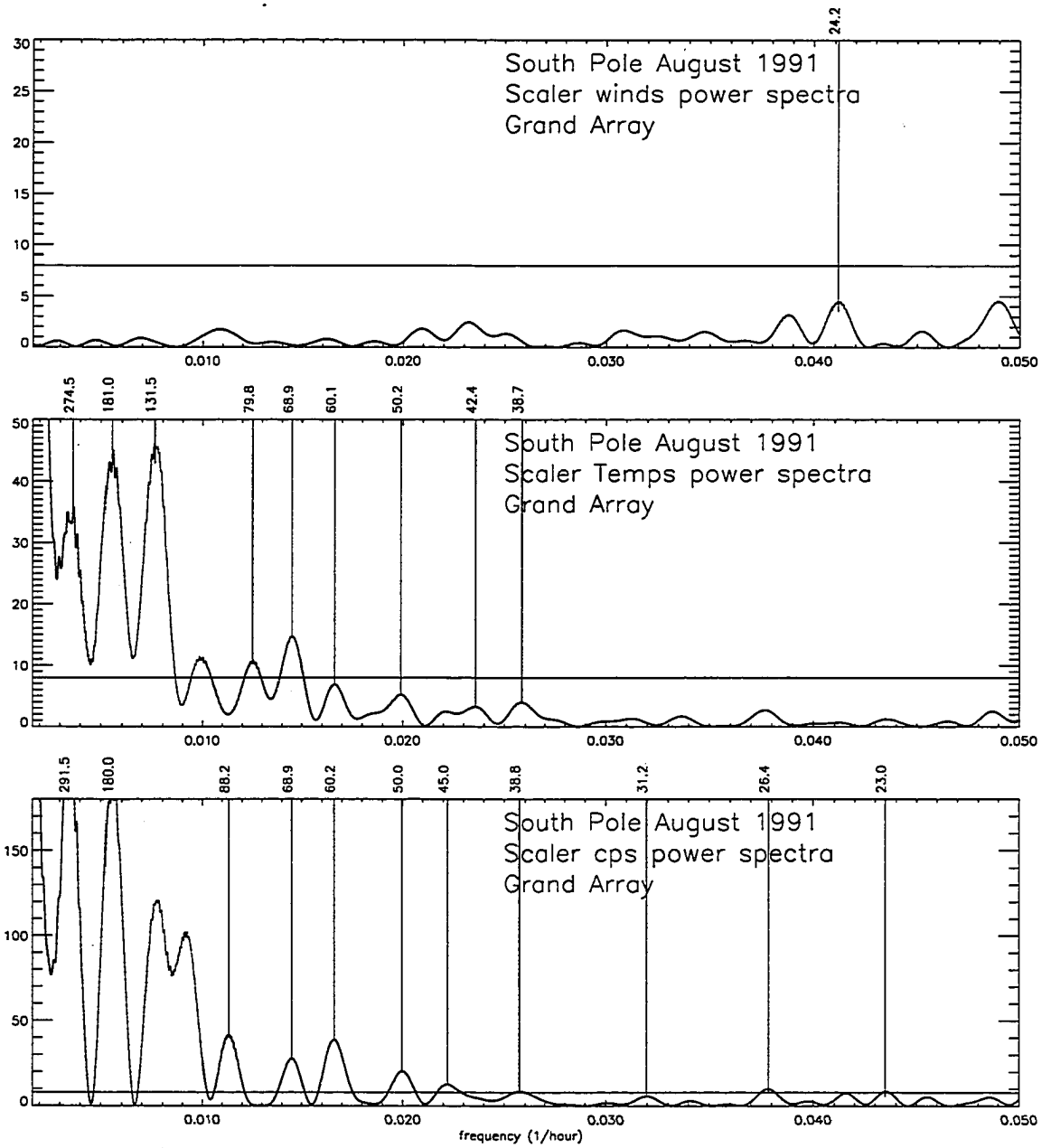

Figure 4.2.7 Grand array analysis for planetary wave structure for August 2-25 wind, temperature, and countrate Lomb-Scargle periodograms of the grand arrays. Normalized power is plotted against frequency (1/hours) for 20-600 hour periods. The 95% confidence level is shown as a horizontal line. Selected periodicities are marked (hours).

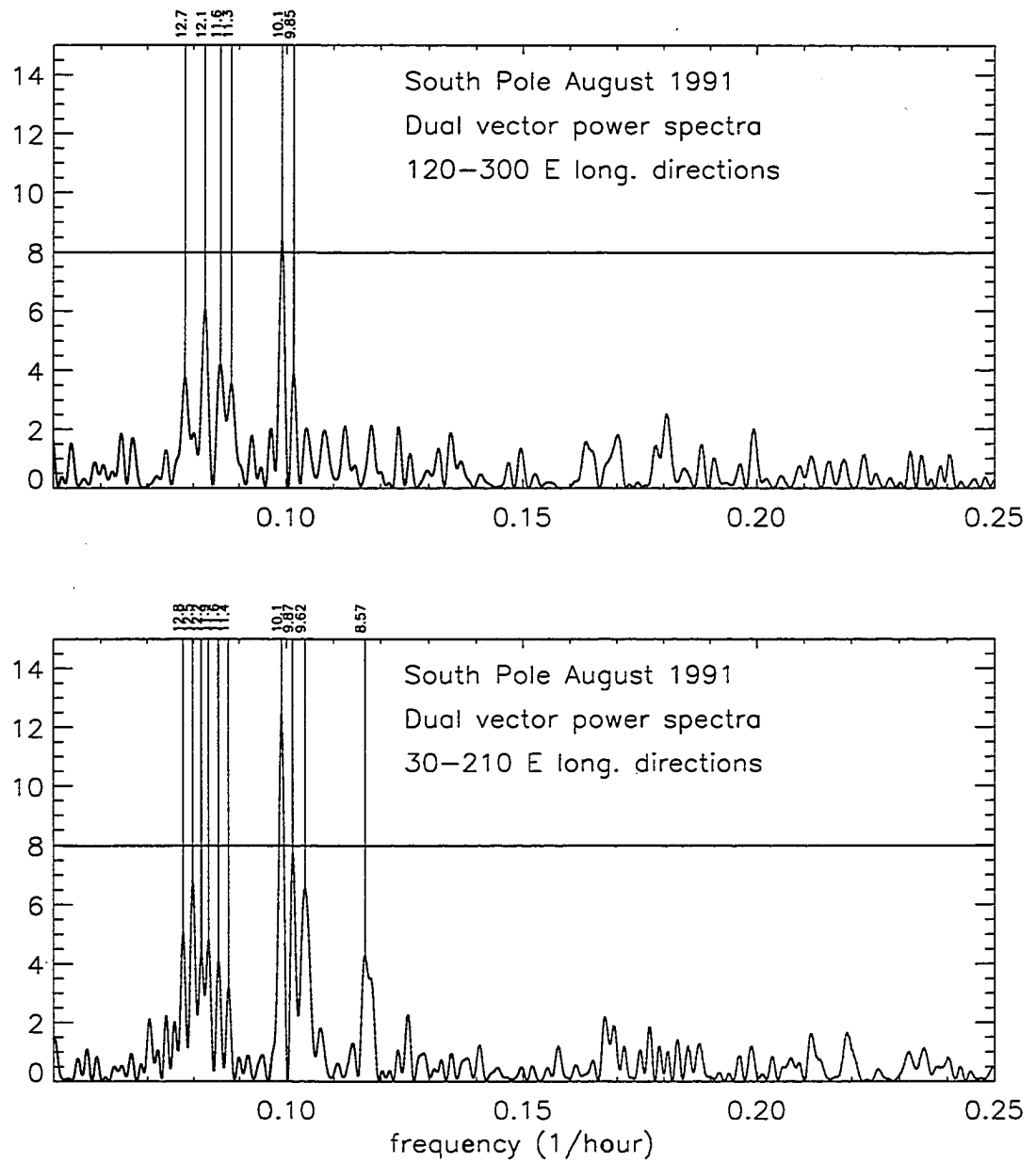

Figure 4.2.8 Near semi-diurnal period, 'Dual-vector' components of the neutral winds for August 2-25. As for Figure (4.2.6) but for the 4-20 hour periods.

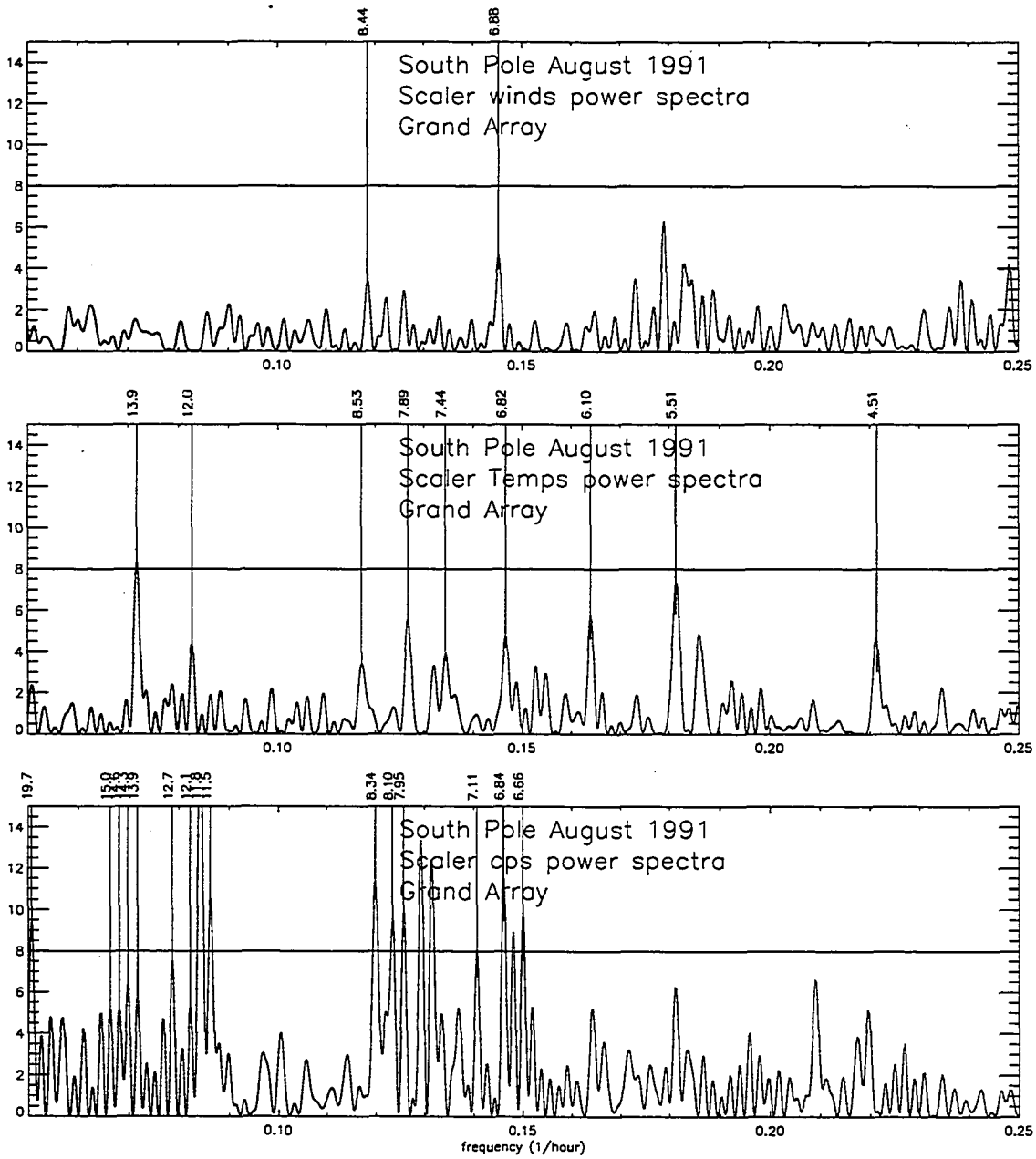

Figure 4.2.9 Grand array analyses of the near semi-diurnal period wave structure for August 2-25. As for Figure (4.2.7) but for the 4-20 hour periods.

fit would be this good by chance, (Press, 1986). A model fit is considered believable if $Q \geq .1$ and may even be acceptable for $Q \geq .001$ but are highly questionable for $Q < .001$, (Press, 1986). A straight-line fit gives $Q \sim 1.8 \times 10^{-13}$. A two step fit returns Q values of .81 and .50 (for each portion of the step) well above the value for a believable fit.

Space-Time analysis of the spectra

A large degree of azimuthal variability is shown in the power and phases plotted in the previous panels. Part of the emphasis of this work is the effort to characterize this variability. The following analysis provides a presentation which leads to an interpretation of this variability.

Recently the 10.1, ~12.2 hour, and a ~2.3-day oscillation have been reported as wavenumber one features by Hernandez et al., (1992, 1993), and Fraser et al. (1991). The other large features identified above, although they do not exceed the 95% confidence level, are nonetheless interesting since they demonstrate the azimuthal variability and thus the dynamics of the region. In fact I would expect any non-linear wave activity would affect the phase and amplitude of the waves involved perhaps to the extent where they were no longer coherent enough to be identified and thus vanish from the spectra. I now proceed with the temporal examination of the time series with a sliding time window. In Figures (4.2.11)-(4.2.13) are shown the time-dependent spectra for this period as in section 4.1.2 except I have used a 288 hour data window so as to isolate the 4, 3, 2 and 2.3-day features.

The time dependence in the short period region

In the lower panels of Figures (4.2.11)-(4.2.13) the results from the analysis of the temperature and dual-vector wind components are shown for the short period group.

In the temperatures I note a 12 hour modulation which appears as a sideways 'V' interference pattern pointing towards the long periods. This 'V' pattern appears vertically centered near hour 280. This pattern is an artifact of the fitting technique.

There is a lack of thermal activity around the 10 hour region. Near the semi-diurnal period two distinct peaks, the 12 and 13 hour features, diminish around hour 260 and coalesce into a 12.5 hour feature. Several of these thermal features are enhanced after hour 260, including a 14 hour one.

In the 30-210 E longitude directions wind components three features are obvious as streaks of red, one near 10 hours, one near 9.9 hours, and one near 8.5 hours. Also near the end of the period near hour 400 three ~semi-diurnal features appear at ~11.7, 12.2,

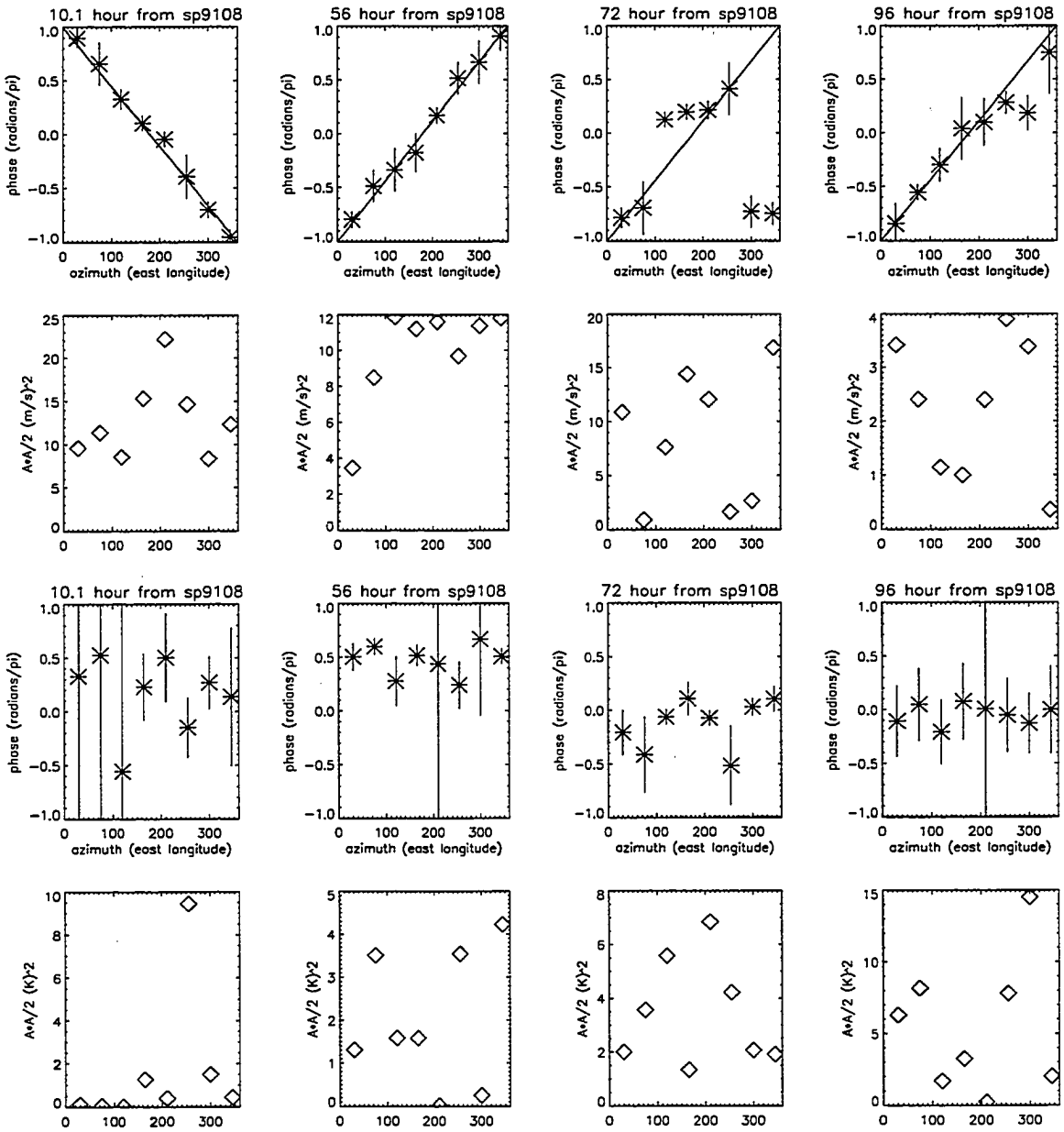

Figure 4.2.10 Wave-number analysis for selected features from the full period spectra for August 2-25. The azimuthal phase dependence for the neutral wind (first, or top, row) are shown with a wavenumber one progression (solid line) drawn for reference. The phase dependence for the temperature is shown in the third row. The associated derived power from the harmonic fits for each azimuth are shown in second/fourth row for the wind/temperature fit. The 10.1, 56, 72, and 96 hour oscillation wavenumber analyses are shown in this figure.

and 12.5 hours. Also a low power feature appears near 14 hours around the same time. I draw attention to the variable relative separation between the three prominent streaks.

The 120-300 E longitude component is quite different from those at 30-210 E. The 10 hour streak is not as prominent and weakens in the middle of the period. However there is also a very weak 9.8 hour feature which bows out around hour 290 when the 10 hour oscillation weakens, as in the 30-210 E longitude directions panel. Near the end of the period the same features as in the 30-210 E longitude directions are present, namely the 9.8, 10, 11.7, 12.2, and 12.7 hour ones.

The time dependence in the long period region

In the upper panels of Figures (4.2.11)-(4.2.13) the full period results from the analysis of the temperature and dual-vector wind components are shown. There is a broad band of thermal activity centered on 9 days. Around hour 202 this feature narrows and shifts into a band which spans 10-12.5 days. This band almost disappears near hour 320 but is re-enhanced slightly as it spreads back out to 10 days and continues to the end of the period. Also near hour 202 a 4-day thermal response increases in power and shifts first towards 5-days where it is enhanced and then back to 4.5 days where it weakens and continues to shift to 4-days where it is again enhanced. The end of this 6-day cycle, near hour 280, is accompanied by an $\approx$3-day enhancement in a 3-day thermal oscillation. Near the end of the period coincident with the re-enhancement of the long period band the 4-day feature reappears and lasts to the end of the period.

In the 30-210 E longitude directions a clear 'Y' shaped feature begins as a 60-80 hour band which shifts to a 63-85 hour band near hour 170. This continues until hour 288 when the feature separates. The left channel retains its power level and settles into the higher frequency near a 2.4-day period. The right channel is more variable as it moves through lower and lower frequencies, rebrightens near the 4-day period then decays off into the 4.7-day period. In the longer periods the broad band at 10-12 days spreads into higher frequencies, spanning the 6-12 day range. This expansion remains until hour 260 where it spreads further to almost 5-days and then quickly retreats to the 9-day period when the 'Y' splits. Here the band remains until hour 320 when it almost vanishes. This broad band resumes where it left off about 30 hours later and continues until the end of the period. This feature has two enhancements; one prior to the splitting of the 'Y' and its first retreat and the other prior to its second retreat and subsequent near extinction. Another interesting correlation is the absence of power in the $\sim$25-35 hour periods when the base of the 'Y' is broadest and the broad band is extended to the highest frequencies.

The 120-300E component is very different from the other component. The broadband spreads more quickly to the 5-day periods and remains there until hour 288 where the long period portion diminishes leaving a 6-9 day band. This band itself diminishes near hour 370 and as in the other component re-enhances after about 30 hours. Two other features at 1.9 and 2.3-days begin the period strong, weaken, and coalesce. Eventually around hour 290 this coalesced feature separates to spawn the 2.3-day feature. The 2.3-day is enhanced as the longer period broadband feature decays and 3 and 4-day features appear. These 2.3 and 3-day diminish and the 4-day broadens to the 3.3-4 day range and eventually decays as the broadband feature becomes re-enhanced.

The 3-day feature in the planetary period region

At the center of the 'Y' in Figure (4.2.12) is the 3-day oscillation, this deserves a closer examination. I will also look at the other features in this pattern, that is, the 4-day and 2.3-day.

Recall that the phase progression for the 3-day wave showed a stationary phase pattern. In Figure (4.2.14) I show the *all-azimuth* analysis for this 72±9 hour oscillation. Also recall that when referring to significance for the harmonic fits I am referring to amplitude above the 2σ level as derived in section 3.3.2. This is the result of an harmonic fit (amplitude and phase) of 4 cycles in the 288 hour window. In the upper right panel the wind amplitude is significant throughout the first 2/3 of the period in almost all directions and is strongest in the 30-210 E longitude directions directions (parallel and anti-parallel to the mean wind). Most of the significant amplitude is just west of the mean wind directions.

In the lower right panel the fitted phase for the wind has a jump near the N and S azimuths throughout most of the period with ~constant phases before and after the jump as seen in top row, third column panel of Figure (4.2.10).

In Figure (4.2.14) I find that the 3-day wind oscillation changes with the derived mean wind. The mean wind remains in the 75°E azimuth for the first 2/3 of the period then shifts 90° westward to 345°E, increases in magnitude to $\approx$ 8 m/s and persists at this elevated value to the end of the period. Coincident with the change in direction of the mean wind is a westward shift of the wind harmonic amplitude maxima about 90° and a decrease in the amplitude. Furthermore, during and after the shift, the wind phase has more of a sloped appearance (reduced bi-level pattern).

The 3-day temperature oscillation is enhanced when the derived mean wind changes directions. The temperature amplitude behaves similarly before and after the shift.

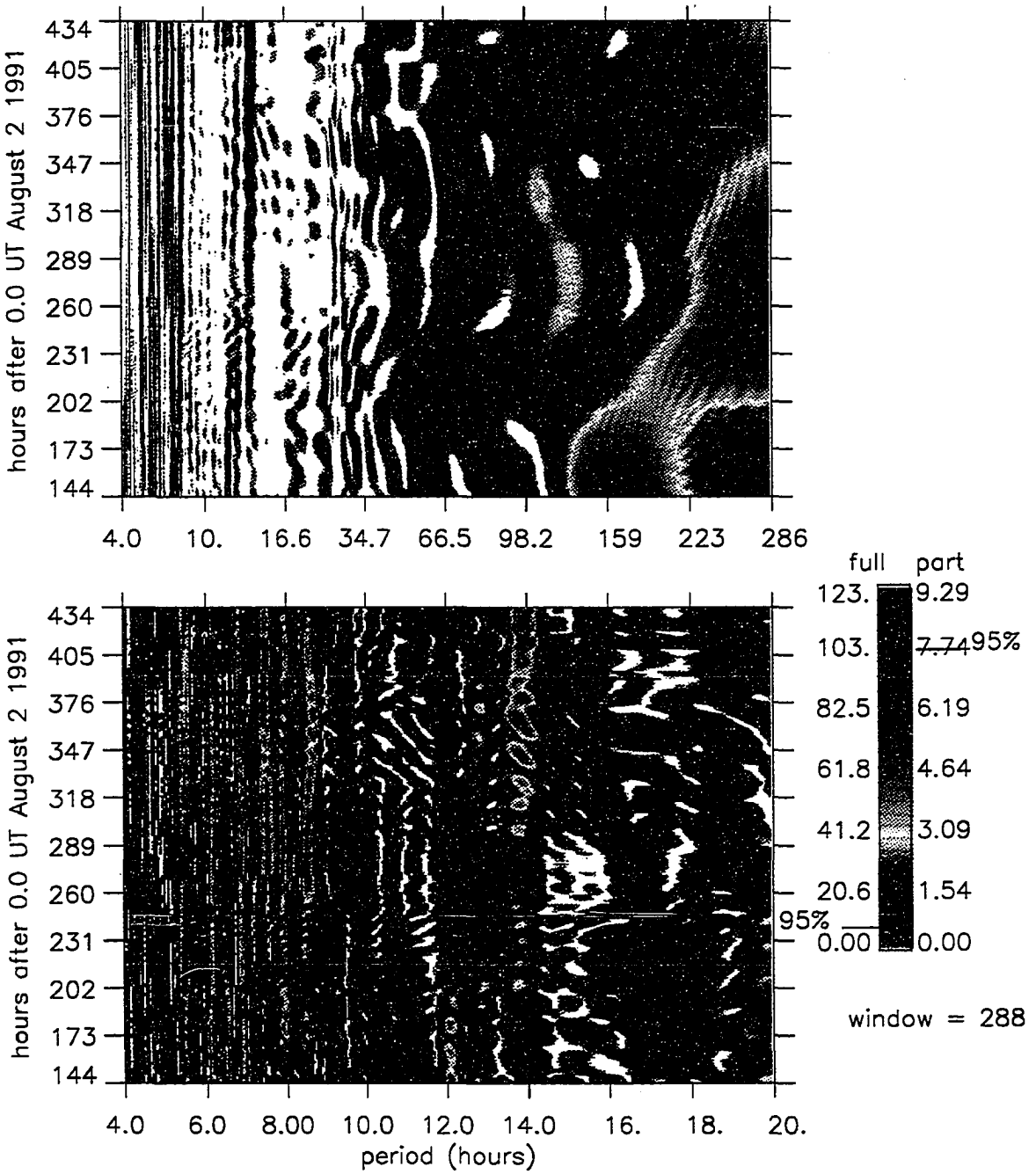

Figure 4.2.11 Time dependent grand array analyses for the temperature structure from August 2-25. As for Figure (4.1.7) with a sliding window of 288 hours. The upper panel is the spectral range from 4 hours to 1/2 the data period (286 hours). The lower panel is the spectral range from 4-20 hours.

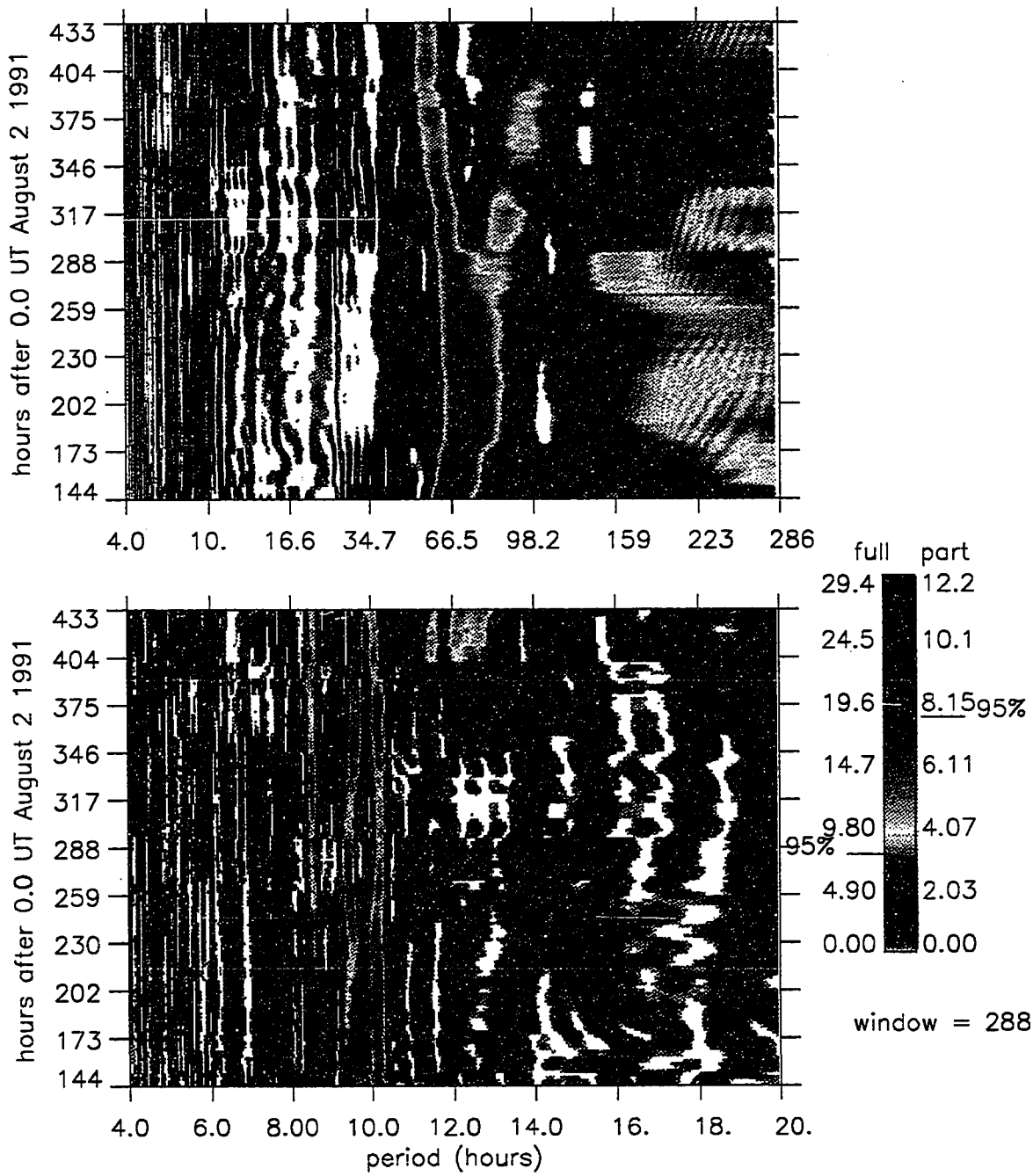

Figure 4.2.12 Time dependent 'dual-vector' wind structure from August 2-25, 1991 for the 30-210°E azimuths. , as in Figure (4.2.11). Note the branching of a 72 hour spectral feature into two new features which drift apart to form a 56 and 96 hour features.

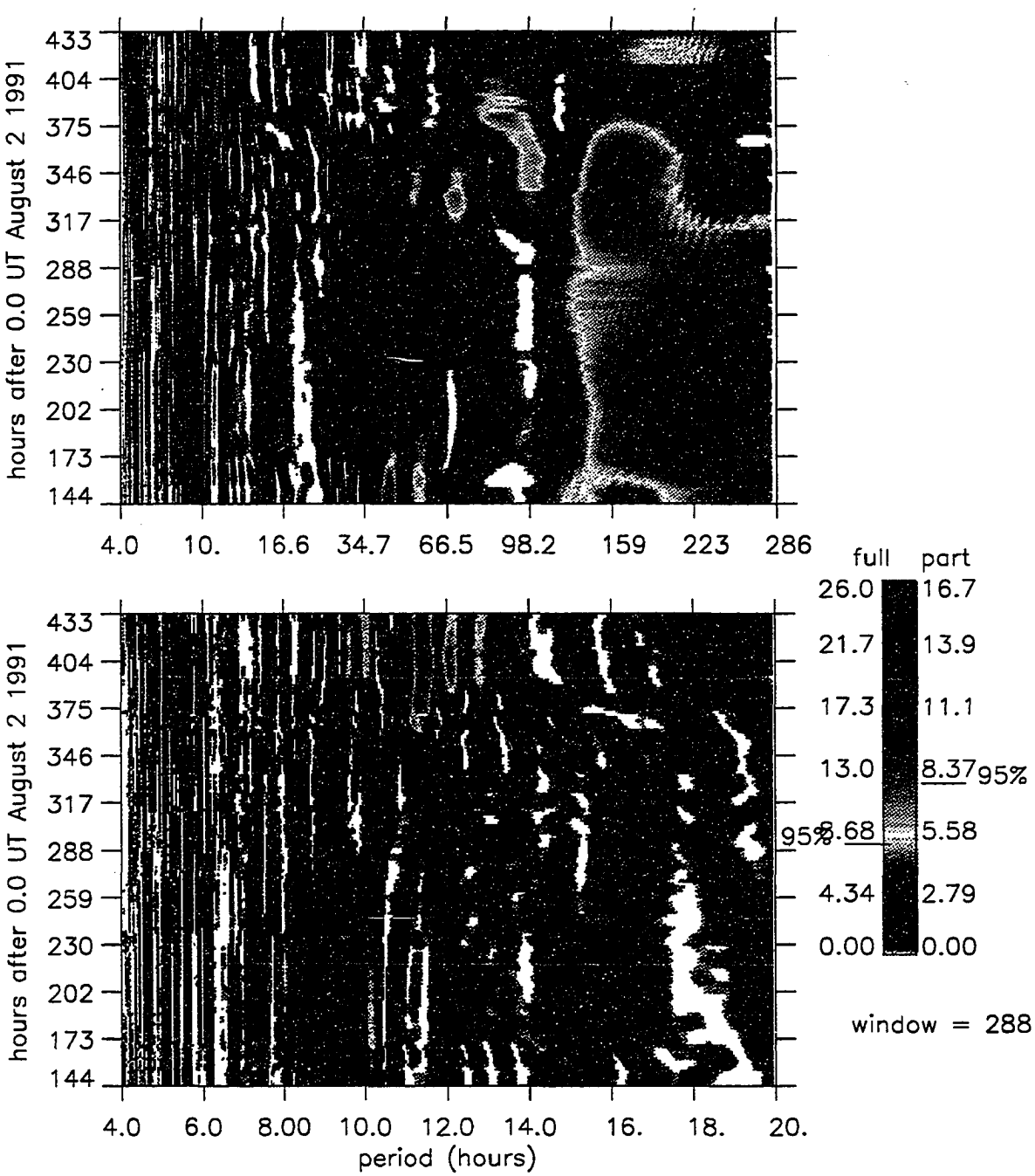

Figure 4.2.13 Time dependent 'dual-vector' wind structure from August 2-25 for the 120-300°E azimuths. As in Figure (4.2.11).

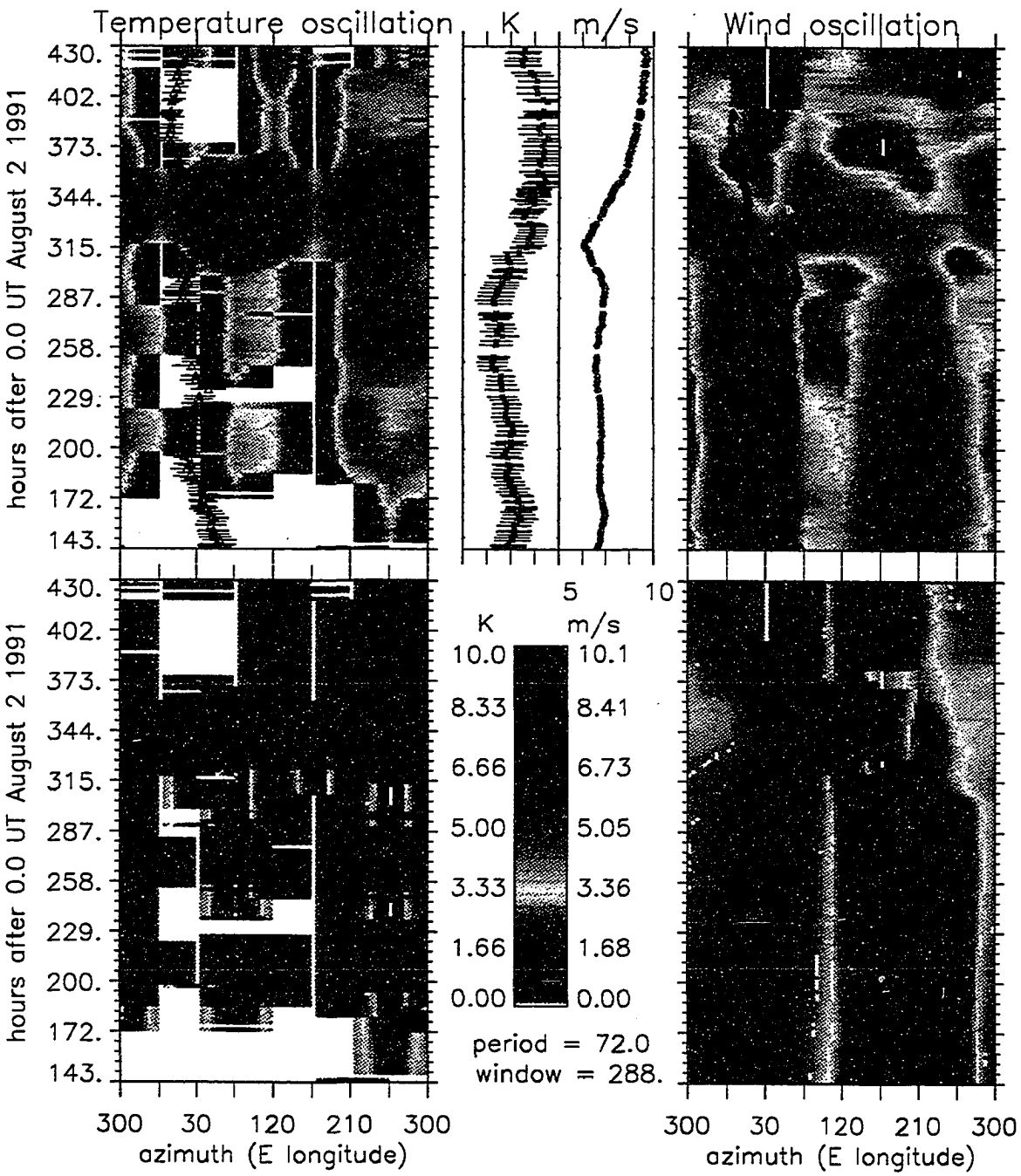

Figure 4.2.14 *All-azimuth* time dependent results for the 3-day oscillation amplitudes and phases derived from the harmonic fit to the time series in a 288 hour sliding window. As for Figure (3.3.7).

During the mean wind shift the temperature amplitude is enhanced in the azimuths where the wind amplitude is decreasing.

In the center panel of Figure (4.2.14) I show that the thermal gradient direction crosses the mean wind direction. The direction of the thermal gradient (hot $\rightarrow$ cold) drifts slowly about 45° from just west of the mean wind direction to just east of it. The thermal wind relation indicates a geostrophic wind to the west of this gradient, in agreement with the latter part of this period.

The changes of thermal gradient magnitude lead those of the mean wind amplitude by about 1.8 days. The minimum (around hour 276) and subsequent rise in the magnitude of the thermal gradient precedes the minimum (around hour 320) of the mean wind magnitude. The maximum for the linear thermal gradient magnitude scale is the indicated max in K.

The time evolution of the actual fit as described in section 3.3.3 for a *single-azimuth* demonstrates the relative analytical response for each time series, that is, the relative amplitude and phase shifts between the wind and temperature fits. If the fits accurately represent the physical waves in the sky the phase relation between the two wave fields can be examined. Unencumbered by statistical significance the harmonic fit time dependence is displayed in Figures (4.2.15)-(4.2.18). In these figures I plot the actual fit amplitude directly below the time series region to which it has been fitted. The fits for two pairs of opposing azimuths are displayed. A time reference (dashed line) at the period midpoint is overdrawn in each figure. The difference $\Delta\phi(t_j, az) = \phi_w(t_j, az) - \phi_T(t_j, az)$ between the fitted phase is plotted in the center of the figures in units of π, ($-\pi$ being on the left and $+\pi$ on the right).

From these figures the following observations are made. A temperature harmonic amplitude enhancement occurs in all azimuths during the so-called dissipation region. Regular quasi 2-3 day amplitude variations occur in the temperature amplitude of most azimuths. The harmonic winds in opposite azimuths are out of phase and of comparable amplitude. Thus the relative phase $\Delta\phi(t_j, az)$ is $\pm\pi$ different in opposite directions. Although the relative phase between different azimuths is somewhat arbitrary it is also observed that with the exception of the NE and SW directions, where the temperature fit is quite variable, the $+\pi$ applies to the N-NE-E-SE semi-circle and the $-\pi$ value to the other half-circle. The harmonic temperatures in opposite azimuths are in phase and of comparable amplitude. Before the dissipation and when the fits are steady (least variable) the phase differences between the thermal and kinetic cycles are $\sim \pm\frac{\pi}{2}$ as in

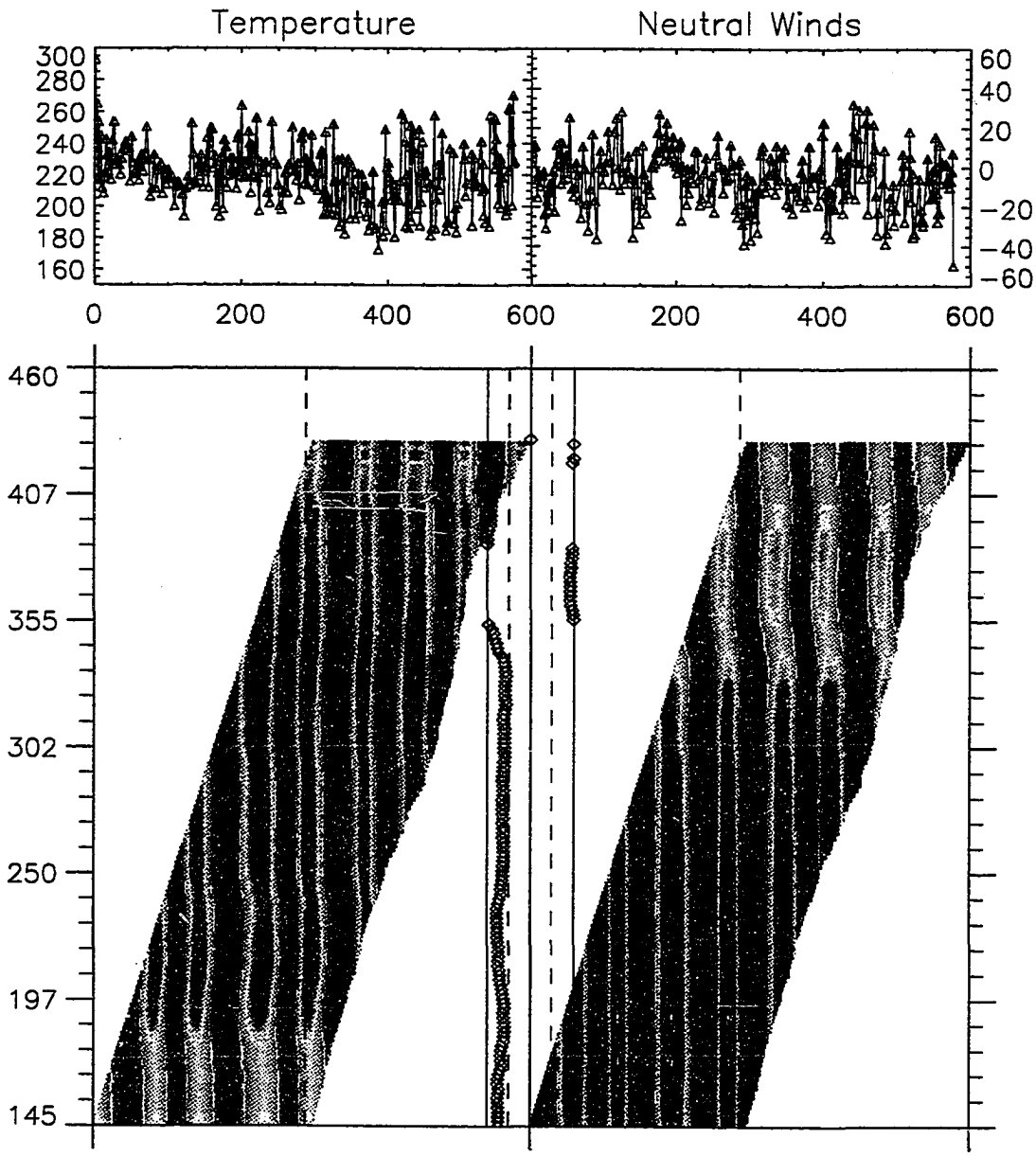

Figure 4.2.15 *Single-azimuth* (210°E) harmonic fit stacked plots for the 3-day oscillation of August 2-25. Format as in Figure (3.3.9). Results for the 210°E direction using a 288 hour sliding window are shown. Note the $\frac{\pi}{2}$ relative phase prior to the branching and $\pm\pi$ afterwards.

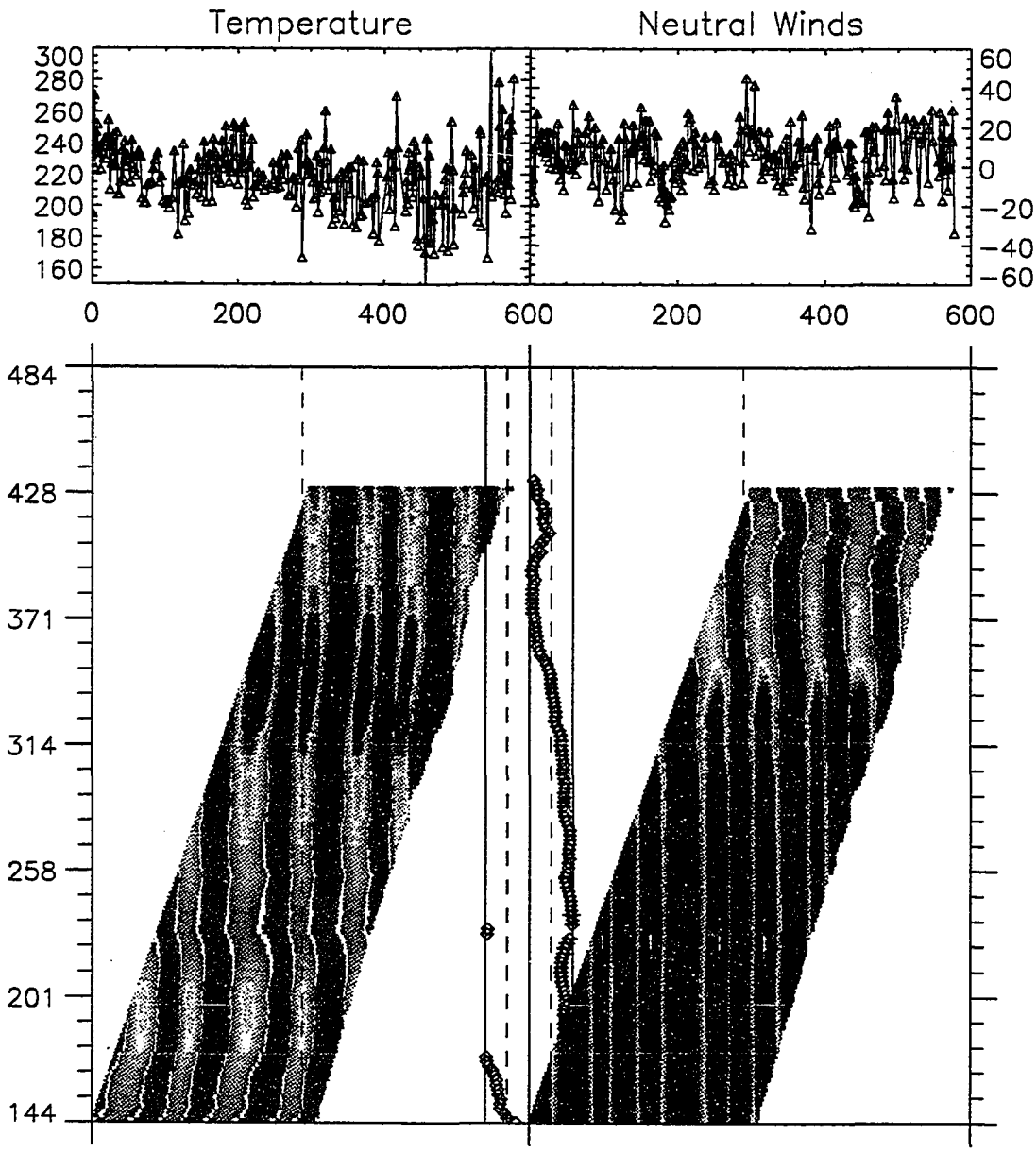

Figure 4.2.16 *Single-azimuth*(30°E) harmonic fit stacked plots for the 3-day oscillation of August 2-25. Format as in Figure (3.3.9). Results for the 30°E direction with the 288 hour sliding window.

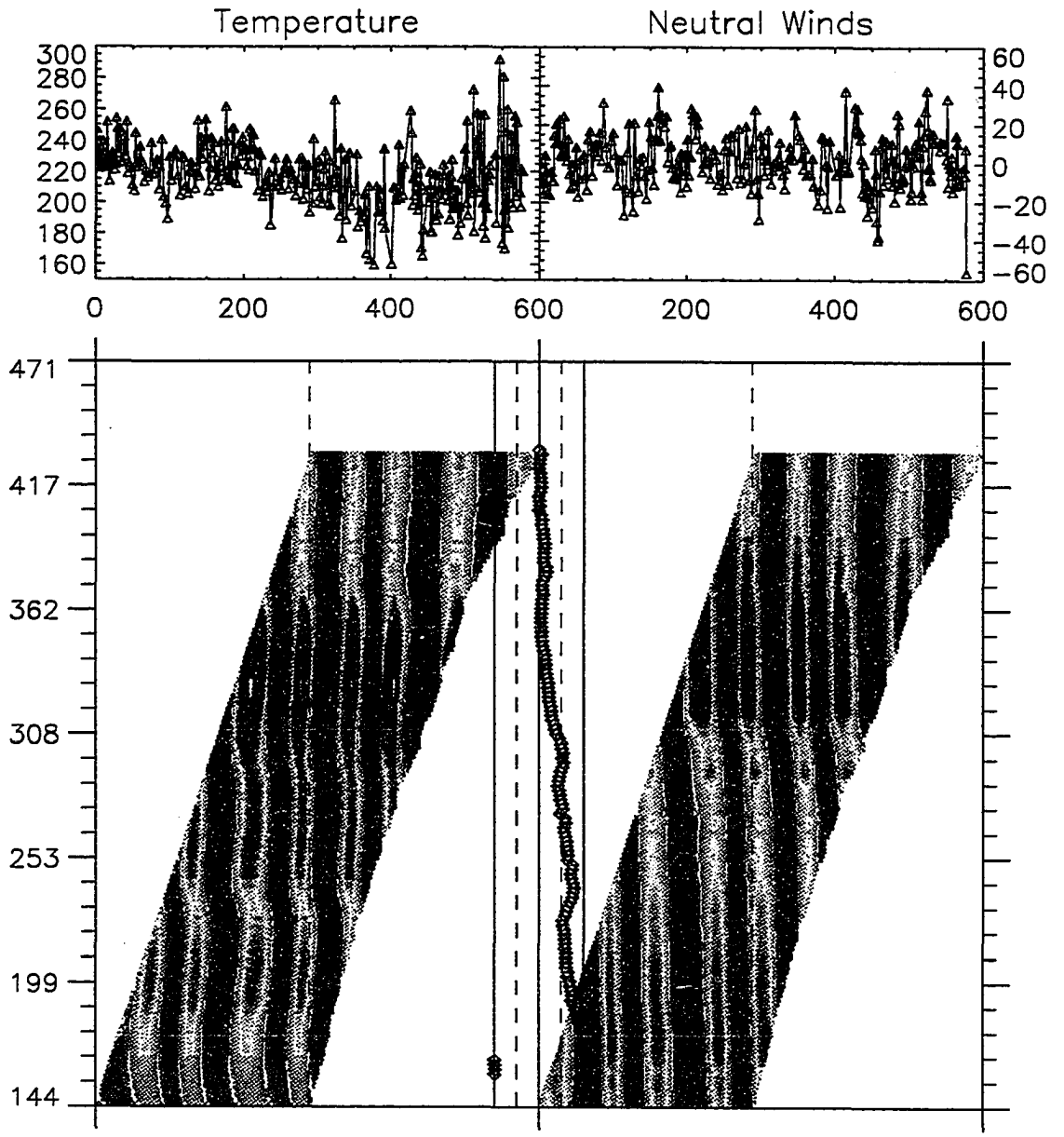

Figure 4.2.17 *Single-azimuth*(75°E) harmonic fit stacked plots for the 3-day oscillation of August 2-25. Format as in Figure (3.3.9). Results for the 75°E direction with the 288 hour sliding window.

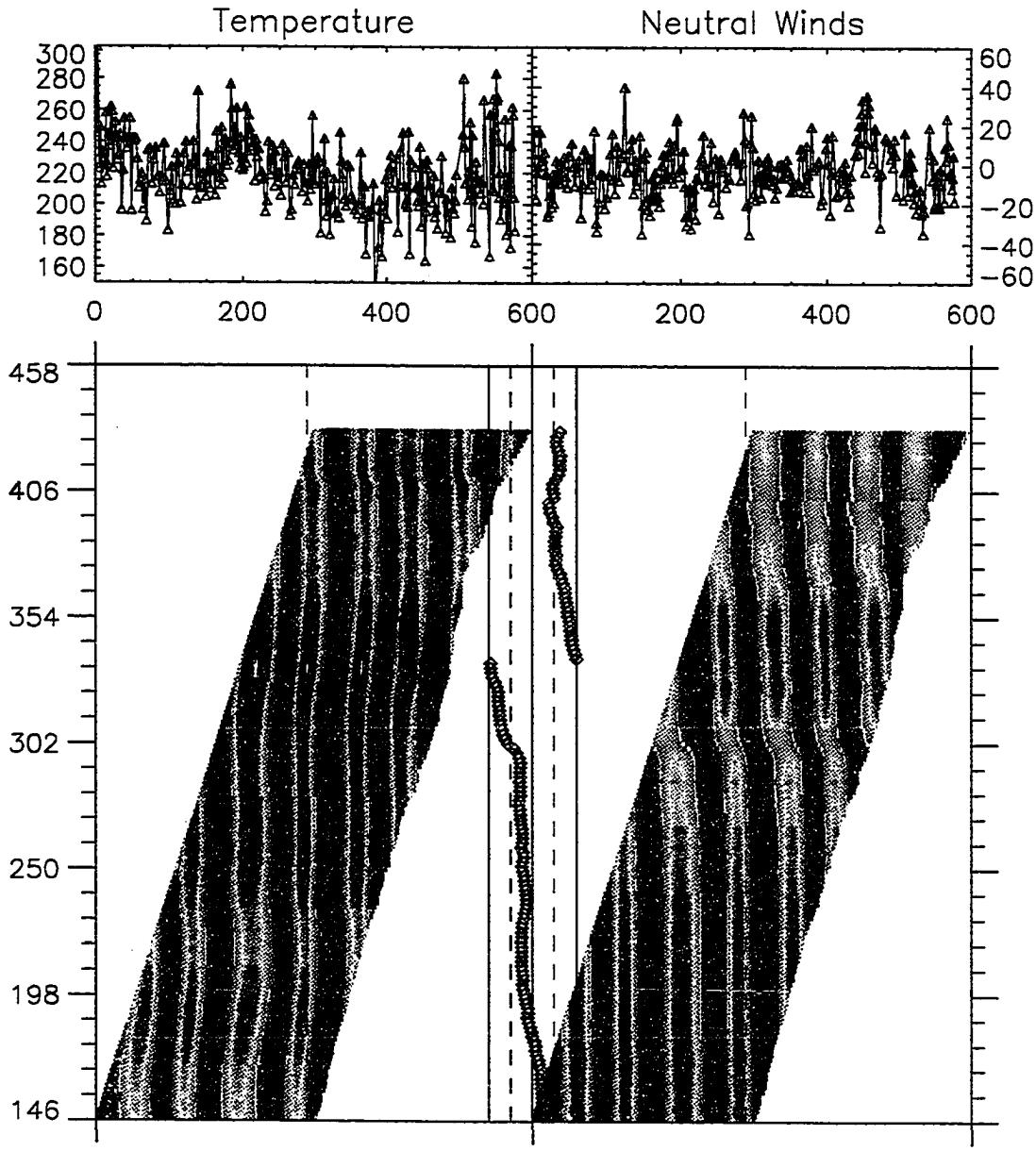

Figure 4.2.18 *Single-azimuth*(255°E) harmonic fit stacked plots for the 3-day oscillation of August 2-25. Format as in Figure (3.3.9). Results for the 255°E direction with the 288 hour sliding window.

Figure (4.2.15) from the beginning of the period until hour 330. And again the $\sim +\frac{\pi}{2}$ applies to the N-SE hemisphere and the $\sim -\frac{\pi}{2}$ to the S-NW one. During the harmonic amplitude decrease, when the mean wind direction swings from SE through the E the wind phase is retarded in these directions (SE-NW and 30-210 E longitude directions) and advanced in the others (NE-SW and N-S). Furthermore $\Delta\phi(t_j, az) \rightarrow 0$ in the SE hemisphere (parallel to the mean wind) and to $\pm\pi$ in the NW hemisphere, (against the wind). Thus it appears from the foregoing observations that there is a $\sim \frac{\pi}{2}$ phase difference between neutral wind and kinetic temperature oscillations which changes by $\sim \frac{\pi}{2}$, putting them directly in or out of phase, at the same time that the neutral wind amplitude decreases.

The 4-day feature in the planetary period region

In Figure (4.2.19) the analysis for the 96 $\pm$ 18 hour periodicity is shown. These panels show some similar features as the 3-day ones just discussed. The temperature enhancement is in the same azimuths and of the same amplitude and prior to this the most significant thermal amplitudes are in the north. The temperature phase is constant in this period of enhancement. The wind amplitude begins to rise in the 30-210 E longitude directions prior to the mean wind change in direction and the thermal event. At the onset of the mean wind change the significant thermal amplitude appears to spread eastward, increase in magnitude, and continue until the end of the period. The wind phase panels show mostly wavenumber one with one max, one min and a gradual change. After the amplitude increase it shows a clear wavenumber one behavior.

The 2.3-day feature in the planetary period region

In Figure (4.2.20) the analysis for the 56 $\pm$ 5.5 hours is shown. This is one of the most significant and persistent features in the spectrum. It shows wind amplitude in almost all directions throughout the period. This amplitude is enhanced in the N-NE and S-SW directions as the mean wind changes and this enhancement spreads eastward into the 30-210 E longitude azimuths. At the onset of the mean wind change the temperature amplitude is also enhanced in the E, SE, and S directions and ceases after the wind settles into the NE. The wind phase is wavenumber one and appears to have a phase shift at the time of the mean wind change.

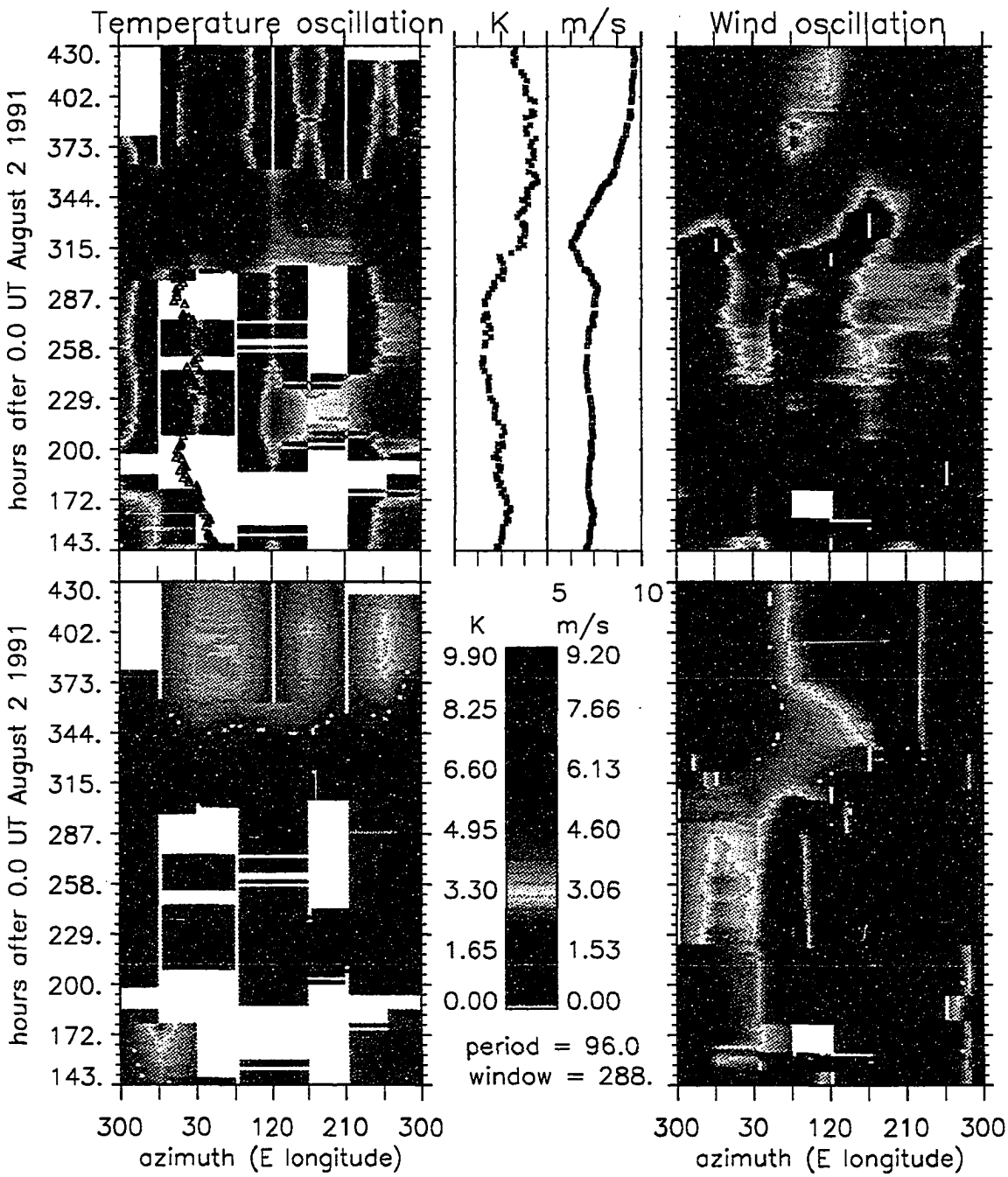

Figure 4.2.19 *All-azimuth* time dependent results for the 4-day oscillation amplitudes and phases derived from the harmonic fit to the time series in a 288 hour sliding window. As for Figure (3.3.7).

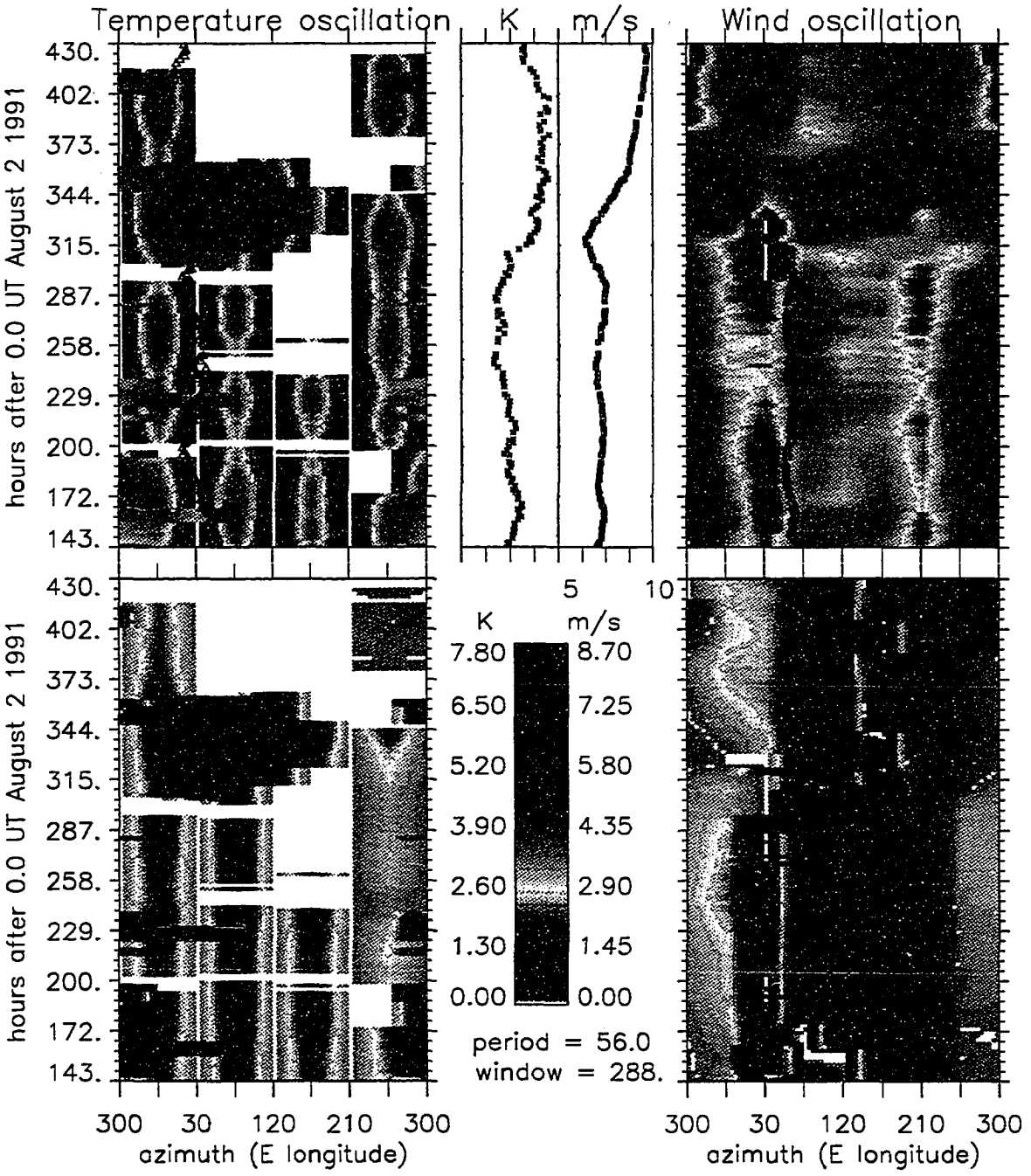

Figure 4.2.20 *All-azimuth* time dependent results for the 2.3-day oscillation amplitudes and phases derived from the harmonic fit to the time series in a 288 hour sliding window. As for Figure (3.3.7).

4.3.1 Results from the 1992 period: the time series

In Figures (4.3.1), (4.3.2), and (4.3.3) the Doppler winds, kinetic temperatures, and relative intensities for July 1-13, 1992 are shown.

This period is broken up with 6 periods of bad weather and during half the period the moon is up.

Compared with the previous two seasons the wind amplitudes are small. The Doppler winds derived from opposing directions (those separated by 180°) are anti-correlated. These anti-correlations are generally aligned between W-NW-N-NE and the SW-S-SE-E semi-circles. The temperature series are generally correlated in all directions. The period mean countrate is $\approx$ 50cps and is highest in the N-W at 53 cps. The intensity is depressed during the poor weather period. All directions appear well correlated as with the temperature series.

In the winds there is a long $\sim$80 hour oscillation in the first 150 hours which is admittedly difficult to see. An increase in the uncertainties after hour 160 can be seen as well as gaps in the series which are discussed below. The zenith winds are small and show no apparent structure.

In Figure (4.3.4) the daily mean winds are shown for all directions and in Figure (4.3.5) those for the daily mean kinetic temperatures is given as for the 1991 period. From the daily means the temperature appears to have a 10-day 10°K amplitude oscillation. The temperatures are lowest in the middle of the period around hours 100-200. The temperatures and countrates are correlated.

The countrate time series shows the effects of the moon in the later third of the period with an elevated countrate. There are diurnal peaks in the countrates which travel westward. The amplitude of the peak increases from 0900 July 5 when the lunar depression angle was $\sim$ 0° and the moon was 30% illuminated, through July 12 when the angle was near 23° with the disk 90% illuminated. The solar depression for this time of the year was $\approx$ 18° and should not illuminate the atmosphere below about 500km. In the zenith the countrate increases steadily after moonrise. The observed gaps at the peak centers are due to the rejection of the derived parameters based on a goodness-of-fit parameter which is a measure of the resolvability of the doublet. The seasonal mean intensity with the spikes is $\approx$ 70cps, ignoring the spikes the mean is 50 cps, in agreement

with the 1991 values. Again the mean seasonal countrate shows the North-West direction to be on average the highest.

4.3.2 Results from the 1992 period: Spectral content of the time series

The spectra for this season is shown in Figures (A.10)-(A.15) for the full period neutral wind, kinetic temperature, relative intensity. Again I note the differences between the panels indicating the asymmetry.

In Figures (A.10) and (A.11) many peaks rise above the 95% confidence level and these wind panels show larger SNR than those of the 1991 season. The most significant spectral features in the planetary range are the ~9, 4.9, 4.2, 3.4, 2.6, 1.8, 1.4, and 1.25 days and in the semi-diurnal range the ~11.7, 10.5, 9.9, and 9 hour peaks are largest.

In general the E-W azimuths, (directions parallel and anti-parallel to the mean wind, see Figure (4.3.13)), have the most structure also those azimuths just north of these, to the left of the mean wind direction, have increased structure. I also note that the 9, 4.9, 2.6, and 1.8 day peaks fall off in descending amplitude.

In the temperature spectra shown in Figures (A.12) and (A.13) some peaks associated with those of the winds are seen and the strongest of these are the 9, 5, 3.7, and 2.7-day periods. Also there are 1.8 and 1.2-day features in some panels. In the short period region ~11.6, 10.5-9.9, and 7.4 hour peaks are present.

The countrate spectra in Figures (A.14) and (A.15) show little azimuthal asymmetry. The diurnal with harmonics and sub-harmonics are present as ~ 8, 4.2, 3.3, 1.8, 1, .5, and .3 days. In addition to these the 2.7-day is also present and with the exception of the diurnal feature in the S only those features with periods longer than 2.7-day are above the significance level.

In Figure (4.3.6) the dual-vector analysis is shown for this period. In the top panel the planetary range for N-S component is seen to have the first eight peaks above the 95% confidence level. These are the 9.5, 5, 3.3, 2.7, 2, 1.6, and 1.4 day peaks as was found for the individual panels in appendix 1. These are also quite broad features as indicated in the asymmetry found in the single azimuth panels. In the bottom panel a single very broad feature is found which also exceeds the 95% level. Within this feature, especially significant peaks at 8 and 5 days can be seen.

In Figure (4.3.7) the analysis for the grand arrays is shown. In the top panel for the winds I am surprised to find a wavenumber zero feature near 1.3-days and I again I find

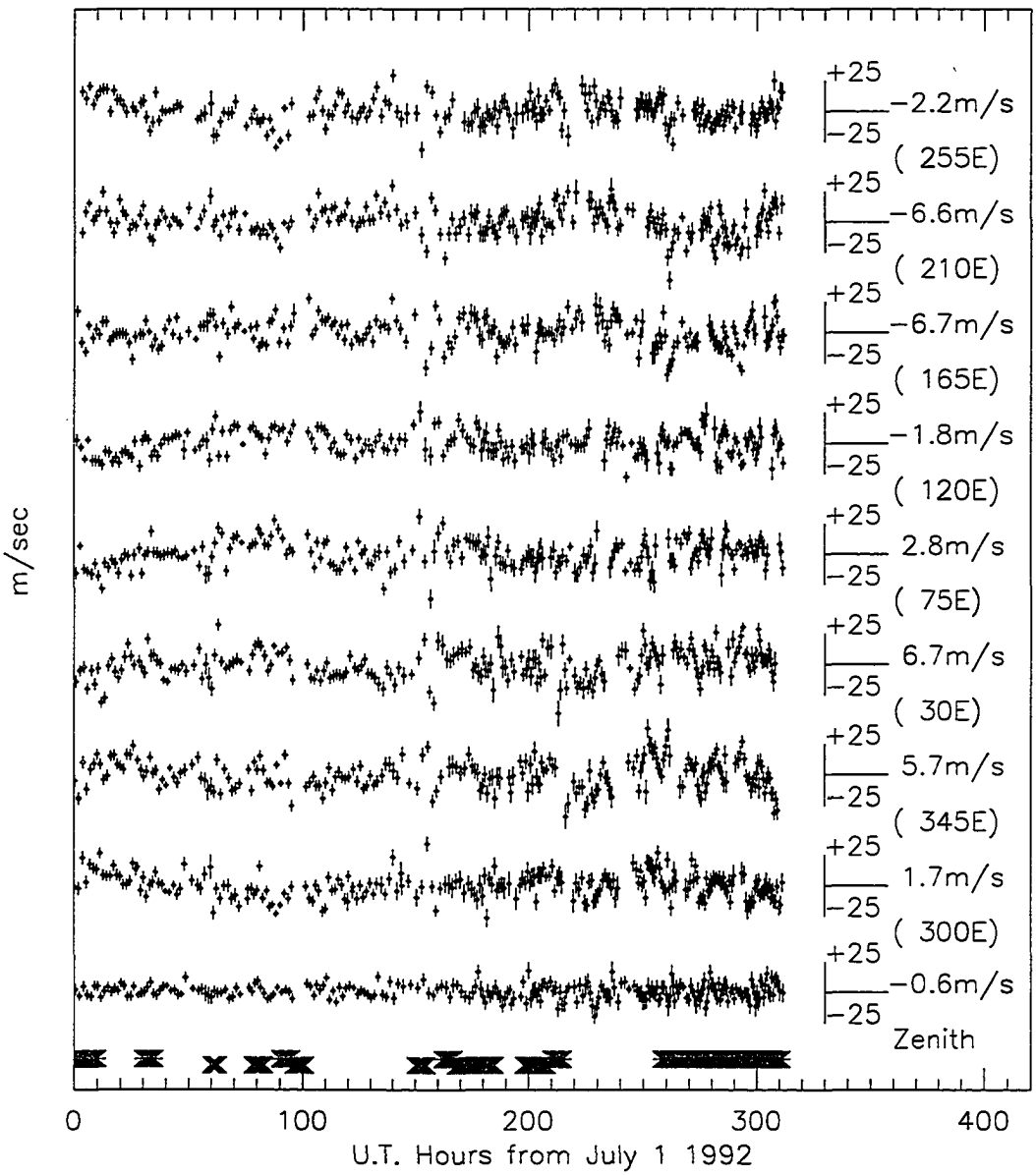

Figure 4.3.1 Doppler winds from July 1-13, 1992 derived from OH(6-2) emissions at 8399Å over South pole station for the eight different azimuths and the zenith measurements. The fluctuations about the mean wind value are shown. The mean and the azimuth for each series is indicated on the right. Each azimuth has its own vertical axis in m/s. Error bars are derived from propagation of counting statistics errors through the non-linear least-squares fit.

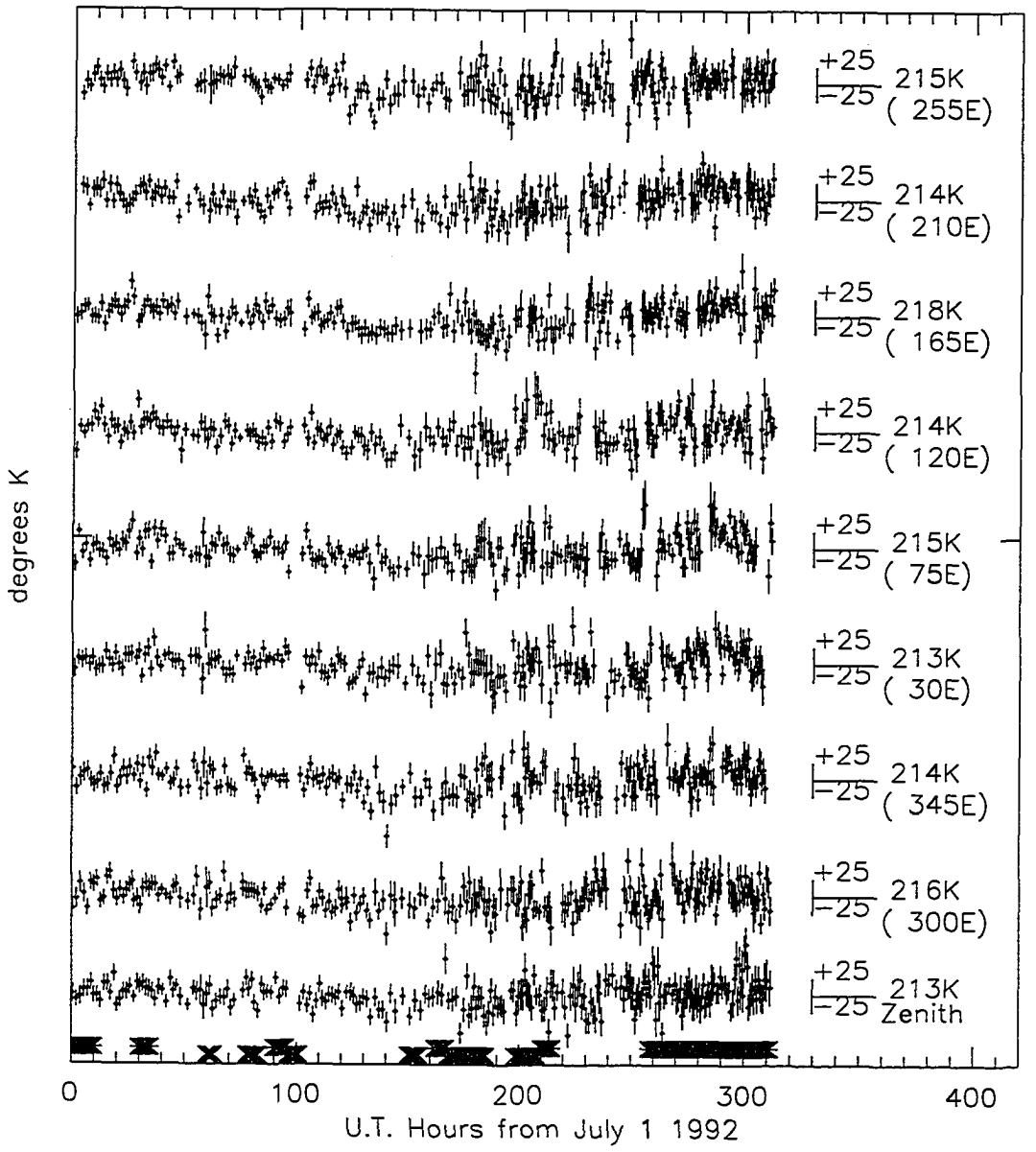

Figure 4.3.2 Kinetic temperatures from July 1-13, 1992 , as in Figure (4.3.1) but for the temperature.

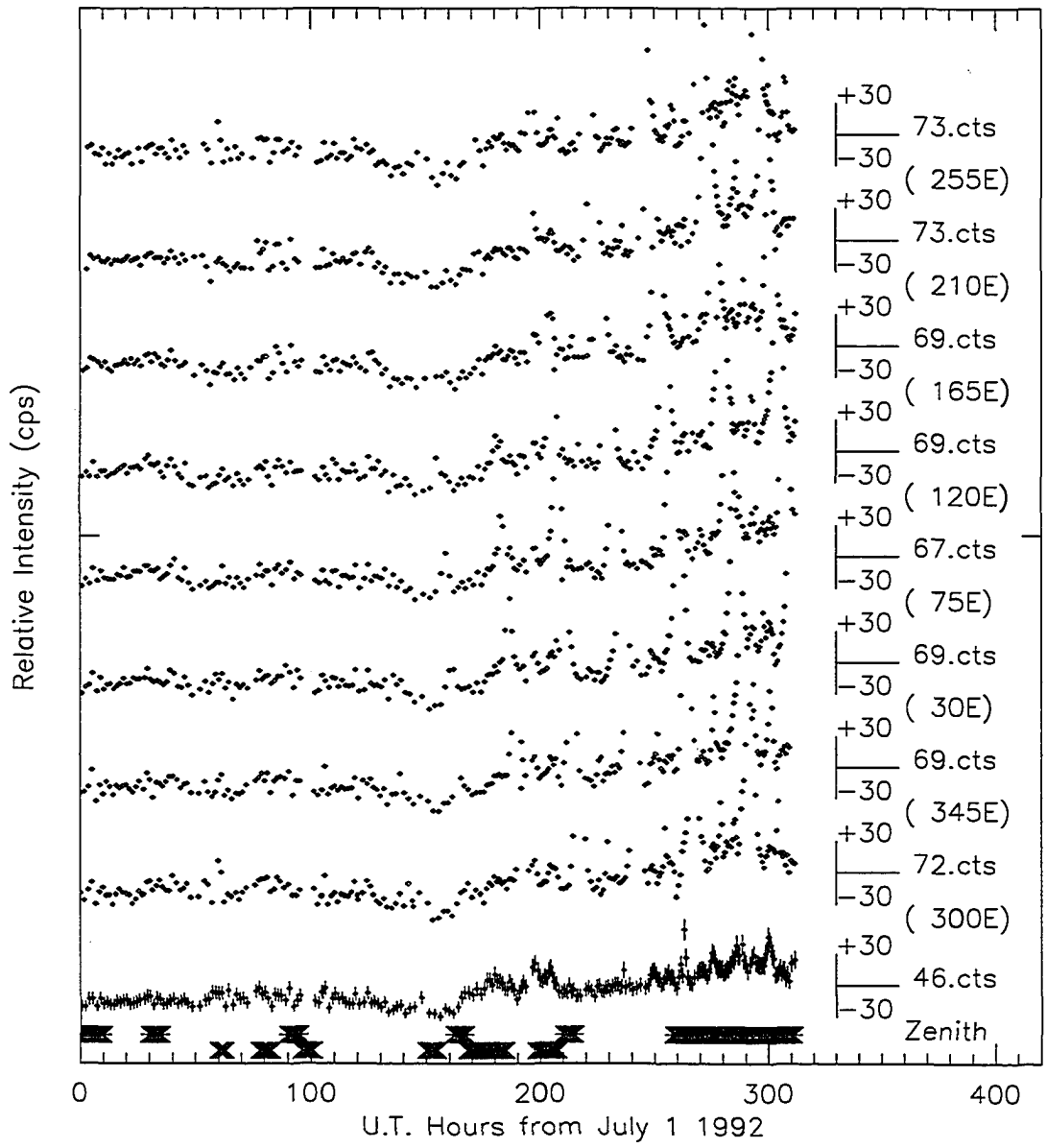

Figure 4.3.3 Countrates from July 1-13, 1992 , as in Figure (4.3.1) but for the countrates.

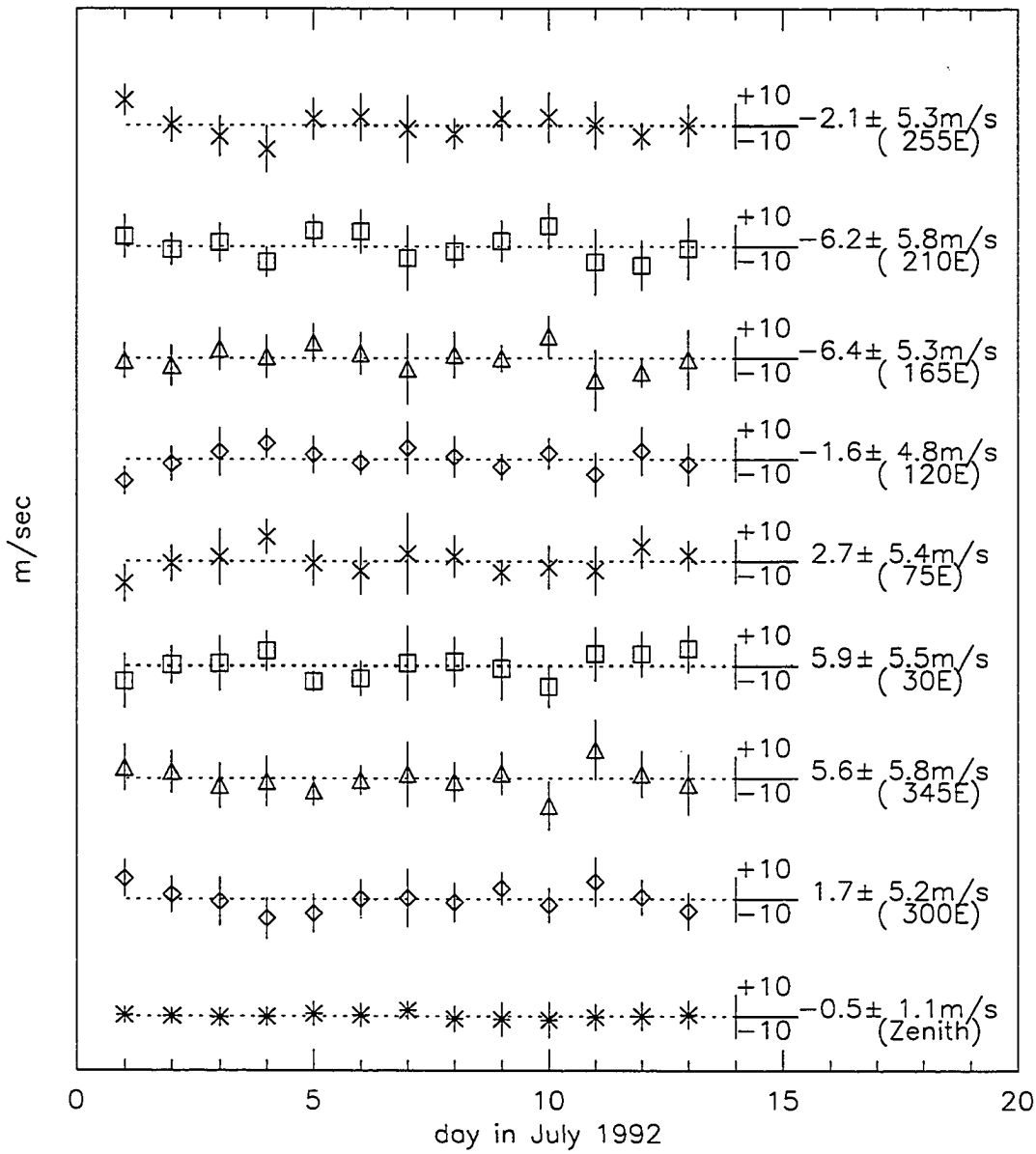

Figure 4.3.4 Daily mean Doppler winds from July 1-13, 1992 , as in Figure (4.3.1) but for the daily mean values. The full period mean value is indicated on the right.

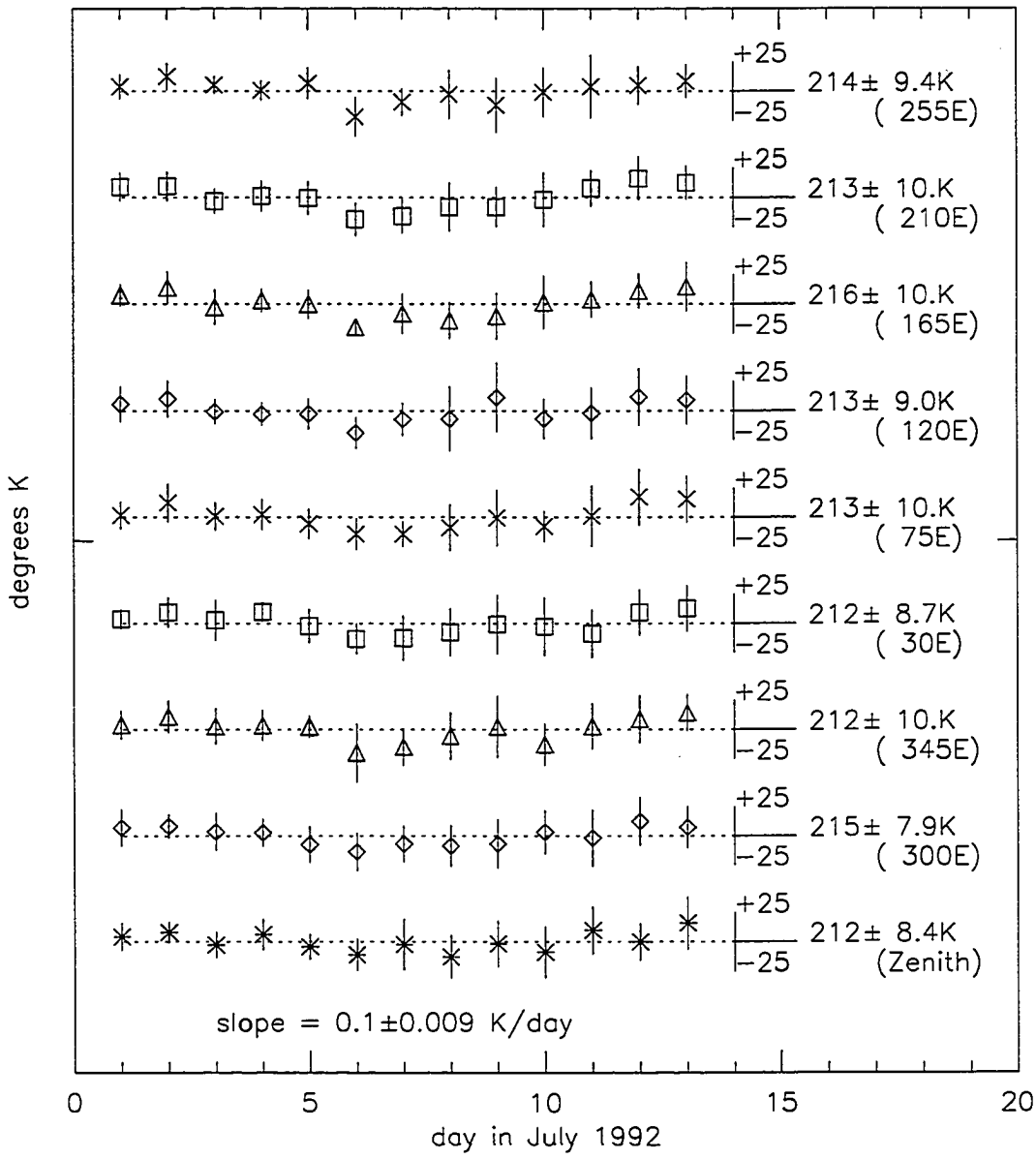

Figure 4.3.5 Daily mean Kinetic temperatures from July 1-13, 1992 , as in Figure (4.3.1) but for the daily mean values. The full period mean value is indicated on the right. A straight line fit to the temperature means indicates a negligible seasonal temperature slope.

a diurnal peak as for 1991, (Figure 4.2.15). The center panel for the temperatures shows the 9, 5, 3.7, 2.7, 1.8, and 1.2 day peaks several of which have associated wind peaks. In Figure (4.3.8) the short period dual-vector neutral wind spectra is shown. Only three peaks in the N-S are above the 95% level and in the grand array analysis shown in Figure (4.3.9) the temperature panel shows some associated power at 7.8 and 6.3 hours but no other significant associations.

Once Again I find the wavenumber separation into westward phase progressing wavenumber one semi-diurnal group wind oscillations and eastward phase progressing wavenumber one planetary group oscillations. This season the cutoff is at 16 hour periods instead of 20 as for the first two seasons. Once again the temperature oscillations are wavenumber zero.

Some exceptions to this general observation are the 4.9-day temperature oscillation and the 4.2-day wind oscillation. The 4.9-day temperature oscillation appears as a wavenumber one and to be 180° out of phase from the 4.9-day wind oscillation phase progression. This feature accompanies the 10-day oscillation and may be a sub-harmonic. It is larger than the 10.1-day in NE-SW directions and indicates a possible mode preference for the conditions of the atmosphere in this period. wavenumber analysis shows the associated 10-day temperature oscillation to be a wavenumber zero and the wind oscillation as an eastward progressing wavenumber one. The 4.2-day wind feature shows the most power of all wind features and is not present in the temperature spectra. This wind oscillation shows a stationary or standing phase pattern.

In Figures (4.3.10)-(4.3.12) the time dependence of the spectra is examined. A 180 hour sliding data window is used. There is a discontinuity near hour 185 in the panels when the 180 hour window enters the data gap around hour 95 and the spectral power changes discontinuously. There are also less obvious jumps about every 20 hours, beginning at hour 105, throughout the panel. The general features are still unambiguous. Also in Figure (4.3.10) the sideways 'V' pattern artifact as noted in the 1991 panels is seen.

The time dependence of the long period region

In upper panels of Figures (4.3.10)-(4.3.12) the long period portions of the temperature and dual-vector components can be examined. In these three panels it appears that the three power distributions seem to exclusively occupy different spectral regions with the exception of a 4-day feature and the longest periods at the far right edge of the panel.

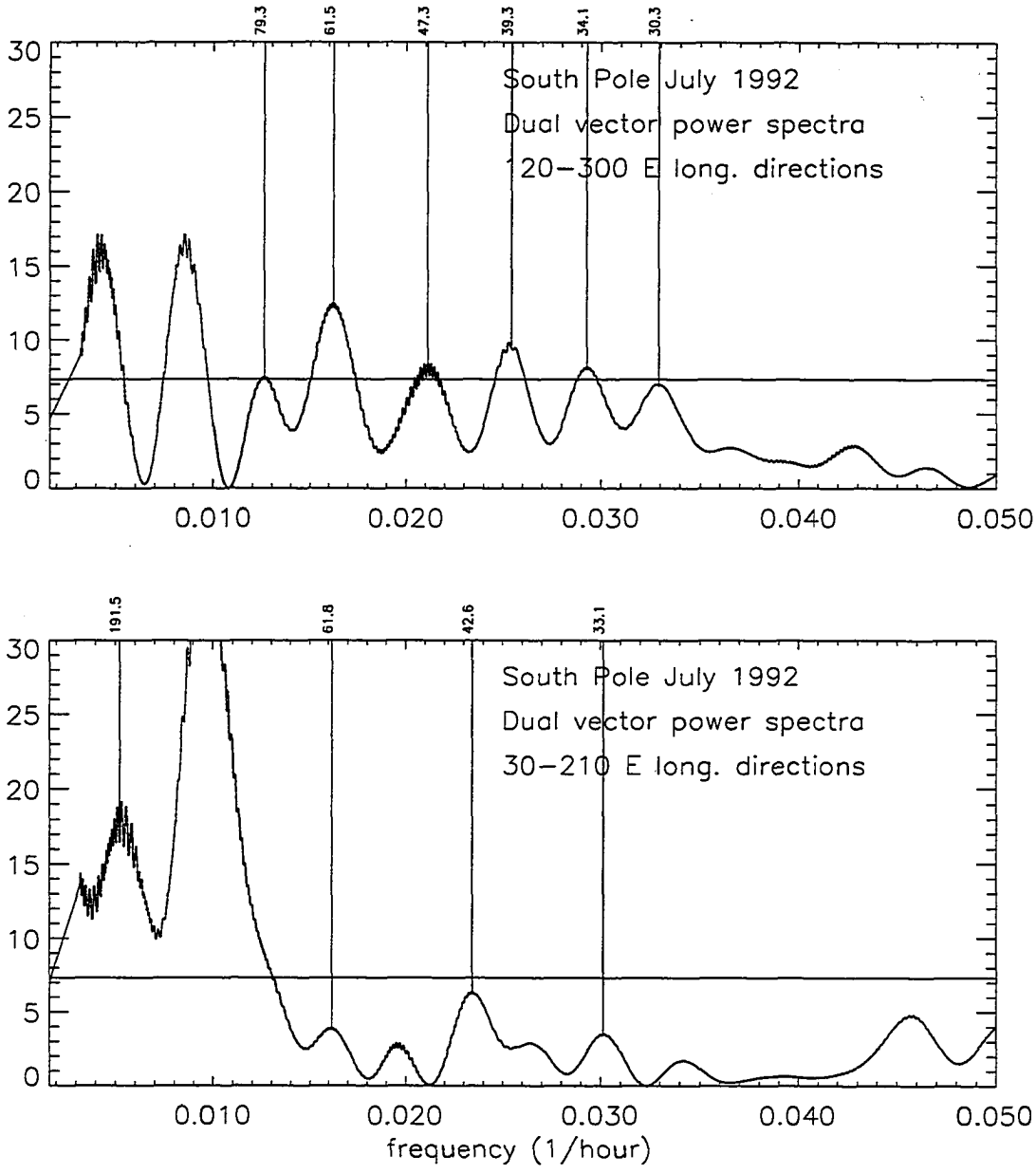

Figure 4.3.6 Planetary wave period, 'Dual-vector' components of the neutral winds for July 1-13. Lomb-Scargle periodograms of the dual-vector components. Normalized power for the 120-300°E component (upper) and the 30-210°E longitude component (lower) is plotted against frequency (1/hours) for 20-300 hour periods. The 95% confidence level is shown as a horizontal line. Selected periodicities are marked (hours).

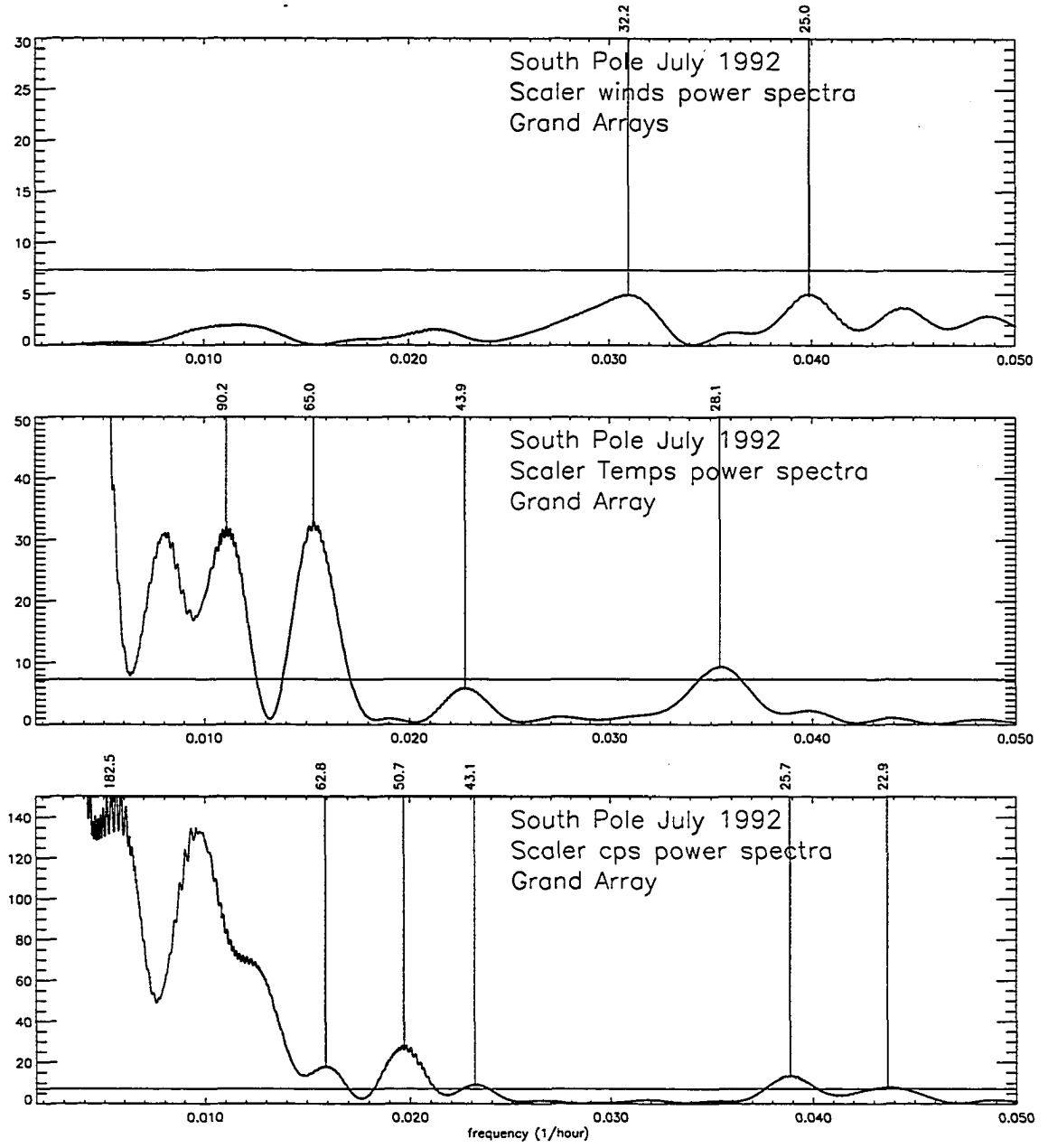

Figure 4.3.7 Grand array analyses for planetary wave structure for July 1-13 wind, temperature, and countrate Lomb-Scargle periodograms of the grand arrays. Normalized power is plotted against frequency (1/hours) for 20-300 hour periods. The 95% confidence level is shown as a horizontal line. Selected periodicities are marked (hours).

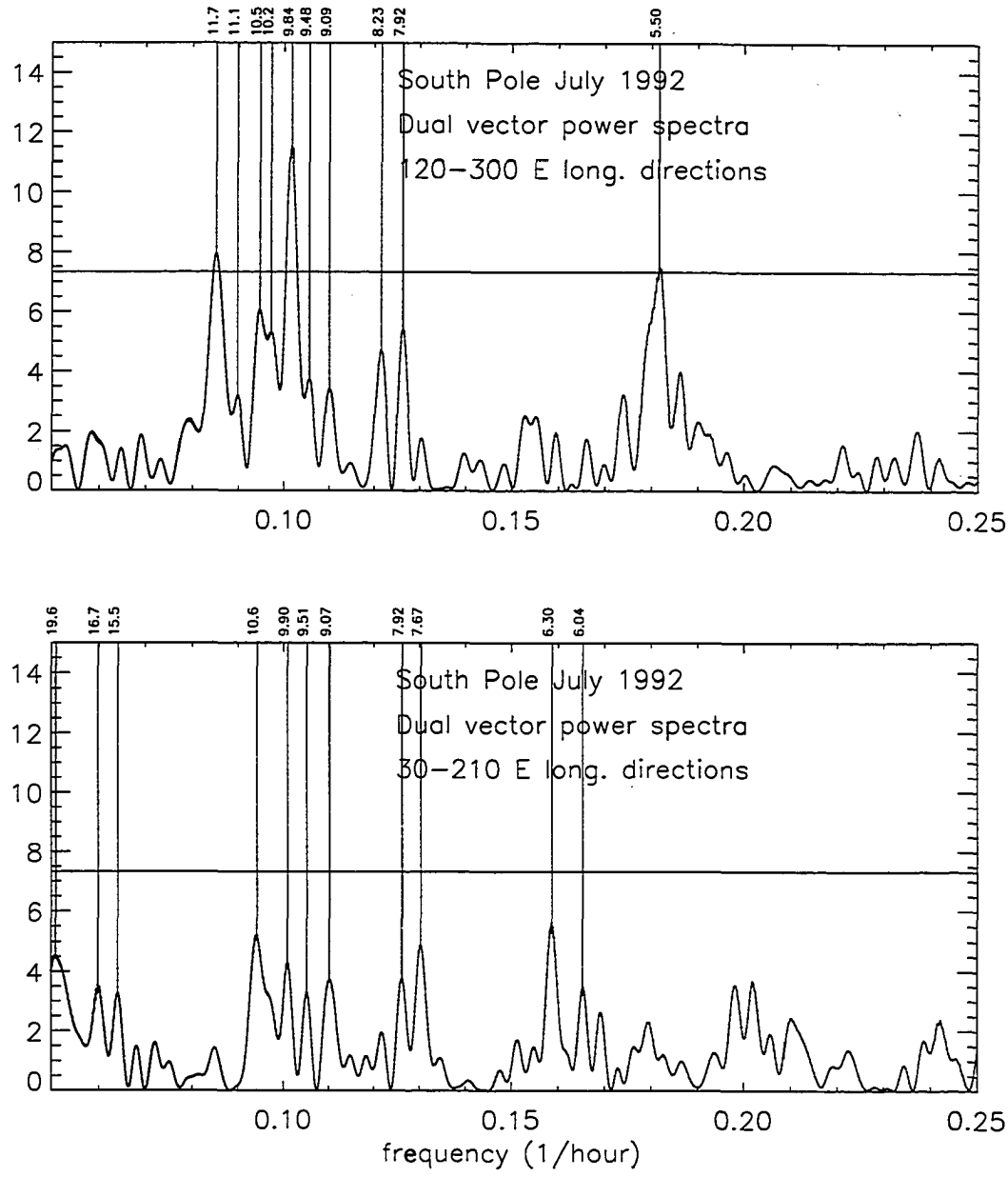

Figure 4.3.8 Near semi-diurnal period, 'Dual-vector' components of the neutral winds for July 1-13. As for Figure (4.3.6) but for the 4-20 hour periods.

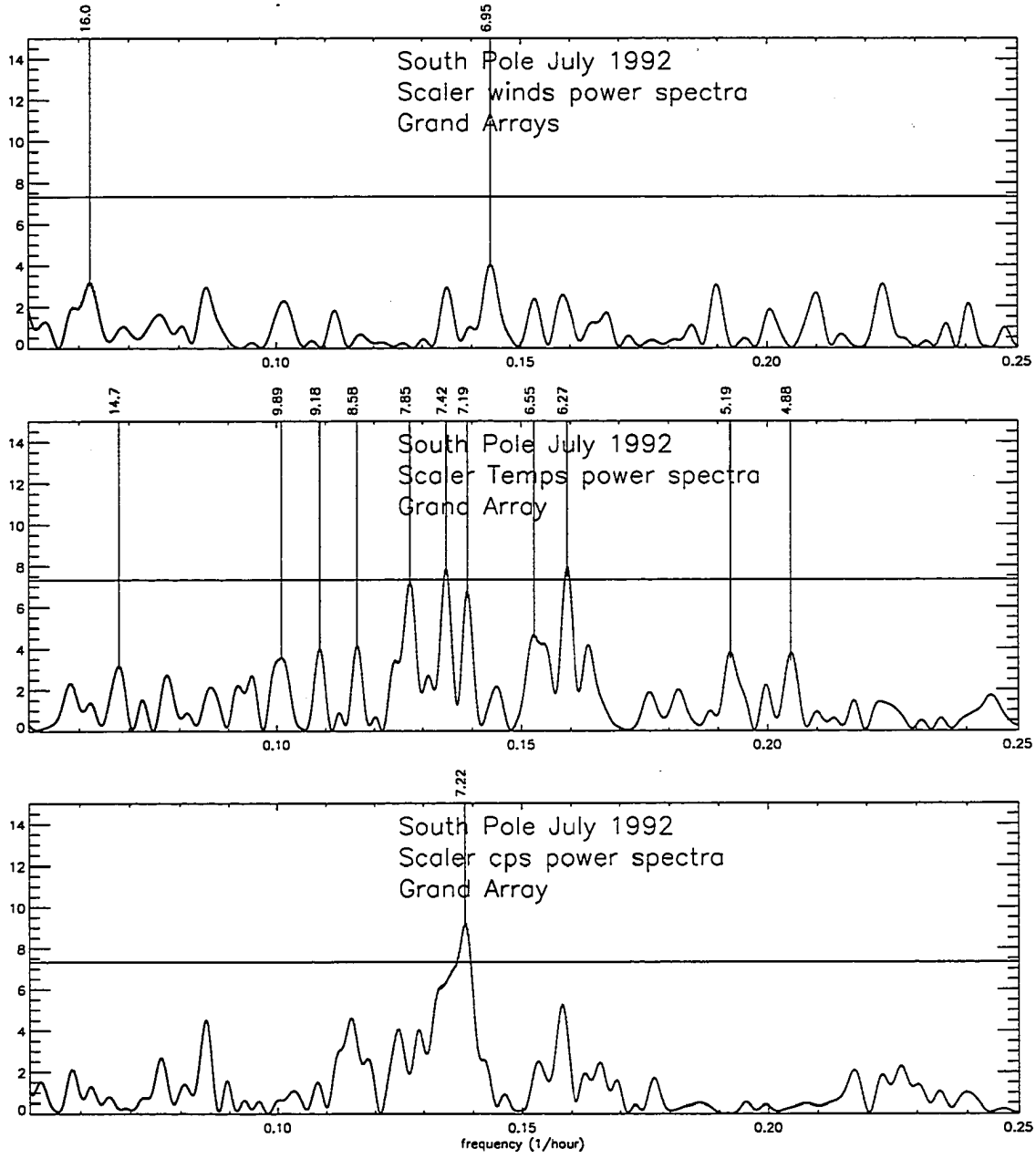

Figure 4.3.9 Grand array analyses of the near semi-diurnal period wave structure for July 1-13. As for Figure (4.3.7) but for the 4-20 hour periods.

In the first half of the panel, for the temperature analysis, prior to hour 150 the spectral power tends to move towards higher frequencies with the 3.3-day feature moving into the 2.4-day period and the 5.5-12 day broadband spreading to a 4.5-12 day band. The distinct void at 4.9-days which begins near hour 95 is consistent with the wavenumber one determination for this temperature feature. In the second half the broadband retracts just as it expanded. A 4-day feature appears and the 2.3-day reappears and moves into the 2.7-day period.

In the E-W wind component the dominant feature is a 3.3-5 day broadband centered on 4-days which extends to the 12-day periods near the later 1/4 of the panel. Two other evanescent features at 1.5 and 2.3 day appear for about 2 days.

In the N-S component there is a large broadband feature part of which drifts off to higher frequencies an a part which continues up the low frequency end of the panel. This splitting maps out a fairly vacant spectral region the shape of the long period portion of the E-W component. Some overlap occurs for the 4-day winds around hour 142 and the 2.7-day around hour 180.

The time dependence of the short period region

The short period temperature and dual-vector components are shown in the lower panels of Figures (4.3.10)-(4.3.12). In the temperature panel near the 15 and 17 hour periods strong features are seen to oscillate with time in frequency and power. As mentioned is section 4.1.2 until further investigation these modulations are not taken to be significant. However, the central frequency about which these oscillations take place drifts towards lower frequency for these features. In the E-W wind component the 16 hour feature drifts to coalesce with a 14 hour oscillation and then re-separates after $\approx$30 hours. This event overlaps with the thermal oscillations near 13 and 15 hours where the 15 hour drifts into a 14 hour feature and bifurcates. Other drifting features are the 11.3 hour thermal feature which drifts off into the 11.9 hour region from hour 100 to 159, and a weak 9.9 hour E-W wind feature which drifts into the 10.6 hour one from hour 90 to 130.

In the thermal power a 7.4 hour oscillation appears to have originated from the 6.3 hour feature, splitting off near hour 160 and steadily drifting to the longer 7.4 hour period, strengthening as it goes. In the N-S components an 8 hour feature splits into a 7.9 and 8.2 pair around hour 150, these later features appear in the full period analysis.

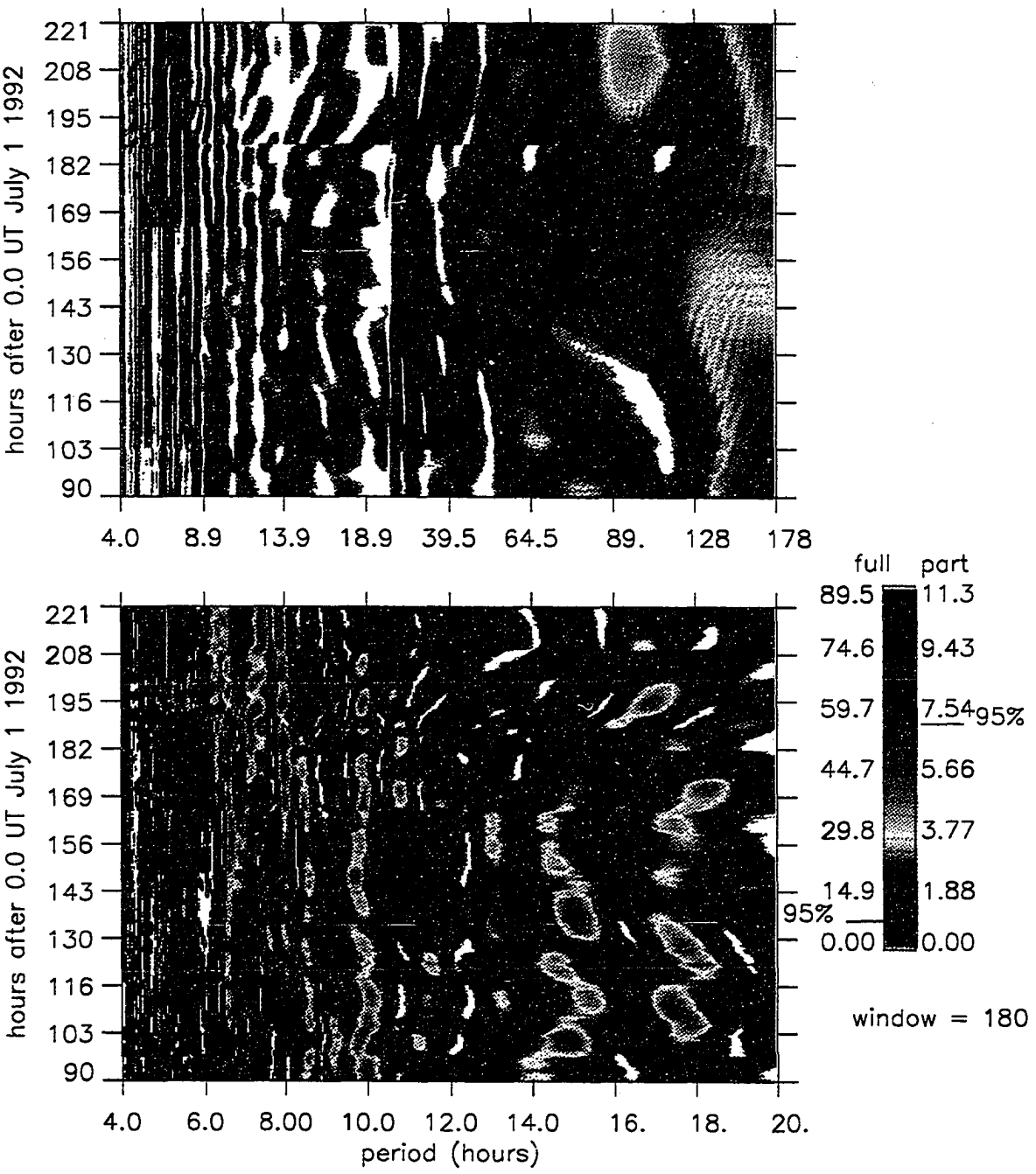

Figure 4.3.10 Time dependent grand array analyses for the temperature structure from July 1-13. As for Figure (4.1.7) with a sliding window of 180 hours. The upper panel is the spectral range from 4 hours to 1/2 the data period (178 hours). The lower panel is the spectral range from 4-20 hours.

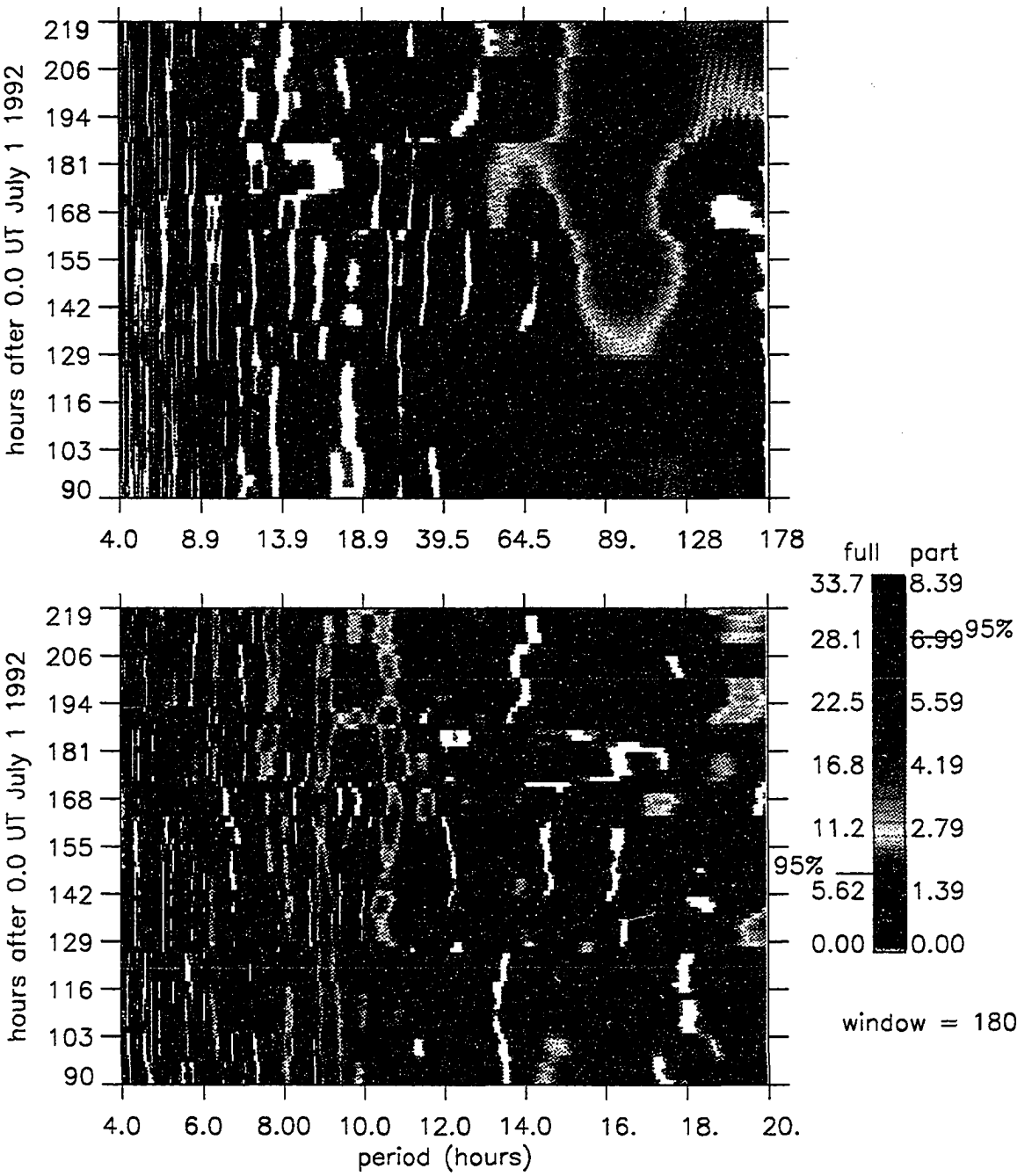

Figure 4.3.11 Time dependent 'dual-vector' wind structure from July 1-13 for the 30-210°E azimuths. As in Figure (4.3.10). Note the relative drifting of spectral features in the lower panel.

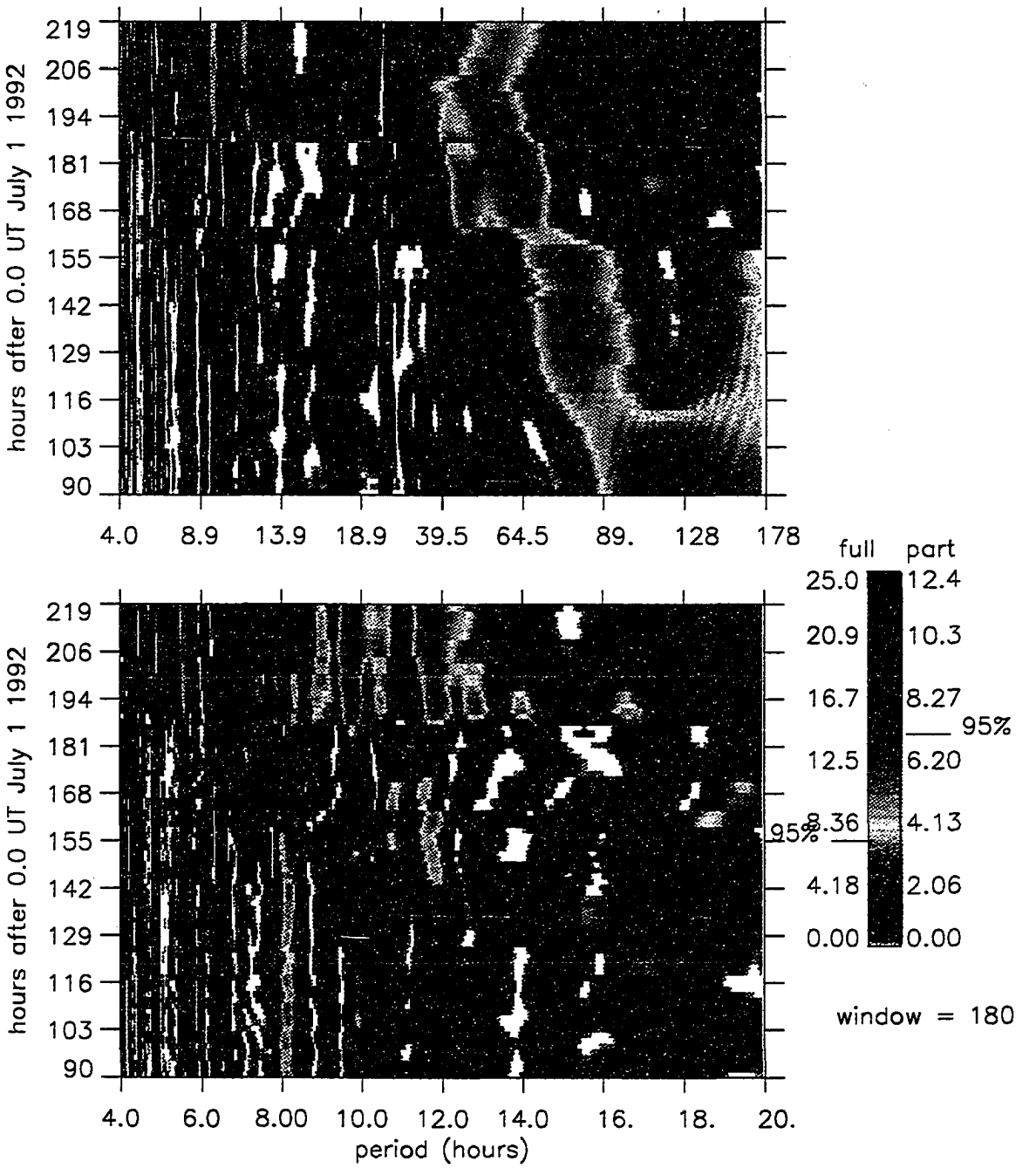

Figure 4.3.12 Time dependent 'dual-vector' wind structure from July 1-13 for the 120-300°E azimuths. As in Figure (4.3.10).

Wind and associated temperature oscillations occur at ~9.9, 7.8 In the N-S component an enhancement of power occurs in many features after hour 188 including a semi-diurnal wind oscillation.

Finally Figure (4.3.13) shows the *all-azimuth* analysis for the 9.8±.3 hour oscillation with a 156 hour window. In the wind amplitude panel the amplitude is seen to start and end the period in all azimuths. Between hours 130-170 the oscillation is confined to the SE-S-SW azimuths. Also at this time the wind phase loses the wavenumber one pattern it exhibits at the beginning and end of the period. The temperature panel shows consistent thermal activity in the NE and all temperature phase is constant. The thermal gradient shows cooler skies in the SW during the middle of the period which is otherwise in the E. The mean wind is fairly steady blowing from W to E and rises in speed from 4.5 to 9 m/s from hour 170 to the end of the period.

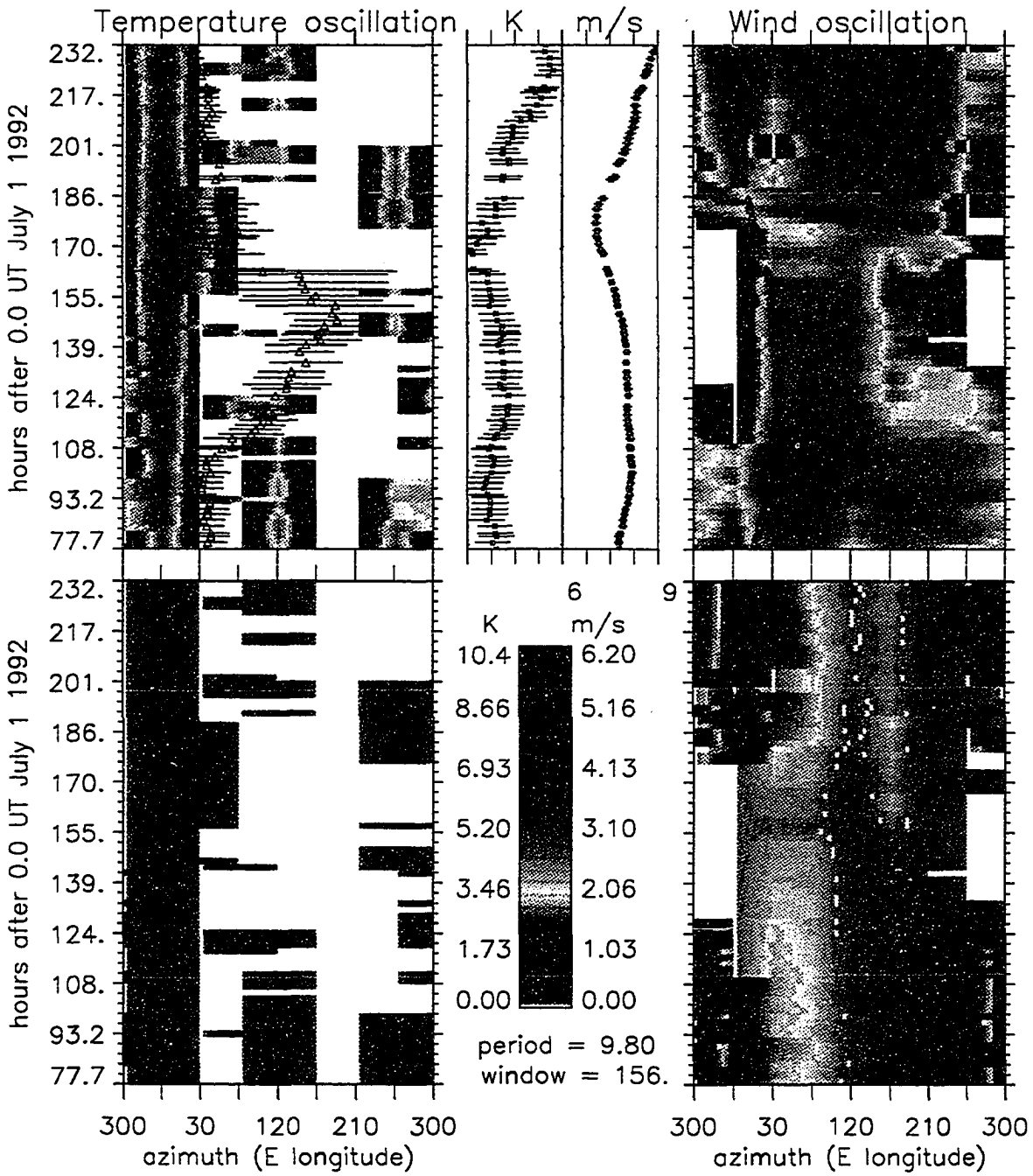

Figure 4.3.13 *All-azimuth* time dependent results for the 9.9 hour oscillation amplitudes and phases derived from the harmonic fit to the time series in a 156 hour sliding window. As for Figure (3.3.7).

Chapter 5 Summary and Conclusions

5.0 General Discussion

An important dynamical property of our planetary atmosphere is its ability to support wave motions. Global scale waves in the Earth's thin atmospheric layer are forced by solar heating of the atmosphere and flow across the planet's surface.

Near the rotation poles the tilt of the Earth's rotation axis produces seasonal variations in the solar energy input. In the polar middle atmosphere this energy input produces large scale horizontal pressure gradients centered on the poles. Initially the atmosphere responds with a meridional flow which is then turned by the Coriolis effect producing the polar vortices. In the winter polar middle atmosphere this meridional flow is poleward and generates an eastward circulation or vortex. In the summer polar middle atmosphere this thermally driven vortex is westward.

Dynamical forcing is also important in determining the mean polar atmospheric flows. Buoyancy and planetary waves modify the vortical flows to produce a pair of counter rotating vortices, one above the other. In winter, the slower eastward propagating portion of the internal buoyancy wave spectrum is absorbed as waves travel upwards, depositing their momentum and accelerating the mean flow. The remaining westward waves and faster eastward ones reach the upper mesopause where they become unstable and break. The westward momentum of the waves is deposited near the mesopause, reversing the mean flow to produce a counter rotating vortex above the stratospheric one. The long period planetary waves are likewise filtered. In this case periods over about 7 days in the eastward portion of the spectra would be removed, leaving the shorter period eastward and westward components. The westward components will be absorbed in the mesospheric westward circulation particularly near the pole where they are slower. Wave momentum is coupled to the mean flow, accelerating the vortex.

In the stratospheric vortex the mechanical dissipation of eastward waves accelerates air parcels to be deflected by the Coriolis torque in the equatorward direction transporting material out of the vortex center. This transport, in addition to the downwelling of

cold air, will draw air down into the vortex to maintain geostrophic balance. In the upper mesosphere, the mechanical forcing of westward waves carries a poleward transport accumulating air in the vortex center which will further enhance the downflow drawing in the lower thermospheric air. This air will adiabatically compress and heat up causing this winter upper vortex to be warm centered upon equilibration.

The net flow between hemispheres is from the cold summer upper mesospheric pole to the warm winter one. At the summer pole, the warm stratosphere has an equatorward flow and a westward circulation. The upwelling warm air is combined with the poleward transport of air parcels caused by wave dissipation to increase the pressure at the center of this vortex. In the upper mesospheric vortex the mechanical forcing is eastward and the Coriolis torque is equatorward which tends to produce a low pressure. Equilibration then is accomplished by air parcel transport from the warm lower vortex which adiabatically expands and cools to produce the cold summer mesospheric vortex center.

The presence of a mean wind at South Pole can be interpreted as being due to an offset or distorted polar vortex. The combination of planetary waves in the mean zonal flows will distort the vortex. For primarily wavenumber one oscillations this distortion should elongate the vortex in one dimension and place a mean flow over the pole. In addition to the mean wind a distortion will show asymmetric oscillation amplitudes around the pole. Assuming a wavenumber one type distortion, showing a single elongation, in the elongated directions the zonal absorption will take place further from the pole leaving smaller amplitudes to observe as compared to the orthogonal directions.

This investigation presents data which relates to the polar upper middle atmosphere (UMA). Data from three brief periods from three different years (1990-1992) are used in this work. This data is the result of sampling the OH layer in the UMA over South Pole Station for line-of-sight Doppler information at a 30°' elevation angle in eight (4 in 1990) 45° azimuth steps around the pole and one in the zenith. This has yielded 9 (4 in 1990) azimuthally separated time series containing OH^* Λ-doubled emission profiles.

I have characterized the observed wavefields of the southern polar UMA OH layer. To obtain the necessary data I developed analytical techniques for the reduction of emission profiles from the neutral OH^* molecule in the UMA measured with a Fabry-Perot Spectrometer. These very low light level nighttime airglow emissions are multiple-line profiles. Reduced wind and temperatures from them are subject to large uncertainties if

the counting statistics are not properly treated. Proper treatment usually means counting for a long time in order to improve the SNR which involves the loss of spatial and temporal resolution.

The development of the NL^2S method for extraction of the geophysical parameters of the Doppler widths and shifts from this multiple-line feature was accomplished for the first time and has opened the door for the simultaneous analysis of the dynamic parameters of wind and temperature from the same volume of gas. Along with this development was the determination that, for low signal multiple-line structures, the previously used methods based on the discrete Fourier transform (DFT) suffered from poor determination of the different peak separations. Variations in the derived DFT coefficients caused by uncompensated beats between adjacent lines led to large variations in the derived temperatures. Having acquired the data and developed a method for reducing it I was able to advance the following observations and conclusions.

5.1.1 The mean flow results and the nature of the vortex

This characterization began with the mean state of the layer. I have found a cross-polar mean wind in each of the periods analyzed here and that the measured wind fluctuations were organized around this cross-polar mean wind. The daily mean temperatures showed a seasonal temperature trend with a reversal of a .4°K/day warming in May to a -.8°K/day cooling in August, consistent with the passage through the warm winter mesopause season. The existence of a cross-polar wind was not a new discovery and having been reported by Hernandez et al., (1992), where it was suggested as possibly due to long period waves or the existence of a polar vortex, offset from the rotation pole. It is an interesting result that this wind seemed to be so closely related to the organization of the basic symmetry in the wind field around the pole.

From the discussion above I expect westward circulation around a warm south polar UMA. If I presume the observed mean winds to be caused by this type of vortex I can infer the position of the vortex as perpendicular to these mean winds. Furthermore a thermal gradient will also indicate the direction towards the center of the vortex.

In May 1990 the mean temperature was 214°K with a mean wind of 3 m/s and a thermal gradient of 6°K over the sampled sky or 2.3°K/degrees latitude with the atmosphere warmer in the 110°E direction. In August 1991 the mean temperature was 217°K with a mean wind of 5.5 m/s and a thermal gradient of -1.1°K over the sampled

sky in the 30°E azimuth direction. In July 1992 the mean temperature was 213°K with a mean wind of 7 m/s and a negligible thermal gradient.

In general the mean winds are westwards from the thermal gradient which is consistent with the thermal wind equation derived from the assumption of geostrophic conditions. However the angular separation is not observed to be 90°. Still this 'quasi-geostrophic' behavior can be used to infer the position of a supposed polar vortex with the understanding that it is a rough estimate. In the May period this position is estimated to be 275-290°E direction towards South America, for July in the 165-300°E direction towards the south Pacific ocean, and for August in the 30°E direction towards South Africa. Simply based on the mean wind direction gives a polar vortex displacement for May in the 330°E, for July and August in the 270°E direction. These values imply an east-west motion of the of a displaced vortex center.

If this mean wind were the result of very long period planetary waves crossing the pole and I ignore the theoretical difficulties implied by a planetary wave crossing the rotation pole the data would require a wave of sufficient period and amplitude to produce at least an average value equal to the season's mean wind. In 1990 this would require a 4 m/s 24-day wave, in 1991 a 9.9 m/s 50-day wave would be needed, and in 1992 a 7.8 m/s 26-day wave. Waves of these periods, (20-60 days), if not stationary with respect to the surface would move so slowly that they could be considered stationary over this time period, i.e., a tropical '40-day' wave , (Madden and Julian 1971, 1972, Yasunari, 1980) had a speed of less than one degree per day. In the case of the wave just described the oscillation was seen to be trapped below the 80 hPa level. A 62-day surface pressure oscillation has be reported by Shapiro, (1970), from 7 Antarctic stations so at least these waves are not entirely unlikely. In any case stationary waves of this sort would create distortions in a polar vortex and thus have the same appearance as that of a displaced vortex or the creation of a multi-celled pattern as seen in the northern polar stratospheric vortex. Satellite images of the ozone hole over south pole maps the stratospheric polar vortex and shows tremendous distortions by long period global scale waves, (Bowman, 1993).

5.1.2 The fluctuations in time series

The initial examination of the time series for gross features (long period features) shows the temperature series to be correlated in all azimuths as well as correlated with

the major features of the countrate series. The winds are anti-correlated in opposite directions and these opposite directions are divided by the mean wind direction. For example, in the beginning of the May 1990 period the Doppler winds from the 210 and 300°E directions appear correlated and are anti-correlated with their opposing directions (those separated by 180°). This implies a phase jump along the 165-345°E direction. The mean wind direction for the beginning of this period is towards 170°E and has a speed of 2 m/s. Towards the end of the period the correlation switchs to the winds in the 300 and 30°E directions implying a phase jump along the 75-255°E direction. The mean wind gradually increases to ~6 m/s (see Figure 4.1.12) as it turns towards the 130°E direction. This phase jump indicates a stationary phase pattern for these long period waves. For the 1991 period the correlations imply a phase jump along ~90-170°E direction until around August 20 after which the jump appears along the ~45-225°E direction. The mean wind for the first part of the period is in the 75°E direction and switches to 345°E by the end of the period, (see Figure 4.2.17). In the 1992 period the correlated azimuths are those in the 210-345°E directions implying the phase jump along the 0-180°E direction. The mean wind blows ~6 m/s towards the 0°E direction.

In virtually every case I have seen in this work whenever spatial information was coupled with the amplitudes or spectral information asymmetries were found. Although exciting to discover the asymmetry in the distribution of spectral amplitude it should not have been unexpected based on the previous discussion. The organization of the wind fluctuations around the mean wind indicates that any spectral decomposition will also have asymmetry.

5.1.3 Spectral investigation of the time series

The derivation of the power spectra for the three periods showed the asymmetry in the different azimuth panels for the winds and the temperatures. Another new discovery from this presentation was the grouping of the spectral power and the different nature of the constituents between the groups and the similarities within each group. The long period group, which I have been referring to as the planetary group, has periods longer than about 20 hours and the second, short period group, which I have been calling the semi-diurnal (s.d.) group has periods between 7-13 hours. The wavenumber analysis of the features in the winds and temperatures show that, with a few exceptions, all the wind features exhibit wavenumber one phase progression around the pole and the

temperatures wavenumber zero. Furthermore the phase progression is eastward for the planetary group and westward for the s.d. group. This wavenumber selection is not completely unexpected as pointed out in Hernandez et al., (1992), the winds near the pole vary as $[cos(\phi)]^{|s-1|}$ and the temperatures vary as $[cos(\phi)]^{s}$ for the wavenumber 's'. Then for $\phi \rightarrow 90$ one expects the winds with $s = 1$ and temperature oscillations with $s = 0$ to be dominant. Physically all longitudinal variations should vanish at the pole in order to avoid discontinuity.

Exceptions to the wavenumber selection from the 1990 period include an 8-day wind oscillation and an 11.3 hour temperature feature. The phase progression of the 8-day oscillation appears as a stationary phase pattern as one might expect from a standing wave. That of the 11.3 hour thermal oscillation shows a steeper than wavenumber one slope (between wavenumbers one and two) but is still westward in accordance with its membership in the s.d. group. As a side note the semi-diurnal migrating tide is a wavenumber two and possibly the source of this oscillation. The 8-day wind oscillation in 1991 also shows the stationary phase pattern. Also showing this phase pattern are in 1991 the 3-day wind feature in 1991 and a 4.2-day wind oscillation in the 1992 period.

The results of section 1.3 show that $s = 1$, s.d. group oscillations with a westward phase speeds belong to the inertio-gravity wave class in panel (b) of Figure (1.3.1). The group I call the planetary group with eastward phase speed will only fit in this figure for equatorially trapped modes with positive equivalent depths, panel (a), or negative equivalent depths (forced), panel (d). In the case of the equatorially trapped modes some form of ducting may have passed them into the polar region.

From the figures for the *single-azimuth* presentation I found the phase relationship between the thermal and wind oscillations to be $\pi/2$ as one might expect for a pressure-temperature oscillation. This is fine for the gravity wave modes but the planetary modes are theoretically pure kinetic energy, that is the restoring force being the planetary vorticity causes the atmospheric parcels to 'circulate' meridionally in little ellipses, always in motion, as the wave moves past so that no thermal response is necessary. The answer to this is that it is most likely not this theoretical abstraction and does contain some associated non-horizontal motion. I do find in many cases an associated thermal component of the oscillations as discussed above. The outcome is that the relative phase is $\pi/2$ during 'normal' non-dissipative propagation and '0' during dissipation or enhancement.

The discovery of this wavenumber zero selection for the temperatures allows me to ignore the azimuthal information and treat all temperatures in one 'grand array' and

giving wave spectra improved statistical reliability. In this analysis I expected to find the winds, as predominantly wavenumber one, practically absent and the temperatures relatively unchanged in content from the individual azimuth panels, but increased in significance. Indeed this was the case. I also note the absence of the 11.3 hour thermal oscillation in the results for the 'grand array' as I have effectively filtered all wavenumber one information out. A similar reduction was possible in the winds as I resolved the 8 azimuthal series into a single vector and analyzed two orthogonal components of this new vector. The results for the wind components (termed the dual-vector components) retain their spatial asymmetry and had the added advantage of better SNR.

5.1.4 Time dependent spectral results

The foregoing discoveries and analyses provide some information about the static mean and spectral character of the region, but any successful characterization must address its dynamic nature. In keeping with the dynamic picture of the region I examined the temporal nature of the spectra and the residual mean state. The temporal evolution of the spectral content in a sliding time window were derived for the temperature 'grand array' and the dual-vector components. Two other temporally sensitive presentations, the *all-azimuth* and *single-azimuth* presentations, provided the individual azimuth information. From these analyses comes another exciting result; that not only does the azimuthal distribution of spectral amplitude appear locked into the direction of the mean wind but that in some cases oscillations cannot survive if the mean wind changes directions. As seen in section 4.2.2 the rapid change in the direction of the mean wind preceded the extinction of the 3-day wave and the enhancement of the 2.7 and 4-day ones. One has to ask whether it was the amplitude or the direction of the wind or either of them which precipitated the event. The causal relation is not proved. It is unlikely that the local mean wind amplitude is the direct cause. If I assume a critical Doppler shifting dissipation process for planetary wave breaking, in analogy with gravity wave breaking, then no spectral content should exist below a critical frequency which would be determined by the local mean wind speed. Having calculated this critical frequency as a function of the mean wind I find many features to exist below it, the planetary 3-day wave being one of them.

Following the change in the mean wind direction the mean wind speed is enhanced. This could be an indication of the dissipation process dumping the wave momentum into

the mean wind. The dissipation of the 3-day wave was accompanied by the dissipation of a 2-day wavenumber one either of which could have contributed eastward momentum into the eastward mean. The dip in the mean wind speed just prior to the dissipation as the thermal oscillation bursts may be another indication of the dynamic process but requires further study. (It is curious that the rise in the thermal amplitude is $\approx 2°K/day$ for both the 3-day and this 2-day which is of the same order as the solar UV and EUV heating rates, (Mlynczak and Solomon, 1991) for thermally forced atmospheric waves originating from the troposphere.) It is not clear whether the wave was truly dissipated or coupled to other modes although it is unlikely that the production of thermal energy which accompanied the process would allow complete conversion.

If this interpretation is valid for whatever physical mechanism, this would lead one to conclude that the mean wind may be capable of determining the spectral makeup of the polar region.

Another apparent Doppler effect is observed as frequency shifting which is apparent in the time dependent results for both the grand-arrays and the dual-vector analyses. Also the frequency drifting of spawned features often shows differential shifting with increased relative separation between the spawned features. The spawned feature on the lower frequency side drifting more and providing most of the new relative separation. When thermal features are associated with wind features any drifting or spawned features are also present and have the same sense (drift direction).

5.2 Conclusions and Future work

Conclusions

I. Variable cross-polar mean winds exist and if associated with a polar vortex implies a vortex shifted off the rotation pole. Furthermore this vortex appears to move longitudinally.

II. The daily mean temperature trend from May-July-August shows a transition from a warming in May to a cooling in August, which may indicate the passage through the warm winter mesopause.

III. Spatial asymmetries in wave activity lead to spatial asymmetries in the distribution of spectral amplitude around the pole. In the case of the 3-day wave of 1991 the asymmetry is locked into the direction of the mean wind direction.

IV. Spectral analysis of the variations in this layer indicate the existence of two distinct groups: a planetary wave group with periods above ~2 days and a near semi-diurnal group with periods of ~7-13 hours. (This study is limited to the 2 hour - 25-day period region by the sampling rate and data length.)

V. Phase analysis of wind oscillations of these two distinct groups shows the planetary group to exhibit eastward phase progression with some exceptions, whereas the near semi-diurnal group exhibits westward phase progression. And a changeover near periods of 20 hours.

VI. Phase analysis shows the wind oscillations to be dominated by azimuthal wave-number one and the temperature oscillations to be dominated by azimuthal wave-number zero.

VII. Stationary phase or standing phase patterns exist in the wind oscillations and are exceptions to V.

VIII. Two cases of dissipating planetary waves have been found. In each case the wave is dissipated in one wavelength. For each of the 72 and 48 hour cases an accompanying thermal amplitude oscillation increase of $\approx$ 2°K per day is observed.

IX. Several cases of mode coupling are found. One type is where one mode splits into two which continue with a variable relative frequency separation and another type where two modes coalesce into one.

X. When both neutral wind and temperature oscillations exist the relative phase between them is $\pm\pi/2$ during stable propagation and 0 during conditions of dissipation or enhancement.

XI. Some planetary wave wind oscillations have associated temperature oscillations indicating a measurable departure from a pure rotational wave interpretation.

XII. Local Doppler shifting of planetary waves is not consistent with local mean wind variations.

Future work indicated

The dynamic interaction of global scale oscillations in the polar upper middle atmosphere (UMA) is evidenced in its variable spectral content. The specific nature of these interactions is unresolved. The planetary wave-polar vortex system appears to drive the UMA transport of material between the rotation poles and either reflect, via mode coupling, or absorb wave energy originating from low latitudes. The actual filter or selection of the portion of the spectrum to be absorbed or reflected is undetermined and thus so is the amount of energy and momentum flux into the polar region. These planetary waves appear to be an important source of momentum and material transport into the south polar region. The coupling of global scale waves in the polar mesosphere and their azimuthal asymmetry should be observable in lower latitudes. The complete filtering of westward planetary wave features from the south pole UMA should be observable as distinctly different behaviors in the observations of mid to high latitude eastward and westward planetary waves. If this filtering is taking place near the mesospheric region then the effective global scale of the filtered westward waves must be shortened relative to the penetrating eastward ones and mode coupling of the type observed here should show transient enhancements in the mid-latitude planetary wave amplitudes.

More spatial information (vertical and latitudinal) is needed to resolve these outstanding questions of global scale interactions in the polar regions. The measurement of vertical wavelength and phase speed added to the horizontal information can be used to derive momentum flux and resolve the question of whether dissipation or reflection is taking place. The examination of the spectral content with latitudinal dependence could demonstrate the interaction of the wavefields with the mean zonal flow and the spectral filtering characteristics. These measurements could be accomplished with the radars at McMurdo and Adelaide for the vertical profiles and the horizontal measurements with the FPSs at South Pole and Mt. John (and hopefully, a new one at McMurdo). These would give a broad latitude determination of the spectrum. Additionally the feedback of reflected global wave energy should be observable from these lower latitudes. With the addition of the Svalbard and Poker Flat Fabry-Perot spectrometers the Northern hemisphere could be examined for this feedback as well.

Longer periods of data would allow extension of the spectral investigation into the longer periods above which no planetary waves exist. This may set a limit on the length of data series needed to investigate the significant portion of the spectra.

References

Avery, S. K., R. A. Vincent, A. Phillips, A. Manson, F. Vial, J. M. Forbes and G. J. Fraser, High latitude tidal behavior in the mesosphere and lower thermosphere, *J. Atmos. Terr. Phys.*, **51** , 595-608, 1989.

Andrews, D.G., J.R. Holton, C.B. Leovy, *Middle Atmosphere Dynamics*, Academic Press Inc., 1987

Babcock, H.D., A Study of the green auroral line by the interference method, *Astrophys. Journ.*, **57**, p.209, 1923

Baker, J.B., A.T. Stair, Rocket measurements of the altitude distribution of the hydroxyl airglow, *Phys. Scri.*, **37**, 611-622, 1988

Bates D.R., M. Nicolet, The Photochemistry of Atmospheric Water Vapor, *J. Geophys. Res.*, **55**, 3, September 1950

Battaner, E., and M.L. Sanchez-Saavedra, Temperature Measurement of the High Atmosphere by Optical Methods, *Annales Geophysicae*, **2**, 1, 67-72, 1984

Bevington, P.R. *Data Reduction and Error Analysis for Physical Sciences*, McGraw-Hill Book Company, p.43, 1969

Born, M., E. Wolf, *Principles of Optics*, Pergamon Press, 322-340, 1959

Bowman, K.P. and N.J. Mangus, Observations of deformation and mixing of the total ozone field in the Antarctic polar vortex, *J. Atmos. Sci.*, **50**, 17, 2915-2921, September 1993

Chabbal,R., Research on the best conditions for using a Fabry-Perot photo-electric spectrometer, *Journal des Recherches, CNRS*, **24**, pp.11-12 and 138-186, 1953

Chamberlain, J.W., *Physics of the Airglow and the Aurora*, Academic Press, p.569,1961

Chamberlain, J.W., F.L. Roessler, *Astrophys. J.*, **121**, 2, p.541, 1955

Chapman, S. and R. S. Lindzen, *Atmospheric Tides*, D. Reidel Publishing Company, 1970.

Chapman, S., and Cowling, *The mathematical theory of non-uniform gases*, University Press, 86-88, 1952

Chimonas, G., C. O. Hines, Doppler ducting of atmosphere gravity waves, *J. Geophys. Res.*, **91** , 1219-1230, 1986.

CIRA 1972, *COSPAR International Reference Atmosphere 1972 Akademie Verlag*, 1972

CIRA, COSPAR International Reference Atmosphere: 1986 Part II: Middle Atmosphere Models, *Adv. Space Res.*, **10**, 12, 1990

Collins, R., Observations of a 12 H wave in the mesopause region at the South Pole, *Geophys. Res. Lett.*, **19**, 57-60, January 1992

Conner, J.F., R.W. Smith, G. Hernandez, Techniques for deriving Doppler temperature from multiple-line Fabry-Perot profiles: An analysis, *Appl. Opt.*, **32**, 23, 10 August 1993

Conner, J., R.W. Smith, G. Hernandez, High Latitude Mesopause and Lower Thermosphere Wave Spectra From Amundsen-Scott Station., *A.G.U. presentation*, December 1992

Coxon, J.A., K.V.L.N. Sastry, J.A. Austin, D.H. Levy, The microwave spectrum of the OH $X^2\Pi$ radical in the ground and vibrationally-excited ($\nu \leq 6$) levels, *Can. J. Phys.*, **57**, 1979

Coxon, J.A., Optimum molecular constants and term values for the $X^2\Pi(\nu \leq 5)$ and $A^2\Sigma^+(\nu \leq 3)$ states of OH, *Can. J. Phys.*, **58**, p. 946, 1980

Coxon, J.A., and S.C. Foster, Rotational analysis of hydroxyl vibration-rotation emission bands: Molecular constants for $X^2\Pi(6 \leq \nu \leq 10)$, *Can. J. Phys.*, **60**, p. 47, 1982

Elvey, C.T., Observations of the light of the night sky with a photoelectric photometer, *Astrophysical Journal*, **97**, 1, 65-71, 1943

Fels, S.B., Radiative-dynamical interactions in the middle atmosphere, *Adv. Geophys.*, **28A**, 277-300, 1985.

Forbes, J. M., Atmospheric Tides 1. Model description and results for the solar diurnal component, *J. Geophys. Res.*, **87** , 5222-5240, 1982a.

Forbes, J. M., Atmospheric Tides 2. The solar and lunar semidiurnal components, *J. Geophys. Res.*, **87** , 5241-5252, 1982b.

Forbes, J. M., M. Hagan, Diurnal Propagating Tide in the Presence of Mean Winds and Dissipation: A Numerical Investigation, *Planet. Space Sci.*, **36**, 579-590, 1988

Forbes, J. M., F. Vial, Monthly Simulations of the Solar Semidiurnal Tide in the Mesosphere and Lower Thermosphere, *J. Atmos. Terr. Phys.*, **51**, 649-662, 1989

Forbes, J. M., F. Vial, Semidiurnal Tidal Climatology of the E-Region, *J. Geophys. Res.*, **96**, A2, 1147-1157, 1991

Francis, S. H., Lower atmospheric gravity modes and their relation to middle-scale traveling ionospheric disturbances, *J. Geophys. Res.*, **78**, 8289-8295, 1973.

Fraser, G. J., Summer circulation in the Antarctic middle atmosphere, *J. Atmos. Terr. Phys.*, **46** , 143-146, 1984.

Fraser, G. J., Monthly mean winds in the Mesosphere at 44S and 78S, *Pure Appl. Geophys.*, **130** , 291-301, 1989.

Fraser, G. J., G. Hernandez, R.W. Smith, Eastward-moving 2-4 day waves in the winter Antarctic mesosphere, *Geophys. Res. Lett.*, **20**, 15, 1547-1550, August 6, 1993

Fritts, Shear Excitation of Atmospheric Gravity Waves, *J. of the Atmos. Sci.*, **39**, 1936-1952, Sept. 1982

Fritts, D.C., Research status and recommendations from the Alaska workshop on gravity waves and turbulence in the middle atmosphere, Fairbanks, Alaska, 18-22 July 1983, *Bulletin, American Meteorological Society*, 149-159, 1984

Fritts, D.C., Gravity wave saturation in the middle atmosphere: A review of theory and observations, *Rev. Geophys. Space Phys.*, **22**, 275-308, 1984

Fritts, D.C., and R.A. Vincent, Mesospheric momentum flux studies at Adelaide, Australia: Observations and a gravity wave-tidal interaction model, *J. Atmos. Sci.*, **44**, 605-619, 1987

Fritts, D.C., A review of gravity wave saturation processes, effects and variability in the middle atmosphere: A review of theory and observations, *Pure Appl. Geophys.*, **130**, 343-371, 1989

Fritts, D.C., and L. Yuan, Measurement of momentum fluxes near the summer mesopause at Poker Flat Alaska, *J. Atmos. Sci.*, **46**, 2569-2579, 1989

Gill, T.P., *The Doppler Effect*, Academic Press, 1965 p.47-62

Groves, G.V., Comparisons of new results with CIRA 1965 with emphasis on the IQSY data. A review for the region 30 to 100 km, *Adv. Space Res.*, VIII, 741-760, 1967

Hamwey, R.M., A spectrophotometric study of hydroxyl emissions from a high latitude winter mesopause, *M.S. thesis*, Univ. of Alaska-Fairbanks, 1985

Hays, P.,R. Roble, A Technique for Recovering Doppler Line Profiles from Fabry-Perot Interferometer Fringes of Very Low Intensity, *Applied Optics*, **10**, 1, 193-200, 1971

Heaps H.S., G. Herzberg, Intensity Distribution in the Rotation-Vibration Spectrum of the OH Molecule, *Zeitschrift für Physik*, **133**, 48-64, 1952

Hedin, A.E., A revised Thermospheric model based on mass spectrometer and incoherent scatter data: MSIS-83 *J. Geophys. Res.*, **88**, A12, 10170-10188, 1983

Herzberg, G., *Molecular Spectra and Molecular Structure- Spectra of Diatomic Molecules*, Van Nostrand Company, 1950

Herman, R.C., G.A. Hornbeck, *Astrophys. J.*, **118**, 2, p.214, 1953

Hernandez, G., Analytical description of a Fabry-Perot spectrometer. 4: Signal noise limitations in data retrieval; winds, temperature, and emission rate, *Applied Optics*, **17**, 18, 1978

Hernandez, G., *Fabry-Perot Interferometers*, Cambridge University Press, 1986

Hernandez, G., R.W. Smith and J.F. Conner, Neutral Wind and Temperature in the Upper Mesosphere Above South Pole Antarctica *Geophys. Res. Lett.*, **19**, 1, 53-56, January 3, 1992b

Hernandez, G., Analytical description of a Fabry-Perot spectrometer. 5: Optimization for minimum uncertainties in the determination of Doppler widths and shifts, *Appl. Opt.*, **17**, 3826, 1978

Hernandez, G., R.W. Smith, G.J. Fraser, and W.L. Jones, Large scale waves in the upper-mesosphere at Antarctic high-latitudes, *Geophys. Res. Lett.*, **19**, 1347-1350, 1992a

Hernandez, G., G.J. Fraser, and R.W. Smith, Mesospheric 12-hour oscillation near South Pole, Antarctica, *Geophys. Res. Lett.*, **20**, 1787-1790, 1993

Hernandez, G. and J.L. Smith, Mesospheric wind determinations and the P(2) lines of the OH (8-3) band, *Geophys. Res. Lett.*, **5** , 534-537, 1984.

Hernandez, G., R.W. Smith, R.G. Roble, J. Gress and K.C. Clark, Thermospheric dynamics at the South Pole, *Geophys. Res. Lett.*, **17** , 1255-1258, 1990.

Hill, E., J.H. Van Vleck, On the quantum mechanics of the rotational distortion of multiplets in molecular spectra, *Phys. Rev.*, **32**, 250-272, 1928

Jenkins, G.H., D.G. Watts, *Spectral analysis and its applications*, Holden-Day, 282-284, 1968

Johnson, R.M., Sondrestrom incoherent scatter radar observations during the lower thermosphere coupling study: September 21-26, 1987 *J. Geophys. Res.*, **96**, 1081-1090, 1991

Johnson, R.M., T.S. Virdi, High-latitude thermospheric neutral winds at EISCAT and Sondrestrom during LTCS-1, *J. Geophys. Res.*, **96**, 1099-1116,1991

Johnson, R.M., V.B. Wickwar, R.G. Roble and J.G. Luhmann, Lower thermospheric winds at high latitude: Chatanika radar observations, *Annales Geophysicae*, **5A(6)**, 383-404, 1987.

Krassovsky, V.I., *The Airglow and the Aurorae*, Pergamon Press, Ed. E.B. Armstrong and A. Dalgarno, p.197, 1955

Krassovsky, V.I., N.N. Shefov, V.I. Yarin, Atlas of the Airglow Spectrum 3000-12400Å, *Planet. Space Sci.*, **9**, 883-915, 1962

Kvifte, G.J., Nightglow OH Rotational Temperatures and Intensities, *Planet. Space Sci*, **15**, 1515-1523, 1967

Lomb, N.R., Least-squares frequency analysis of unequally spaced data, *Astrophysics and Space Science.*, **39**, 447-462, 1976

Longuet-Higgins, M.S., The eigenfunctions of Laplace's tidal equations over a sphere, *Phil. Trans. Roy. Soc. London*, **A262**, 511-607, 1968.

Manson, A. H., C.E. Meek, M. Massbeuf, J.L. Fellous, W.G. Elford, R.A. Vincent, R.L. Craig, R.G. Roper, S.K. Avery, B.B. Balsley, G.J. Fraser, M.J. Smith, R.R. Clark, S. Kato and T. Tsuda, Mean winds of the upper middle atmosphere (70-110 km) from the global radar network: comparisons with CIRA 72 and new rocket and satellite data, *Adv. Space Res.*, **7** , 143-153, 1987.

Murgatroyd, R.J., Winds and temperatures between 20 km and 100 km - a review, *Quart. J. R. Meteor. Soc.*, **83**, 417-458, 1957

Murgatroyd, R.J., and R.M. Goody, Sources and sinks of radiative energy from 30 to 90 km, *Quart. J. Roy. Met. Soc.*, **84**, 225-234, 1958

Manson, A. H., C.E. Meek, Schminder, Kürschner, R.R. Clark, Müller, R.A. Vincent, A. Phillips, G.J. Fraser, Singer, E.S. Kazimirovsky *J. Atmos. Terr. Physics*, **52**, 3, 175-183, 1990

Manson, A.H., C.E. Meek, S.K. Avery, G.J. Fraser, R.A. Vincent, A. Phillips, R.R. Clark, Schminder, Kürschner, and E.S. Kazimirovsky, Tidal winds from the mesosphere, lower thermosphere global radar network during the second LTCS campaign: December 1988, *J. Geophys. Res.*, **96**, 1117-1128, 1991

McPherson, D.H., A. Vallance Jones, A Study of the Latitude Dependence of OH Rotational Temperatures for Canadian Stations, *J. Atmos. Terr. Phys.*, **17**, 302-308, 1960

Meinel, A.B., OH emission bands in the spectrum of the night sky, *Astrophys. J.*, **112**, 120-130, 1950

Mlynczak, M. G., S. Solomon, Middle Atmosphere Heating by Exothermic Chemical Reactions Involving Odd-Hydrogen Species, *Geophys. Res. Lett.*, **18**, 1, 37-40, January 1991

Minkowski, R., J. Bruck, True and Apparent Breadth of Spectral Lines, *Zeitschrift für Physik*, **95**, 5-c, 299-301, 1935.

Miyahara, S., Yu. I. Portnyagin, J.M. Forbes, T.V. Solovjeva, Mean zonal acceleration and heating of the 70 to 100-km region, *J. Geophys. Res.*, **96**, A2, 1225-1238, Feb. 1991

Neuber, R., P. von der Gaten, U. von Zahn, Altitude and Temperature of the Mesopause at 69°N Latitude in Winter, *J. Geophys. Res.*, **93**, D9, 11093-11101, Sept. 20, 1988

Press, W.H., S.A. Teukolsky, *Computers in Physics*, **2**, 6, 77, 1988

Press, William H., Brian P. Flannery, Saul A. Teukolsky, and William T. Vettering, *Numerical Recipes: The Art of Scientific Computing*, New York: Cambridge University Press, 1986

Price, G., R.A. Vincent, F. Jacka, Winds and Temperatures in the Mesosphere and Lower Thermosphere at Mawson Antarctica, *ANARE Res. Notes 48*, **p. 148**, Antarct. Div., Dep. of Sci., Aust. Natl. Antarct. Res. Expd., Kingston, Tasmania, 1987.

Rees, M.H., *Physics and chemistry of the upper atmosphere*, Cambridge University Press, p.163, 1988

Roach, F.E., Helen Petit, and D.R. Williams, The height of the atmospheric OH emission, *J. Geophys. Res.*, **55**, 2, 1950

Roble, R. G., R.E. Dickinson and E.C. Ridley, Seasonal and solar cycle variations of the zonal mean circulation in the thermosphere, *J. Geophys. Res.*, **82** , 5493-5504, 1977.

Rogers, J. W., R.E. Murphy, A.T. Stair, J.C. Ulwick, K.D. Baker, and L.L. Jensen, Rocket-borne radiometric measurements of OH in the auroral zone, *J. Geophys. Res.*, **78**, p.7023, 1973

Salah, J.E., R.M. Johnson, and C.A. Tepley, Coordinated incoherent scatter radar observations of the semidiurnal tide in the lower thermosphere, *J. Geophys. Res.*, **96**, 1071-1080, 1991

Salby, M.L., Rossby normal modes in nonuniform background configurations. Part II: Equinox and solstice conditions, *J. Atmos. Sci.*, **38**, September 1981

Scargle, J.D., Studies in astronomical time series analysis. II. Statistical aspects of spectral analysis of unevenly spaced data, *Astrophysical J.*, **263**, 835-853, 1982

Shapiro, R., H. Stolov, Surface Pressure Variations in Polar Regions, *Journal of the Atmospheric Sciences*, **27**, p.1021, 1970

Shepherd, G.G., *Atmospheric Emissions*, ed. McCormac and Omholt, Van Nostrand Reinhold Company, p.411, 1968

Sivjee, G. G., R. L. Walterscheid, J. H. Hecht, R. M. Hamwey, G. Schubert and A. B. Christensen, Effects of atmospheric disturbances on Polar mesopause airglow OH emissions, *J. Geophys. Res.*, **92**, 7651-7656, 1987.

Stubbs, L.C., J.S. Boyd, F.R. Bond, Measurement of the OH Rotational Temperature at Mawson, East Antarctica, *Planet. Space Sci.*, **31**, 8, 923-932, 1983

Suzuki, Katsuhisa, Takao Tohmatsu, An Interpretation of the Rotational Temperature of the Airglow Hydroxyl Emissions, *Planet. Space Sci.*, **24**, 665-671, 1976

Tetenbaum, D., J.M. Holt, and J.E. Salah, High resolution observations of the lower thermosphere at Millstone Hill during the September 1987 LTCS campaign, *Adv. Space Res.*, **10(6)**, 277-280, 1990

Ulwick, J.C., K.D. Baker, D.J. Baker, A.J. Steed, W.R. Pendelton, Jr., K. Grossmann, and H.G. Bruckelmann, Mesospheric minor species determinations from rocket and ground-based IR measurements, *J. Atmos. Terr. Phys.*, **49**, 855-862, 1987.

Walterscheid, R.L., Inertio-gravity wave induced accelerations of mean flow having an imposed periodic component: implications for tidal oscillations in the meteor region, *J. Geophys. Res.*, **86** , p.9698, 1981.

Walterscheid, R.L., G.G. Sivjee, G. Schubert, and R.M. Hamwey, Large amplitude semidiurnal temperature variations in the polar mesosphere. Evidence of a pseudotide. *Nature*, **324** , 347-349, 1986.

Walterscheid, R.L., G. Schubert, J.M. Strauss, A Dynamical-Chemical Model of Wave-Driven Fluctuations in the OH Nightglow, *J. Geophys. Res.*, **92**, A2, 1241-1254, February 1987a

Walterscheid, R.L., G. Schubert, A Dynamical-Chemical Model of Tidally Driven Fluctuations in the OH Nightglow, *J. Geophys. Res.*, **92**, A8, 8775-8780, August 1987b

Williams, P.F.B., OH nightglow observations and temperature determination at Davis, Antactica, *ANARE Res. Notes 48*, **p.176**, Antarct. Div., Dep. of Sci., Aust. Natl. Antarct. Res. Expd., Kingston, Tasmania, 1987.

Viereck, R.A., A review of mesospheric dynamics and chemistry, *Reviews of Geophysics*, **29**, pt.2, 1132-1142, 1991

Viereck, R. A. and C. S. Deehr, On the interaction between gravity waves and the OH Meinel (6-2) and the O atmospheric (0-1) bands in the polar night airglow. *J. Geophys. Res.*, **94** , 5497-5504, 1989.

Vincent, R.A., Planetary and gravity waves in the mesosphere and lower thermosphere, *Adv. Space Res.*, **10**, 1987

Volland, H., *Atmospheric tidal and planetary waves*, Kluwer Academic Publishers, 1988

Witt, G., J. Stegman, B. H. Solheim and E. J. Llewellyn, A measurement of the O_2 ($b^1\Sigma_g^+ - X^3\Sigma_g^-$) atmospheric band and the OI(^1S) green line in the nightglow, *Planet. Space Sci.*, **27**, 341-350, 1979.

Yashimoto, H., Wave dynamics in the mesospheric hydroxyl layer, *Ph.D. dissertation*, Geophysics Laboratory, Air Force Systems Command, Hanscom, GL-TR-90-0211, 1990

Appendix A Full period Lomb and Scargle type periodograms.

This appendix contains the periodograms from the three periods. Figure (A.1) contains 5 panels for the neutral wind periodograms for May 22-30, 1990. From top to bottom (300°E), (30°E), (210°E), (120°E), and Zenith.

Figure (A.2) contains 5 panels for the kinetic temperature periodograms for May 22-30, 1990. From top to bottom (300°E), (30°E), (210°E), (120°E), and Zenith.

Figure (A.3) contains 5 panels for the countrate periodograms for May 22-30, 1990. From top to bottom (300°E), (30°E), (210°E), (120°E), and Zenith.

Figure (A.4) contains 4 panels for the neutral wind periodograms for August 2-25, 1991. From top to bottom (300°E), (345°E), (30°E), and (75°E).

Figure (A.5) contains 5 panels for the neutral wind periodograms for August 2-25, 1991. From top to bottom (120°E), (165°E), (210°E),(255°E), and Zenith.

Figure (A.6) contains 4 panels for the kinetic temperature periodograms for August 2-25, 1991. From top to bottom (300°E), (345°E), (30°E), and (75°E).

Figure (A.7) contains 5 panels for the kinetic temperature periodograms for August 2-25, 1991. From top to bottom (120°E), (165°E), (210°E),(255°E), and Zenith.

Figure (A.8) contains 4 panels for the countrate periodograms for August 2-25, 1991. From top to bottom (300°E), (345°E), (30°E), and (75°E).

Figure (A.9) contains 5 panels for the countrate periodograms for August 2-25, 1991. From top to bottom (120°E), (165°E), (210°E),(255°E), and Zenith.

Figure (A.10) contains 4 panels for the neutral wind periodograms for July 1-13, 1992. From top to bottom (300°E), (345°E), (30°E), and (75°E).

Figure (A.11) contains 5 panels for the neutral wind periodograms for July 1-13, 1992. From top to bottom (120°E), (165°E), (210°E),(255°E), and Zenith.

Figure (A.12) contains 4 panels for the kinetic temperature periodograms for July 1-13, 1992. From top to bottom (300°E), (345°E), (30°E), and (75°E).

Figure (A.13) contains 5 panels for the kinetic temperature periodograms for July 1-13, 1992. From top to bottom (120°E), (165°E), (210°E),(255°E), and Zenith.

Figure (A.14) contains 4 panels for the countrate periodograms for July 1-13, 1992. From top to bottom (300°E), (345°E), (30°E), and (75°E).

Figure (A.15) contains 5 panels for the countrate periodograms for July 1-13, 1992. From top to bottom (120°E), (165°E), (210°E),(255°E), and Zenith.

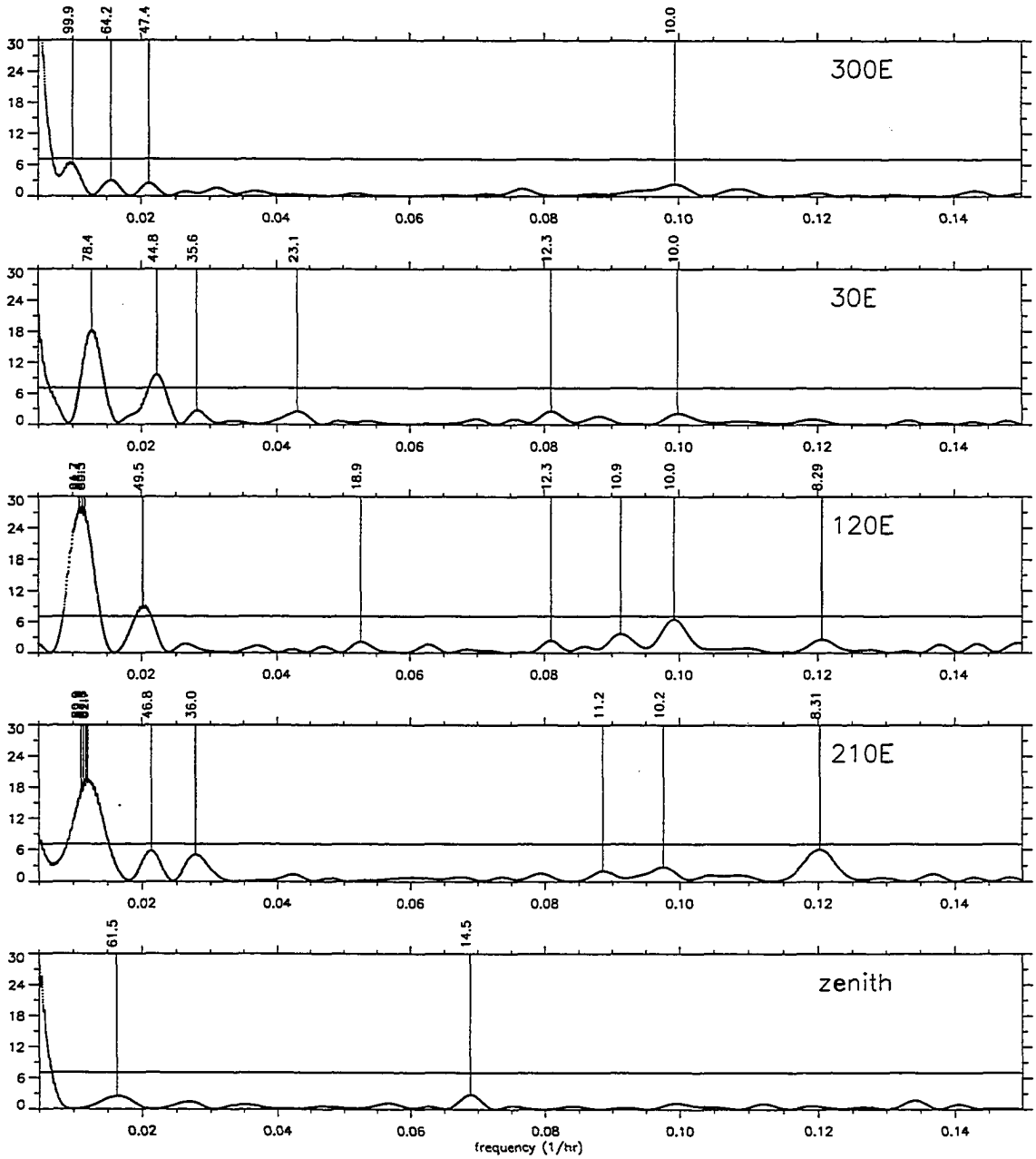

Figure A.1 Neutral wind power spectra from May 22-31, 1990 from OH(6-2) emissions at 8399Å over South pole station looking in all (four) observing azimuths and the zenith. The Lomb-Scargle derived 95% confidence level are indicated by a horizontal line.

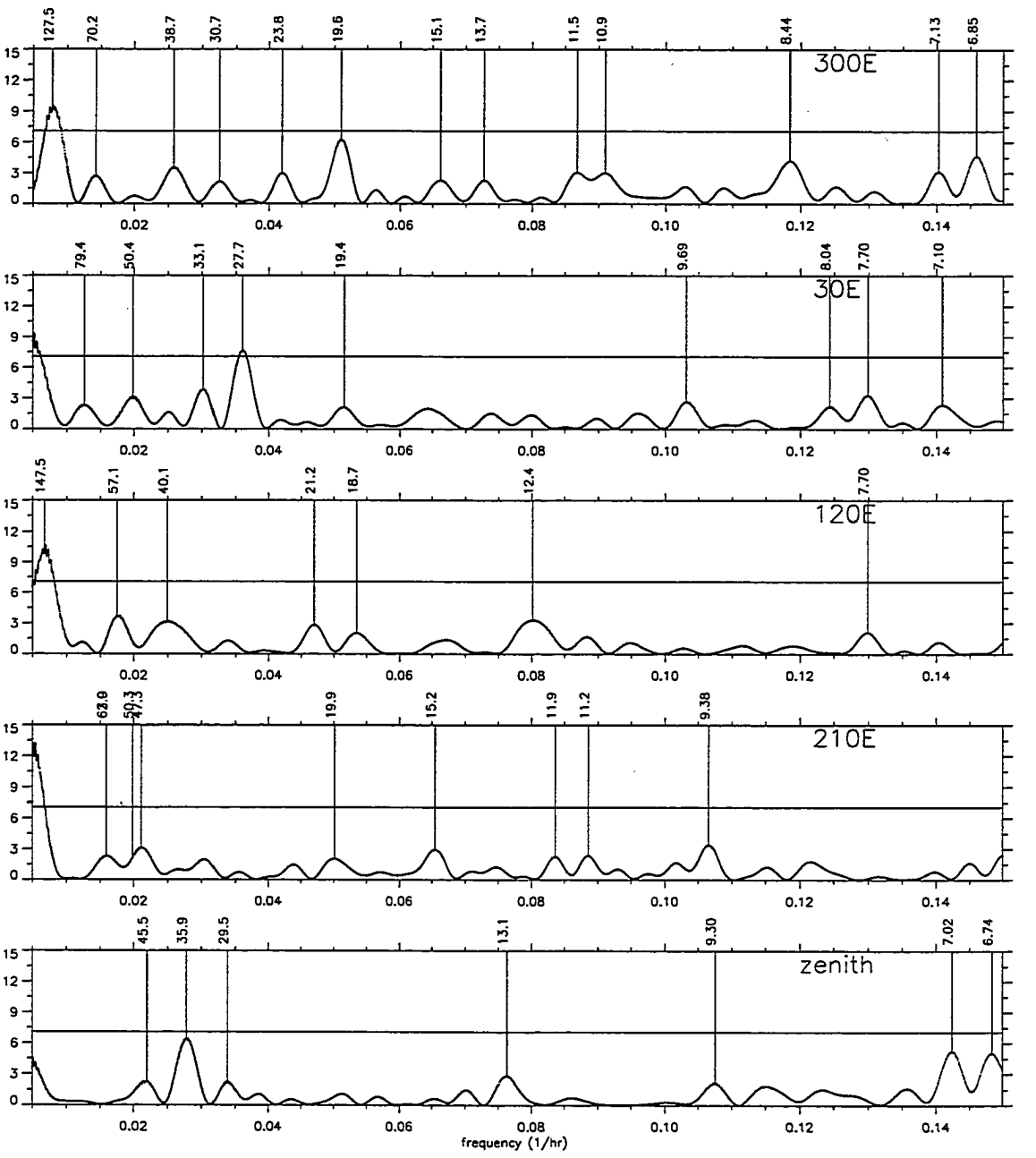

Figure A.2 Temperature power spectra from May 22-31, 1990 as in Figure (A.1).

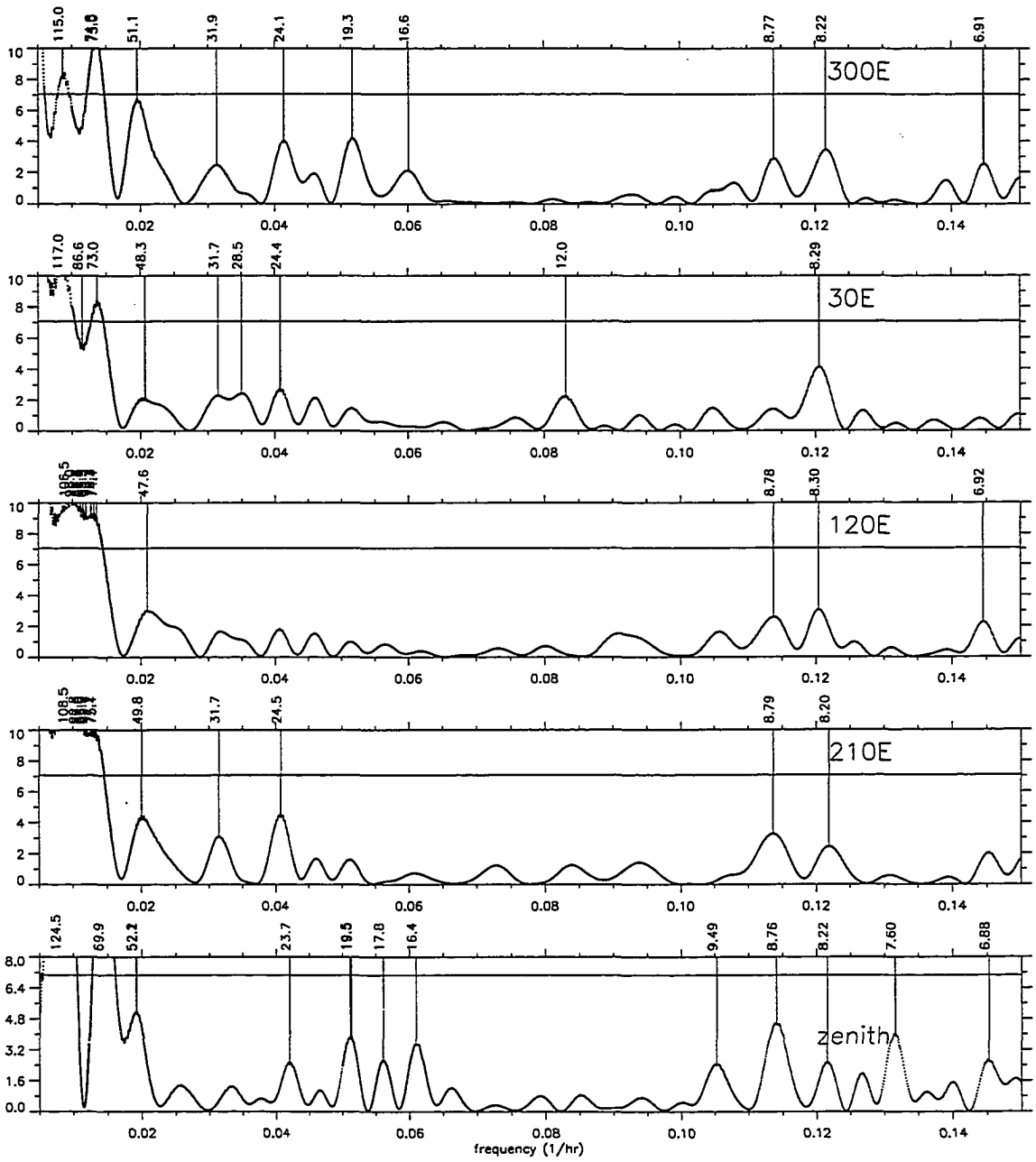

Figure A.3 Intensity power spectra from May 22-31, 1990 as in Figure (A.1).

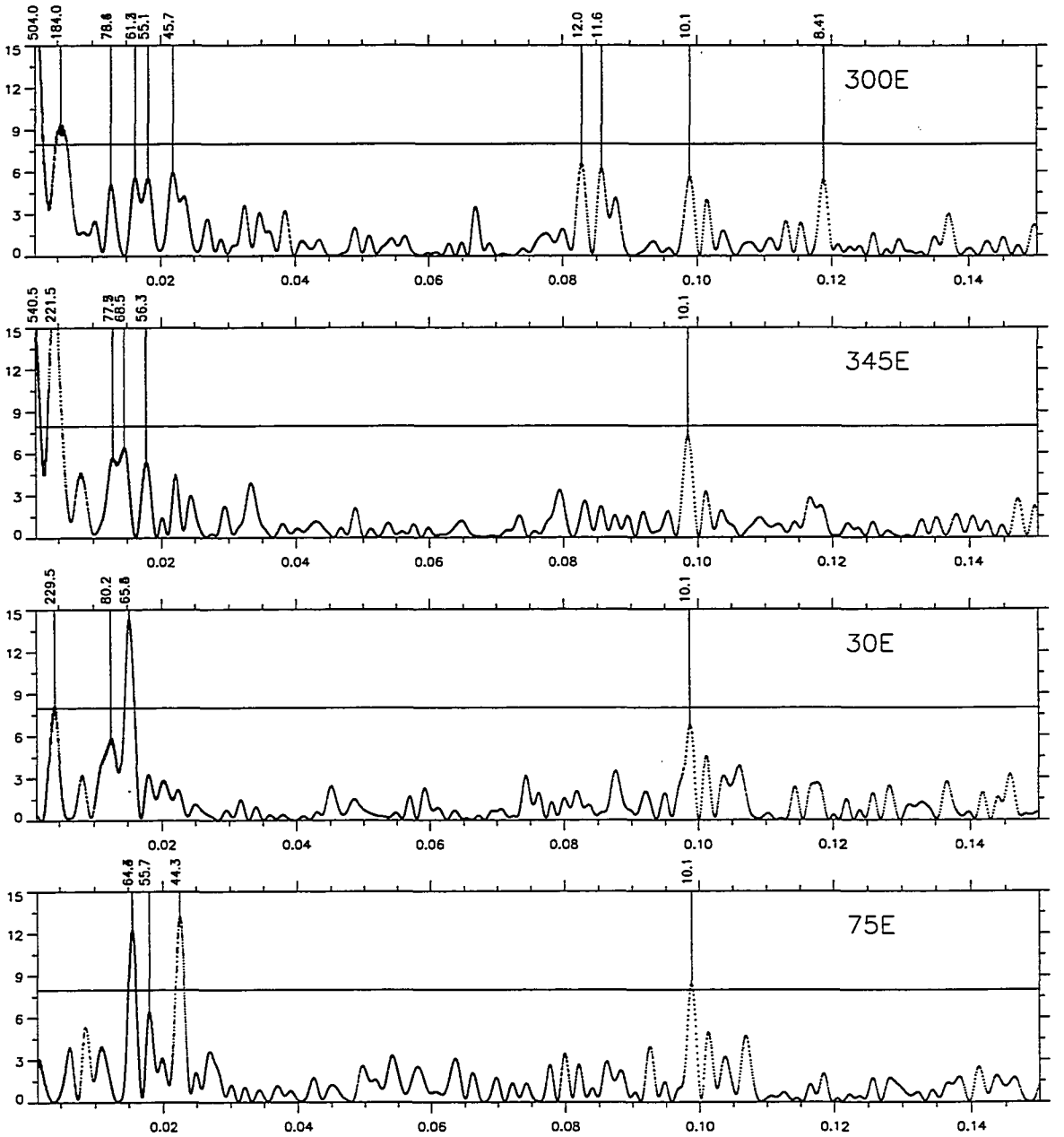

Figure A.4 Neutral wind power spectra from August 2-25, 1991 derived from OH(6-2) emissions at 8399Å over South pole station for the first four (of eight) observing azimuths. The Lomb-Scargle derived 95% confidence level are indicated by a horizontal line.

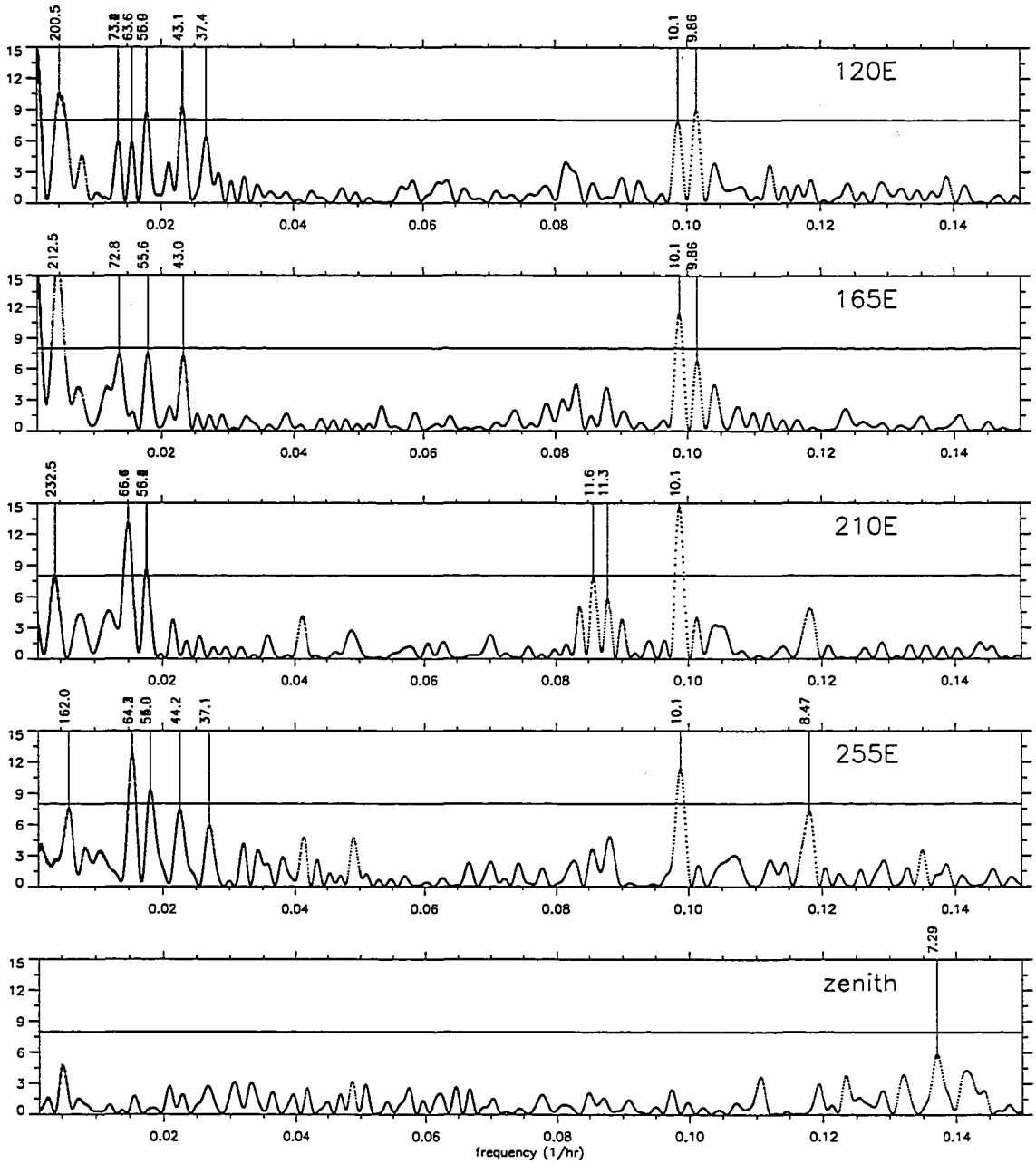

Figure A.5 Neutral wind power spectra from August 2-25, 1991 as for Figure (A.4) but for the second four (of eight) observing azimuths and the zenith.

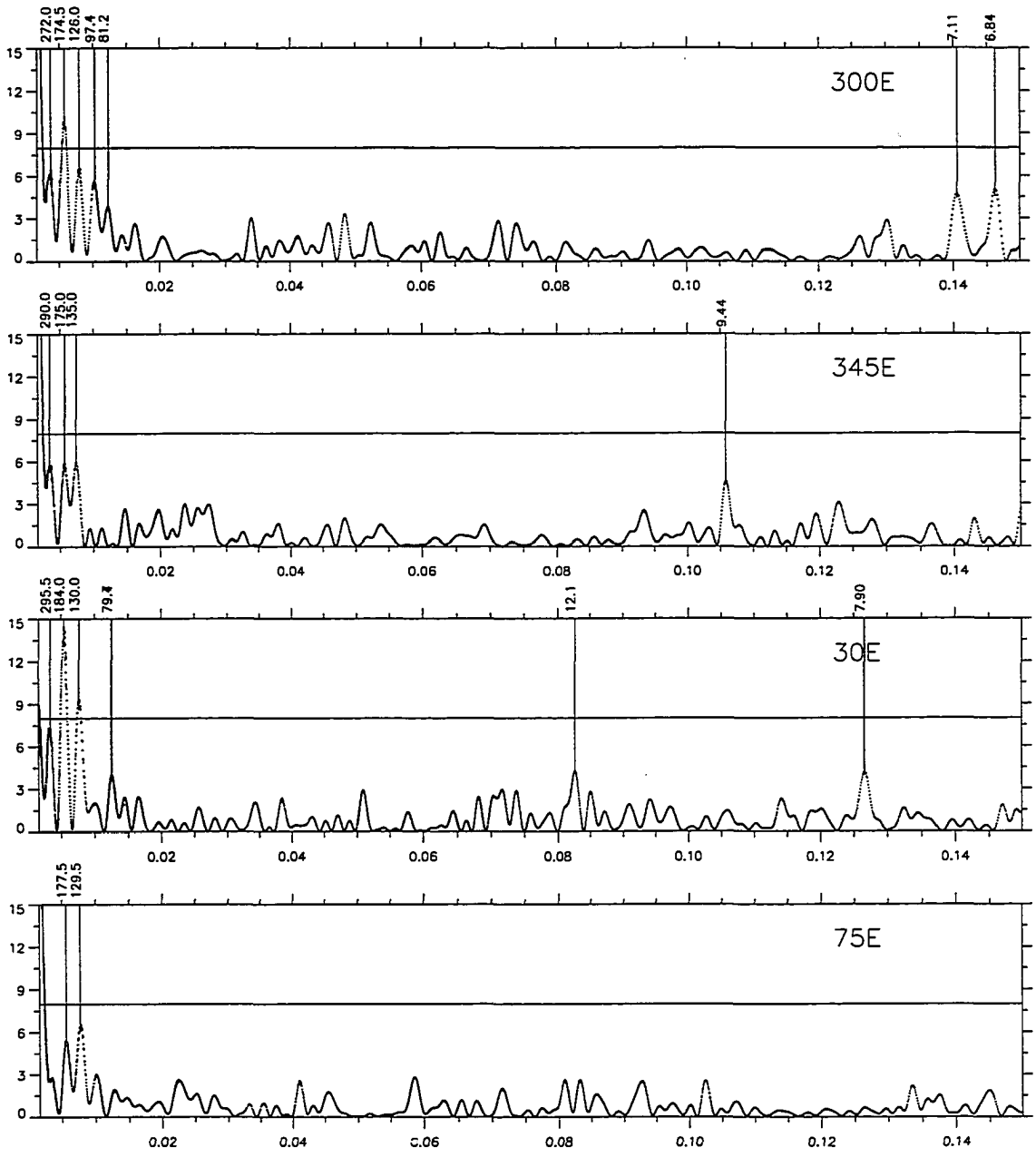

Figure A.6 Temperature power spectra from August 2-25, 1991 as in Figure (A.4).

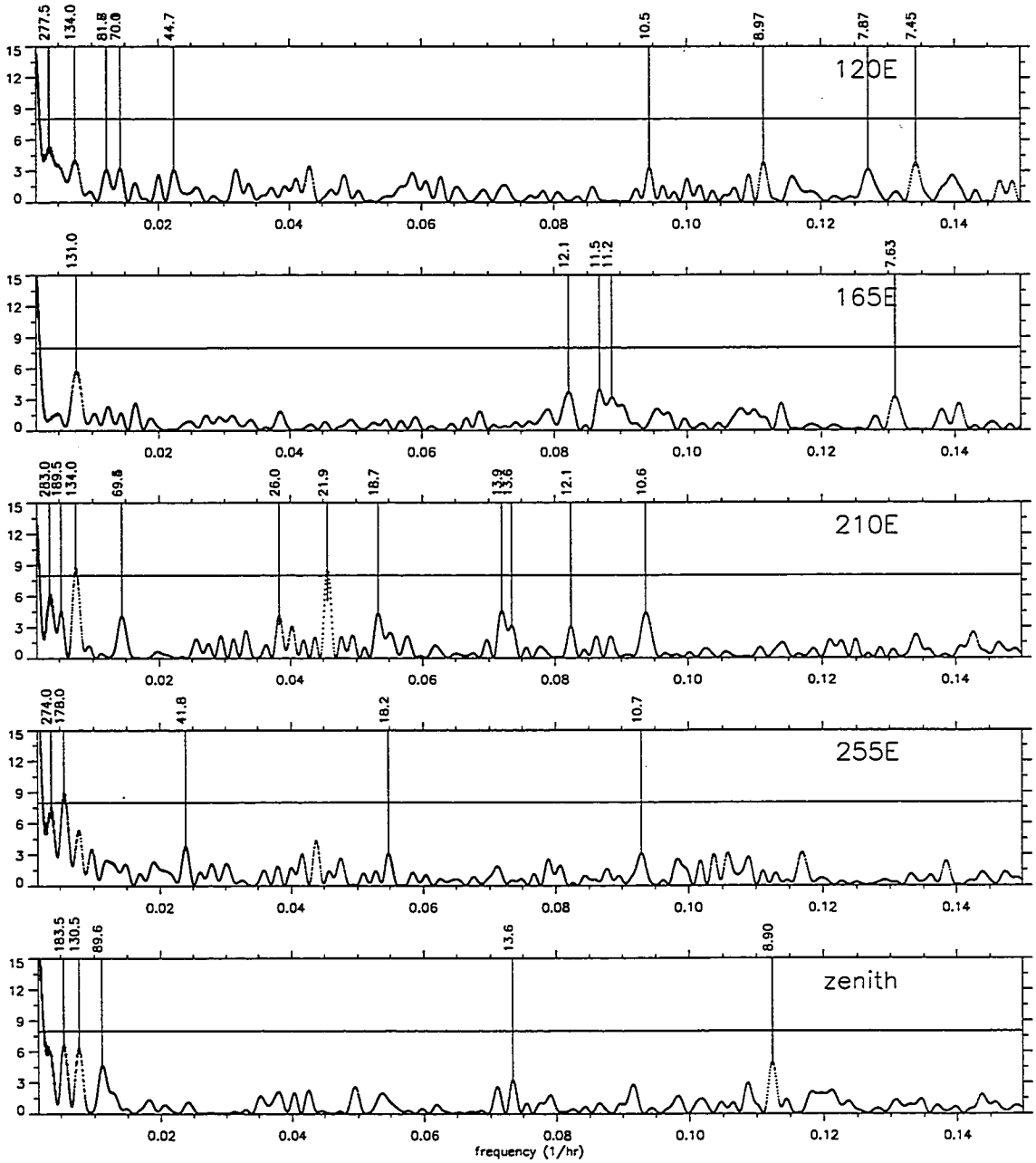

Figure A.7 Temperature power spectra from August 2-25, 1991 as in Figure (A.5).

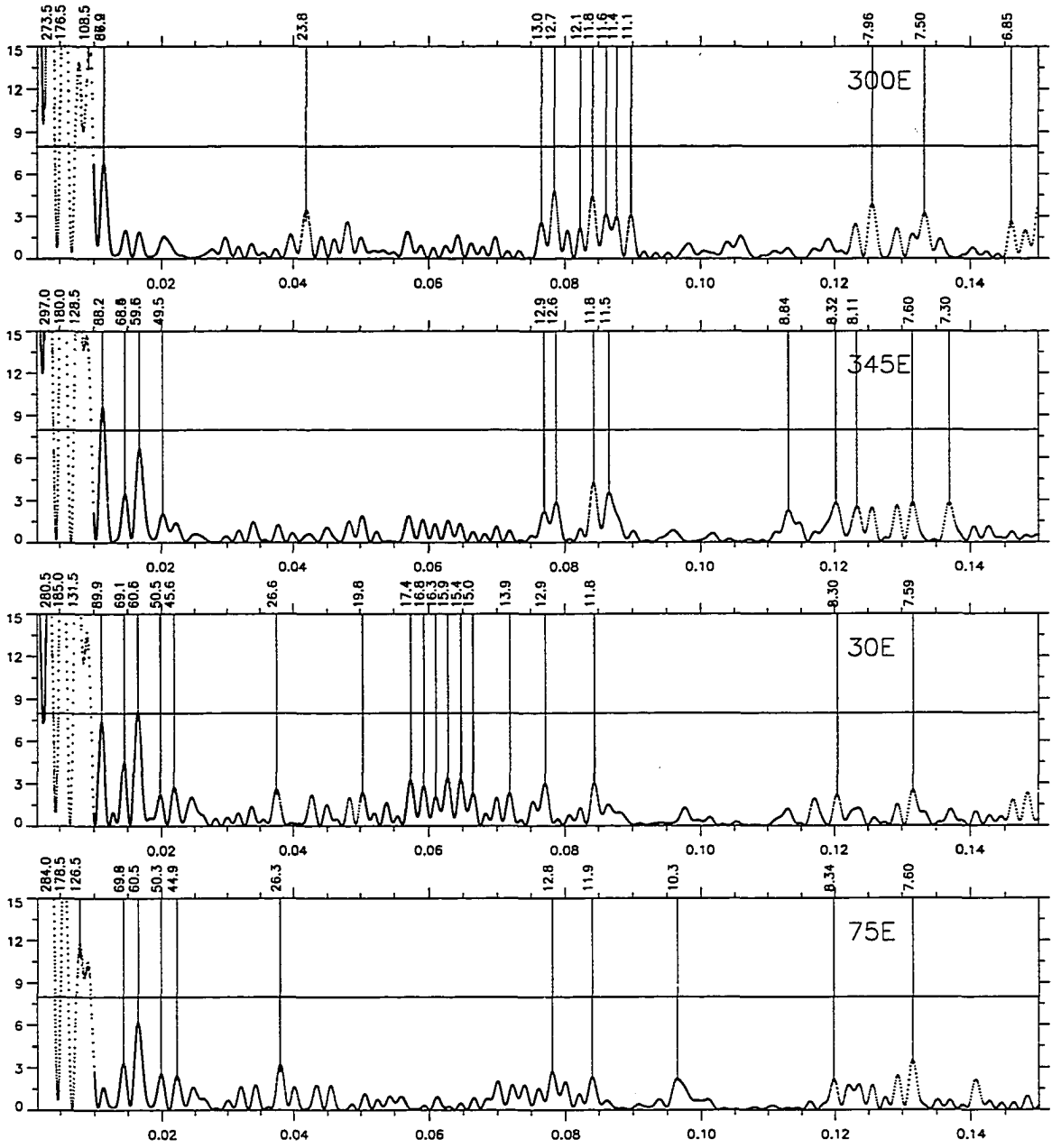

Figure A.8 Intensity power spectra from August 2-25, 1991 as in Figure (A.4).

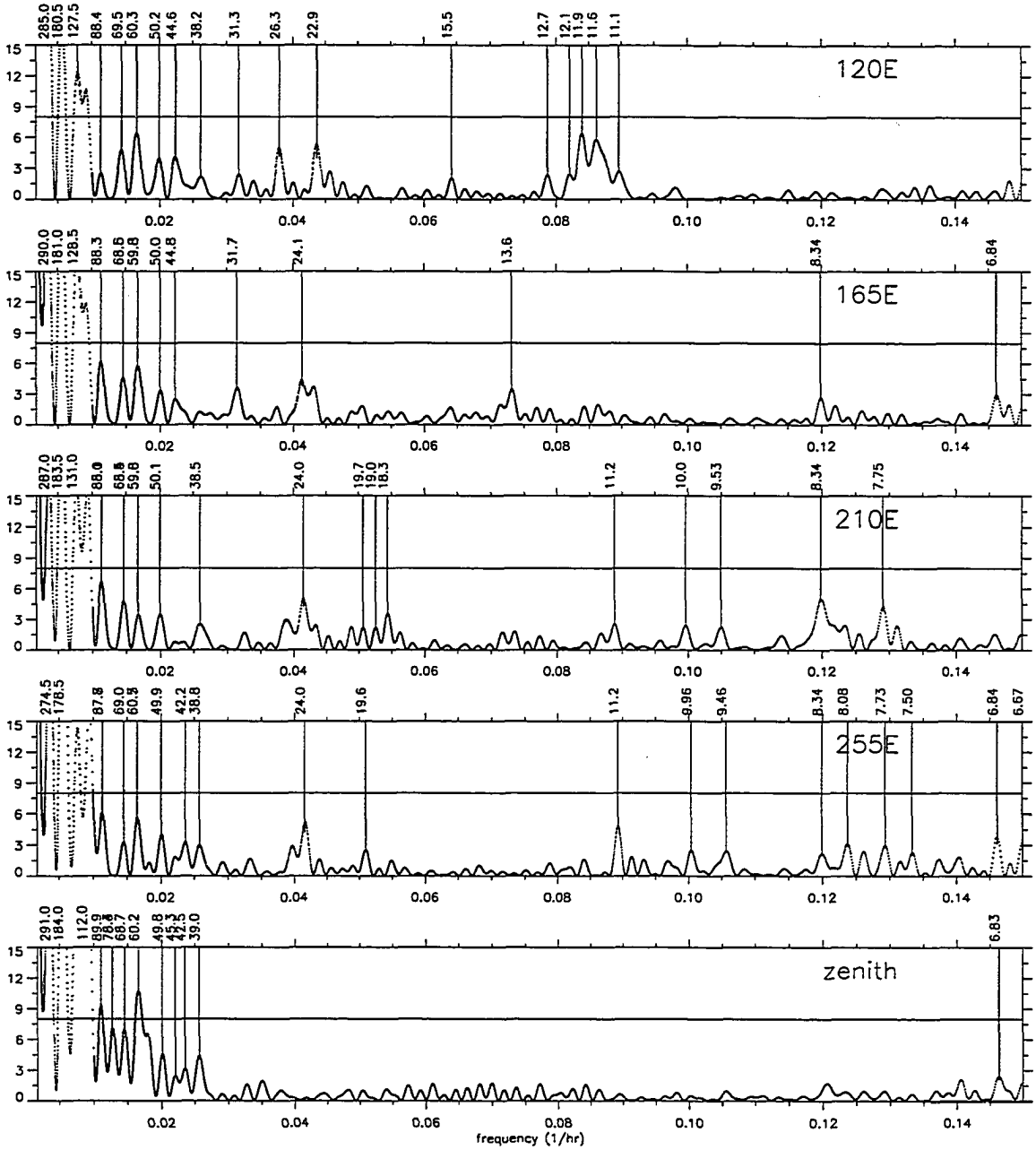

Figure A.9 Intensity power spectra from August 2-25, 1991 as in Figure (A.5).

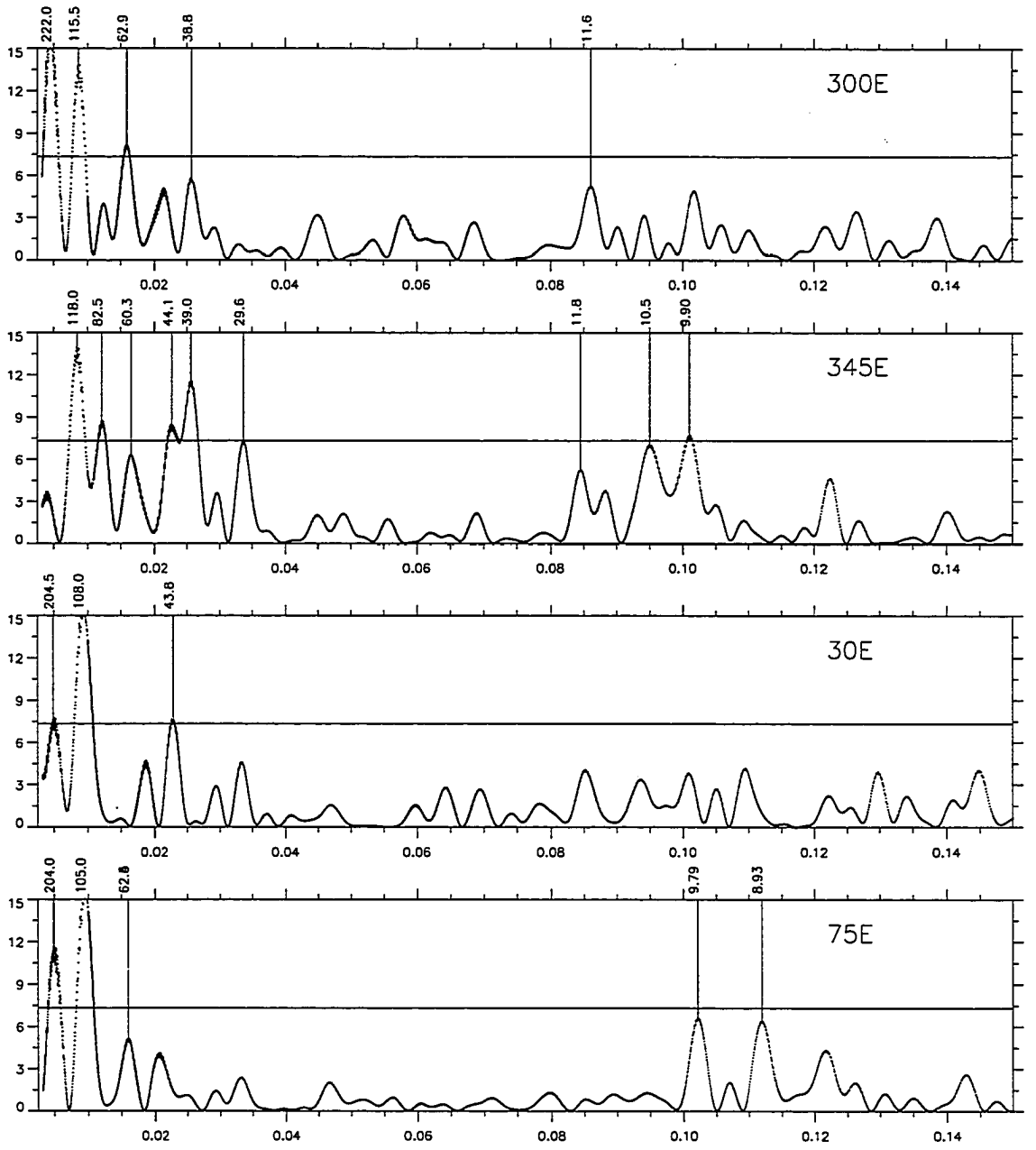

Figure A.10 Neutral wind power spectra from July 1-13, 1992 derived from OH(6-2) emissions at 8399Å over South pole station for the first four (of eight) observing azimuths. The Lomb-Scargle derived 95% confidence level are indicated by a horizontal line.

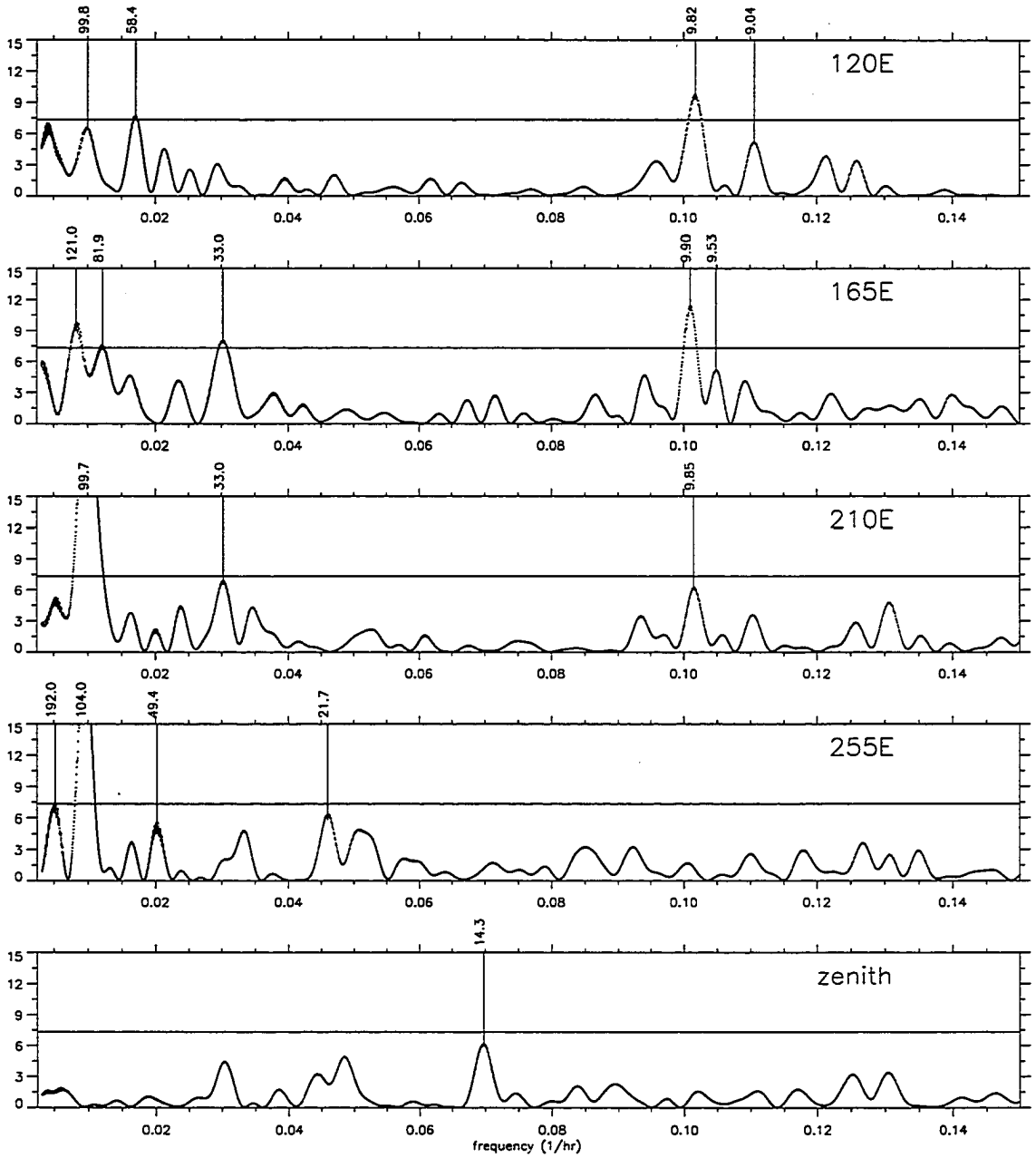

Figure A.11 Neutral wind power spectra from July 1-13, 1992 as for Figure (A.10) but for the second four (of eight) observing azimuths and the zenith.

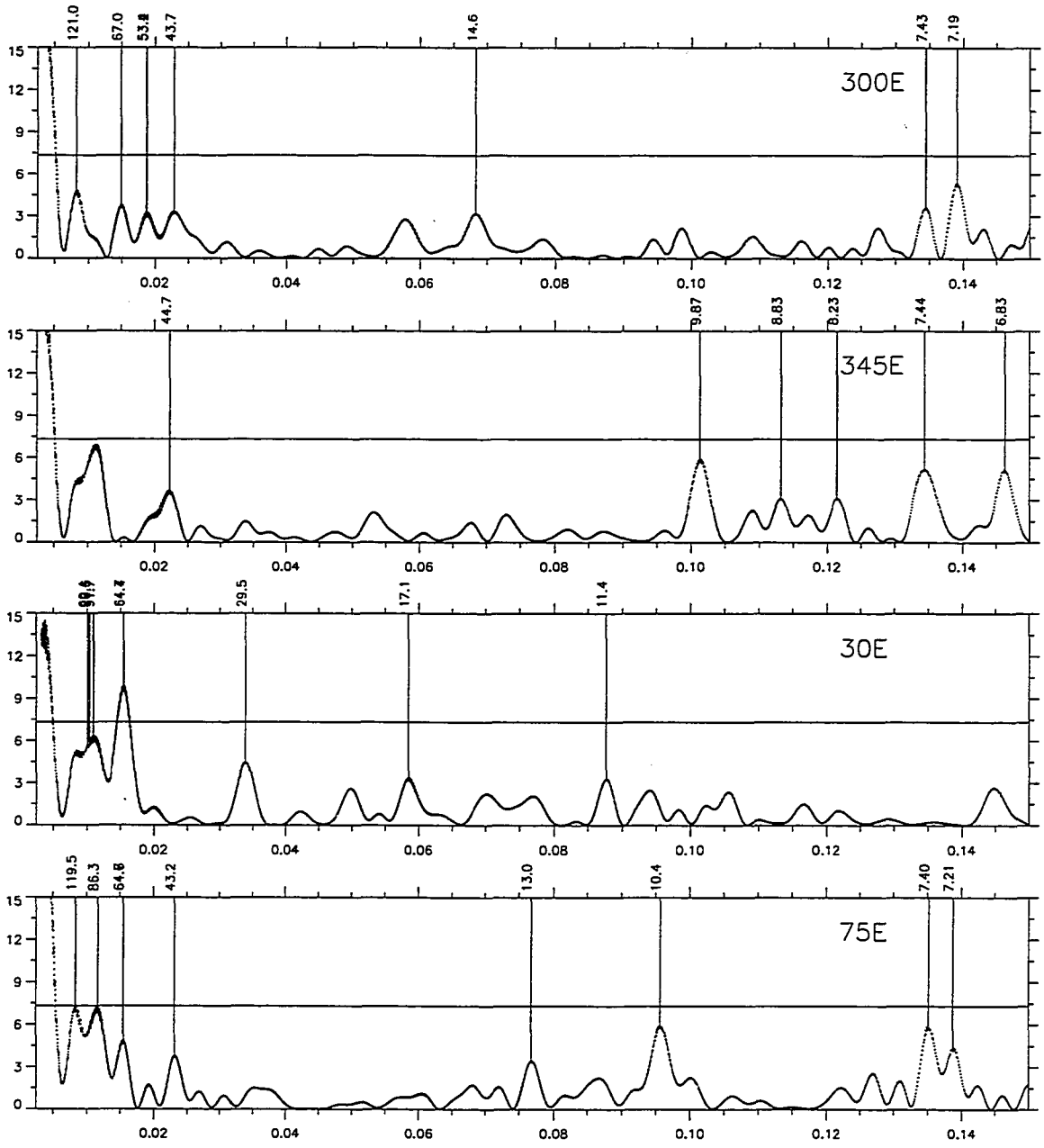

Figure A.12 Temperature power spectra from July 1-13, 1992 as in Figure (A.10).

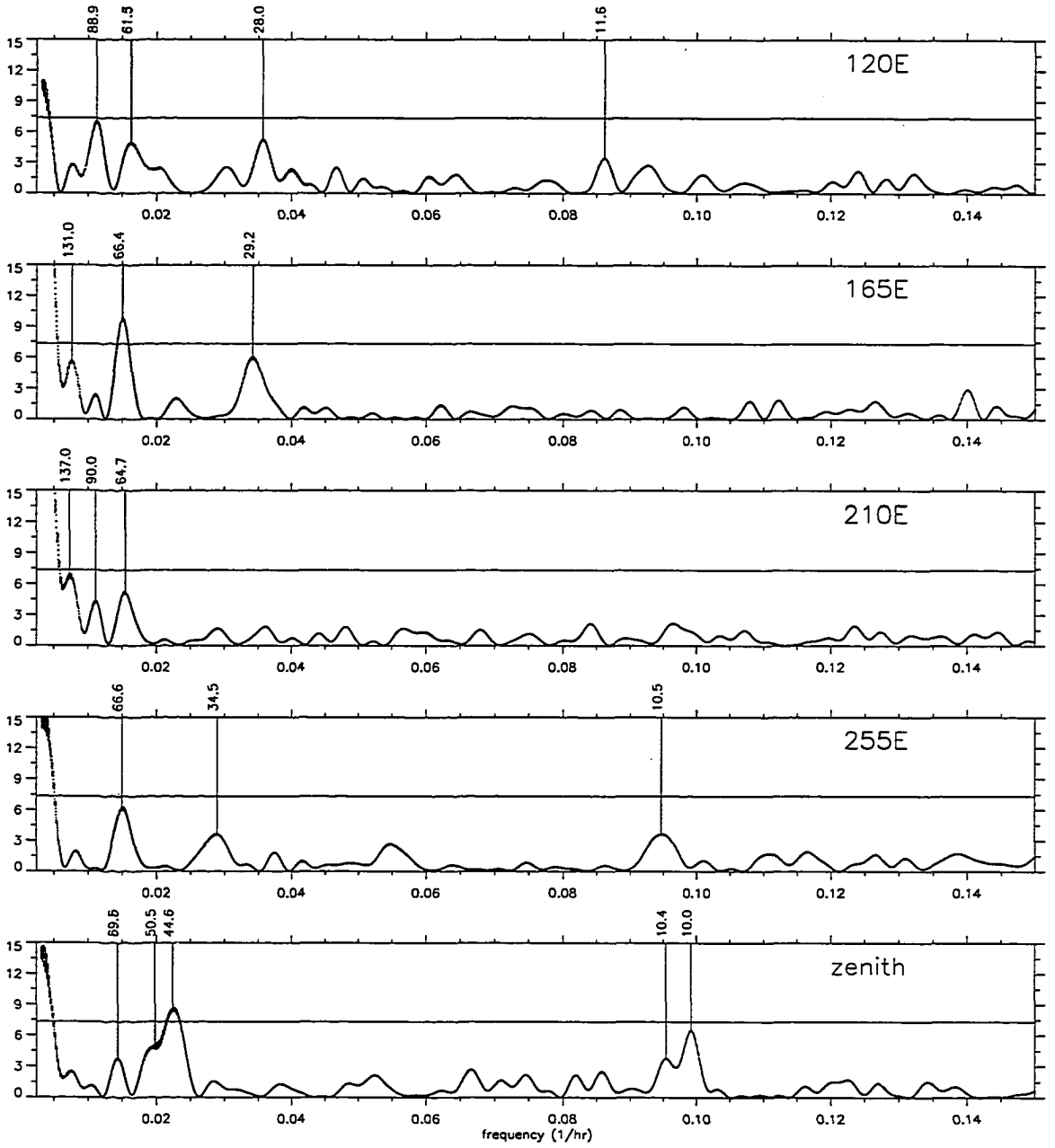

Figure A.13 Temperature power spectra from July 1-13, 1992 as in Figure (A.11).

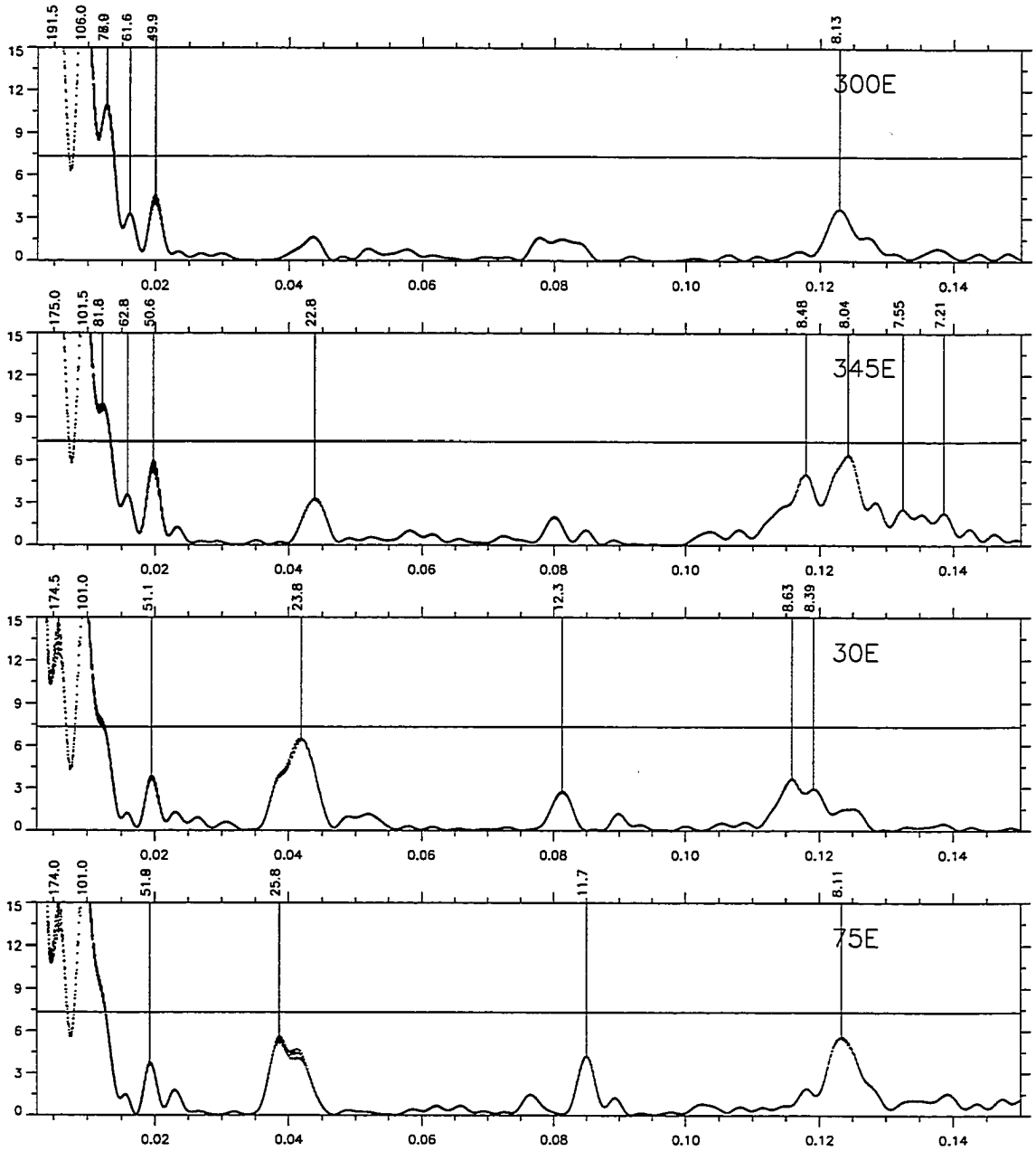

Figure A.14 Intensity power spectra from July 1-13, 1992 as in Figure (A.10).

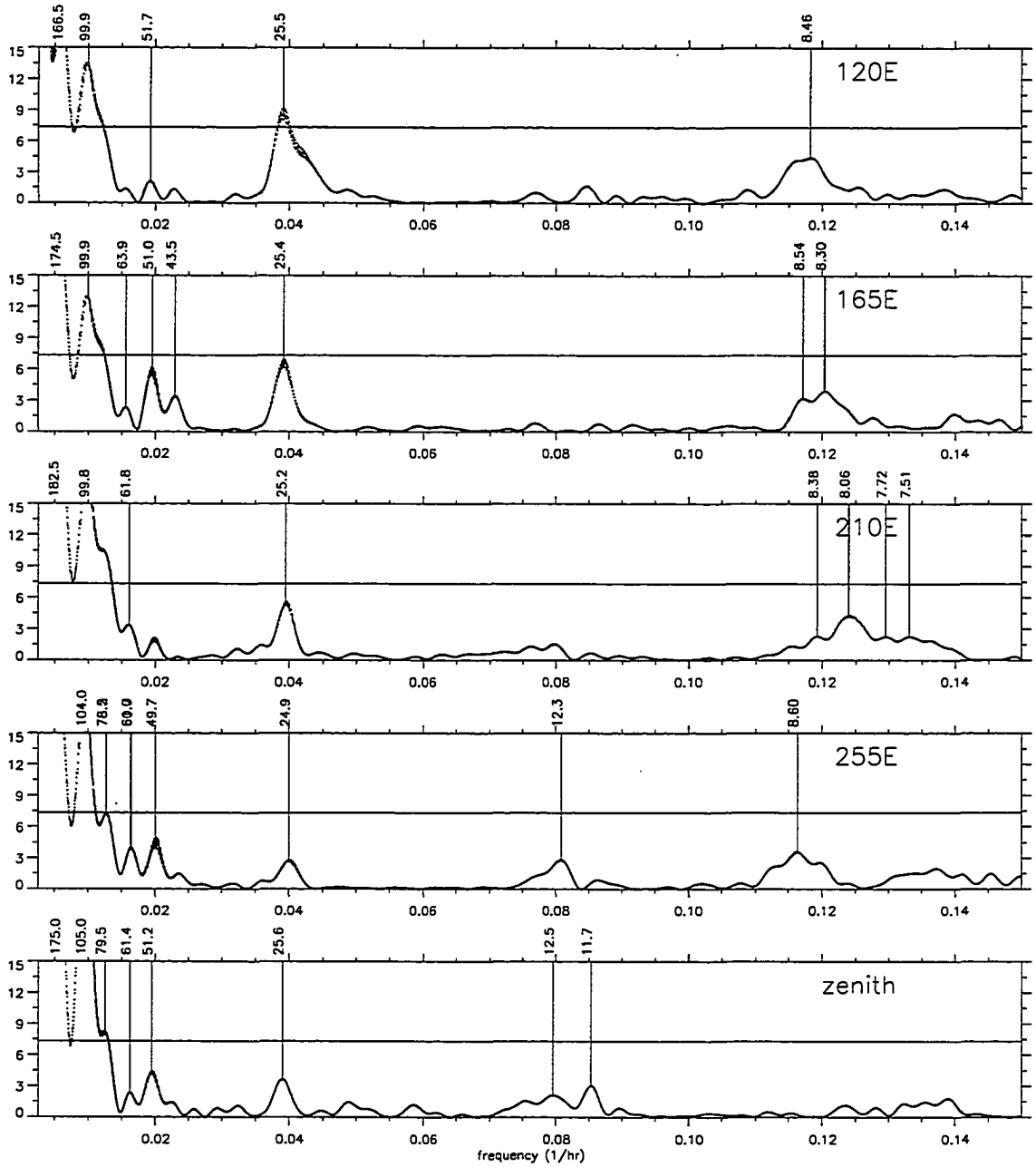

Figure A.15 Intensity power spectra from July 1-13, 1992 as in Figure (A.11).

Appendix B Elementary derivations for the FPI theory

This appendix is intended to explain specific key parameters discussed in the body of the thesis. The bulk of this material is found in many texts and in particular the work of Hernandez (1986) is drawn upon for the most part.

Consider a plane-parallel slab of refractive index μ with partially reflective surfaces upon which a plane wave of monochromatic radiation is incident at an angle Φ to the normal, (see Figure (B.1)). At the first surface, the wave is divided into two plane waves, one reflected, and directed towards lens L' and the other transmitted towards lens L. And this division process by partial reflection and transmission continues inside the slab. The phase lag, Φ, between two emerging waves, is determined by:

$$\text{path difference } = 2l - s = 2\left(\frac{d}{\cos\Theta}\right) + \frac{2d\sin^2\Theta}{\cos\Theta} = 2d\cos\Theta. \tag{B.1}$$

Now for the phase lag

$$\Phi \stackrel{\text{def}}{=} \Delta\phi = \frac{\Delta\phi}{\Delta t}\Delta t \tag{B.2}$$

where Δt is the transit time through the distance 'd', and $\frac{\Delta\phi}{\Delta t}$ the phase velocity. Thus

$$\Phi = 2\pi\nu\frac{2d\cos\Theta}{c/\mu} \tag{B.3}$$

where c is the speed of light in vacuum and ν the frequency in a vacuum. Consider each surface to be described by its complex reflection and transmission amplitude coefficients with r and t for reflections or transmission from an external surface and r' and t' for reflections or transmissions from an internal surface. For an incident wave of amplitude

$A^{(i)}$ the amplitude of each successive wave reflected from the plate is:

$$rA^{(i)}, t^2r'A^{(i)}e^{i\Phi}, t^2r'^3A^{(i)}e^{2i\Phi}, \ldots t^2r'^{(2p-3)}A^{(i)}e^{i(p-1)\Phi}, \ldots$$

and transmitted:

$$tt'A^{(i)}, tt'r'^2A^{(i)}e^{i\Phi}, tt'r'^4A^{(i)}e^{2i\Phi}, \ldots tt'r'^{2(p-1)}A^{(i)}e^{i(p-1)\Phi}, \ldots$$

The reflected and transmitted amplitudes focused by the lenses are then given by

$$\begin{aligned} A^{(r)}(\Phi) &= \{r + t^2r'e^{i\Phi} + t^2r'^3e^{2i\Phi} + \ldots t^2r'^{(2p-3)}e^{i(p-1)\Phi} + \ldots\}A^{(i)} \\ &= \left[\left(1 - e^{i\Phi}\left(\mathcal{R} + \mathcal{T}\right)\right)\mathcal{R}^{1/2}\right]\left(1 - \mathcal{R}e^{i\Phi}\right)^{-1}A^{(i)} \end{aligned} \tag{B.4}$$

for the reflected light and

$$\begin{aligned} A^{(t)}(\Phi) &= \{tt' + tt'r'^2e^{i\Phi} + tt'r'^4e^{2i\Phi} + \ldots tt'r'^{2(p-1)}e^{i(p-1)\Phi} + \ldots\}A^{(i)} \\ &= \mathcal{T}\left(1 - \mathcal{R}e^{i\Phi}\right)^{-1}A^{(i)} \end{aligned} \tag{B.5}$$

for the transmitted waves. Where the geometric progression has been extracted as $p \rightarrow \infty$. From Fresnel's equations the following relations can be derived:

$$tt' = \mathcal{T}$$

$$r = -r'$$

$$r^2 = r'^2 = \mathcal{R}$$

where

$$\delta = 2\Delta\phi + 2\chi$$

and χ is the phase change upon reflection on each of the surfaces. Now for the intensities, $\mathcal{I}^{(r)} = A^{(r)}A^{(r)^*}$, get

$$\mathcal{I}^{(r)} = \frac{\left(1 - 2\mathcal{R} + \mathcal{T}\cos(\delta) + \left(\mathcal{R} + \mathcal{T}\right)^2\right)\mathcal{R}}{1 + \mathcal{R}^2 - 2\mathcal{R}\cos(\delta)}\mathcal{I}^{(i)} \tag{B.6}$$

and similarly for the transmitted intensity,

$$\mathcal{I}^{(t)} = \frac{\mathcal{T}^2}{1 + \mathcal{R}^2 - 2\mathcal{R}\cos(\delta)}\mathcal{I}^{(i)}. \tag{B.7}$$

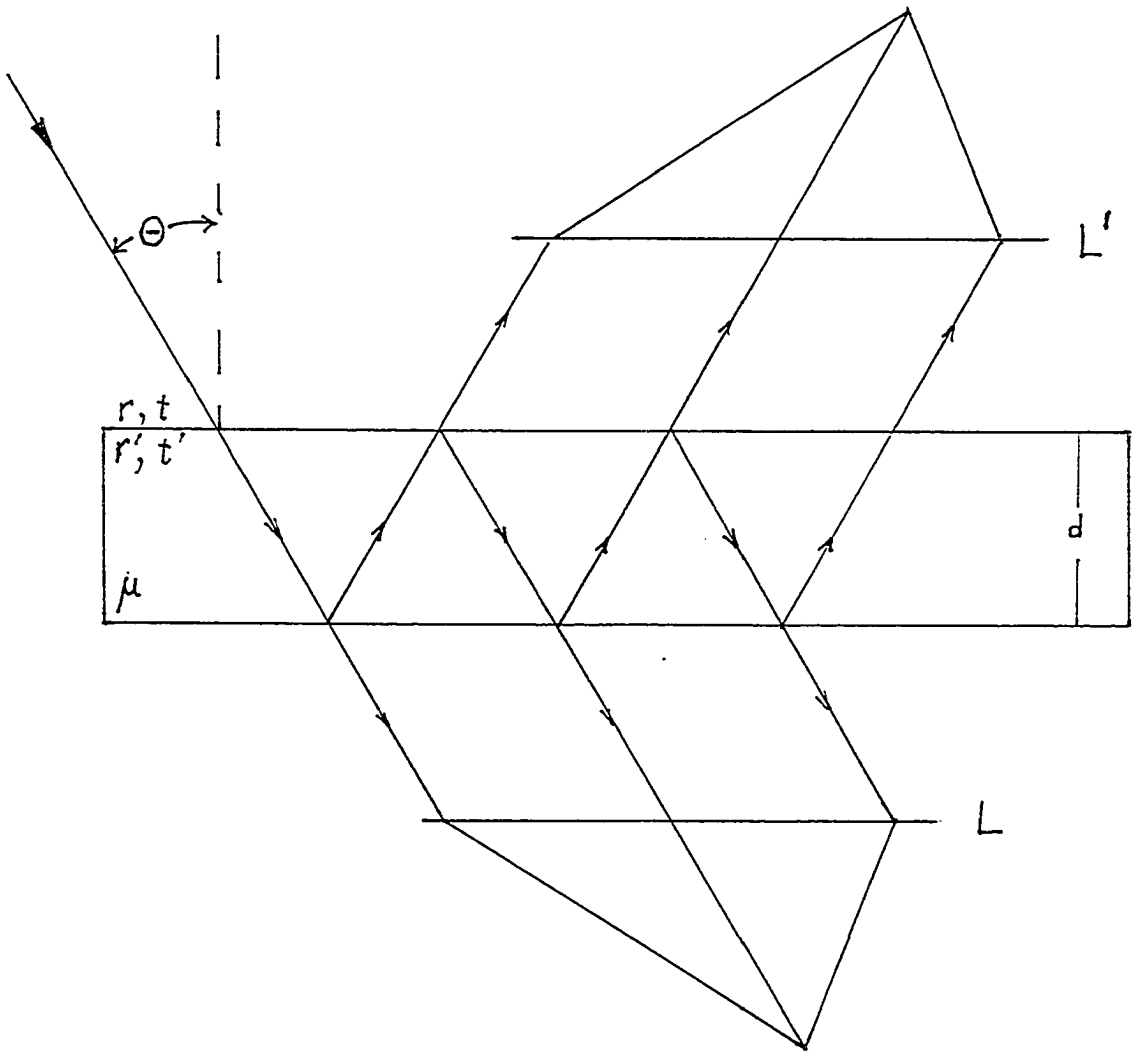

Figure B.1 Ideal etalon optical geometry showing the reflection and transmission raypaths. The external surfaces of the slab of refractive index μ have reflection and transmission coefficients r and t, respectively and those for the surfaces inside the slab are r′ and t′ . L and L′ are lenses and Θ is the angle of incidence of the initial ray. d is the physical thickness of the slab.

In general $\mathcal{A}_e + \mathcal{R} + \mathcal{T} = 1$, with $\mathcal{A}_e$ = the absorption/scattering coefficient of the slab. Eliminating $\mathcal{T}$ we can recast (B.7) as

$$\mathcal{I}^{(r)} = \left[1 - \frac{\mathcal{A}_e}{(1-\mathcal{R})}\right]^2 \frac{(1-\mathcal{R})}{(1+\mathcal{R})} \left[1 + 2\sum_{m=1}^{m=\infty} \mathcal{R}^m cos(m\delta)\right] \tag{B.8}$$

or equivalently as

$$\mathcal{I}^{(r)} = \left[1 - \frac{\mathcal{A}_e}{(1-\mathcal{R})}\right]^2 (1-\mathcal{R})^2 \left[1 + \mathcal{R}^2 - 2\mathcal{R}cos(\delta)\right]^{-1} \tag{B.9}$$

Expressions (B.8) and (B.9) were derived for monochromatic light incident at an angle Θ. For more general applications I am interested in quasi-monochromatic light from an extended source, that is, incident over a range of angles. It is found that for an arbitrary source with source coefficients s_k the etalon response is given by

$$\mathcal{I}^{(r)} = \left[1 - \frac{\mathcal{A}_e}{(1-\mathcal{R})}\right]^2 \frac{(1-\mathcal{R})}{(1+\mathcal{R})} \left[1 + 2\sum_{k=1}^{k=\infty} \mathcal{R}^k s_k cos(2\pi k \frac{\sigma_0}{\Delta\sigma} cos\Theta)\right] \tag{B.10}$$

For a gaussian distribution in intensity of a small wavelength range of a Doppler shifted spectral emission from a particular molecular species. Representing this source distribution $\mathcal{S}$ as

$$\mathcal{S} = \left[\frac{ln(2)}{\pi}\right]^{1/2} \frac{1}{dg} exp[-(\frac{\sigma - \sigma_0}{dg})^2 ln(2)] \tag{B.11}$$

with the transform coefficients

$$s_k = exp[-(\pi k \frac{dg}{\Delta\sigma\sqrt{ln(2)}})^2]. \tag{B.12}$$

The convolution of this source with the etalon response is then given as

$$\mathcal{I}^{(r)} = \left[1 - \frac{\mathcal{A}_e}{(1-\mathcal{R})}\right]^2 \frac{(1-\mathcal{R})}{(1+\mathcal{R})}$$

$$\times \left[1 + 2\sum_{k=1}^{k=\infty} \mathcal{R}^k exp[-(\pi k \frac{dg}{\Delta\sigma\sqrt{ln(2)}})^2] cos(2\pi k \frac{\sigma_0}{\Delta\sigma} cos\Theta)\right] \tag{B.13}$$

In a real instrument there are other effects which alter the resultant intensity distribution observed. We can represent the flux the detector sees by

$$\mathcal{I}(\sigma) = IA\epsilon\tau_L\Omega\tau_{e,\Omega}. \tag{B.14}$$

We have been discussing $\tau_{e,\Omega}$ the etalon transmission function. A is the useful area of the etalon, ϵ is the quantum efficiency of the detector, I is the irradiance of the source

(photons/unit time-unit area-steradian), τ_L is the etalon loss not included in $\tau_{e,\Omega}$. This is further convolved with the scanning aperture and surface defects functions. Integrating over the finite aperture

$$\mathcal{I}(\sigma) = IA\epsilon\tau_L \int_0^{2\pi} \int_0^{\Theta_2} \tau_e(\sigma) sin\Theta d\Theta d\Phi \tag{B.15}$$

for the open circular aperture. Including the, as yet unknown, defects represented by the coefficients d_k in the general coefficients a_k as

$$a_k = R^k s_k d_k$$

we can write

$$\tau_e(\sigma) = \mathcal{I}(\sigma) = \left[1 - \frac{\mathcal{A}_e}{(1-\mathcal{R})}\right]^2 \frac{(1-\mathcal{R})}{(1+\mathcal{R})} \left[1 + 2\sum_{k=1}^{\infty} a_k cos(2\pi k \frac{\sigma}{\Delta\sigma} cos\Theta)\right]. \tag{B.16}$$

The angle Θ is related to the order by

$$cos\Theta_2 = n_2/n_0 = (1 - f/2n_0)$$

and with $f^* = f/2$ the solution of (B.15) is given as

$$\mathcal{I}(\sigma) = IA\epsilon\tau_L 4\pi f^* {n_0}^{-1} \left[1 - \frac{\mathcal{A}_e}{(1-\mathcal{R})}\right]^2 \frac{(1-\mathcal{R})}{(1+\mathcal{R})}$$

$$\times \left[1 + 2\sum_{k=1}^{k=\infty} a_k sinc[2kf^*] cos(2\pi k[\frac{\sigma}{\Delta\sigma} - f^*])\right] \tag{B.17}$$

Where second order terms of $\sigma_0 - \sigma_i/\sigma_0$ have been neglected. This expression shows the expected sinc function response and the solid angle is seen as $\Omega = 4\pi f^*/n_0$. The coefficients 'a_k' are once again redefined to absorb the sinc function coefficients. Further the wavenumber dependence is transformed into sample space as the fsr or $\Delta\sigma \rightarrow T$ samples and the wavenumber $\sigma \rightarrow x$. Then

$$\mathcal{P}(x) = IA\epsilon\tau_L 4\pi f^* {n_0}^{-1} \left[1 - \frac{\mathcal{A}_e}{(1-\mathcal{R})}\right]^2 \frac{(1-\mathcal{R})}{(1+\mathcal{R})} \left[1 + 2\sum_{k=1}^{k=\infty} a_k cos(2\pi k[\frac{x - x_0}{T}])\right] \tag{B.18}$$

where we have set the constant $2\pi k f^* = x_0/T$. $P(x)$ now represents the total flux seen at a detector from a general quasi-monochromatic source represented by the coefficients s_k.

Appendix C Elementary derivations for optimization of the FPS

In this appendix the final expression (equation) for the total flux detected by a Jacquinot and Dufour type Fabry-Perot spectrometer with an open circular aperture is used to derive expressions for the uncertainties σ_v and σ_τ related to the best estimates of peak position x_0 and Gaussian widths dg. The final expressions for the uncertainties are given in terms of the normalized width parameters 'f^*' for the scanning aperture, 'a^*' the etalon reflectivity parameter, and 'dg^*' for the lineshape parameter. The calculation is demonstrated for unit valued "applications variables", such as intensity and etalon area, so that these enter as linear scaling factors in the final expressions. The derivations here follow the work done by Hernandez (1979, 1986).

From the general expression for the total flux detected (appendix 2)

$$\mathcal{P}(x) = IA\epsilon\tau_L 4\pi f^* {n_0}^{-1}\left[1-\frac{\mathcal{A}_e}{(1-\mathcal{R})}\right]^2\frac{(1-\mathcal{R})}{(1+\mathcal{R})}$$

$$\times\left[1+J+2\sum_{k=1}^{k=\infty}a_k cos(2\pi k[\frac{x-x_0}{T}])\right]. \qquad \text{(C.1)}$$

A new quantity 'J' has been introduced to represent the effects of light leakage 'B' where $J = B/I$. Now with $sinc(x) = sin(\pi x)/\pi x$

$$a_k = \mathcal{R}^k \times S_k \times d_k \times sinc(2kf^*)$$

$$S_k = exp[-\frac{\pi^2 k^2 (dg^*)^2}{ln(2)}]$$

$$d_k = dfc_k \times dfr_k = sinc(2kdf_C^*)\times exp[-\frac{\pi^2 k^2 df_G^{*2}}{ln(2)}].$$

Where I is the irradiance of the source (photons/unit time-unit area-steradian), A is the useful area of the etalon, ϵ is the quantum efficiency, τ_L is the etalon and system transmission losses, $f^* = f/2$ where f is the aperture size (in orders), n_0 is the central order of interference, T the profile periodicity in x units, and $\mathcal{A}_e$ is the etalon absorption and scattering coefficient.

For ease of demonstration represent this expression as

$$\mathcal{P}(x) = b_0 + 2\sum_{k=1}^{k=\infty} b_k cos(2\pi k[\frac{x - x_0}{T}]) \tag{C.2}$$

and the relation to the original a_ks is as follows

$$Q = IA\epsilon\tau_L 4\pi f^* n_0{}^{-1}\left[1 - \frac{\mathcal{A}}{(1-\mathcal{R})}\right]^2 \frac{(1-\mathcal{R})}{(1+\mathcal{R})} \tag{C.3}$$

Including B for the background (thermionic emission, light leakage, background or continuous light sources).

$$J = B/I \tag{C.4}$$

$$W = \int_0^T P(x)dx = Q(1+J)T \tag{C.5}$$

$$b_0 = Q(1+J) = W/T \tag{C.6}$$

$$b_k = Qa_k = Wa_k/[T(1+j)] \tag{C.7a}$$

the separate sine and cosine coefficients are

$$s_k = \frac{1}{T}\int_0^T \mathcal{P}(x)sin(\frac{2\pi kx}{T})dx = b_k sin(2\pi kx_0/T) \tag{C.8}$$

$$c_k = \frac{1}{T}\int_0^T \mathcal{P}(x)cos(\frac{2\pi kx}{T})dx = b_k cos(2\pi kx_0/T) \tag{C.9}$$

so that

$$b_k = \frac{1}{T}\int_0^T \mathcal{P}(x)cos(\frac{2\pi}{T}k(x - x_0))dx = Qa_k = ({s_k}^2 + {c_k}^2)^{1/2} \tag{C.7b}$$

$$x_{0_k} = \frac{1}{2\pi kT} tan^{-1}[s_k/c_k]. \tag{C.10}$$

The inherent noise in the values of $\mathcal{P}(x)$ is determined by Poisson statistics. Since we sample the spectrum in 'T' equidistant equal-time steps $\mathcal{P}(x)$ can be considered band-limited to $k = 1, 2, 3, \ldots, T$ and for sufficient counts ($\geq$ 20) at each step the uncertainty in the series coefficients is given by Bevington (1969) as

$$\sigma_{b_k}^2 = \sum_{i=0}^{i=T}\left[\sigma_{P(x_i)}^2\left(\frac{\partial b_k}{\partial P(x_i)}\right)^2\right]. \tag{C.11}$$

$$\left(\frac{\partial b_k}{\partial P(x_i)}\right) = \frac{1}{T}\frac{\partial}{\partial P(x)}\int_0^T \mathcal{P}(x)cos(\frac{2\pi}{T}k(x - x_0))dx = \frac{1}{T}cos(\frac{2\pi}{T}k(x - x_0))$$

so that

$$\sigma_{b_k}^2 = \sum_{i=0}^{i=T}\left[[b_0 + 2\sum_{k=1}^{k=\infty} b_k cos(2\pi k[\frac{x-x_0}{T}]\frac{1}{T^2}cos^2(\frac{2\pi}{T}k(x-x_0))\right]$$

$$= \frac{Q}{2T}[1 + J + a_{2k}cos^2(\frac{4\pi k x_0}{T})] \qquad \text{(C.13)}$$

and with the previous definitions leads to the uncertainty in the line position

$$\sigma_{x_{0_k}} = \frac{[1 + J - a_{2k}cos^2(\frac{4\pi k x_0}{T})]}{8QT\pi^2 k^2 {a_k}^2} \qquad \text{(C.16)}$$

defining

$$x_0 = [\sum_{k=1}^{k=N}\frac{x_{0_k}}{\sigma_{x_{0_k}}^2}]/[\sum_{k=1}^{k=N}\frac{1}{\sigma_{x_{0_k}}^2}] \qquad \text{(C.19)}$$

then

$$\sigma_{x_0}^2 = \left[\sum_{k=1}^{k=N}\frac{1}{\sigma_{x_{0_k}}^2}\right]^{-1} \qquad \text{(C.20)}$$

for the N statistically meaningful coefficients. By statistically meaningful one must consider the influence of the inherent statistical noise as the value of the coefficients decrease at some point the random fluctuations of the Poisson noise become significant in these spectral coefficients. Hernandez (1986) uses the t-test, for 100 points, and determines the criterion for the lack of statistical significance at the 95% confidence level occurs when

$$|b_k/\sigma_{b_k}| \leq 2.0. \qquad \text{(C.18)}$$

More discussion on the practical application of the determination of N is included in §2.3. Using the as yet unspecified value of $N = T/2$ as the Nyquist limit for T samples and substituting get

$$\sigma_{x_0}^2 = \left(8\pi^2 QT\left[\sum_{k=1}^{k=N}(a_k k)^2\left[1 + J - a_{2k}cos^2(4\pi k\frac{x_0}{T})\right]^{-1}\right]\right)^{-1}. \qquad \text{(C.22)}$$

Transforming this uncertainty to a velocity uncertainty with

$${\sigma_v}^2 = {\sigma_{x_0}}^2 c^2 {n_0}^{-2}$$

and rearranging obtain

$${\sigma_v}^2 IAT\epsilon\tau_L dg^{*2} n_0 = \left(32\frac{\pi^3}{c^2}\left[1 - \frac{\mathcal{A}}{(1-\mathcal{R})}\right]^2\frac{(1-\mathcal{R})}{(1+\mathcal{R})}\right)^{-1}$$

$$\times\left(f^*(dg^*)^2\left[\sum_{k=1}^{k=N}(a_k k)^2\left[1 + J - a_{2k}cos^2(4\pi k\frac{x_0}{T})\right]^{-1}\right]\right)^{-1}. \qquad \text{(C.24)}$$

This expression can be used to determine the best parameters for operation in observing

the line position. The numerical solutions of equation C.24 for different values of f^* was performed and one example for $f^* = .128$ is shown in Figure (C.1).

A similar treatment gives the expression for the temperature uncertainty except that since the lineshape is more critical the instrument coefficients must be separated from the source coefficients. Assuming that these coefficients are known so precisely that I may ignore any uncertainty they might otherwise introduce as small compared to the measurement uncertainty. From the source coefficients S_k one finds

$$2\pi^2 n_0^2 \mathrm{k} A\tau/Mc^2 = \pi^2 \frac{(dg^*)^2}{ln(2)}$$

and from earlier definitions

$$b_k = Qa_k = Q\mathcal{R}^k \times d_k \times sinc(2kf^*) \times exp[-k^2\gamma\tau]$$

for $\gamma = 2\pi^2 n_0^2 \mathrm{k} A/Mc$.

Defining a new quantity U_k as

$$U_k = ln(\frac{b_k}{d_k}) = ln(Q) - k^2\gamma\tau$$

such that

$$\sigma_{U_k}^2 = \frac{\sigma_{b_k}^2}{{b_k}^2} + \frac{\sigma_{d_k}^2}{{d_k}^2}$$

giving

$$\sigma_{U_k}^2 = \frac{[1 + J + a_{2k}cos^2(4\pi k\frac{x_0}{T})]}{2QT{a_k}^2}. \tag{C.29}$$

where as stated the $\sigma_{d_k}^2/{d_k}^2$ has been ignored. The best estimate of τ is then given by

$$\tau = \frac{1}{\gamma}\left[\left(\sum_{k=1}^{k=N} U_k w_k \sum_{k=1}^{k=N} k^2 w_k\right)\sum_{k=1}^{k=N} w_k - \sum_{k=1}^{k=N} U_k k^2 w_k\right]$$

$$\times\left[\sum_{k=1}^{k=N} k^4 w_k - \frac{\left(\sum_{k=1}^{k=N} k^2 w_k\right)^2}{\sum_{k=1}^{k=N} w_k}\right]^{-1}. \tag{C.30}$$

with $w_k = 1/\sigma_{U_k}^2$. Further manipulation gives

$$(\frac{\sigma_\tau}{\tau})^2 \frac{IAT\epsilon\tau_L}{n_0} = \left(8\pi^5\left[1 - \frac{\mathcal{A}_e}{(1-\mathcal{R})}\right]^2 \frac{(1-\mathcal{R})}{(1+\mathcal{R})^{-1}}\right)^{-1}$$

$$\times \left(f^*(dg^*)^4 \left[\sum_{k=1}^{k=N} w_k k^4 - \left(\sum_{k=1}^{k=N} w_k k^2 \right)^2 \left(\sum_{k=1}^{k=N} w_k \right)^{-1} \right] \right)^{-1} \qquad \text{(C.33)}$$

where in this equation

$$w_k = {a_k}^2 \left[1 + J + a_{2k} cos^2(4\pi k \frac{x_0}{T}) \right]^{-1}. \qquad \text{(C.34)}$$

Expression C.33 is proportional to the slope in a linear least-squares deconvolution (Bevington, (1969)). (For a purely Doppler-broadened profile the slope is proportional to the temperature.)

The numerical solutions of equation C.33 for several values of f^* was performed as for equation C.24 and one of these, for $f^* = .064$ is shown in Figure (C.2).

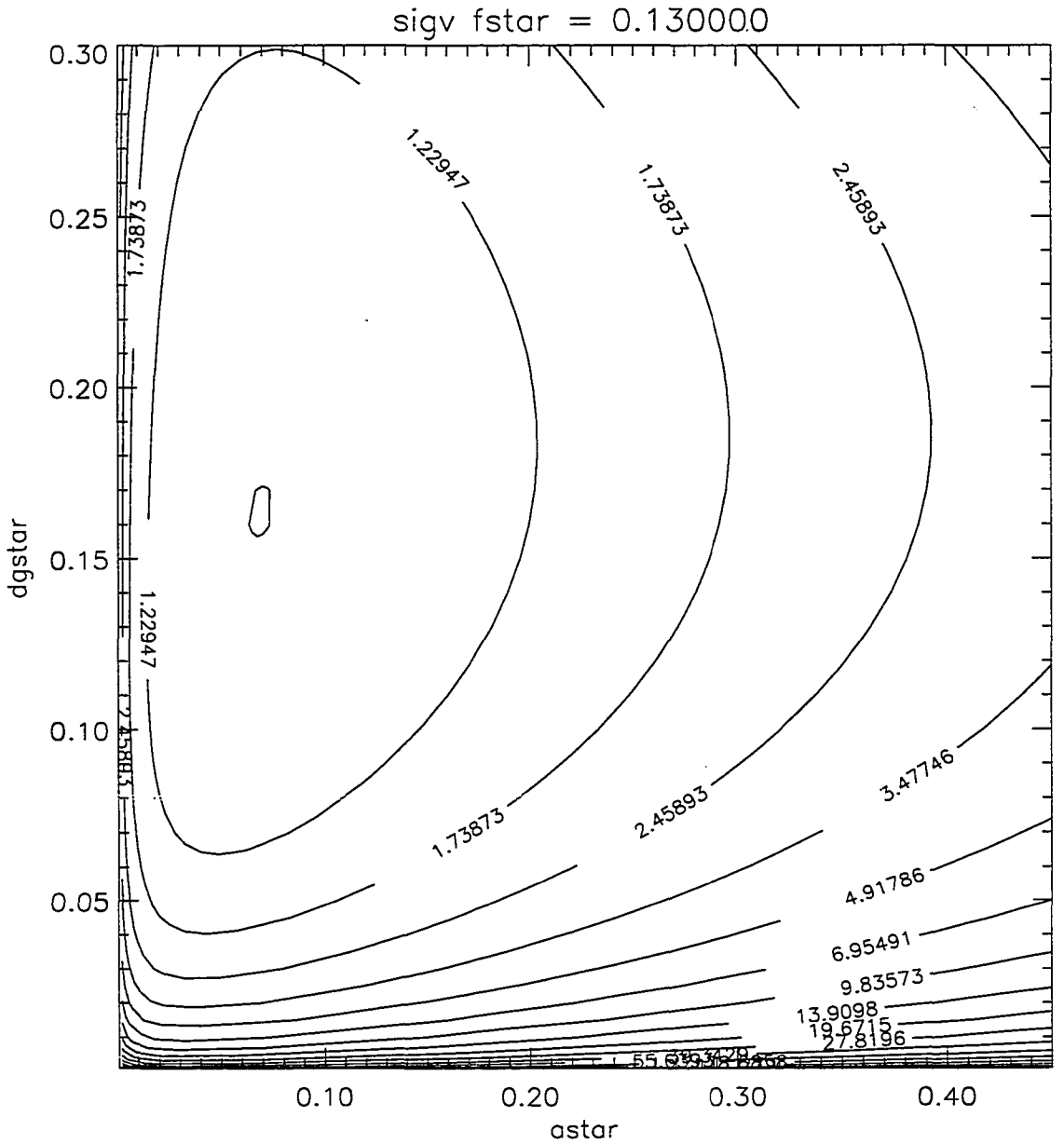

Figure C.1 Uncertainty topology for the determination of the line center for a single-line profile. $\sigma_v \times \sqrt{IAT\epsilon\tau_L dg^{*-2} n_0}$ contours indicate the uncertainty as a function of dg^* and a^*. The contours are separated by factors of $\sqrt{2}$. Here for a value of $f^* = .130$ the minimum is .87 at $dg^* \sim .107$ and $a^* \sim .07$.

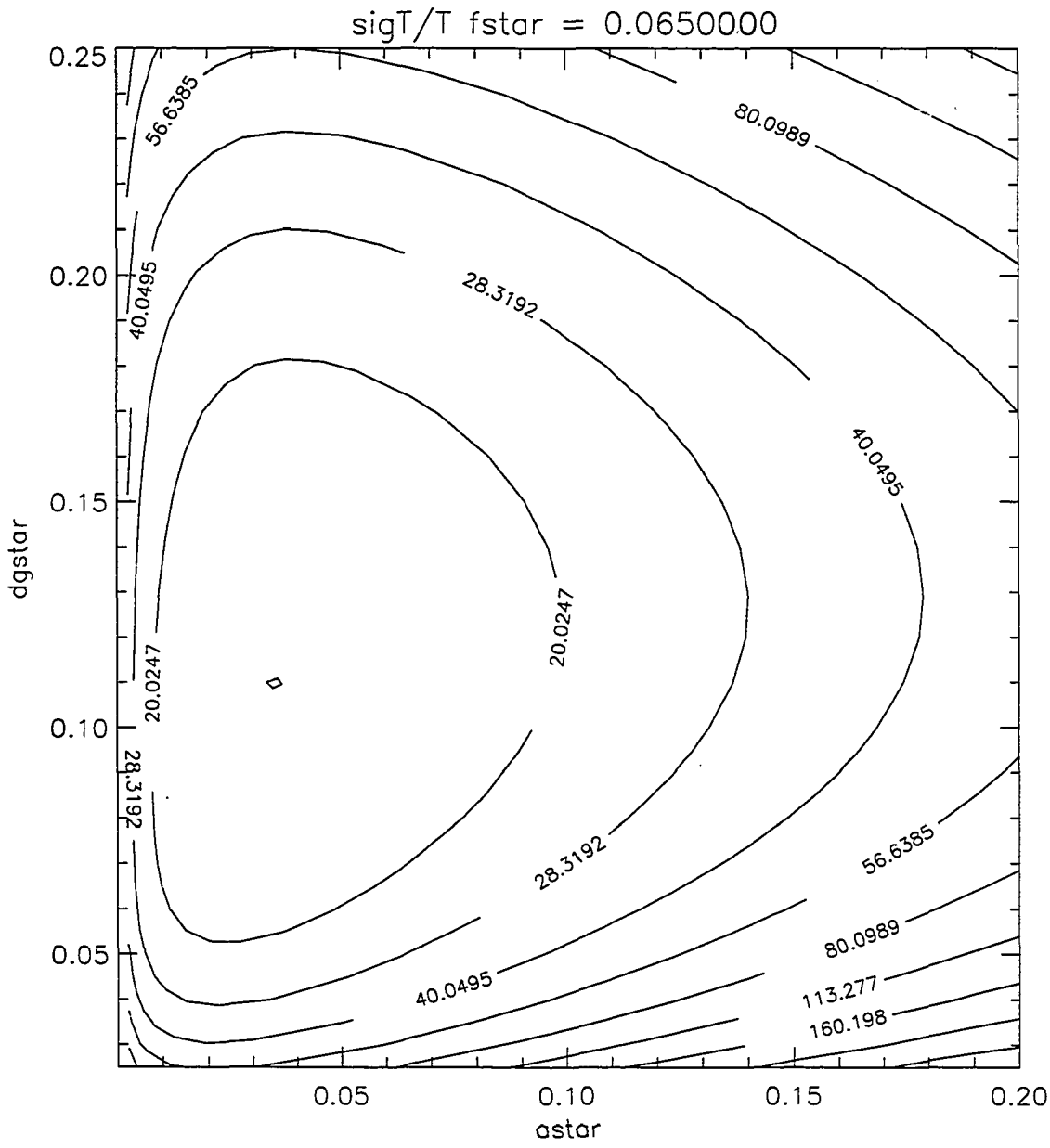

Figure C.2 Uncertainty topology for the determination of the line width for a single-line profile. $\frac{\sigma_T}{T} \times \sqrt{IAT\epsilon\tau_L n_0{}^{-1}}$ contours indicate the uncertainty as a function of dg^* and a^*. The contours are separated by factors of $\sqrt{2}$. Here for a value of $f^* = .065$ the minimum is 14.19 at $dg^* \sim .11$ and $a^* \sim .035$.

Appendix D Derivation of Laplace's tidal equations

Outline of the following derivations

In this appendix the 'primitive equations' for atmospheric motions are derived using the equations of motion, continuity of mass, the first law of thermodynamics, the ideal gas equation and some simplifying assumptions. I follow the developments of Holton, (1975), Andrews, (1987), Volland, (1988), and Longuet-Higgins, (1968), to obtain Laplace's tidal equations for the oscillations of a thin of fluid on the surface of a rotating sphere.

The basic hydrodynamic and thermodynamic laws of a single ideal gas of constant molecular weight 'M' may be represented by, e.g., Volland (1976),

$$\frac{d\mathbf{v}}{dt} = -2\Omega \times \mathbf{v} - \frac{1}{\rho}\nabla p + g + F$$

for the equation of motion;

$$\frac{d\rho}{dt} = -\rho \nabla \cdot \mathbf{v}$$

expressing mass continuity;

$$\frac{dT}{dt} = -2(\gamma - 1)T\nabla \cdot \mathbf{v} + \frac{Q}{c_v}$$

the first law of thermodynamics; and

$$p = \rho R T$$

for an ideal gas.

In these $\frac{d}{dt} = \frac{\partial}{\partial T} + \mathbf{v} \cdot \nabla$ is the total time derivative, $\mathbf{v} = (u, v, w)$ is the velocity vector as (east, north, up), Ω is the vector of the Earth's rotation and $|\Omega| = 7.292 \times 10^{-5} s^{-1}$, $\mathbf{F}$ is the momentum force per unit mass, Q is the net heat input per unit mass or net heat flux divergence, $\gamma = \frac{c_p}{c_v}$ the ratio of specific heats, and $R = \overline{R}/M = c_p - c_v$ for the universal gas constant, $\overline{R}$ Simplifications of the fundamental equations of motion using scale analysis are made. These are the assumption of small temperature amplitudes as compared to the mean state temperature, (rarely are the amplitudes expected to reach 15% of the mean state in the UMA). In addition to this the vertical momentum equation was replaced by hydrostatic balance, the vertical component of the Coriolis force is neglected as small outside equatorial regions. Finally a thin shell approximation is used and the distance r from any point in the atmosphere to the center of the earth was replaced by a mean radius a, and $z = r - a$ is the height above the ground.

Derivation of the primitive equations

In addition the vertical coordinate $z^* = r - a$ is not used and the log-pressure coordinate z is

$$z \equiv -Hln(p/p_s) \tag{D.1}$$

$$p = p_s e^{-z/H}, \tag{D.2}$$

With z the vertical coordinate and spherical coordinates in the horizontal the primitive equations become (Holton, 1975):

$$\frac{Du}{Dt} - \left(f + \frac{utan\phi}{a}\right)v + \frac{\Phi_\lambda}{acos\phi} = X \tag{D.3a}$$

$$\frac{Dv}{Dt} + \left(f + \frac{utan\phi}{a}\right)u + \frac{\Phi_\phi}{acos\phi} = Y \tag{D.3b}$$

$$\Phi_z = H^{-1}R\Theta e^{-\kappa z/H} \tag{D.3c}$$

$$\frac{[u_\lambda + (vcos\phi)_\phi]}{acos\phi} + \frac{(\rho_0 w)_z)}{\rho_0} = 0 \tag{D.3d}$$

$$\frac{D\theta}{Dt} = Q. \tag{D.3e}$$

These are respectively the momentum balance in the zonal and meridional directions, hydrostatic balance in the vertical, continuity of mass, and the thermodynamic relation between diabatic heating and the material rate of change of potential temperature. Φ is the geopotential

$$\Phi \equiv \int_0^{z^*} g dz^* \tag{D.4}$$

and θ is the potential temperature

$$\theta \equiv T(p_s/p)^\kappa \tag{D.5}$$

where $\kappa \equiv R/c_p \approx 2/7$ and c_p is the specific heat at constant pressure.

The horizontal coordinates used are: (λ, ϕ) = (longitude, latitude). The velocity components used are:

$$(u, v, w) \equiv \left[(a cos\phi)\frac{D\lambda}{Dt}, a\frac{D\phi}{Dt}, \frac{Dz}{Dt}\right], \tag{D.6}$$

where $\frac{D}{Dt}$ is the material derivative, of time rate of change following the fluid motion, whose expression in the present coordinates is

$$\frac{D}{Dt} \equiv \frac{\partial}{\partial t} + \frac{u}{a cos\phi}\frac{\partial}{\partial \lambda} + \frac{v}{a}\frac{\partial}{\partial \phi} + w\frac{\partial}{\partial z}. \tag{D.7}$$

The Coriolis parameter (the vertical component of the earth's rotation vector): $f \equiv 2\Omega sin\phi$, where $\Omega = 2\pi/sidereal\ day = 7.292 \times 10^{-5} s^{-1}$ is the earth's rotation rate.

(X, Y) is the unspecified horizontal components of friction, or other nonconservative mechanical forcing.

$Q \equiv (J/c_p)e^{\kappa z/H}$ is the diabatic heating term, where J is the diabatic heating rate per unit mass, which in the middle atmosphere equals the net radiative thermal conduction term; note that J/c_p is expressed in units of Kelvins/day.

$\rho_0(z) \equiv \rho_s e^{-z/H}$ is the basic density, where $\rho_s \equiv p_s/RT_s$. Thus $\rho_0 \equiv p/RT_s$ by eq. (D.2).

Derivation of the thermal wind equation

For steady, purely zonal, symmetric basic unforced flow, $\overline{u} = \overline{u}_0$, $\overline{w}_0 = \overline{v}_0 = 0$ the primitive equations (D.3b,c) can be manipulated and to give the thermal wind eqn (D.11c) as:

$$\overline{u}_0\left[\frac{(\overline{u}_0 tan\phi)}{a} + f\right] + \frac{\overline{\Phi}_{0\phi}}{a} = 0 \tag{D.11a}$$

$$\overline{\Phi}_{0z} = \frac{R\overline{\theta}e^{-\kappa z/H}}{H} \tag{D.11b}$$

in the spherical primitive case. Eliminating $\overline{\Phi}_0$ here gives

$$\frac{\partial \overline{u}_0}{\partial z}\left[\frac{(2\overline{u}_0 tan\phi)}{a} + f\right] = \frac{-R}{aH}\frac{\partial \overline{\theta}_0}{\partial \phi}e^{-\kappa z/H} = \frac{-R}{aH}\frac{\partial \overline{T}_0}{\partial \phi}. \tag{D.11c}$$

Derivation of the linearized spherical primitive equations

Consider all primed quantities of order $\alpha \ll 1$ and put

$$u = \overline{u}_0 + u' + O(\alpha^2), \qquad v = v' + O(\alpha^2).$$

Substitution into equations (D.3) with equations (D.11) gives

$$\overline{D}u' + v'\left[\frac{(\overline{u}cos\phi)_\phi}{acos\phi} - f\right] + \overline{u}_z w' + \frac{\Phi'_\lambda}{acos^2\phi} = X' \tag{D.12a}$$

$$\overline{D}v' + \overline{u}\left[\frac{(2\overline{u}tan\phi)}{a} + f\right] + \frac{\Phi'_\phi}{a} = Y' \tag{D.12b}$$

$$\Phi'_z = \frac{R\theta' e^{-\kappa z/H}}{H} \tag{D.10c}$$

$$\frac{[u'_\lambda + (v'cos\phi)_\phi]}{acos\phi} + \frac{(\rho_0 w')_z}{\rho_0} = 0 \tag{D.12d}$$

$$\overline{D}\theta' + \frac{\overline{\theta}_\phi v'}{a} + \overline{\theta}_z w' = Q'. \tag{D.12e}$$

Terms of $O(\alpha^2)$ have been neglected, $\overline{u}_0$ and $\overline{\theta}_0$ have been replaced with $\overline{u}$ and $\overline{\theta}$ as well as

$$\overline{D} \equiv \frac{\partial}{\partial t} + \frac{\overline{u}}{acos\phi}\frac{\partial}{\partial\lambda} \tag{D.13}$$

Now to examine wave disturbances to a resting spherical atmosphere we set the basic flow $\overline{u} = 0$; thus $\overline{\theta}_\phi$ also vanishes by eq. (D.11c). Using eq. (D.12c) to substitute for θ' in in Eq. (D.12e) and use the definition of the static stability $N^2 \equiv H^{-1}R\overline{\theta}_z e^{-\kappa z/H}$ to replace $\overline{\theta}_z$ in Eq. (D.12e) become

$$u'_t + fv' + \frac{\Phi'_\lambda}{acos\phi} = X' \tag{D.14a}$$

$$v'_t + fu' + \frac{\Phi'_\phi}{a} = Y' \tag{D.14b}$$

$$\frac{[u'_\lambda + (v'cos\phi)_\phi]}{acos\phi} + \frac{(\rho_0 w')_z}{\rho_0} = 0 \tag{D.14c}$$

$$\Phi'_{zt} + N^2 w' = \kappa J'/H \tag{D.14d}$$

where $\kappa J'/H$ also equals $\frac{RQ'e^{-\kappa z/H}}{H}$.

For a conservative or unforced case set $X' = Y' = J' = 0$ and use separation of variables to separate the vertical from the horizontal and time dependence

$$(u', v', \phi') = e^{z/2H} U(z)[\tilde{u}(\lambda, \phi, t), \tilde{v}(\lambda, \phi, t), \tilde{\Phi}(\lambda, \phi, t)] \tag{D.15a}$$

and

$$w' = e^{z/2H} W(z) \tilde{w}(\lambda, \phi, t) \tag{D.15b}$$

Substitution of eqn. (D.15a) into eqns. (D.14a,b) (with $X' = Y' = 0$ and cancellation of the $e^{z/2H}U$ factor yields the following two equations,

$$\tilde{u}_t - f\tilde{v} + \frac{\tilde{\Phi}_\lambda}{a cos\phi} = 0 \tag{D.16a}$$

$$\tilde{v}_t + f\tilde{u} + \frac{\tilde{\Phi}_\phi}{a} = 0 \tag{D.16b).}$$

Substitution of eqn. (D.15a,b) into eqns. (D.14c,d) (with $J' = 0$) yields the following pair of equations,

$$U(acos\phi)^{-1} [\tilde{u}_\lambda + (\tilde{v} cos\phi)_\phi] + \left(W_z - \frac{W}{2H}\right) \tilde{w} = 0 \tag{D.17a}$$

$$\left(U_z - \frac{U}{2H}\right) \tilde{\Phi}_t + N^2 W \tilde{w} = 0 \tag{D.17b}$$

Without loss of generality we can choose

$$U = \frac{dW}{dz} - \frac{W}{2H} \tag{D.18a}$$

and substitution into eqn. (D.17b) yields

$$-\left(W_{zz} - \frac{W}{4H^2}\right) / N^2 W = \tilde{w} / \tilde{\Phi}_t = (gh)^{-1} \tag{D.18b}$$

where $(gh)^{-1}$ is a separation constant and h has dimensions of length. Then eqns (D.18a,b) and eqn (D.17a) give

$$(acos\phi)^{-1} [\tilde{u}_\lambda + (\tilde{v} cos\phi)_\phi] + (gh)^{-1} \tilde{\Phi}_t = 0 \tag{D.16c}$$

and the outer terms in eqn (D.18b) yield

$$\frac{d^2 W}{dz^2} + \left(\frac{N^2}{gh} - \frac{1}{4H^2}\right) W = 0 \tag{D.19a}$$

Equations (D.16a-c) for the horizontal and time structure are called *Laplace's tidal equations*, and are identical to those for small disturbances to a thin layer of fluid on a sphere,

where the fluid has mean depth h much less than the radius a of the sphere, $\tilde{u}$ and $\tilde{v}$ are the velocity components, and $g^{-1}\tilde{\Phi}$ is the departure of the fluid depth from its mean value. The separation constant h is called the *equivalent depth.* Equation (D.19a) is called the *vertical structure equation*; from eqs. (4.2.2), (D.15), and (D.18, the lower boundary condition, $(z = 0)$, can be written

$$\frac{dW}{dz} + \left(\frac{RT(0)}{gh} - \frac{1}{2}\right)\frac{W}{H} = 0 \qquad \text{(D.19b)}$$

Appendix E Aperture Calculations

Here I will relate the physical size of the aperture to the aperture finesse $\mathcal{N}_{ap}$.

Recall the equation for interference:

$$2nt\cos(\theta) = p\lambda \tag{E.1}$$

where $n = 1$ is the index of refraction, $t = 20mm$ is the gap, p is the order of interference, and $\Delta\sigma$ is the spectral width (fwhh) in cm^{-1} (or Kaysers).

Then the central order of interference p_0, (when $\theta = 0$), gives

$$p_0 = \frac{2t}{\lambda}. \tag{E.2}$$

For $\theta \approx 0$ using $\cos(\theta) \approx 1 - \theta^2/2$ get

$$p = \frac{2t}{\lambda}(1 - \frac{\theta^2}{2}) = p_0 - \frac{t}{\lambda}\theta^2.$$

The fractional order change, Δp, is

$$\Delta p = p_0 - p = \frac{t}{\lambda}\theta^2, \text{ since } p_0 > p. \tag{E.3}$$

Also for "small" θ $\cos(\theta) \approx 1$ and

$$\frac{2t}{p} \approx \lambda$$

so

$$2t\frac{dp}{-p^2} = d\lambda$$

Substituting $2t/\lambda$ for p and $(t/\lambda)\theta^2$ from equation (E.3) for dp get

$$-2\frac{d\lambda}{\lambda} = \theta^2. \tag{E.4}$$

Now $\sigma = 1/\lambda$ so

$$d\sigma = -\frac{1}{\lambda^2}d\lambda \tag{E.5}$$

whereby using equations D4 and D5 we get

$$2\lambda d\sigma = \theta^2. \tag{E.6}$$

Finally, since

$$\tan(\theta) = \left(\frac{1}{2}\right) ap/L,$$

where ap is the aperture diameter and L is the focal length of the lens forming the

interference fringes. Then for "small" θ

$$\theta = \tan^{-1}\left(\sqrt{2\lambda d\sigma}\right) \approx \sqrt{2\lambda d\sigma} \approx \frac{ap}{2L}. \qquad \text{(E.7)}$$

For the instrument at South Pole $L \approx 65cm$ and $t \approx 2cm$. With this gap the FSR is 250 mK. Then for a .225 cm aperture at $\lambda = 5.577 \times 10^{-5} cm$ I find $d\sigma = .027\ cm^{-1}$ or 27 mK for a finesse $\mathcal{N}_{ap} \sim 10.8$. And for $\lambda = 8.399 \times 10^{-5} cm$ I find $d\sigma = 18$ mK for a finesse $\mathcal{N}_{ap} \sim 13.8$.

Some further calculations give

$$\text{central order } p_0 = \frac{2t}{\lambda} = 47624.7172$$

for $\lambda = 8.399 \times 10^{-5} cm$ and at the edge of the aperture

$$\text{order } p = \frac{2t}{\lambda}\cos\left[\frac{ap}{2L}\right] = 47624.6458$$

giving a fractional order change across the aperture of

$$\Delta p = .0714.$$